THE SUBSURFACE RESISTIVITY STRUCTURE OF KILAUEA VOLCANO, HAWAI'I

A DISSERTATION SUBMITTED TO THE GRADUATE DIVISION OF THE
UNIVERSITY OF HAWAII IN PARTIAL FULFILLMENT
OF THE REQUIREMENTS FOR THE DEGREE OF

DOCTOR OF PHILOSOPHY

IN GEOLOGY AND GEOPHYSICS

May 1982

By

James Puupai Kauahikaua

Dissertation Committee:

Eduard Berg, Chairman
Fred Duennebier
George P. L. Walker
Peter Crooker
Frank C. Frischknecht

ACKNOWLEDGEMENTS

I especially thank Frank Frischknecht for the opportunity to work for the U.S. Geological Survey and for his constant encouragement, Charlie Zablocki for the opportunity to participate in his Kilauea projects and his guidance, and Dallas Jackson for his considerable logisitic help and support and for sharing his intimate knowledge of Kilauea volcano. I am also grateful for the cooperation and encouragement of the entire staff of the Hawaiian Volcano Observatory, and Craig Crissinger in particular. Jerry Bradley, Dick Sneddon, and the U.S.G.S. electronics lab in Denver, Colorado built and maintained the electronic equipment. Early versions of the manuscript were greatly improved by the review efforts of the committee chairman, Ed Berg. Jill Mahoney drafted all the figures and Jan Danek typed the final manuscript. Finally, I am deeply indebted to my wife, Sari, for her persevering support and encouragement during this entire project.

ABSTRACT

Using the controlled-source electromagnetic technique, resistivity soundings were obtained at 49 locations around the summit caldera and upper rift zones of Kilauea volcano. Each sounding consisted of vector measurements of the magnetic field induced by a large-moment horizontal loop current source at discrete frequencies between 0.04 and 8 Hz. The source-to-sensor distances ranged from 2.5 to 13 km. The data have been computer-inverted to produce a best-fitting horizontally layered earth model.

Although each sounding's interpretation is different in detail, the volcano's structure appears simple and can be represented by four, subhorizontal layers. The surface layer is highly resistive and coincides with the dry, basaltic overburden. At a depth of 500 to 1000 m, resistivities decrease abruptly to between 30 and 50 ohm-m, marking the top of the water-saturated zone. The third layer occurs between 2 and 3 km depth and has a resistivity of less than 10 ohm-m and a total conductance of about 200 mhos. This layer is underlain everywhere by highly resistive rock to a depth of at least 6 km, the estimated limit of penetration by this study. Pockets of low resistivity (less than 20 ohm-m) occur irregularly within the high-resistivity basement.

Because of its widespread occurrence, the shallower conductive layer (layer 3) is probably water-saturated rock at high temperature; however, the possibility of thin, intruded sills of magma contributing to the low resistivities cannot be refuted. The pockets of low resistivity within layer 4 occur at a depth of 5 km and are believed to be

magma chamber 2 to 3 km deeper than models derived from earthquake hypocenter location and surface deformation studies.

TABLE OF CONTENTS

TABLE OF CONTENTS (continued)

LIST OF TABLES

LIST OF FIGURES

LIST OF FIGURES (continued)

LIST OF FIGURES (continued)

LIST OF FIGURES (continued)

LIST OF FIGURES (continued)

LIST OF ABBREVIATIONS AND SYMBOLS

CSEM	controlled-source electromagnetic
$\vec{E}$	electric field (V/m)
$\vec{H}$	magnetic field intensity (A/m)
ϵ	dielectric permittivity
μ	magnetic susceptibility
t	time (s)
$\vec{J}$	electric current density
f	frequency (Hz)
ω	$=2\pi f$, frequency (radians)
σ	electrical conductivity, (mho/m)
ρ	$=1/\sigma$, resistivity (ohm-m)
r,ϕ,z	cylindrical coordinates
d	layer thickness
h	layer depth
a	source loop radius
i	$=\sqrt{-1}$, if not used as a subscript
$I(\omega)$	source current (A)
$\delta(x)$	Kronecker delta, $\delta(o)=1$, $\delta(x)=0$ for $x\neq 0$
r	distance to receiver from source center
k_i^2	$=\omega^2\mu_i\epsilon_i - i\omega\mu_i\sigma_i \cong -i\omega\mu_i\sigma_i$
u_i^2	$=\lambda^2 - k_i^2$
λ	Hankel transform variable
H_p	primary magnetic field intensity
H_z^o	z-component of primary magnetic field
δ	$=\sqrt{2/\mu_0\sigma\omega}$
B	$=r/\delta$, induction number
VMD	vertical magnetic dipole
ϕ_r,ϕ_ϕ,ϕ_z	phase of r,ϕ,z components of magnetic field
α	tilt angle
ϵ_v	vertical ellipticity
β	strike angle
ϵ_h	horizontal ellipticity

LIST OF ABBREVIATIONS AND SYMBOLS (continued)

nT	nanoTesla
Ωm	ohm-m
m	number of layers in inversion model
n	number of data points used in each sounding inversion
k	number of model parameters sought by inversion
ξ	sum of the squared residuals weighted by their errors

I. INTRODUCTION

Kilauea is an active, basaltic shield volcano on the island of Hawai'i. It has two rift zones radiating to the east and southwest from a well-developed summit caldera. Volcanic eruptions generally occur within these features. The dynamic state of the volcano is also revealed by several active fault systems on Kilauea's edifice. A summary geologic map of Kilauea volcano, showing volcanic as well as tectonic features, is shown in Figure 1.

Part of the volcanic structure of Kilauea has been inferred from detailed studies of ground deformation. The summit area usually inflates slowly prior to eruptions and deflates rapidly during eruption or intrusion. The pattern of deformation during these inflation-deflation cycles is consistent with the expansion and contraction of a spherical volume at a depth of 2 to 3 km beneath the area immediately southeast of Halema'uma'u (Fiske and Kinoshita, 1969). This physical model strongly suggests that magma slowly accumulates in a localized area beneath the summit and is at least partially extruded from the area during eruptions or intrusions.

Subsurface magma movements can also be inferred from earthquake hypocenter locations. A significantly greater number of shallow (less than 5 km deep) earthquakes occur during times of inflation than during times of no summit inflation. Earthquake swarms frequently occur immediately before eruptions and generally in two linear zones trending to the southeast and south from the summit storage area (Koyanagi and others, 1976; Ryan and others, 1981). These zones are

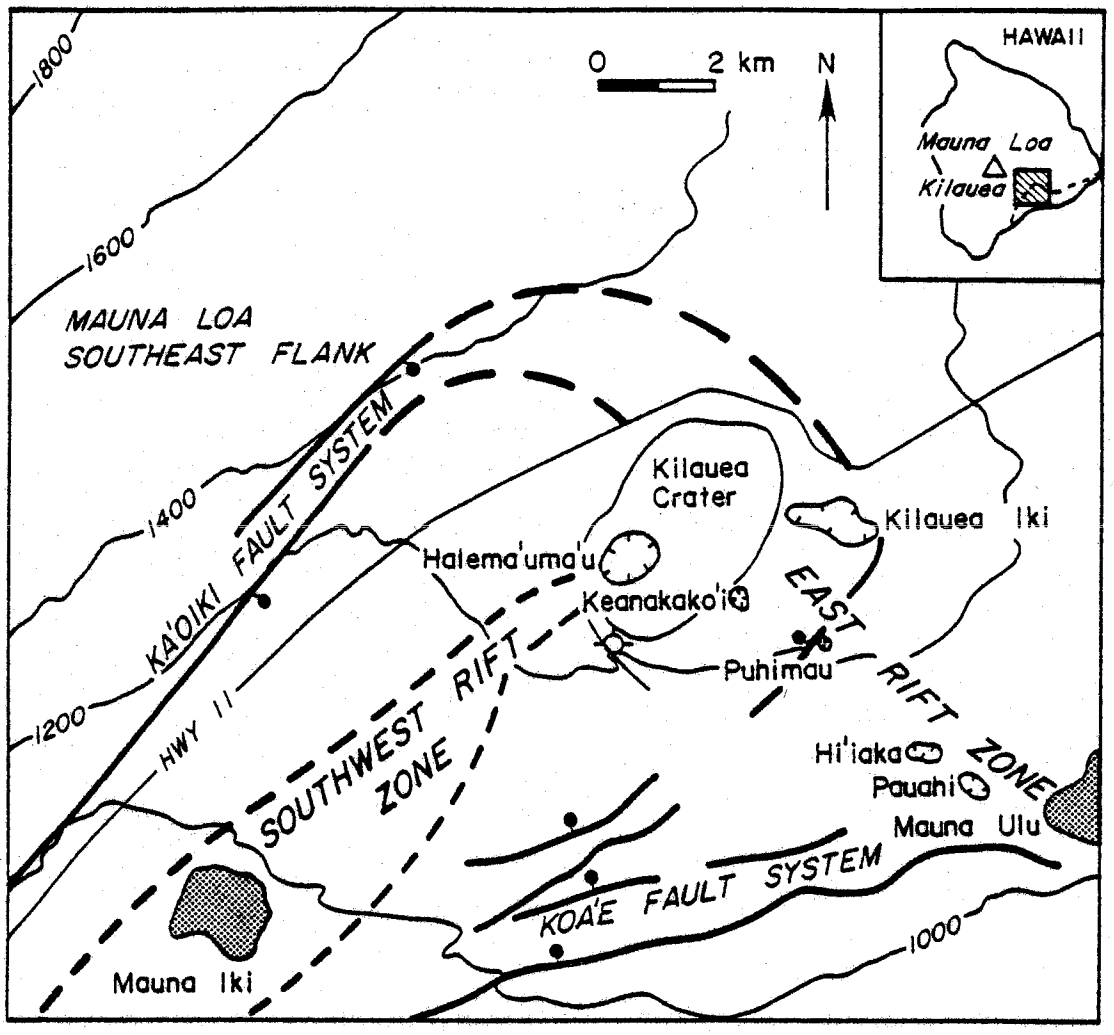

Figure 1. Geologic map of the summit area of Kilauea volcano, Hawai'i showing the crater and its two rift zones. Also shown are two active fault systems - the Ka'oiki and the Koa'e.

located adjacent to eruptive features. If we assume that they are caused by hydraulic opening of fractures via increases in magma pressure (Ryan and others, 1981), then the zones outline the principal lateral intrusive conduits within Kilauea.

The general island structure has also been investigated by geophysical means. Seismic refraction results show that the oceanic crust is depressed beneath Hawai'i; the base of the crust is about 12 km deep beneath Kilauea and dips about 2° to 3° to the northwest (Zucca and Hill, 1980). With an average crustal thickness of about 5 km, the volcanic pile must be about 7 or 8 km thick. Other studies show that the rift zones and summit areas of Hawai'i's volcanoes are underlain by high-velocity (Zucca and Hill, 1980; Crosson and Koyanagi, 1979; Ellsworth and Koyanagi, 1977), high-density (Kinoshita and others, 1963) cores that extend down to the base of the volcanic pile. These cores are probably the result of intense intrusion into the mass of previously erupted lava flows.

Although much is known about the physical structure and mechanical state of the rocks beneath Kilauea, very little is known about their thermal state. A notable exception is the identification of a low-velocity layer at the base of the crust beneath the island of Hawai'i which may be due to abnormally high mantle temperatures (Crosson and Koyanagi, 1979). Of course, inferences can be made about subsurface thermal conditions from the mechanical studies; for example, magma storage areas and conduits must be at temperatures of at least 1050°C. Nevertheless, independent studies of Kilauea's thermal regimes would clearly be useful.

A definitive approach to the determination of deep, subsurface temperatures is the study of electrical resistivities within the volcano. Resistivities of dry basalts decrease approximately exponentially with increasing temperature (Rai and Manghnani, 1977), offering good resolution of subsurface temperatures if the subsurface resistivities can be closely determined. The presence of water reduces basalt resistivities even further; however, unless the water is extremely saline, molten magma has an even lower resistivity.

Three resistivity surveys have already been completed at Kilauea's summit, but none detected any magma bodies directly. The first two studies, both time-domain electromagnetic (TDEM) sounding surveys (Jackson and Keller, 1972; Keller and Rapolla, 1976) of the southwest rift and summit area, were interpreted in terms of a general three-layer model with characteristic resistivities for each layer, but variable depths to the layers. The first layer was assumed to be resistive and therefore "transparent" to the technique. The second layer had a resistivity of 10 to 30 ohm-m and was interpreted as rock saturated with water below the water table. The third layer was found at a depth between 600 and 1500 m and had a resistivity of 4 to 10 ohm-m. This last layer is shallowest beneath the southwest rift zone, and above the inflation center southeast of Halema'uma'u. It represents a decrease of the water resistivity within the basalt-flow pores.

More recently, a direct-current (DC) bipole mapping survey over the upper portions of both rift zones, the summit area, and adjoining flanks of Mauna Loa delineated a vertical resistivity contact between

Kilauea and Mauna Loa (Keller and others, 1977). Resistivities drop to less 20 ohm-m below a depth of 600 to 1500 m beneath Kilauea; a similar drop occurs at much greater depth beneath Mauna Loa's flanks. Resistive basement was detected at a depth of 2 to 2.5 km beneath Kilauea south of the summit caldera.

The results of the two surveys are in pretty good agreement, in spite of the fact that the DC survey was not nearly as detailed as the TDEM survey. Each finds a low resistivity zone at a depth between 600 and 2500 m beneath every area of Kilauea. It is surprising that no laterally-confined low-resistivity bodies representing magma storage areas or conduits were delineated because the earthquake and ground deformation data both suggest that the top of the summit magma storage chamber may be as shallow as 2 km. Magma has a very low resistivity (Frischknecht, 1967; Rai and Manghnani, 1977) and should have been distinguishable by either type of survey.

One problem with DC studies is inadequate resolution at great depths. The combined surveys establish that the vertical section is basically composed (from the top) of a resistive overburden, a thick conductive layer, and a resistive basement below 2500 m. Any DC technique requires interelectrode spacings equal to several times the overburden thickness just to resolve the resistivity of a conductive layer below resistive overburden; even larger spacings would be needed to obtain information below the conductive layer. Very small but shallow lateral changes in resistivity near any of the electrodes can have a masking effect at these larger spacings making it difficult to reliably obtain deep resistivity information with a DC technique.

This problem is particularly acute for the bipole-mapping method (Keller and others, 1975).

An electromagnetic (EM) method is much better suited for penetrating resistive overburden than is a DC method. If measurements are restricted to magnetic fields, then the method is especially sensitive to bodies in which currents can be induced to flow inductively; that is, the method is sensitive to low-resistivity bodies, an ideal attribute for a tool to be used for the determination of volcanic structure where magma is present. Another advantage is that, compared with DC methods, EM methods require relatively short spacings to penetrate resistive overburden (Frischknecht, 1967, p. 17), and by varying the frequency at which the measurements are made an entire depth sounding can be obtained at a single location. EM methods therefore appear well suited for volcanological work.

The TDEM surveys already completed (Jackson and Keller, 1972); Keller and Rapolla, 1976), apparently did not penetrate much deeper than 2 km. The specific reasons for the relatively shallow penetration in these studies are not clear; however, so many advances in instrumentation and computer-aided interpretation have been made since then that a fourth EM survey of Kilauea was thought to be warranted and is the subject of this dissertation.

The objective of this newest study was to determine the resistivity structure beneath Kilauea volcano to a greater depth and with greater precision than the previous studies in the hope of outlining the magma chamber and conduits by their characteristically low resistivity. The chosen approach was a sounding survey of the summit

and upper rift zones of Kilauea, as well as the adjoining flank of Mauna Loa, using a controlled-source electromagnetic (CSEM) method. The field measurements were made over a range of discrete frequencies, rather than a range of times as in the TDEM method, because of the simpler instrumentation requirements. Two or three orthogonal components of the magnetic field were measured rather than one, because the additional data allowed deeper penetration and better resolution of lateral resistivity changes.

II. FUNDAMENTALS OF THE CSEM TECHNIQUE

The basis for most electromagnetic techniques currently used for geophysical exploration is the phenomena that electrical currents are induced in the earth by time-varying electric or magnetic sources. The nature and distribution of these currents is dependent only upon the electrical resistivities within the earth and the frequency and distribution of the source energy; therefore, measurement of these currents, or the magnetic fields produced by them can be used to determine the distribution of electrical resistivities in the earth.

The many sources that are used fall into two categories: natural sources and controlled sources. Natural sources include world lightning activity and currents in the ionosophere and magnetosphere and are used exclusively in techniques such as the magnetotelluric method; however, limiting assumptions must be made and several EM field components must be measured to compensate for the lack of information about source parameters. The limiting assumptions are that the physical sources are farther than several free-space wavelengths from the point of observation so that the EM fields can be approximated as those of a plane wave impinging vertically upon the earth. Reliable field measurements require a minimum of two electric and two magnetic field components (all horizontal) to be recorded to allow for the unknown polarization of the plane wave. A further difficulty with using natural sources, is that the source spectrums are generally poor in energy centered around 1 Hz (Keller and Frischknecht, 1966, p. 200), the band which is most useful for intermediate depth penetration (for

example, 0.5 to 5 km).

The use of controlled sources offers several obvious improvements over natural sources, because almost every aspect of the source can be manipulated. The spectrum of available frequencies can be precisely controlled along with the intensity and, sometimes, the direction of the source. Because of the known nature of the source, fewer assumptions need to be made for geophysical interpretation and fewer components need to be recorded to obtain useful information. As few as one component can be measured, although additional information is obtained with the measurement of more components. What is source signal for a natural source EM study is now interfering noise for a CSEM study; the optimum frequency range for CSEM work is therefore the same one in which natural sources are deficient, 0.1 to 10 Hz. A common type of controlled source is a horizontal loop which is either circular or polygonal in shape and placed on the ground.

II.1 The Theoretical Magnetic Fields Induced by a Horizontal Loop Source over a Horizontally-Layered Halfspace

The magnetic fields induced by a horizontal loop source over a horizontally layered earth model can be determined by solving the appropriate boundary value problem derived from Maxwell's equations in MKS units:

$$\nabla \cdot \vec{E} = 0 \tag{1}$$

$$\nabla \cdot \vec{H} = 0 \tag{2}$$

$$\nabla \times \vec{E} = -\mu \frac{\partial \vec{H}}{\partial t} \tag{3}$$

$$\nabla \times \vec{H} = \epsilon \frac{\partial \vec{E}}{\partial t} + \vec{J} \tag{4}$$

Assuming a time dependence of e^{+iwt} (i.e. single frequency excitation) and μ and ϵ constant, equations (3) and (4) reduce to

$$\nabla \times \vec{E} = -i\omega\mu\vec{H} \tag{5}$$

$$\nabla \times \vec{H} = i\omega\epsilon\vec{E} + \vec{J} = (i\omega\epsilon + \sigma)\vec{E} + \vec{J}_s \tag{6}$$

noting that secondary currents are produced in conducting media ($\vec{J} = \sigma\vec{E}$) while J_s refers to source currents.

II.1.1 Horizontal, Circular Loop Source

The geometry of the problem is shown explicitly in Figure 2. The source loop radius, a, is located at the coordinate origin. As in Figure 2, the subscript, i, will be used to denote different layers, starting with i=0 to represent the air above the layered halfspace and increasing to i=m for the lowermost layer. Taking advantage of the cylindrical symmetry (no azimuthal dependence), equations (5) and (6) reduce to

$$i\omega\mu H_r = \frac{\partial E_\phi}{\partial z} \tag{7}$$

$$-i\omega\mu H_z = \frac{1}{r}\frac{\partial}{\partial r}(rE_\phi) \tag{8}$$

$$\frac{\partial H_r}{\partial z} - \frac{\partial H_z}{\partial r} = (i\omega\epsilon + \sigma)E_\phi + J_s \tag{9}$$

Three more equations can be derived from equations (5) and (6) which relate E_r, E_z, and H_ϕ; however, for a horizontal, circular loop source,

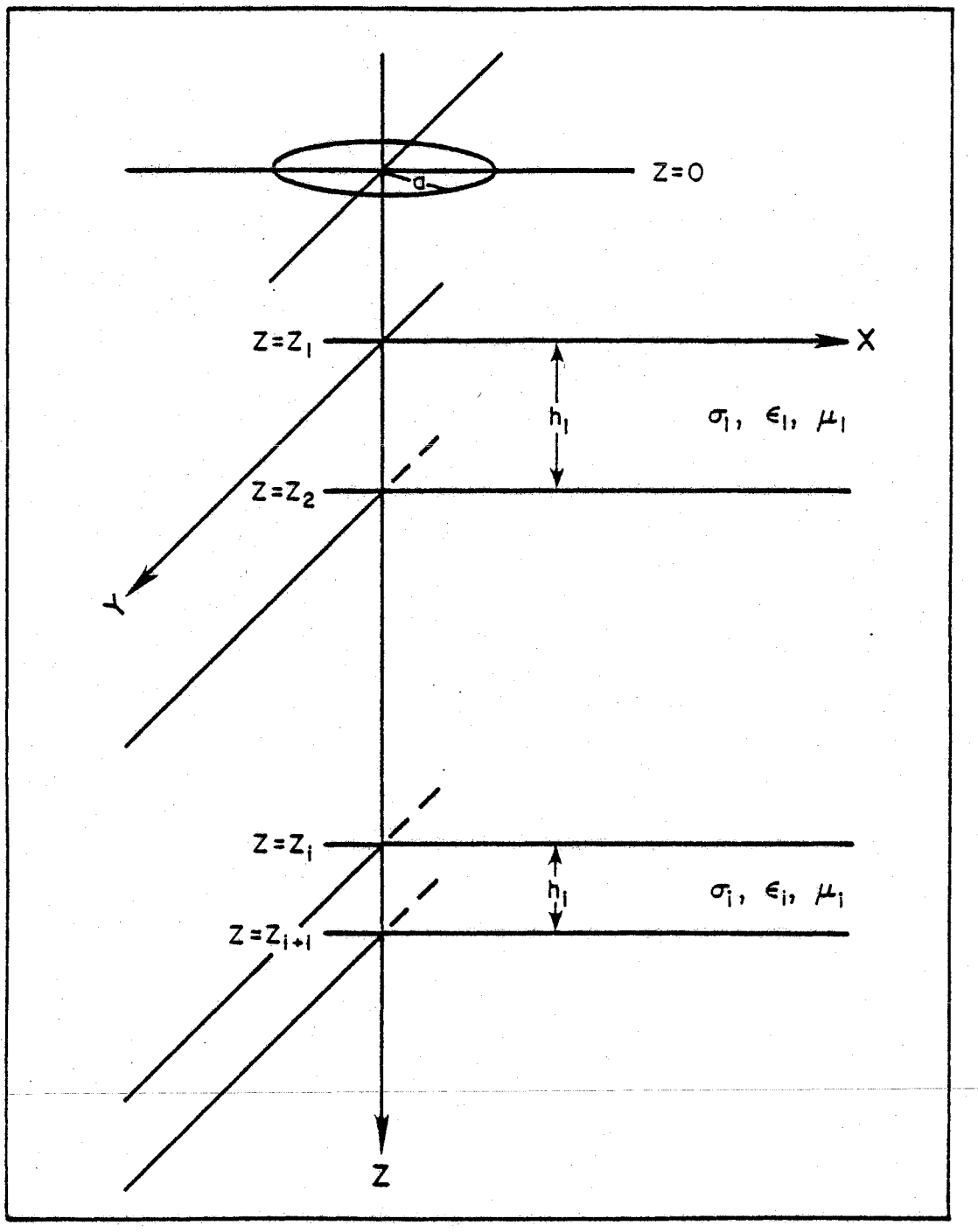

Figure 2. Definition of geometric and electric property variables for a circular loop source over a horizontally layered halfspace.

the source currents are only in the tangential direction and can excite only H_r, H_z, and E_ϕ. The other field components are zero.

The source current density, J_s, can be obtained by integrating the current density of an infinitesimal electric dipole around a circle of radius, a, to yield

$$\vec{J}_s = \frac{I(\omega)\ a\ \delta(r-a)\ \delta(z)}{r}\ \hat{\phi} \tag{10}$$

(Morrison and others, 1969).

The magnetic fields can be eliminated from equation (9), using (7) and (8), to yield a simpler equation in E_ϕ only,

$$\left(\frac{\partial^2}{\partial z^2} + \frac{\partial}{\partial r}\left(\frac{1}{r}\frac{\partial}{\partial r}\, r\right) + k_0^2\right) E_\phi(r,z,\omega) = \frac{I(\omega) i\omega\mu_0\ a\ \delta(r-a)\ \delta(z)}{r} \tag{11}$$

where $k_i^2 = \omega^2\mu_i\epsilon_i - i\omega\mu_i\sigma_i$. (12)

The magnetic fields can be derived later from E_ϕ using equations (7) and (8). Equation (11) is inhomogeneous and need only be solved in the region above the halfspace which contains the source. The first step is to recognize the similarities between (11) and Bessel's equation,

$$\frac{\partial^2\chi}{\partial r^2} + \frac{1}{r}\frac{\partial\chi}{\partial r} + \left(1 - \frac{n^2}{r^2}\right)\chi = 0$$

for order n=1. Bessel's equation has two solutions, J_1 and Y_1, known as Bessel's functions of the first and second kind, respectively; however, only J_1 remains finite for all non-negative arguments. These factors are used to advantage for solving (11) by defining the Hankel transform (really a Bessel transform) pair

$$\int_0^\infty F(r)\ J_1(\lambda r) r dr = \tilde{F}(\lambda) \tag{13a}$$

$$\int_0^\infty \tilde{F}(\lambda)\ J_1(\lambda r) \lambda d\lambda = F(r) \tag{13b}$$

and transforming equation (11) to get

$$\left(\frac{\partial^2}{\partial z^2} - (\lambda^2 - k_0^2)\right)\tilde{E}(\lambda,z,\omega) = i\omega\mu_0 I(\omega)\ a\ \delta(z) \int_0^\infty \frac{\delta(r-a)}{r} J_1(\lambda r) r dr$$

$$= i\omega\mu_0 I(\omega)\ a\ \delta(z)\ J_1(\lambda a). \tag{14}$$

We also recognize that diffusion-wave equation in z which has two solutions, $e^{\sqrt{\lambda^2 - k_0^2}\, z}$ and $e^{-\sqrt{\lambda^2 - k_0^2}\, z}$. The fields must diminish at large distances from the source, so the transformed field becomes

$$\tilde{E}_\phi(\lambda,z,\omega) = \frac{-i\omega\mu_0\ a\ I(\omega)}{2} J_1(\lambda a)\ \frac{e^{-u_0 z}}{u_0} \quad , z > 0$$

$$= \frac{-i\omega\mu_0\ a\ I(\omega)}{2} J_1(\lambda a)\ \frac{e^{+u_0 z}}{u_0} \quad , z < 0 \tag{15}$$

where $u_i = (\lambda^2 - k_i^2)^{\frac{1}{2}}$.

Transforming equation (15) using (13b) yields the primary electric field of a circular loop

$$E_\phi(r,z,\omega) = -\frac{i\omega\mu_0\ a\ I(\omega)}{2} \int_0^\infty \frac{\lambda}{u_0} e^{-u_0|z|} J_1(\lambda a) J_1(\lambda r) d\lambda \tag{16}$$

The term $e^{-u_0|z|}$ incorporates both exponential terms in equation (15).

For the EM fields above a layered halfspace, we need the solution of the homogeneous version of equation (11)

$$\left(\frac{\partial^2}{\partial z^2} + \frac{\partial}{\partial r}\left(\frac{1}{r}\frac{\partial}{\partial r} r\right) + k_i^2\right) E_\phi(r,z,\omega) = 0$$

in each of the layers. Taking the Hankel transform of the above

we get

$$\left(\frac{\partial^2}{\partial z^2} - (\lambda^2 - k_i^2)\right) \tilde{E}_\phi(\lambda,z,\omega) = 0 \ .$$

The solution is, by inspection,

$$\tilde{E}_\phi(\lambda,z,\omega) = E_i^+(\lambda,\omega)e^{-u_i z} + E_i^-(\lambda,\omega)e^{+u_i z} \tag{17}$$

where E_i^+ is the amplitude of the downgoing wave, and E_i^- is the amplitude of the upgoing wave in layer i.

The E_ϕ in each layer is determined by the boundary conditions of continuous horizontal $\vec{E}$ and $\vec{H}$. Wait (1962) uses an input impedance approach to solve this portion of the problem. The input impedance into any layer, i, is defined by

$$Z^i(\lambda,\omega) = \left.\frac{\tilde{E}_\phi(\lambda,\omega)}{\tilde{H}_r(\lambda,\omega)}\right|_{z=z_i} \tag{18}$$

at the surface of that layer. Using equations (7) and (17), the intrinsic impedance within layer i is

$$Z_i(\lambda,\omega) = \frac{-i\omega\mu_i}{u_i} = \frac{E_i^+(\lambda,\omega)}{H_i^+(\lambda,\omega)} = -\frac{E_i^-(\lambda,\omega)}{H_i^-(\lambda,\omega)} \tag{19}$$

For an m-layered earth model, the impedance at the surface of the model can be solved with the following recursion relation by matching impedances at the top and bottom of adjacent layers (continuity of parallel $\vec{E}$ and $\vec{H}$ again). The matching starts at the surface of the lowest layer and works up,

$$Z^i = Z_i \frac{Z^{i+1} + Z_i \tanh(u_i d_i)}{Z_i + Z^{i+1} \tanh(u_i d_i)} \tag{20}$$

and for i=m, $Z^m = Z_m$.

Note that in terms of equation (17), equation (15) can be used to solve for E_0^+ in the region between the source and the layered halfspace $z_1 \geq z \geq 0$

$$E_0^+ = \frac{-i\omega\mu_0 \, a \, I(\omega)}{2 \, u_0} J_1(\lambda a) \, . \tag{21}$$

Combining equations (17) and (19) at $z=z_1$,

$$E_0^+ e^{-u_0 z_1} + E_0^- e^{+u_0 z_1} = \tilde{E}_\phi(\lambda, z_1, \omega)$$

$$\frac{\tilde{E}_\phi(\lambda, z_1, \omega)}{Z} = \frac{E_0^+}{Z_0} e^{-u_0 z_1} - \frac{E_0^-}{Z_0} e^{+u_0 z_1}$$

we get

$$E_0^- = \frac{Z^1 - Z_0}{Z_0 + Z^1} E_0^+ e^{-2u_0 z_1} \tag{22}$$

Substituting (21) and (22) into (17) and inverse transforming via (13b), we finally obtain the full expression for the tangential electric field

$$E_\phi(r,z,\omega) = \frac{-i\omega\mu_0 \, a \, I(\omega)}{2} \int_0^\infty \left[e^{-u_0 |z|} + \frac{Z^1 - Z_0}{Z_0 + Z^1} e^{+u_0 (z-2z_1)} \right] \frac{\lambda}{u_0} J_1(\lambda a) \cdot$$

$$J_1(\lambda r) d\lambda \tag{23}$$

Using equations (7) and (8), the accompanying magnetic fields are

$$H_z = \frac{aI(\omega)}{2} \int_0^\infty \left[e^{-u_0|z|} + \frac{Z^1 - Z_0}{Z_0 + Z^1} e^{+u_0(z-2z_1)} \right] \frac{\lambda^2}{u_0} J_1(\lambda a) J_0(\lambda r) d\lambda \quad (24)$$

$$H_r = \frac{aI(\omega)}{2} \int_0^\infty \left[e^{-u_0|z|} - \frac{Z^1 - Z_0}{Z_0 + Z^1} e^{+u_0(z-2z_1)} \right] \lambda J_1(\lambda a) J_1(\lambda r) d\lambda \quad (25)$$

For most situations in which CSEM techniques are used, the material conductivities are much greater than the product of dielectric permittivity and radian frequency. For example, the dielectric permittivity of almost all geologic materials is no more than 100 times the free space value of 8.5×10^{-12} farad/m. All frequencies used in this study are less than 10 Hz, so the product $\epsilon\omega$ should always be less than 5.6×10^{-8}. Conductivities of Hawaiian rocks are generally greater than 10^{-4} mho/m with rare values as low as 5×10^{-6}; therefore, the propagation constant, k_i, in equation (12) can usually be approximated as

$$k_i^2 = -i\omega\mu_i(\sigma_i - \epsilon_i\omega) \cong -i\omega\mu_i\sigma_i$$

to better than 0.1 percent. This simplification, known as the quasistatic approximation, emphasizes the diffusion nature of EM waves at low frequencies by showing that the governing equation (Equation 11) is the diffusion equation.

II.1.2 Vertical Magnetic Dipole Source

The vertical magnetic dipole (VMD) is the asymptotic limit of a circular loop source when the radius of the loop is small with respect to the distance between source and measuring point, r. The series form of J_1 is (Abramowitz and Stegun, 1970, eq. 9.1.10)

$$J_1(\lambda a) = \lambda a/2[1 - \tfrac{1}{2}\left(\frac{a\lambda}{2}\right)^2 + \ldots]$$

so the Bessel function product in equations (23) through (25) can be approximated by

$$J_1(\lambda a)J_n(\lambda r) = J_1(\lambda'\frac{a}{r})J_n(\lambda') = J_n(\lambda')\frac{\lambda'\frac{a}{r}}{2}[1-\tfrac{1}{2}(\frac{\lambda'\frac{a}{r}}{2})^2 + \ldots]$$

$$\cong \frac{\lambda a}{2} J_n(\lambda r) \qquad n = 0,1 \qquad (26)$$

as long as $r/a > 5$ (Ryu and others, 1970).

II.1.3 Horizontal Polygonal Source

A polygonal source is one which consists of three or more linear, connecting segments. Such a source is easier to construct than a circular one, especially when the dimensions are large. The loop source at Kilauea is actually a four-sided polygon.

The magnetic fields induced by a polygonal source can be computed as the sum of the fields induced by each side of the polygon separately. That is, if H_z^i is the vertical magnetic field of a line source, i, then the vertical field of a polygonal source is

$$H_z = \sum_{i=1}^{N} H_z^i \qquad (27)$$

where line source i extends from (x_i, y_i) to (x_{i+1}, y_{i+1}).

Using the results of Kauahikaua (1978), where the magnetic fields of a horizontal line source are separated into the portion due to current in the line and the portion due to the grounded ends, the expressions for the magnetic fields of the wire alone can be written down directly. Each line segment will produce magnetic fields which are vertical and perpendicular to the line direction over a horizontally layered earth. In the rotated coordinate system (s, p) where the line source is parallel to the s-axis and pointing in the +s direction, the magnetic fields are

$$H_p^i = \frac{-I}{4\pi} \int_{s_i}^{s_{i+1}} \left\{ \int_0^\infty [1 + \frac{Z^1-Z_0}{Z_0+Z^1}] e^{-u_0|z|} \lambda J_0(\lambda r) d\lambda \right\} ds \tag{28}$$

$$H_z^i = \frac{I(p_0-p_i)}{4\pi} \int_{s_i}^{s_{i+1}} \frac{1}{r} \left\{ \int_0^\infty [1 + \frac{Z^1-Z_0}{Z_0+Z^1}] e^{-u_0|z|} \lambda J_1(\lambda r) d\lambda \right\} ds \tag{29}$$

where the field point is (s_0, p_0) and the line extends from (s_i, p_i) to (s_{i+1}, p_{i+1}): $r^2 = (s-s_0)^2 + (p-p_0)^2$. The field components are rotated back to (x, y) coordinate system before summation.

II.2 Comparison of the Magnetic Fields of a Polygonal Source with Those of a Circular and VMD Source

The expressions for the magnetic field of a polygonal source are more complicated than those of a circular or VMD source; therefore, it is useful to know the limits within which the more symmetric source fields behave approximately like those of a polygonal source. With a knowledge of these limits, it is expected that the VMD expressions

might be substituted for the polygonal source field expressions for large values of r/a, with a considerable reduction in computational time. Similarly for a range of intermediate values of r/a, it is expected that the field expressions for a circular source could be substituted for the polygonal source field expressions.

To this end, the ratio of the primary magnetic field produced by a circular and square source (equal area) to that produced by a VMD source is plotted in Figure 3 as a function of source radius divided by the distance from the observation point to the source center (a/r). Also shown are two ratios for the square source to circular source representing the observation point being located off the side and off the corner of the square source. This figure clearly shows that the primary field of a square source can be approximated to better than 1 percent by the primary field of a VMD for values of a/r less than 0.1, and by a circular source for values of a/r between 0.1 and 0.3.

Although these limits were determined for the primary magnetic field of a square source, they appear to be generally valid for the frequency-dependent induced magnetic field of polygonal source like the one used for this experiment at Kilauea. Using a source having the exact shape of the Kilauea source laid over a 10 ohm-m halfspace, both the vertical and radial magnetic fields differed by less than 0.3° and 0.5 percent from those of a 1 km radius circular loop at a distance of 3.33 km (a/r = 0.3). The comparison between the Kilauea loop and a VMD source at a distance of 10 km showed discrepancies of up to 3 percent and 1.6°. To provide the required degree of accuracy, the circular loop (radius of 1 km) field expressions were used for

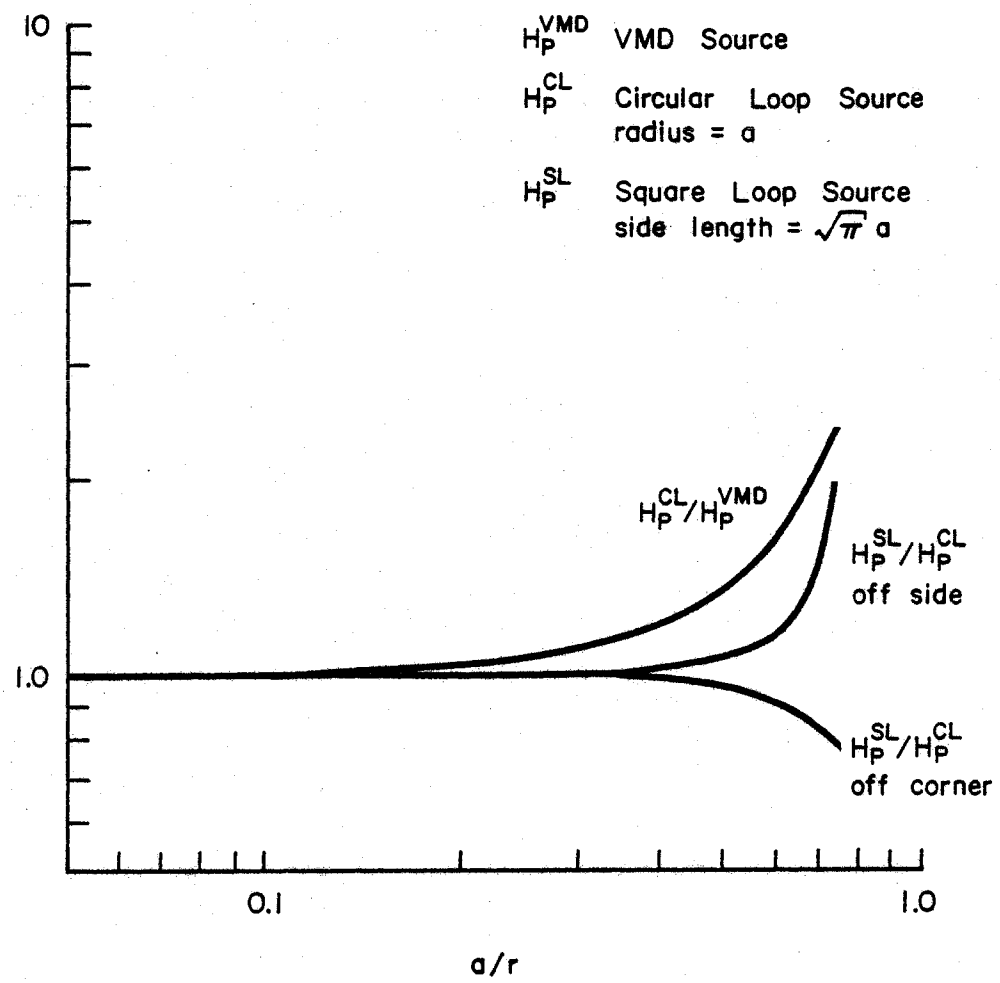

Figure 3. Primary magnetic field ratios for various pairs of horizontal loop sources as a function of the ratio of source dimension to source-receiver distance.

all locations more distance than 3.33 km, while the polygonal source field expressions were used for all closer locations.

II.3 Properties of Theoretical Magnetic Fields Over a Horizontally-Layered Halfspace

As shown in the previous section, the symmetry of the problem dictates that only the vertical and radial components of the magnetic field are nonzero for a cylindrically symmetric horizontal-loop source. Very small tangential fields are observed when close to a nonsymmetric, polygonal source; however, they become insignificant at distances greater than the largest source dimension. For purposes of this general discussion, horizontal loop (polygonal or circular) sources are assumed to generate only vertical and radial magnetic fields over layered halfspaces.

Over a uniform halfspace, magnetic field variations can be uniquely characterized by the value of a composite parameter, called an induction number, B, given by

$$B = r/\delta = r\sqrt{\frac{\mu_0 \sigma \omega}{2}} \tag{30}$$

where r is the horizontal distance between the source center and the point at which the fields are observed, and δ is the skin depth[1]. This can be seen most easily be normalizing all lengths in the field equations by the skin depth; integrals of the form

[1] the distance over which an EM plane wave of frequency, f, traveling in an infinite whole space of conductivity, σ, is attenuated by a factor of 1/e, or about 0.3679, and is shifted in phase by one radian.

$$\int \ldots J(\lambda a)J(\lambda r)d\lambda$$

become

$$\frac{1}{\delta}\int \ldots J(gA)J(gB)dg$$

where $g = \lambda\delta$ and $A = a/\delta$.

For induction numbers less than 0.1, the magnetic field asymptotically approaches the free space or primary field value[2]. In the plane of the source, the primary field is all vertical; however, above or below the source plane, the primary field also has a radial component. As the induction number is increased, the electric currents induced in the halfspace increase in amplitude and become concentrated at progressively shallower depths. It is this property of the induced currents that is the basis for the rule-of-thumb in inductive sounding, that depth of penetration is inversely proportional to the induction number. For larger induction numbers, the induced currents are concentrated at the surface of the halfspace and tend to cancel the primary field of a horizontal loop source. The magnetic field asymptotically approaches zero amplitude at induction numbers greater than 10. An example of the fields over a homogeneous halfspace is shown in Figure 4 plotted against induction number.

When observed as a function of time, the magnetic field vector traces out an ellipse in the vertical-radial plane at a given frequency because the vertical and radial components of the field are,

---

[2] the frequency-invariant field observed in a space free of conductors.

Figure 4. Amplitude and phase of the vertical and radial magnetic fields induced by a VMD source over a homogeneous halfspace. The fields are normalized by the primary field strength and are plotted versus induction number, B.

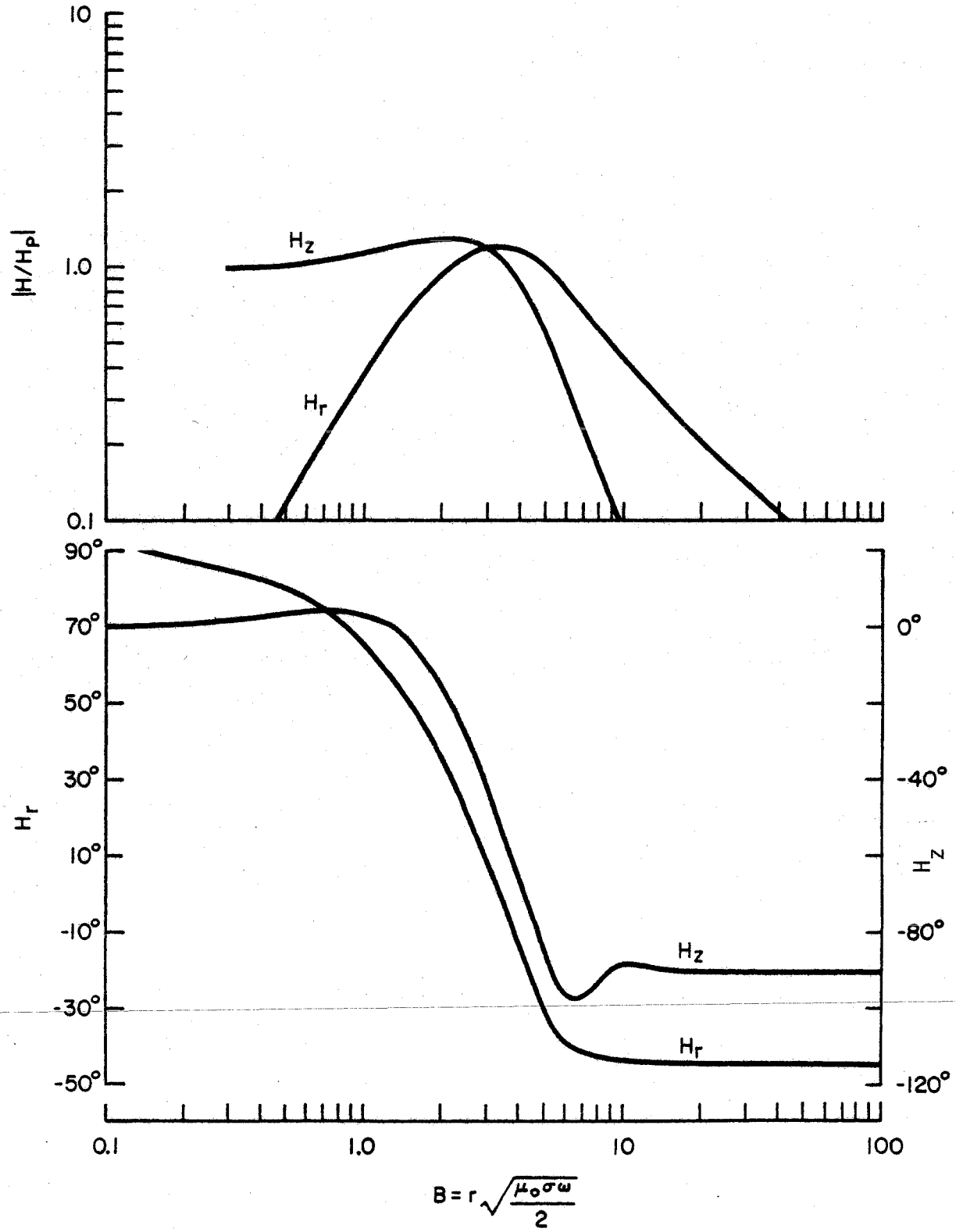
10
1.0
0.1
|H/Hp|
Hz
Hr
90°
70°
50°
30°
10°
-10°
-30°
-50°
Hr
0°
-40°
-80°
-120°
Hz
Hz
Hr
0.1
1.0
10
100
B = r √(μ₀σω/2)

in general, not in phase. The resulting ellipse, called the vertical polarization ellipse, can also be used to characterize magnetic field variations through two parameters - the vertical ellipticity and the tilt angle. These parameters are depicted in Figure 5 while the details of their computation are given in Appendix A.

Over a uniform halfspace, the vertical polarization ellipse is essentially vertical at induction numbers less than 0.1, and it rotates to essentially horizontal for induction numbers greater than 10. This corresponds to tilt angle values from 90° (vertical) to 0° (horizontal). The ratio of minor to major axis (vertical ellipticity) also varies becoming more negative than -0.15 for induction numbers between 0.1 and 10. The negative sign for ellipticity signifies that the magnetic field is rotating in a counter clockwise sense with time when looking in the $+\phi$ (see Fig. 5) direction (Smith and Ward, 1974). Vertical ellipticity is a minimum of -0.47 at an induction number of about 3.3 (see Fig. 6).

The range of induction numbers for which the field response curves are most diagnostic is therefore between 0.1 and 10. Measurements of the magnetic field at a single induction number within this range can be used to determine the resistivity of a uniform halfspace. If the resistivities change with depth in the halfspace, measurements at a range of induction numbers are required.

The resolution of earth resistivities from any measurements depends principally upon the degree of dissimilarity in the corresponding theoretically computed response curves. From their extensive investigation of the fields of a loop source over a two-layer earth,

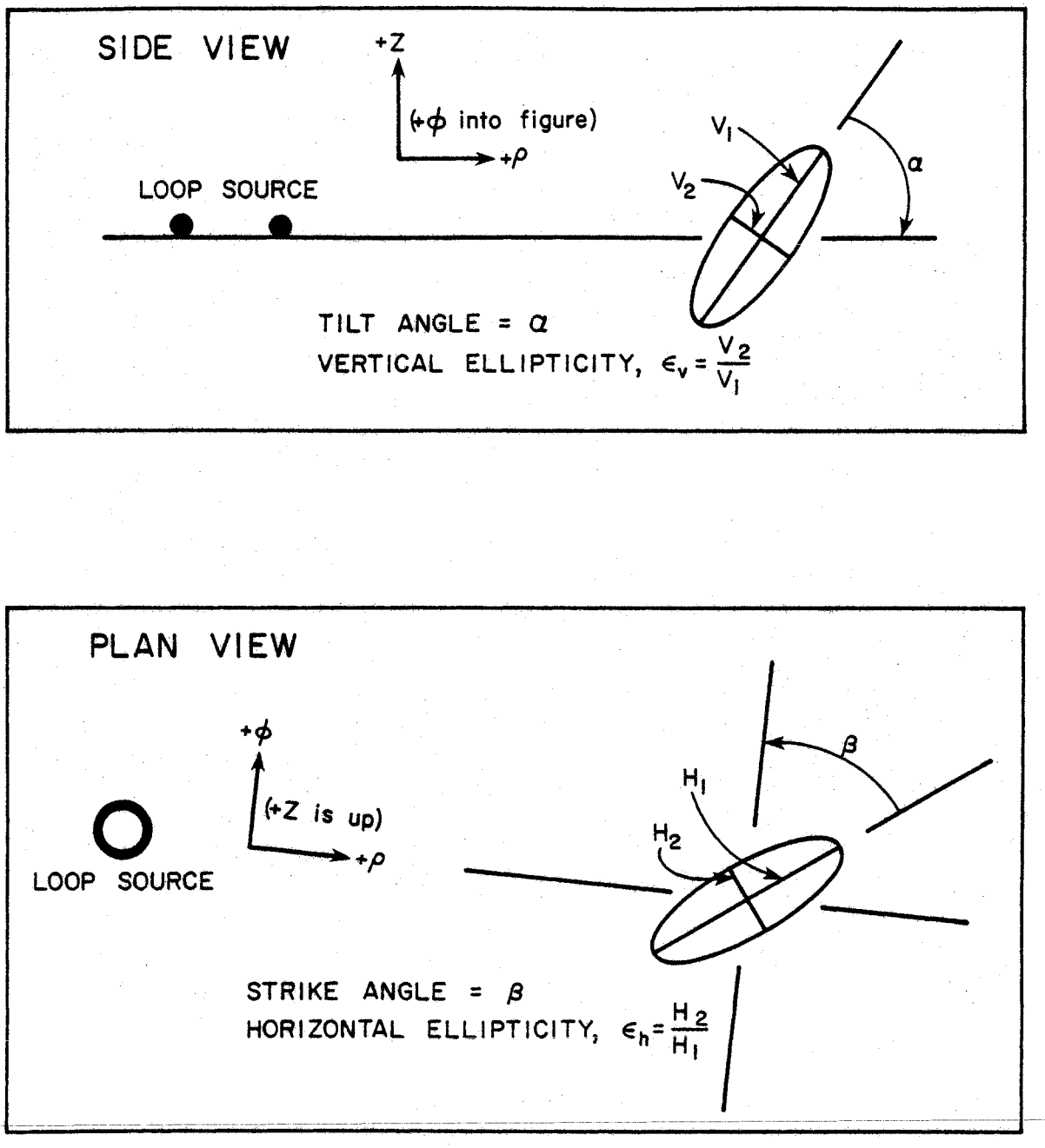

Figure 5. Definition of the parameters for the vertical polarization ellipse (top) and the horizontal polarization ellipse (bottom).

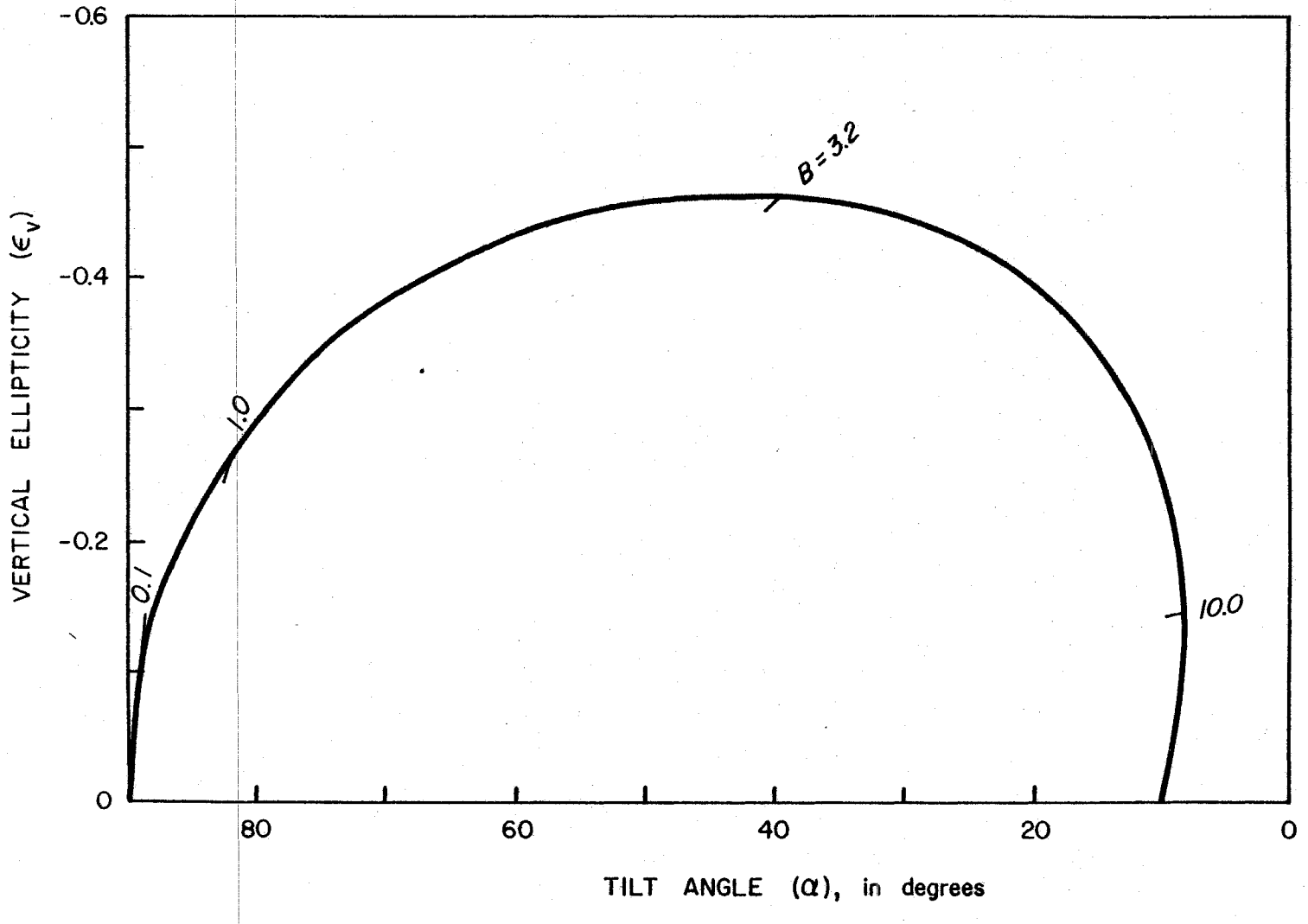

Figure 6. Pseudo-phasor plot of tilt angle and vertical ellipticity for a range of B values over a homogeneous halfspace.

both Frischknecht (1967) and Ryu and others (1970) agree that the best resolution can be obtained over a halfspace where the resistivity decreases rather than increases with depth (also evident from the diffusion nature of the equation in z) and that specific components or quantities have more resolution than others. For example, phase appears to offer more resolution than amplitude measurements, and the radial component offers a greater resolution than the vertical component at depths equal to the distance to the source. In particular, the parameters of the vertical polarization ellipse are concluded to be the most useful quantities for extracting earth resistivity structures (Ryu and others, 1970).

II.4 Properties of Magnetic Fields Over Laterally-Inhomogeneous Structures

Cylindrically symmetric sources over nonsymmetric structures can generate all three components of magnetic field so that, in addition to being elliptically polarized in the vertical-radial plane, the field can also be elliptically polarized in the radial-tangential (horizontal) plane. The horizontal polarization ellipse can be characterized by two more parameters - the horizontal ellipticity and strike angle, which are also depicted graphically in Figure 5. These parameters do not vary from a strike angle of 90° and a horizontal ellipticity of zero anywhere over a horizontally layered structure; however, any departure from these values is a clear indication of lateral resistivity variations in a field survey. The actual behavior of the magnetic field in the presence of such variations will be discussed in Chapter V.2.

III. APPLICATION OF THE CSEM TECHNIQUE AT KILAUEA VOLCANO

The basic requirements of the technique are a large-moment transmitter, or controlled source, and a means of measuring the magnetic field induced by that source. The large moment of the source is usually obtained by construction with large, physical dimensions, and by the utilization of large electric currents. The source at Kilauea is a polygonal loop about 2 km by 2 km which is designed to handle an alternating electric current of 80 amps peak-to-peak. Figure 7 shows the location of the loop source and the 45 sounding locations at Kilauea. The location of the source loop itself was determined more by public safety considerations (the study area is a popular National Park) than by geophysical ones.

Measurement of the induced magnetic field can be accomplished in one of two ways. If the source is pulsed with a square wave, the induced field can be sampled digitally with time so that the fundamental frequency (frequency of the square wave) and several higher harmonics can be resolved using Fourier transform techniques. This approach requires expensive real-time computer processing to be effective, such as in the successful EM-60 system (Morrison and others, 1978). The method chosen for this study is simpler and less expensive. The source is driven with a sine wave at the desired frequency and the receiver circuitry is essentially a sophisticated AC (alternating current) voltmeter that is finely tuned at that frequency. Multi-frequency data is then obtained by repeating these steps at several frequencies. This technique has been used successfully for CSEM

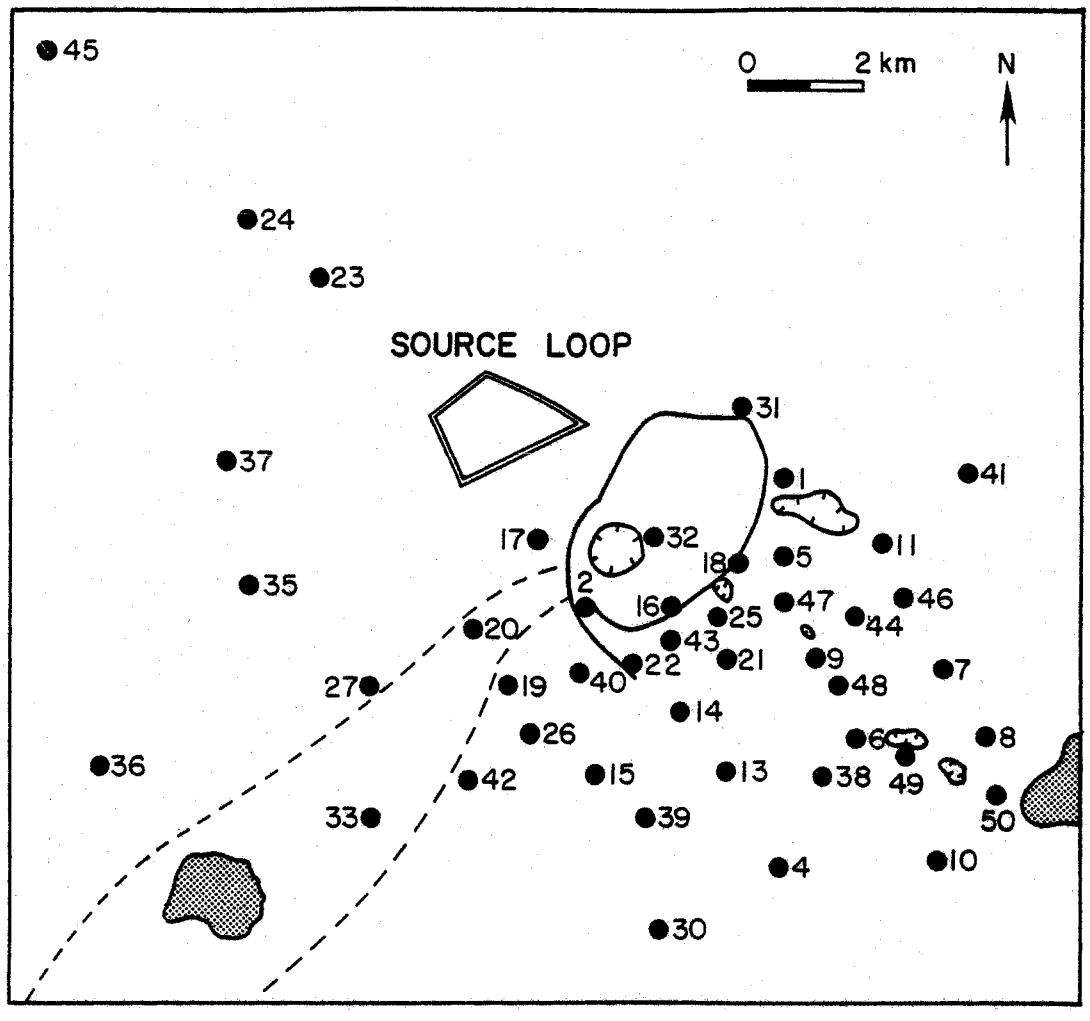

Figure 7. Map of the Kilauea summit area showing locations of the source loop and sounding sites.

soundings at Kilauea Iki, Hawai'i (Frischknecht, 1980, oral communication), Antarctica (Ray Watts, 1980, oral communication), Raft River, Idaho (Anderson, 1977), and Randsburg, California (Anderson, 1978).

III.1 Equipment Description

All equipment is grouped either into the transmitter or receiver systems shown in block form in Figure 8. A full description of the electronics can be found in Cooke and others (1981). Both packages contain a 10 MHz clock and countdown circuitry; that is, a pair of crystal clocks are used for time reference at both the transmitter and receiver locations. The 10 MHz square wave is then "counted down" to the desired frequency (.01 to 8 Hz at ten frequency increments per decade) by switch-selectable logic elements.

III.1.1 Transmitter

The transmitter controller converts the square wave at the desired frequency from the countdown circuitry to a sine-wave at the same frequency. The sine-wave is then amplified to levels appropriate for input to the following stage, the electric motor controller. This unit, manufactured by Robicon Corporation, is intended to produce precisely controlled electric currents large enough to drive heavy electric motors; the current can be controlled by a relatively small voltage input. The electric-motor controller, more simply viewed as a voltage-to-current amplifier, produces 20 amps out per volt in. In our application, the unit produces an 80 amp peak-to-peak sine wave at the desired frequency. This signal is then driven through a wire loop laid out horizontally on the ground. The loop consists of two

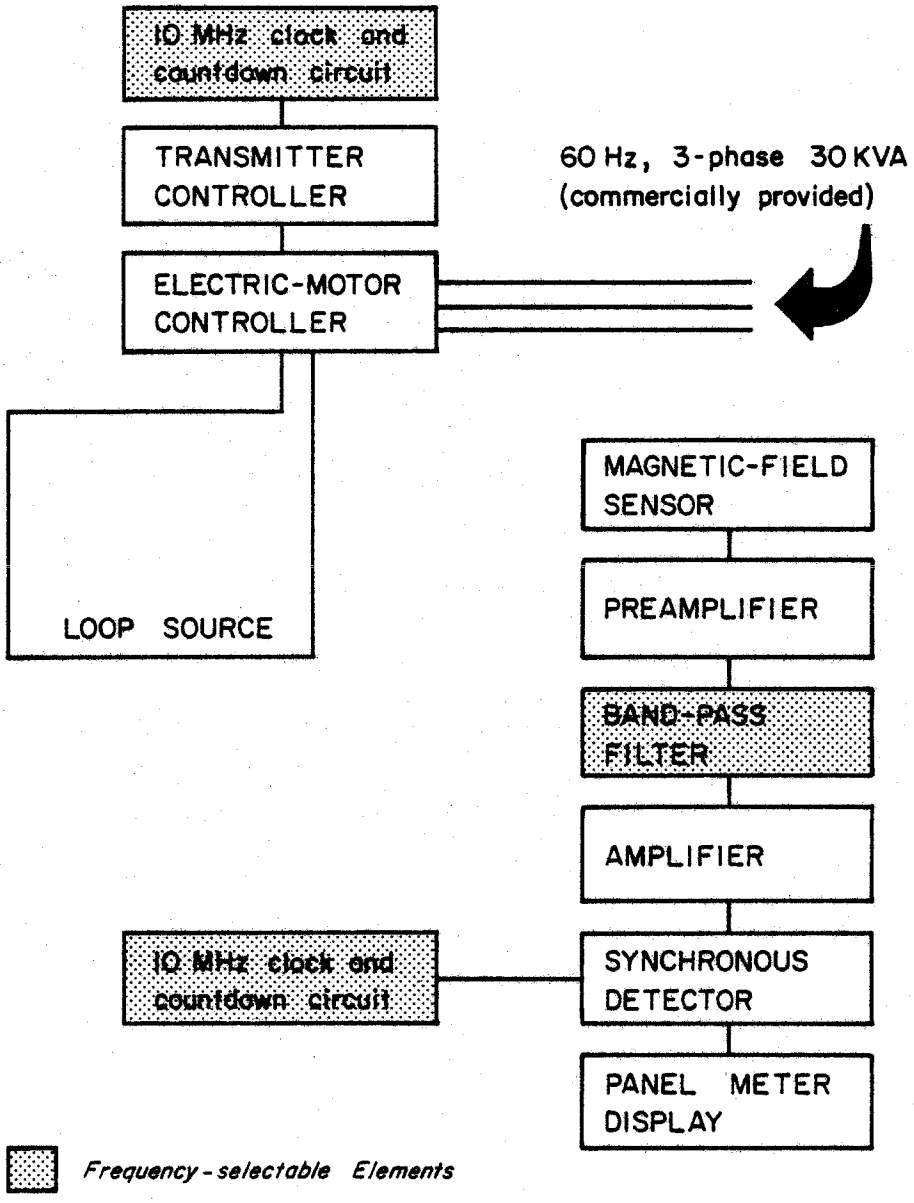

KILAUEA CSEM EQUIPMENT BLOCK DIAGRAM

Figure 8. Block diagram showing the important elements of both the source and receiver instrumentation.

turns of no. 8 aluminum wire (connected in parallel) laid in a rough square about 2 km on a side. The total resistance of the wire loop in this configuration is about 13 ohms.

III.1.2 Receiver

Two different sensors were used during the course of the survey. One sensor consisted of a pair of orthogonally mounted, ferrite-cored, wire coils and preamplifier with a sensitivity of about 0.3 mV/nT at 1 Hz. The more widely used sensor was a three-axis, cryogenic magnetometer with a sensitivity of about 10 mV/nT. The incoming signal was first low-pass filtered and amplified (gain of 10 or 100) by a pre-amplifier near the sensor. The balance of the receiver equipment was separated from the sensor by a 100 m long cable to minimize instrument interference.

The signal from the preamplifier was again filtered using units manufactured by Ithaco. These filters provide narrow, band-pass characteristics with an attenuation of 12 db/octave on either side of the center frequency. The center frequency is switch-selectable at the same frequencies that were provided by the countdown circuits. The filtered signal was then amplified again 1 to 1000 times (in 10 db increments).

The crucial element of the receiver is the synchronous detector. This element multiplies the incoming signal by the output of the receiver's countdown circuit producing the in-phase, or real, portion of the received signal. The out-of-phase, quadrature, or imaginary, portion is produced by a second synchronous detector. It multiplies the incoming signal by the countdown-circuit output which has been

delayed by 90°, or one-quarter cycle. The synchronous detector outputs are usually low-pass filtered with an RC circuit whose time constant is at least 3 periods long. Both the in-phase and out-of-phase rms voltages are displayed on a digital panel meter for manual recording.

III.2 Survey Methods

Field procedures were fairly standard for each sounding. The clocks for both the transmitter and receiver packages were first synchronized using a temporary umbilical connection. The magnetic-field sensor was then buried at the desired location with the x-axis oriented radial to the loop-source center; the sensor was further shielded to minimize vibration by wind. After the various elements of the receiving system were hooked up, the vertical, radial, and, at some locations, the tangential components of the magnetic field induced by the loop source were measured and recorded at several frequencies usually between 0.04 and 8 Hz. The frequencies were simultaneously changed on both the transmitter and receiver systems by maintaining radio contact with an assistant at the transmitter.

The readings at each frequency usually stabilized after the system had averaged at least ten cycles of the induced magnetic field. Typical measurement times would then be at least 10 sec for 1 Hz, almost 2 min for 0.1 Hz, and almost 17 min for 0.01 Hz. At noisier sites, sometimes 100 cycles were necessary for a stable reading. The excessive time required for frequencies below 0.1 Hz, along with the natural tendency for geomagnetic noise to increase below 0.1 Hz, often

precluded obtaining data at these low frequencies. Replicate measurements assured data errors of less than 1 percent in amplitude and 1° in phase (assuming no systematic errors).

While the equipment and procedures described above allow for accurate measurement of the received signal's phase relative to the time base of the 10 MHz clock in the receiver, it is phase measurements relative to the current in the loop that is desired. The two can be quite different if, for example, there is some phase shift of the transmitter signal as it goes through the electric-motor controller. To correct for all phase shifts in the equipment, magnetic field calibration measurements were made at all frequencies while located very close to the loop source. Electrical resistivities are known to be very high at Kilauea's surface, so that at 100 to 300 m from one side of the loop, the induction number is very small and the magnetic field is essentially all primary field; that is, the field will be the same as that measured from the same loop in free space and will be precisely in phase with the current in the loop.

These "calibration" readings also provide information on the relative amplitude attenuation through the electronics. If we assume that the lower frequencies should not be attenuated significantly and normalize the calibration values so that their amplitude at low frequencies asymptotically approach unity, these values can be used to totally correct the data for the effects of the measurement circuitry.

III.3 Data Reduction

The data that were recorded during this study were reduced in three ways. The most straightforward was the conversion to absolute magnitude and phase for each of the magnetic field vector components. The relative component amplitudes and phases were also used to compute polarization ellipse parameters in both the vertical and horizontal planes. In this way, the three-component data could be reduced to two pairs of polarization parameters. Finally, both the vertical and radial magnetic field data and the vertical polarization ellipse data were converted to apparent resistivities prior to interpretation.

III.3.1 Absolute Magnetic Field

This simple conversion is most easily described with a formula involving complex algebra,

$$H = \frac{V^{\circ}\ S}{V^{c}\ G}\ \sqrt{2} \qquad [1]$$

where H is the observed, complex magnetic field, V° is the observed complex (rms) voltage, V^{c} is the complex calibration voltage at the appropriate frequency, G is the gain used to amplify the observed voltage, and S is the sensitivity of the sensor. The procedure for obtaining the calibration values is described in the previous section. Each of the complex quantities has a real part and an imaginary part. As an example of data corrected in this way, Figures 9, 10, and 11 show plots of the three-component data taken at locations 35, 42, and 25, respectively. The data are normalized by the magnitude of the primary field expected at the appropriate distances to demonstrate that the reduced data are of the correct magnitude. These figures

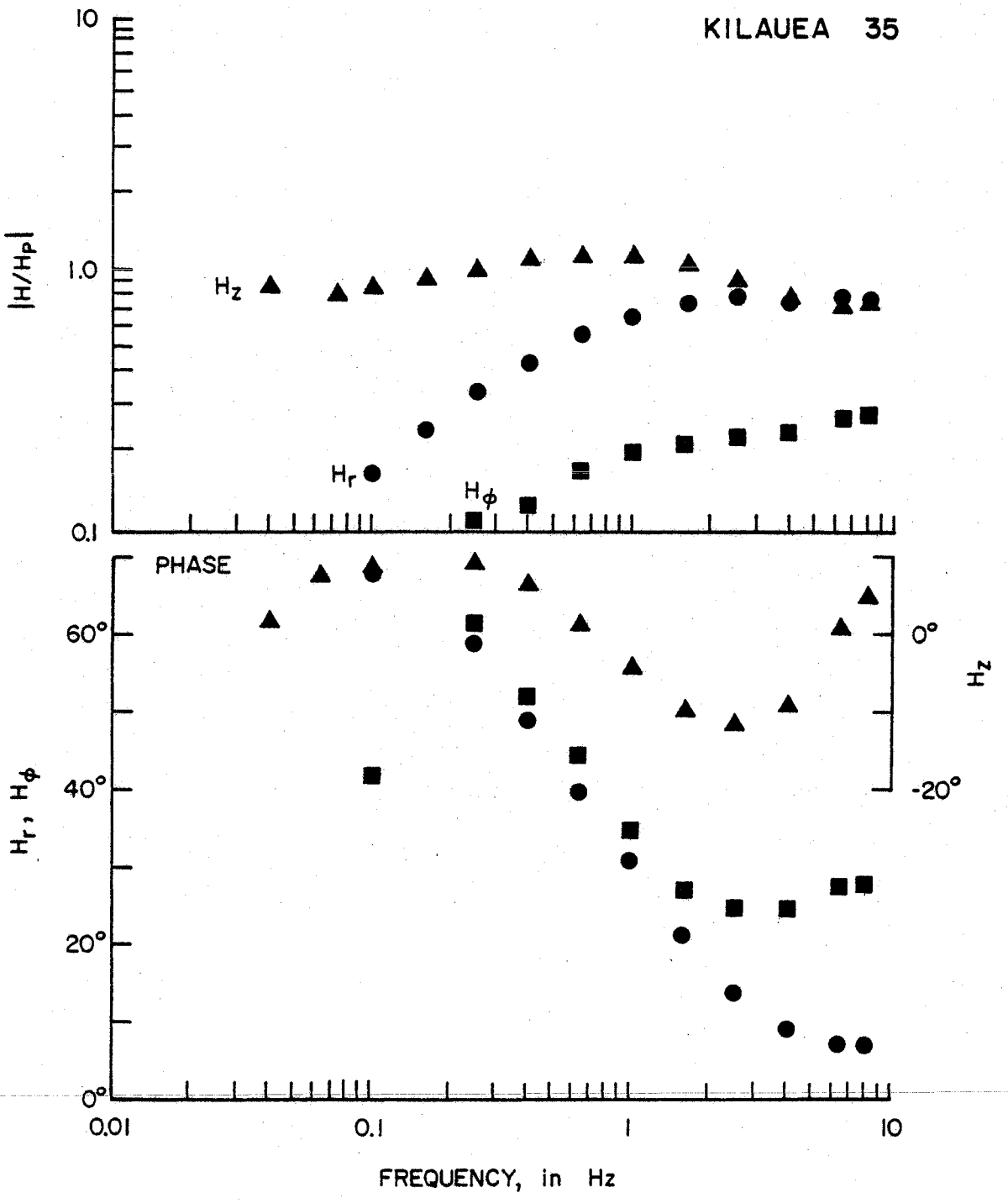

Figure 9. Amplitude and phase for all three components of the magnetic field (normalized by the theoretical primary field) for sounding location 35. Comparison of this plot with Figure 4 shows that the frequency range 0.1 to 10 Hz in this figure corresponds to a range of induction numbers between 1 and 10.

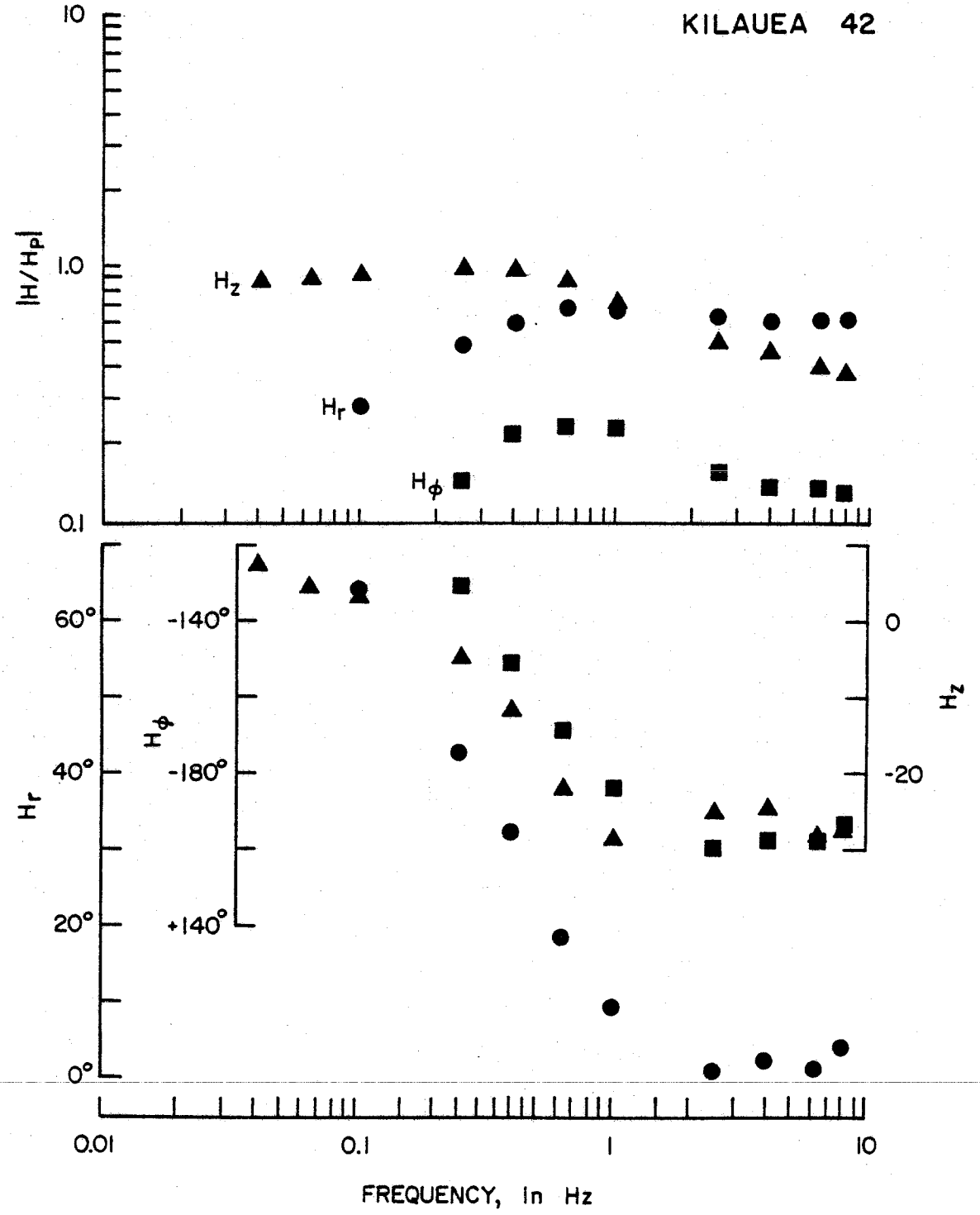

Figure 10. Amplitude and phase for all three components of the magnetic field (normalized by the theoretical primary field) for sounding location 42. Comparison of this plot with Figure 4 shows that the frequency range 0.1 to 10 Hz in this figure corresponds to a range of induction nubmers between 1 and 10.

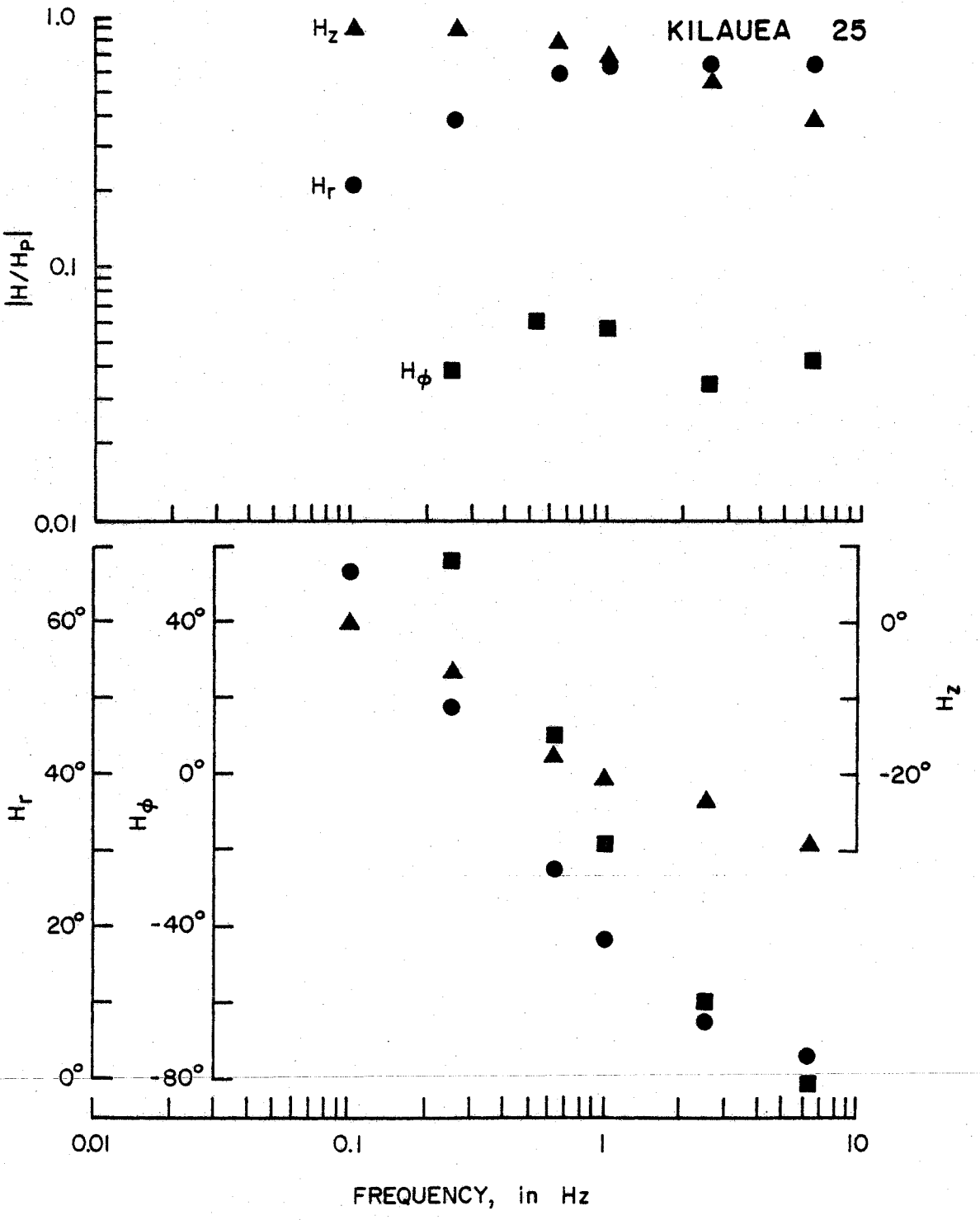

Figure 11. Amplitude and phase for all three components of the magnetic field (normalized by the theoretical primary field) for sounding location 25. Comparison of this plot with Figure 4 shows that the frequency range 0.1 to 10 Hz corresponds to a range of induction numbers between 1 and 10.

should be compared to the theoretical halfspace curves in Figure 4; note that the scale of the abscissa goes as frequency in Figures 9-11 and as square root frequency in Figure 4.

III.3.2 Polarization Ellipse Parameters

Any two components of absolute amplitude and phase data can also be presented as two parameters describing a polarization ellipse in the corresponding plane. The major advantage to this form of data reduction is that the polarization parameters depend only on amplitude ratios and phase differences (and therefore do not require absolute field corrections) and that four absolute quantities (amplitude and phase for two components) can be reduced to two ellipse parameters. A further advantage of using ellipse parameters is that one of them, the ellipticity, is not affected by rotation of the measurement axes within the plane. This property can be valuable if difficulty is encountered in leveling the magnetic sensor.

As normally applied, the vertical and radial magnetic field components are used to compute the parameters of the vertical polarization ellipse, and the radial and tangential magnetic field components are used to compute the parameters of the horizontal polarization ellipse (shown graphically in Fig. 5). As an example, the data from locations 35, 42, and 25 have been converted to vertical polarization ellipse parameters and are shown in Figure 12. For comparison, the theoretical tilt angle and vertical ellipticity over a homogeneous halfspace are plotted in Figure 6.

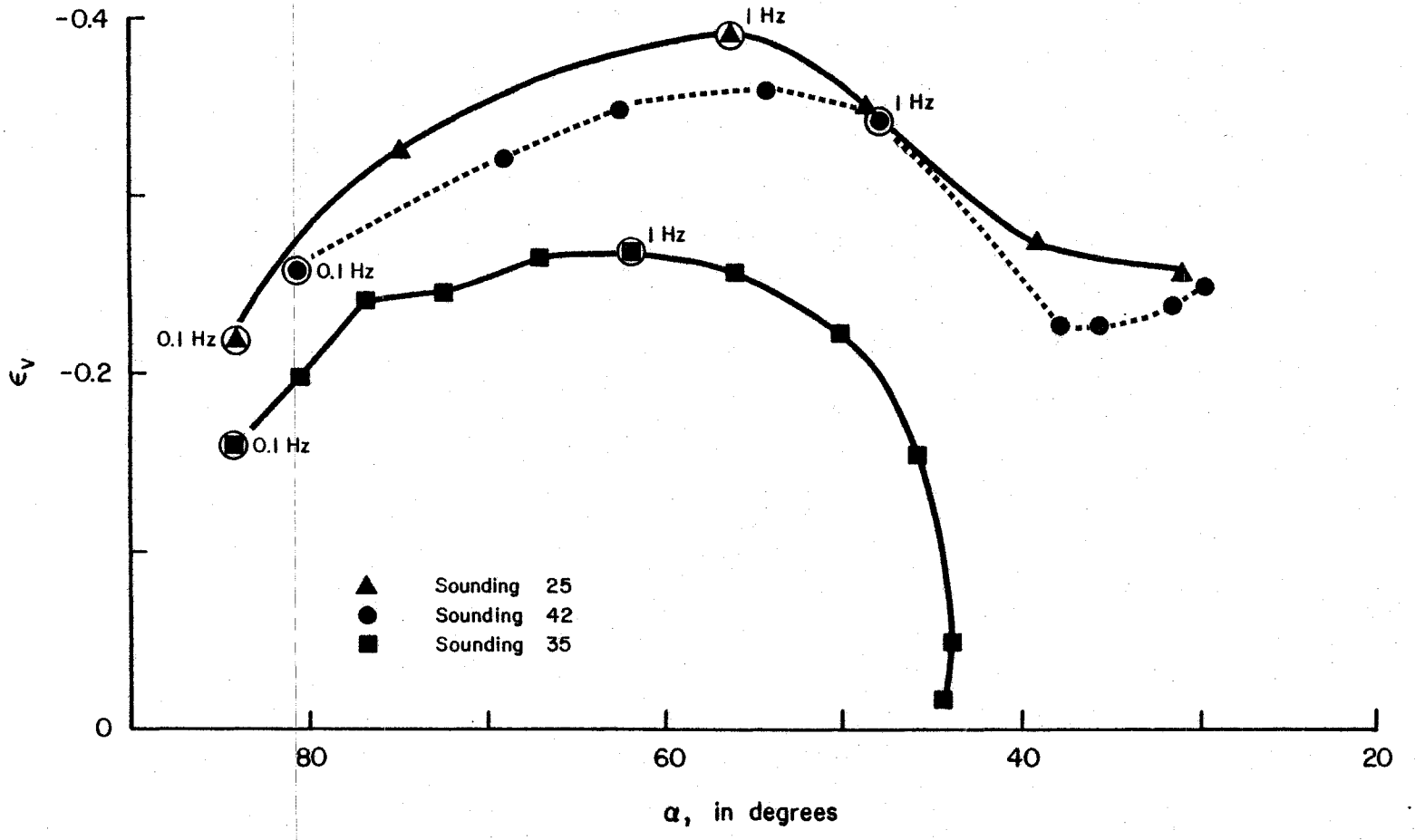

Figure 12. Pseudo-phasor plot of the vertical polarization data for sounding locations 35, 42, and 25. Compare this figure with the theoretical halfspace curve in Figure 6.

III.3.3 Apparent Resistivities

An apparent resistivity, ρa, is defined as the resistivity of a uniform halfspace that would produce the observed data. Therefore, any field measurement of a quantity that is expected theoretically over a halfspace can be converted to an apparent resistivity. For a CSEM study using a horizontal loop source, the expected quantities are amplitude and phase of the vertical and radial magnetic fields (and therefore tilt angle and ellipticity of the vertical polarization ellipse) and the tangential electric field. The apparent resistivities are computed for a particular sounding by finding the value of B at which the field measurement at frequency, f, equals the appropriate theoretical response and inserting the B, f, and r (source-sensor distance) values into the formula

$$\rho a = \frac{r^2}{B^2} \mu_0 \pi f \tag{30a}$$

derived by solving for ρ in equation 30 (note $\rho = 1/\sigma$). Examples of apparent resistivities computed from vertical and radial field phase using this procedure are shown plotted versus frequency in Figure 13. These plots can be very helpful prior to some other form of interpretation because they provide a first-order estimate of the sequence of resistivities sensed. As a rule of thumb, the apparent resistivities for low frequencies are representative of greater depths than those at higher frequencies.

Probably the most important property of the apparent resistivity conversion is that it removes the data variations that would be theoretically expected over a uniform halfspace. This is particularly

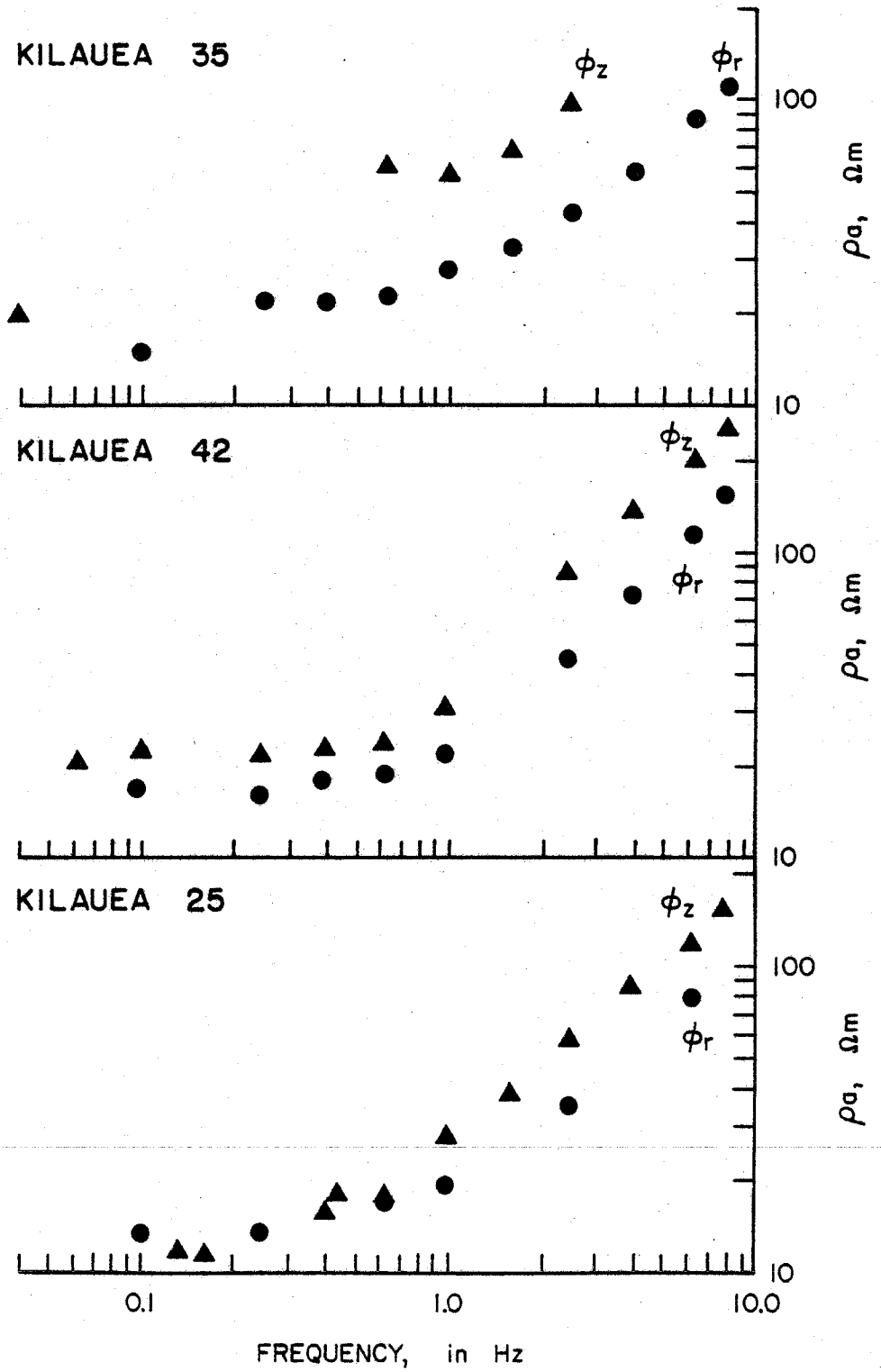

Figure 13. Apparent resistivities plotted versus frequency for sounding locations 35, 42, and 25. Values are derived from both vertical and radial field phase.

useful in analyzing CSEM data in the form of a map at constant frequency, because it removes the data variations due to cylindrical spreading from the source and provides a means of emphasizing subtle departures of the data from the expected spreading pattern.

For the Kilauea data, however, a slightly different approach is used which involves removing the effect of the highly resistive overburden of thickness, d, over a semi-infinite halfspace of resistivity, ρ. In Figure 14, theoretical values of vertical ellipticity are plotted as a function of tilt angle in pseudo-phasor fashion for such a model. Constant induction numbers, B, plot along lines radial to the point (tilt angle = 90°, vertical ellipticity = 0). The procedure is then to use the data (determined from field measurements) to estimate B (and d) by interpolating between the nearest lines in Figure 14. This estimate of B is then used in equation (30a) to calculate ρa, the apparent resistivity. The latter apparent resistivity is not the same as that computed from a theoretical halfspace response, because the effect of the highly resistive overburden has been removed. The apparent resistivity so determined would be identical to that of a semi-infinite halfspace only for $d/r = 0$ (that curve in Fig. 14 is identical to the curve in Fig. 6).

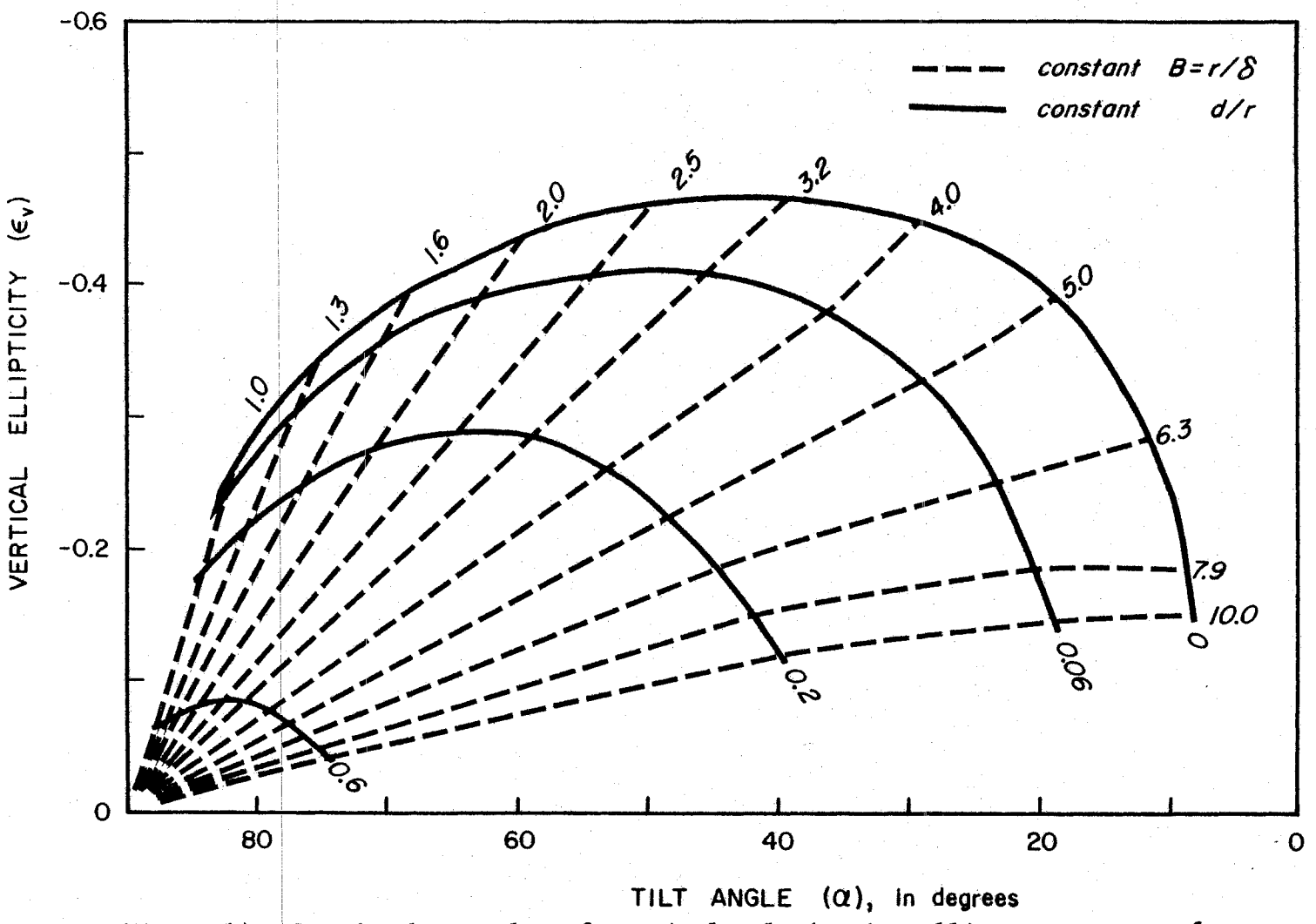

Figure 14. Pseudo-phasor plot of vertical polarization ellipse parameters for source and receiver a distance, d, above a homogeneous halfspace (solid lines). Dashed lines join data points with equal values of the induction number, B, for the lower halfspace.

IV. DISCUSSION OF KILAUEA RESULTS

Over 2200 magnetic field measurements were obtained at the 45 sounding locations occupied during this study. Each of the data sets was then converted to absolute field amplitudes and phases, polarization parameters, and apparent resistivities (using the halfspace procedure for phase data and the procedure removing the overburden for tilt angle and vertical ellipticity data) to produce a final data set of over 5000 values. Presentation of all 5000 would occupy an inordinate number of pages; therefore, only sufficient data are presented in this section to give a clear picture of the general characteristics of the data. Complete data listings can be found in Kauahikaua (1982b).

The various quantities are first presented as separate contoured maps at three frequencies. The vertical magnetic field amplitude (normalized by the theoretical primary field value) and phase is presented at 0.1, 1.0, and 8.0 Hz, whereas each of the polarization parameters are presented at 0.25, 1.0, and 6.3 Hz. The frequency range was chosen to give the best spatial coverage at the widest range of frequencies. In each of these maps, there are a few values which are not easily contoured; these values have been written in. The last set of maps will show apparent resistivities derived from vertical field phase, radial field phase, and the combination of vertical ellipticity and tilt angle at 1 Hz.

Except at the lowest frequency, the vertical magnetic field, shown in Figures 15 to 20, generally decreases in both amplitude and phase with increasing distances away from the loop source. A decrease is expected for induction numbers greater than 2.0 (see Fig. 4); however, the variations noted in the vertical field data taken at 0.1 Hz are not characteristic of the theoretical vertical field over a layered halfspace for induction numbers less than 2.0. The amplitude contours tend to be elongated parallel to the southwest rift at high frequencies and shift to become more parallel to the east rift at low frequencies; the phase contours are also elongated, but shift in the opposite sense, that is, from paralleling the east to paralleling the southwest rift, at lower frequencies.

The vertical ellipticity and tilt angle contours, shown in Figures 21 to 26, are remarkably circular around the source, compared to the vertical field data. The contours are slightly farther apart northwest of the source (Mauna Loa flank) suggesting generally higher resistivities there. Departures from circularity do occur: contours are distorted over the northernmost part of the east rift at high frequencies and are also distorted to become parallel to both rift zones at low frequencies and at distances greater than 5 km.

The horizontal ellipticity and strike angle, which can be viewed as indicators of lateral resistivity changes, are shown in Figures 27 to 32. The strike angle contours are markedly parallel to the east rift, remaining almost unchanged in magnitude from 1.0 to 0.25 Hz. The reader is urged to remember that a strike angle of +60° corresponds to a 30° deviation to the left of radial (when looking from the

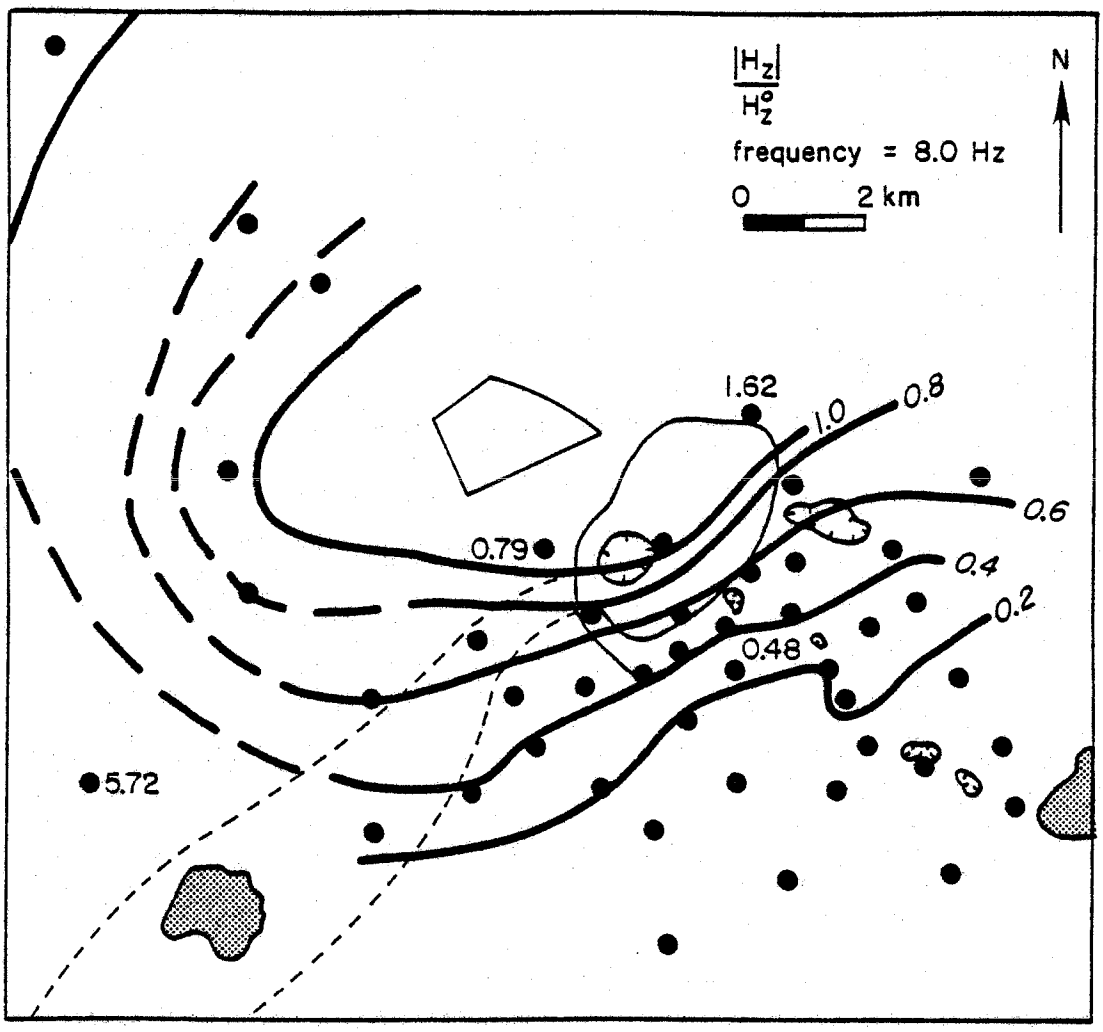

Figure 15. Map of normalized vertical magnetic field amplitude data for 8 Hz.

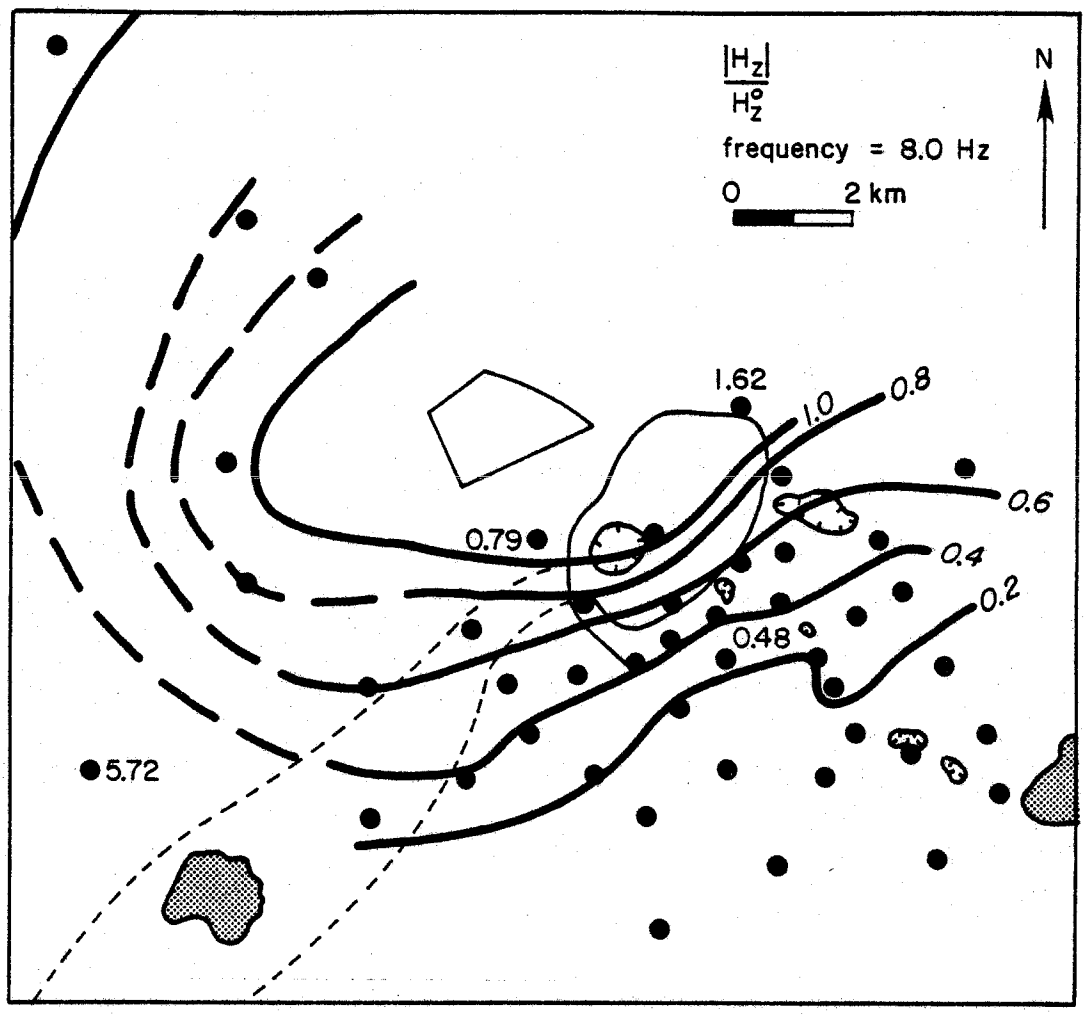

Figure 15. Map of normalized vertical magnetic field amplitude data for 8 Hz.

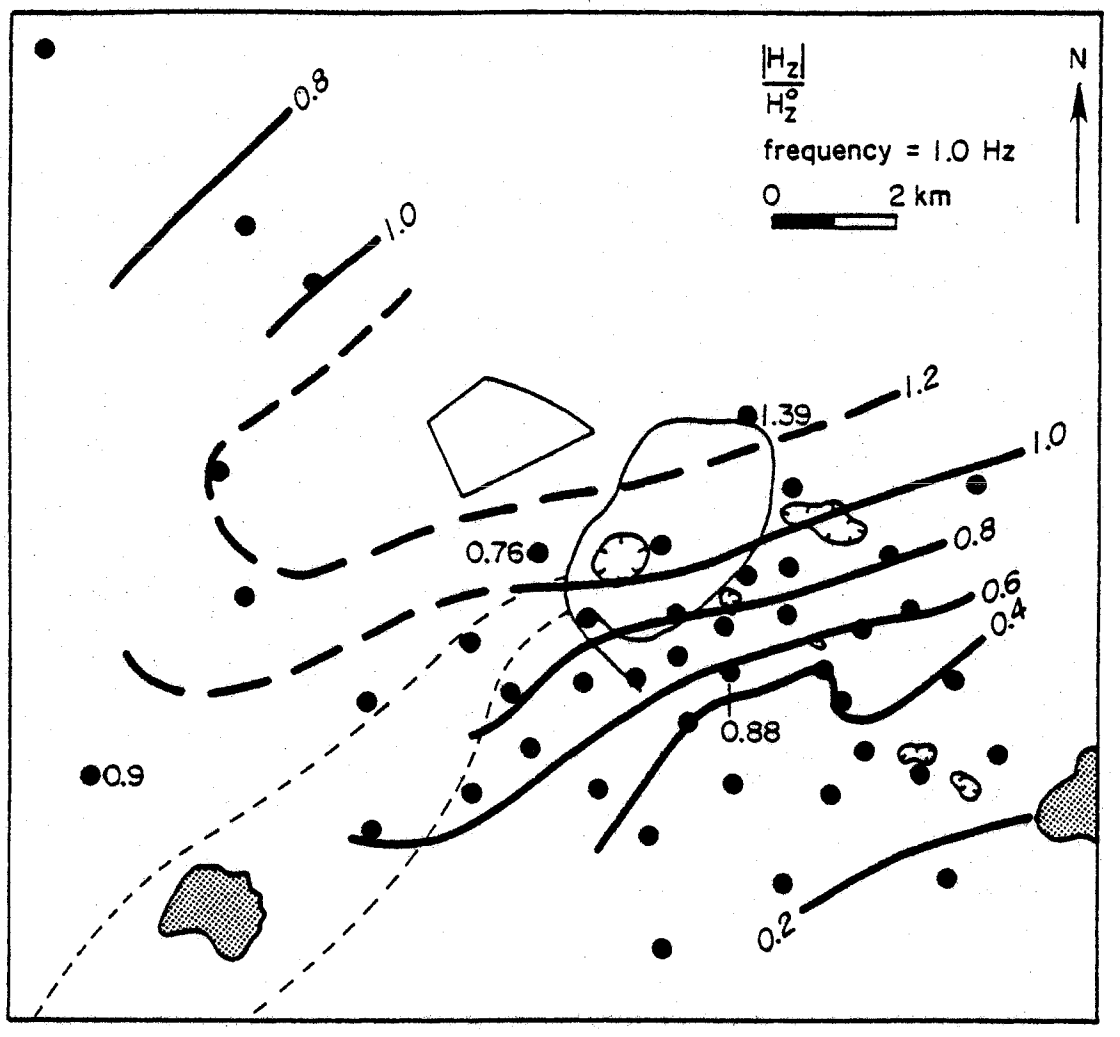

Figure 16. Map of normalized vertical magnetic field amplitude data for 1 Hz.

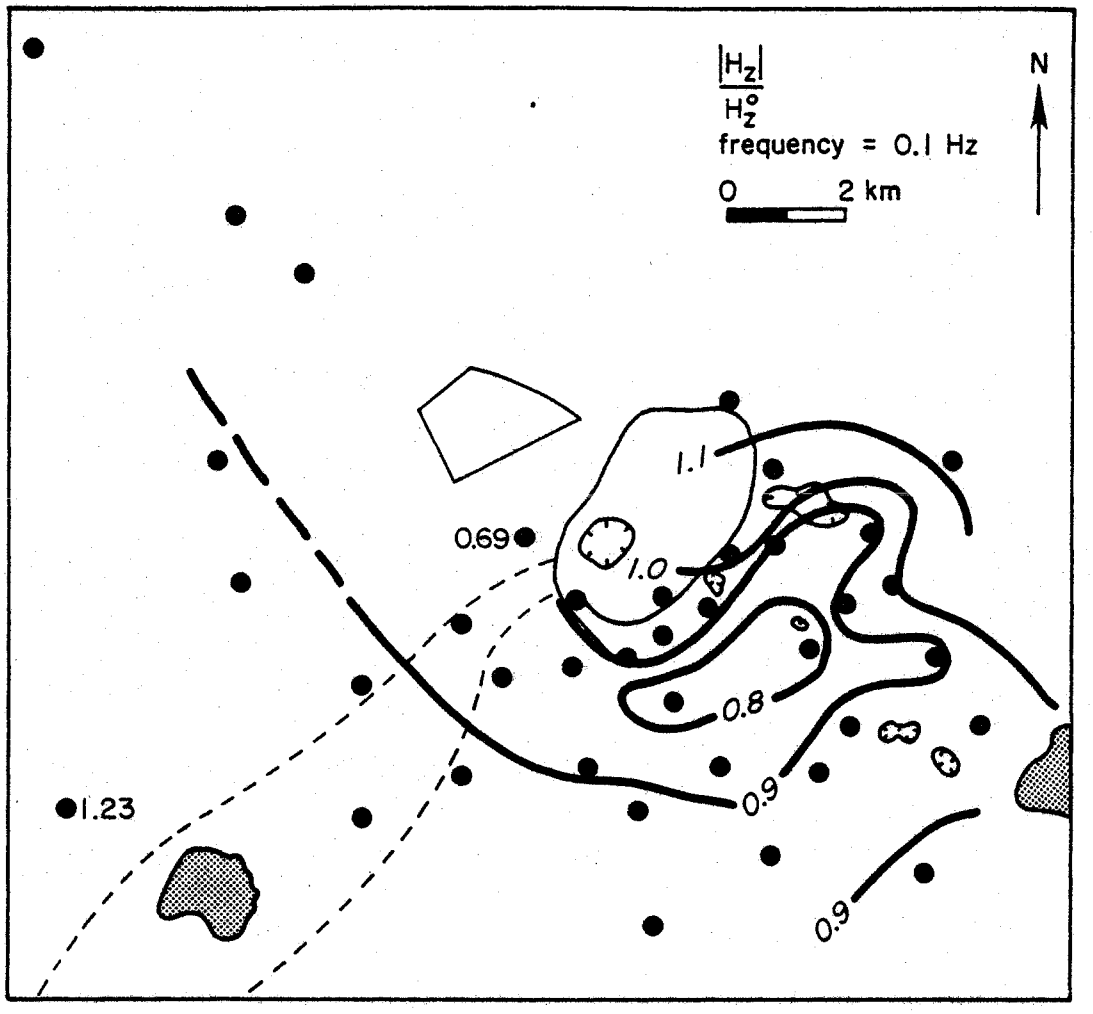

Figure 17. Map of normalized vertical magnetic field amplitude data for 0.1 Hz.

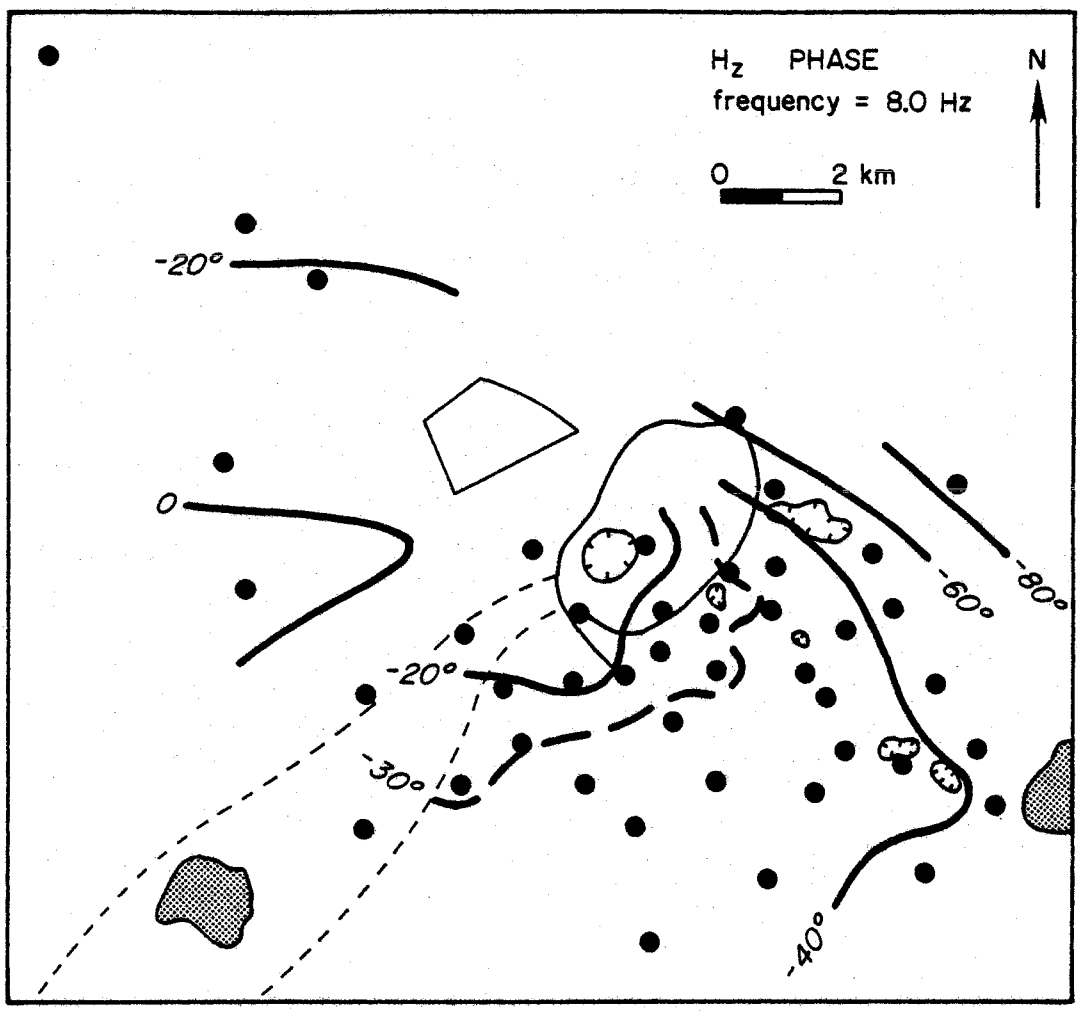

Figure 18. Map of vertical magnetic field phase data for 8 Hz.

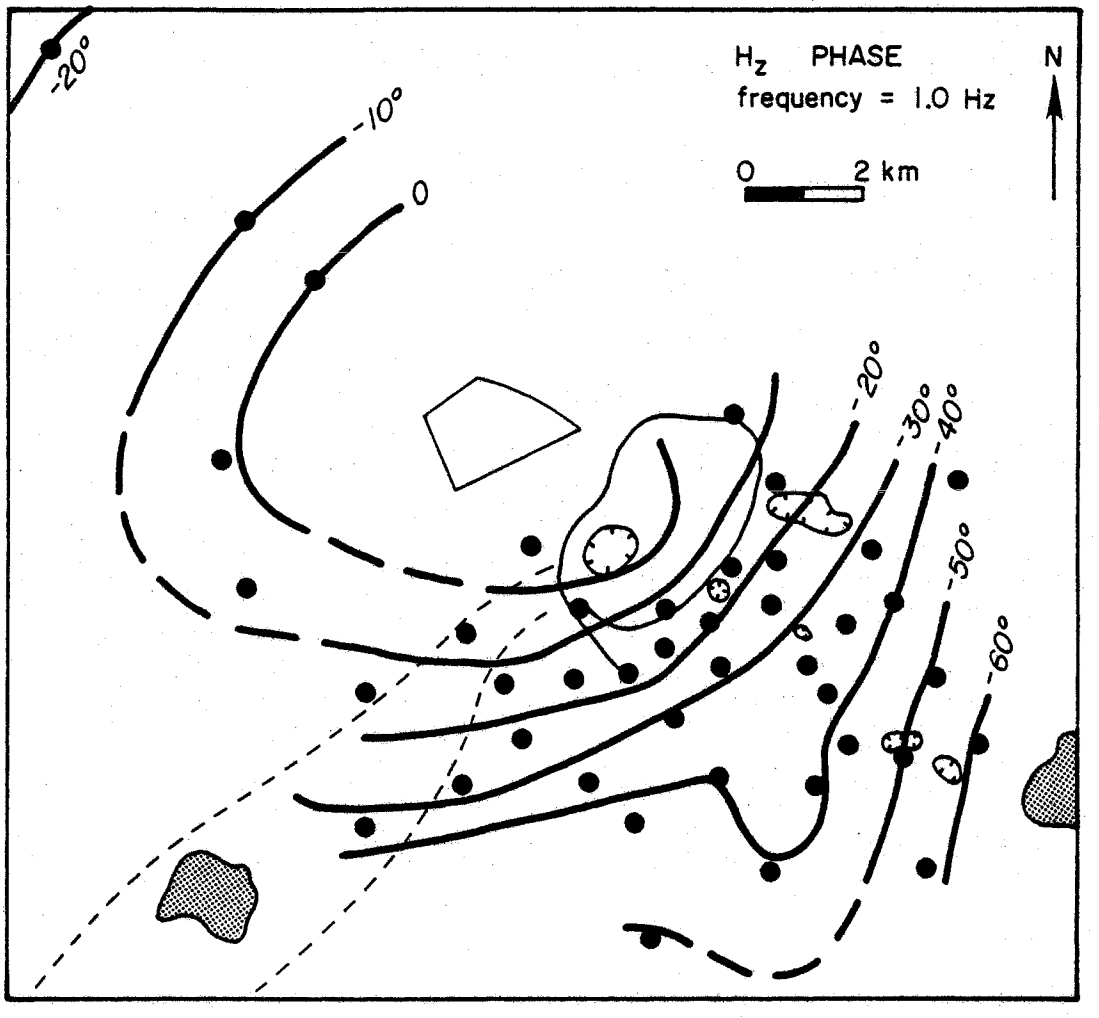

Figure 19. Map of vertical magnetic field phase data for 1 Hz.

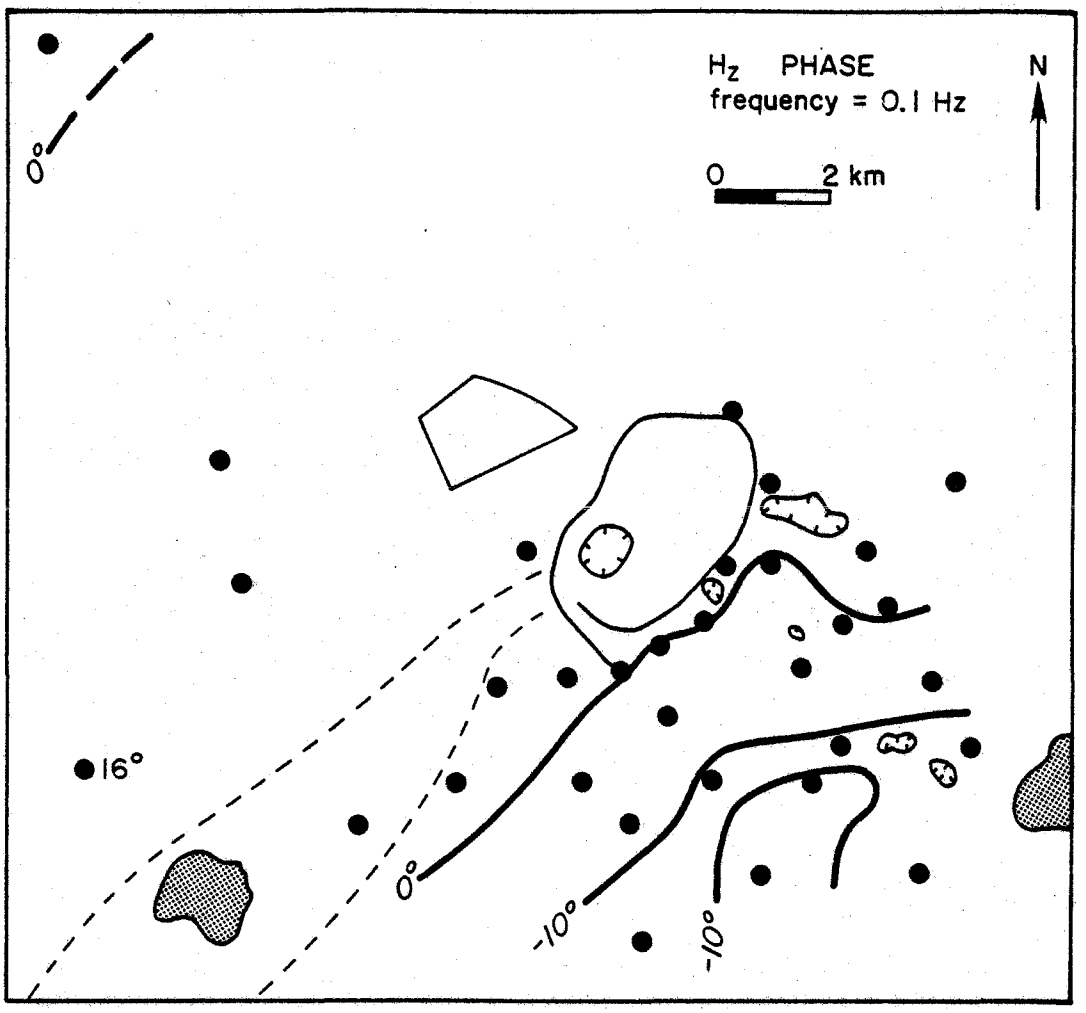

Figure 20. Map of vertical magnetic field phase data for 0.1 Hz.

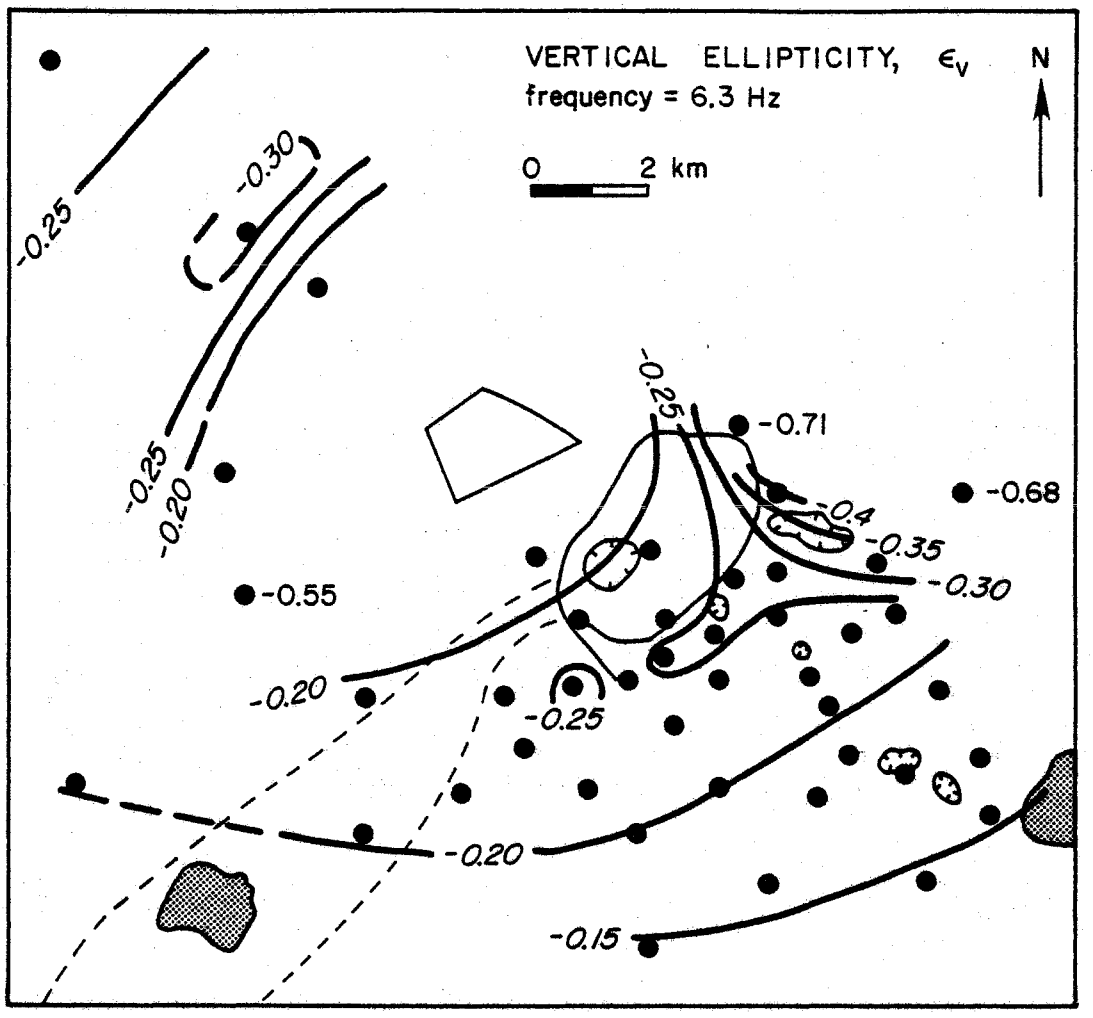

Figure 21. Map of vertical ellipticity data for 6.3 Hz.

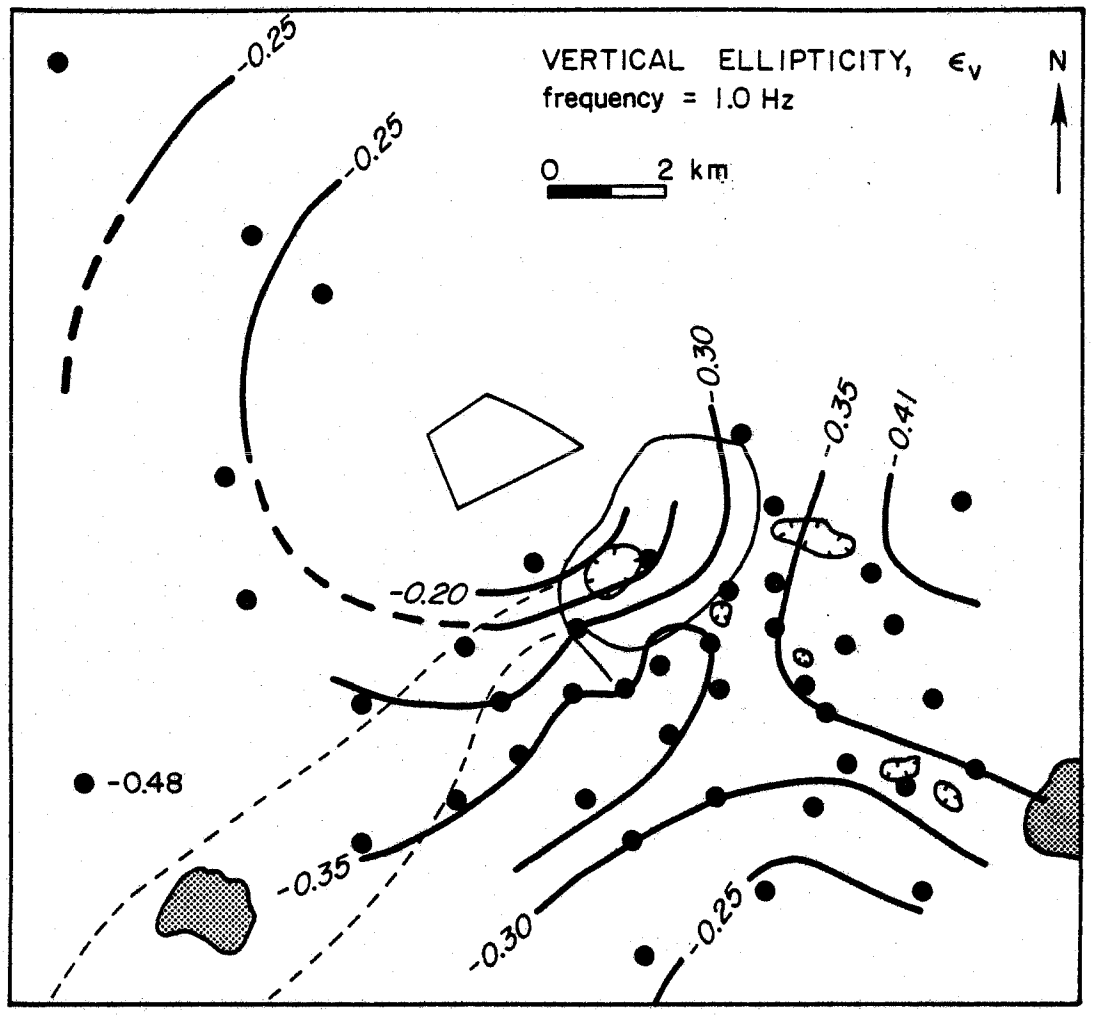

Figure 22. Map of vertical ellipticity data for 1 Hz.

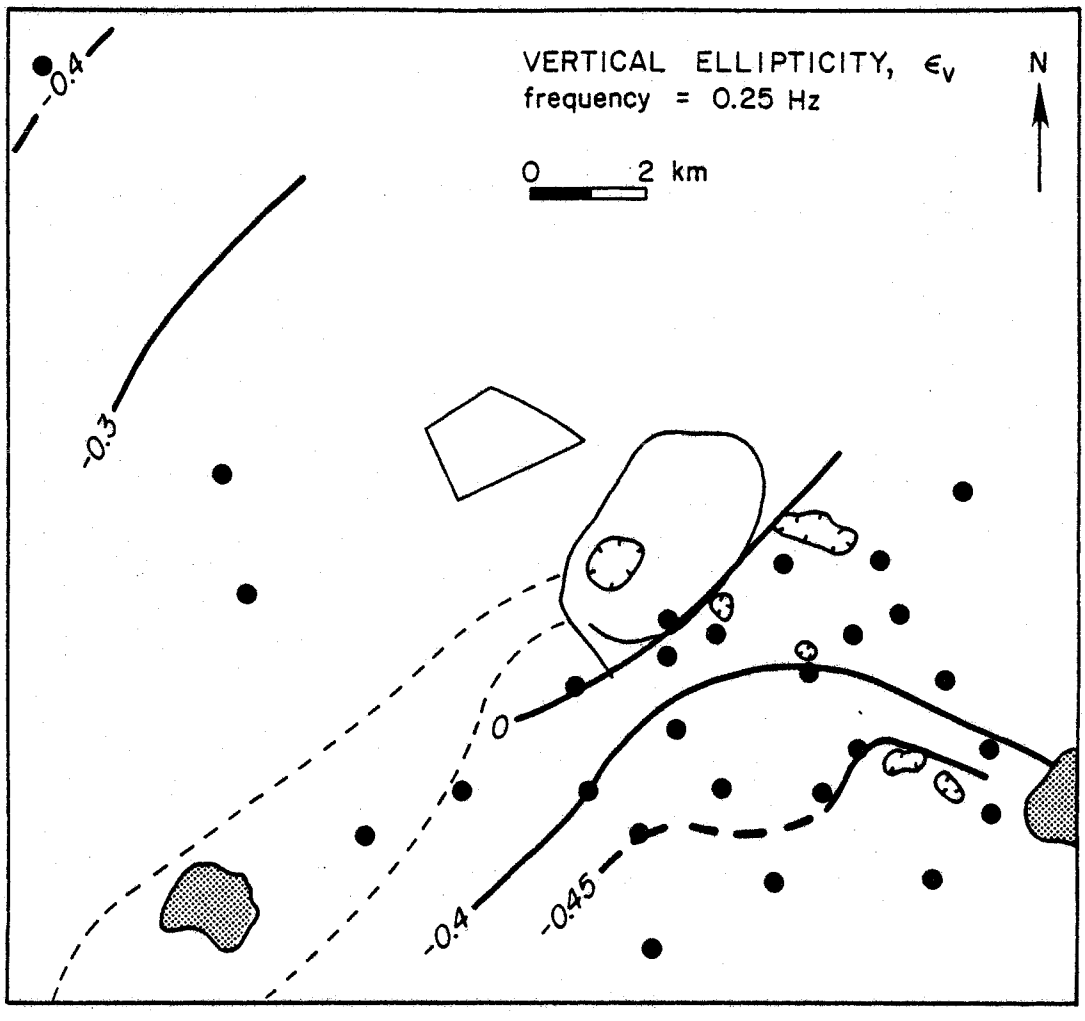

Figure 23. Map of vertical ellipticity data for 0.25 Hz.

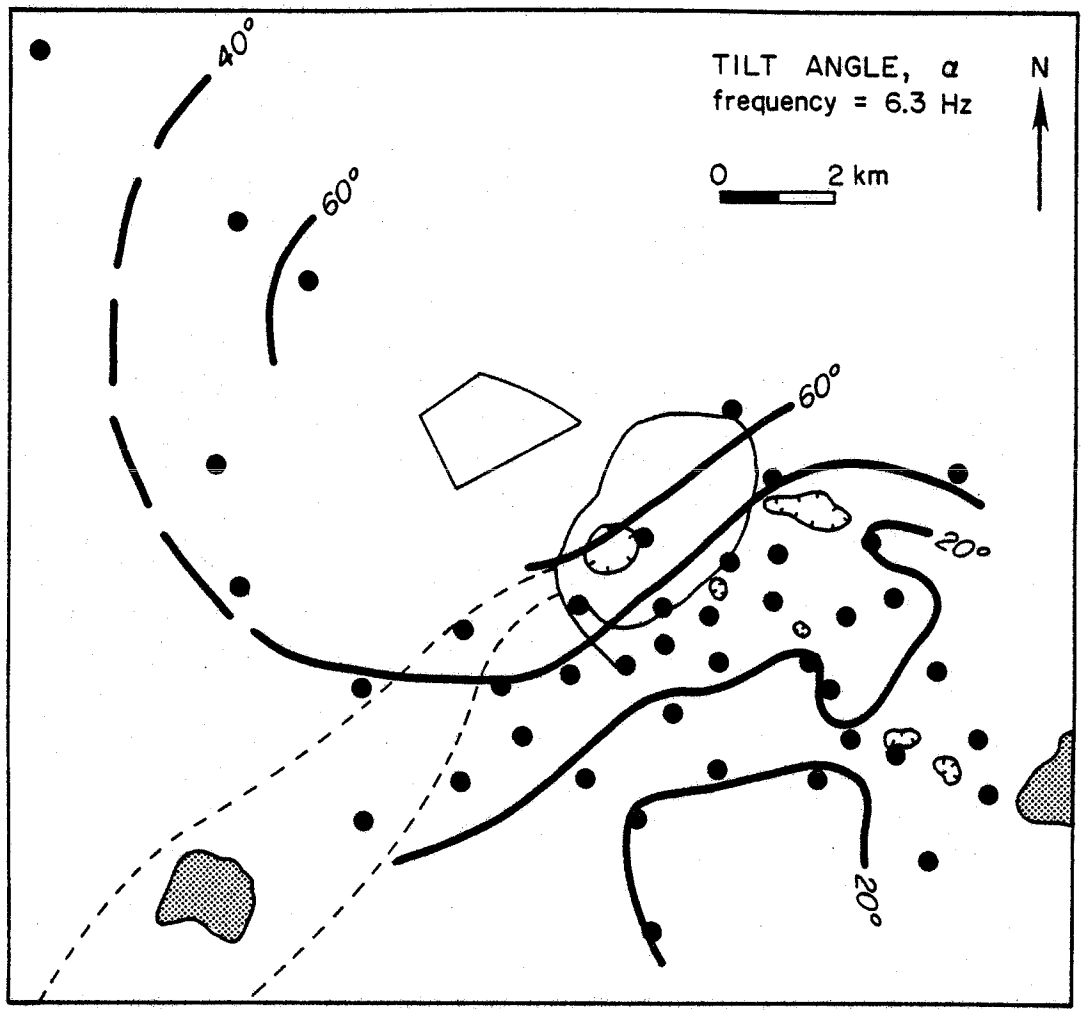

Figure 24. Map of tilt angle data for 6.3 Hz.

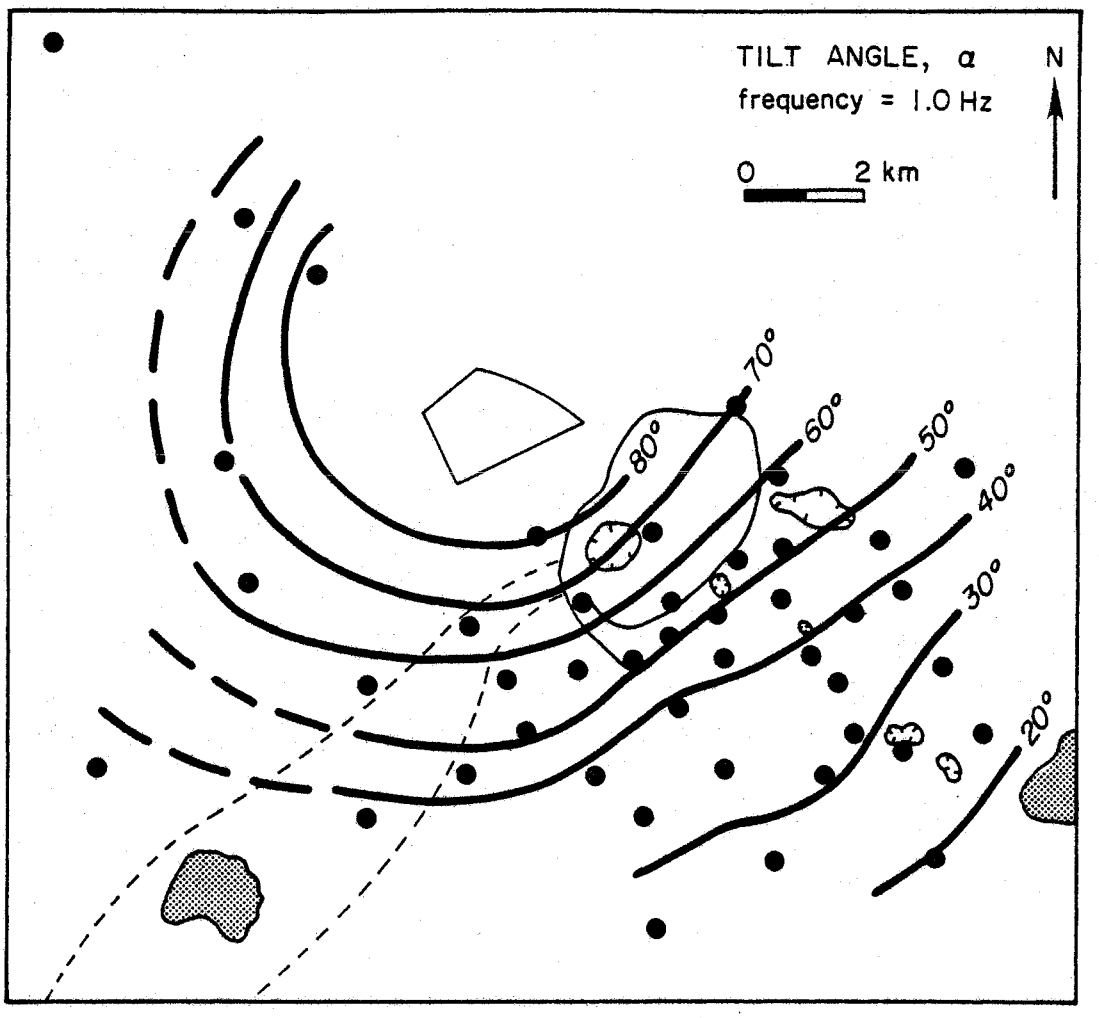

Figure 25. Map of tilt angle for 1 Hz.

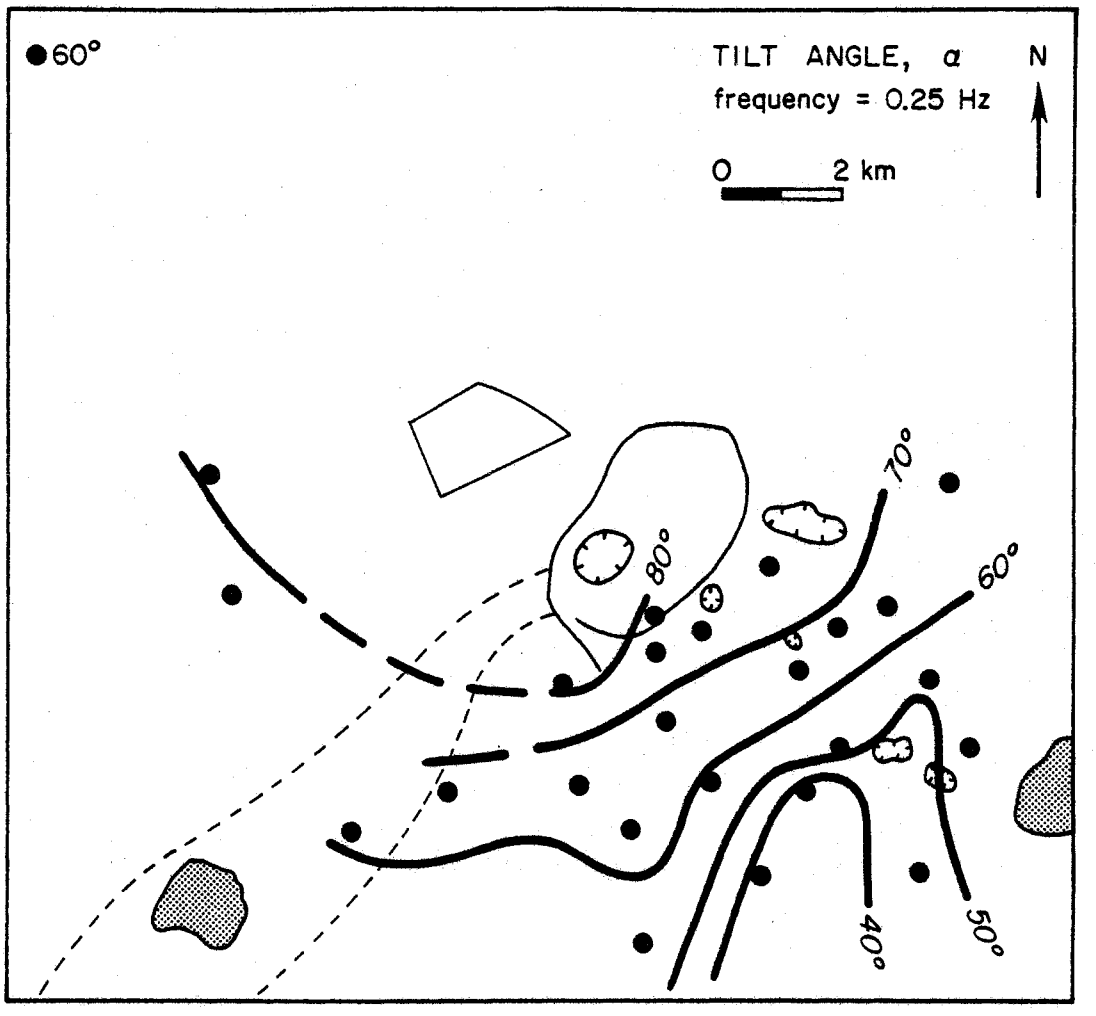

Figure 26. Map of tilt angle data for 0.25 Hz.

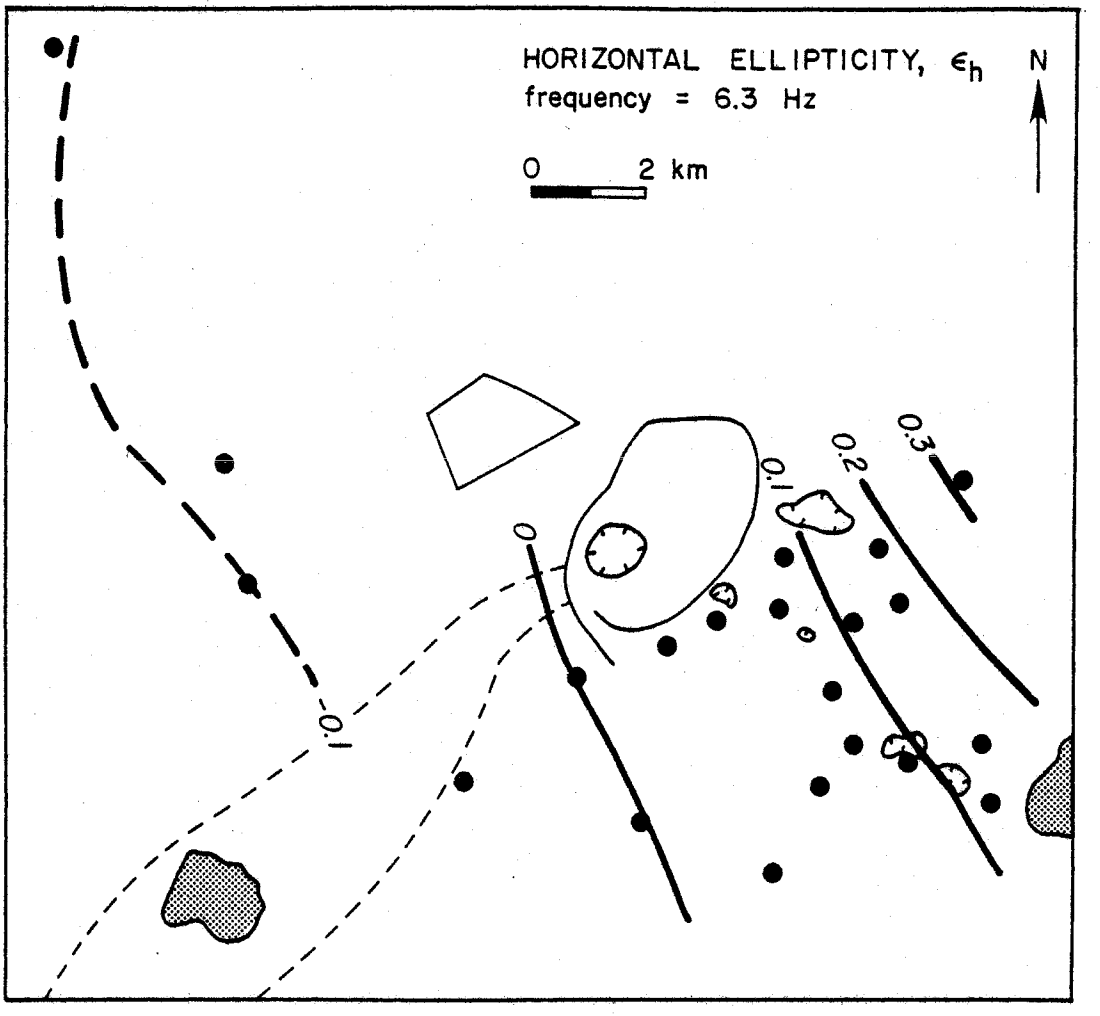

Figure 27. Map of horizontal ellipticity data for 6.3 Hz.

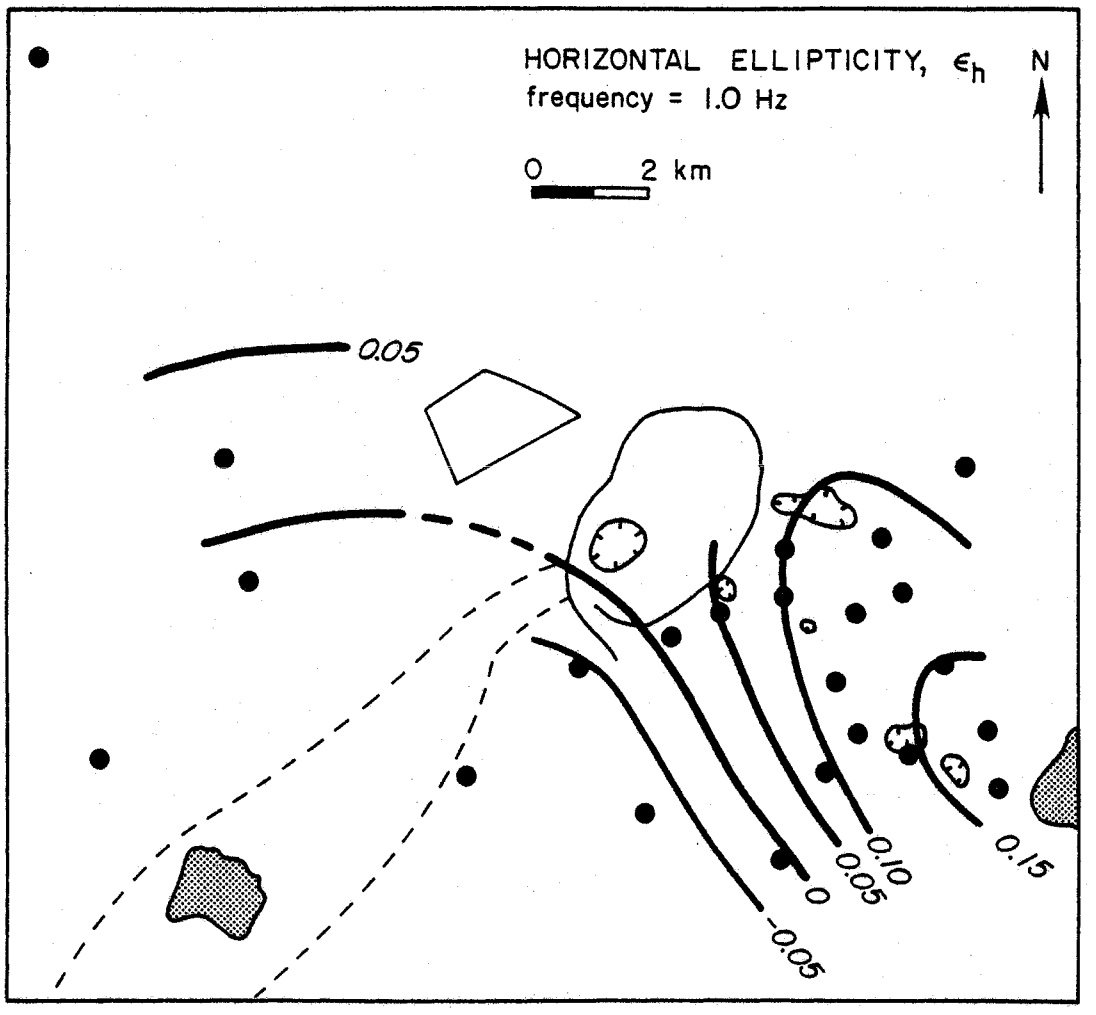

Figure 28. Map of horizontal ellipticity data for 1 Hz.

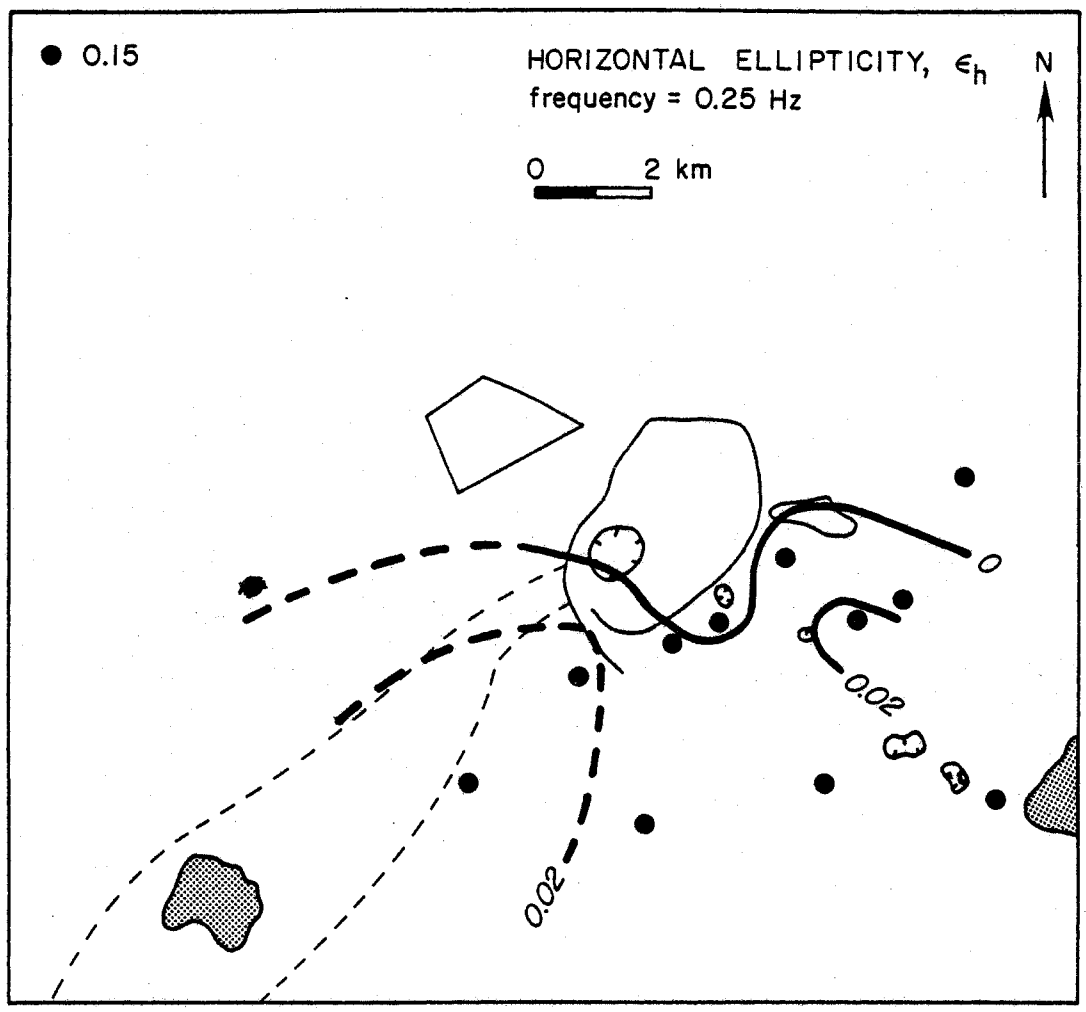

Figure 29. Map of horizontal ellipticity data for 0.25 Hz.

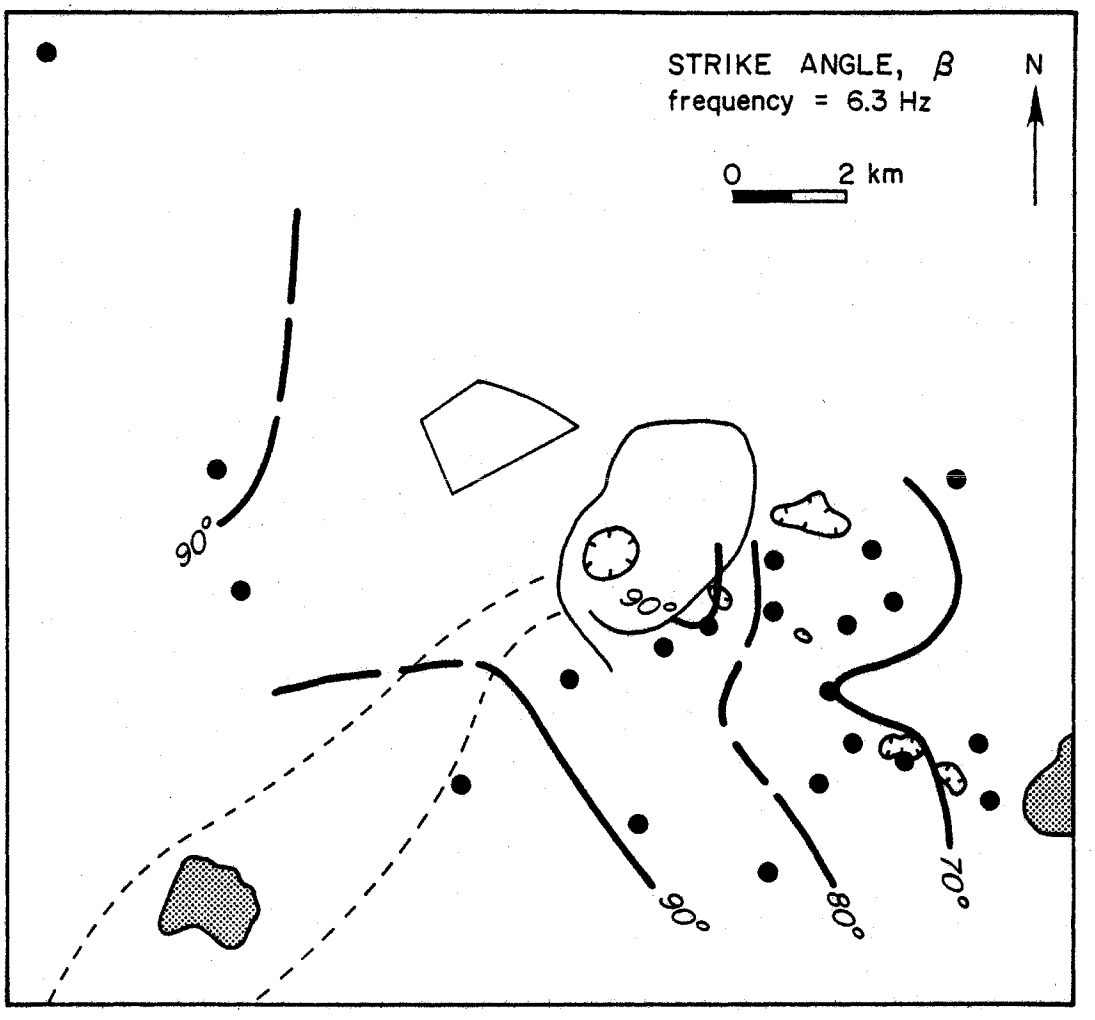

Figure 30. Map of strike angle data for 6.3 Hz.

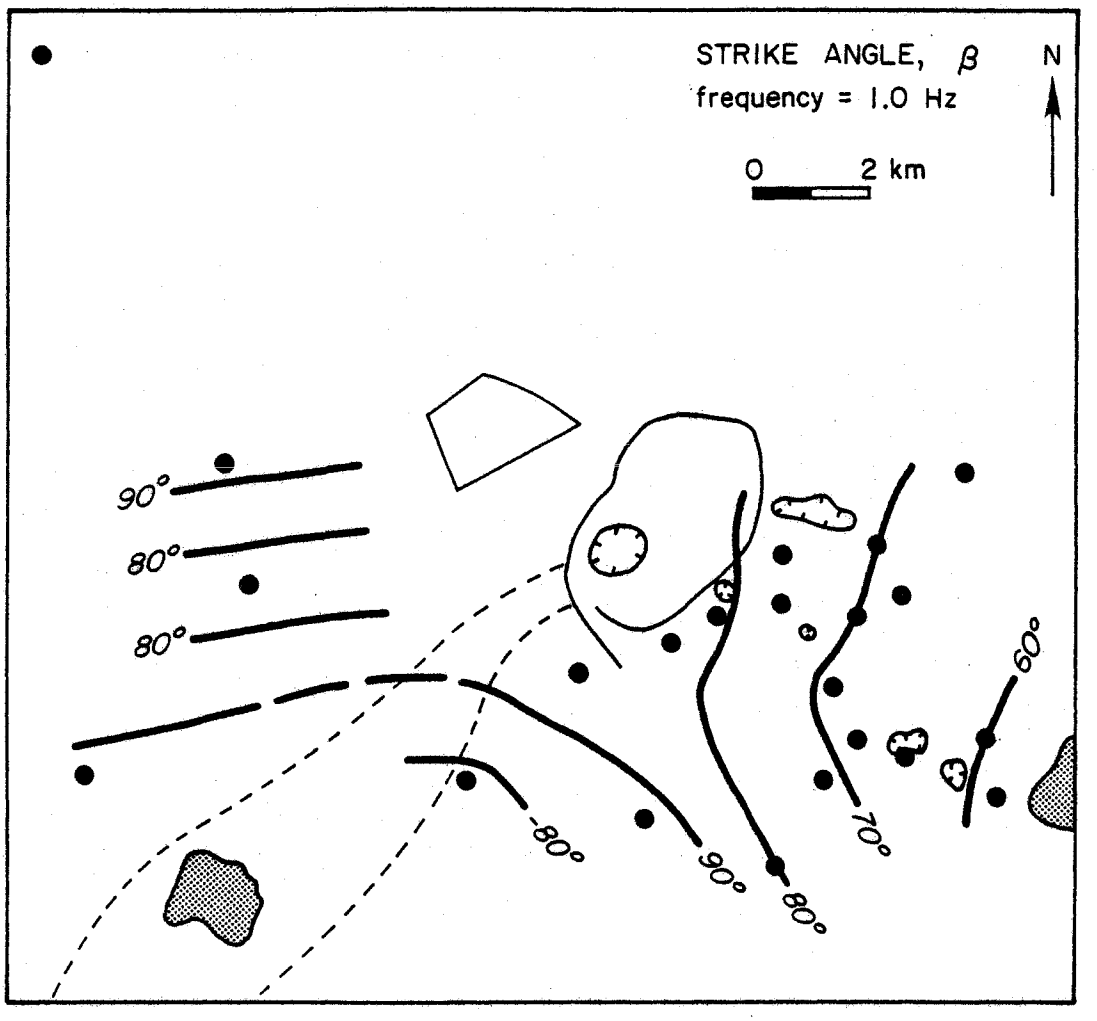

Figure 31. Map of strike angle data for 1 Hz.

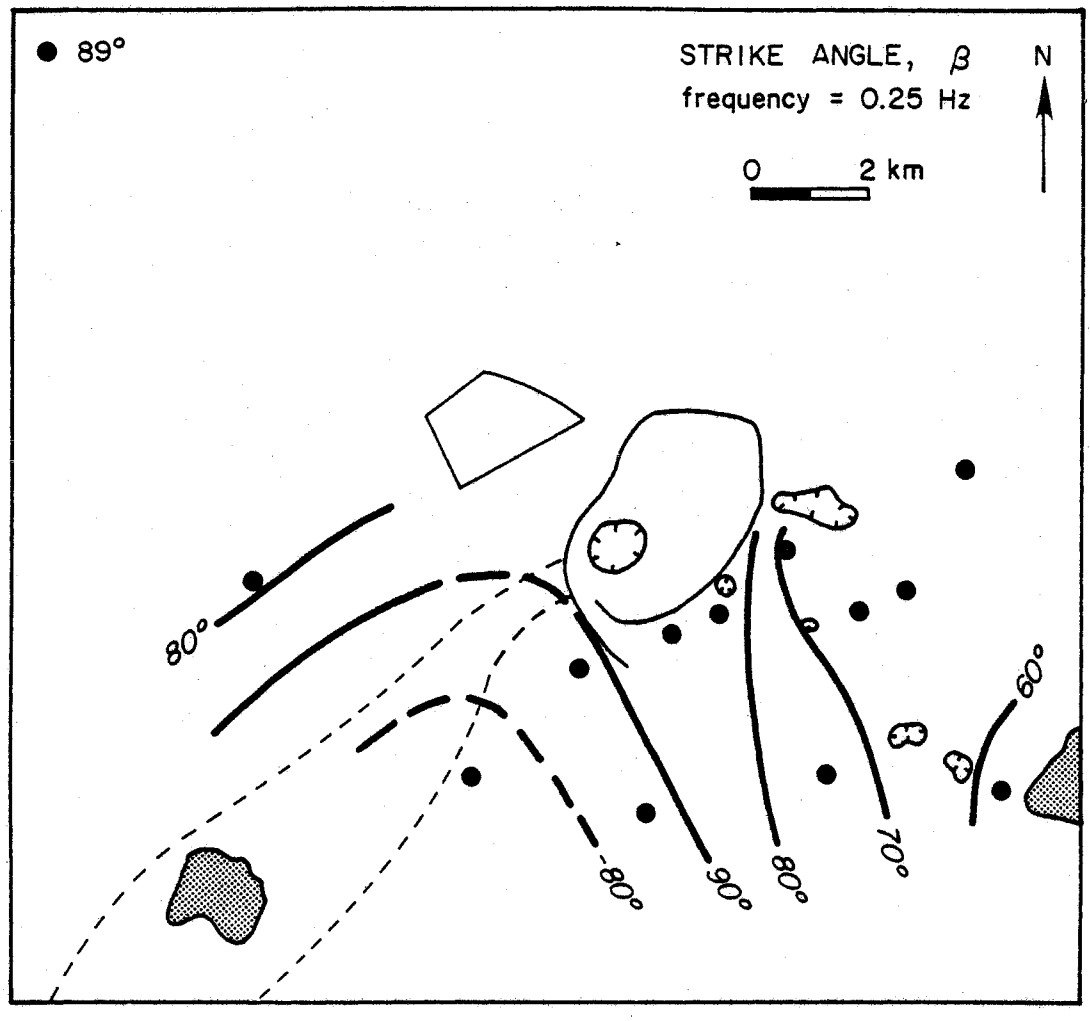

Figure 32. Map of strike angle data for 0.25 Hz.

source to the observation point) for the major axis of the horizontal polarization ellipse. The horizontal ellipticity contours are also parallel to the east rift, but only at high frequencies. At lower frequencies, the values become smaller and the contours tend to close around two positive highs near the upper extremity of the southwest rift zone and the upper east rift zone near Puhimau crater, respectively.

Clearly, a major lateral change in resistivity coincides with the east rift zone trace. All components of the data are distorted either over the rift or immediately east of it. The horizontal polarization ellipse parameter anomalies are the most unambiguous indicator of this lateral resistivity change. The southwest rift also distorts the induced magnetic field, but not as much as the east rift zone. The difference may be due more to a difference in rift orientation relative to the source loop, rather than a difference in size or type of structure.

The final map set shows apparent resistivities at 1 Hz derived from three different quantities: vertical field phase (Fig. 33), radial field phase (Fig. 34), and tiltangle and vertical ellipticity (Fig. 35). The two sets of values derived from the vertical and radial field phases agree quite closely in that the lowest resistivities are observed in the area south of Halema'uma'u pit crater; however, the particular apparent resistivity values do not agree, the ones in Figure 34 being consistently lower than those in Figure 33. The apparent resistivities derived from the vertical polarization ellipse parameters are also low in this area, but their significance is

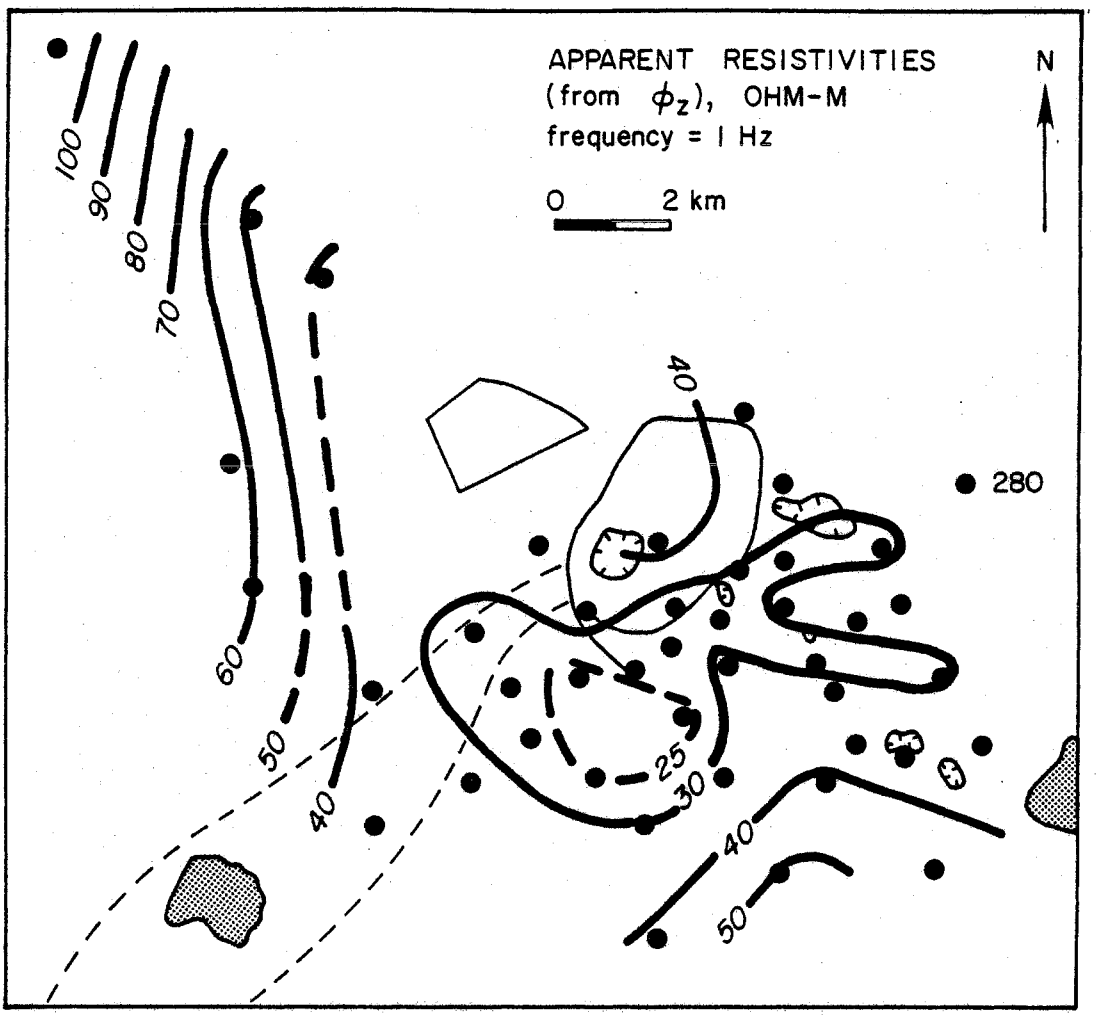

Figure 33. Map of apparent resistivity data for 1 Hz derived from vertical field phase measurements, using the halfspace procedure.

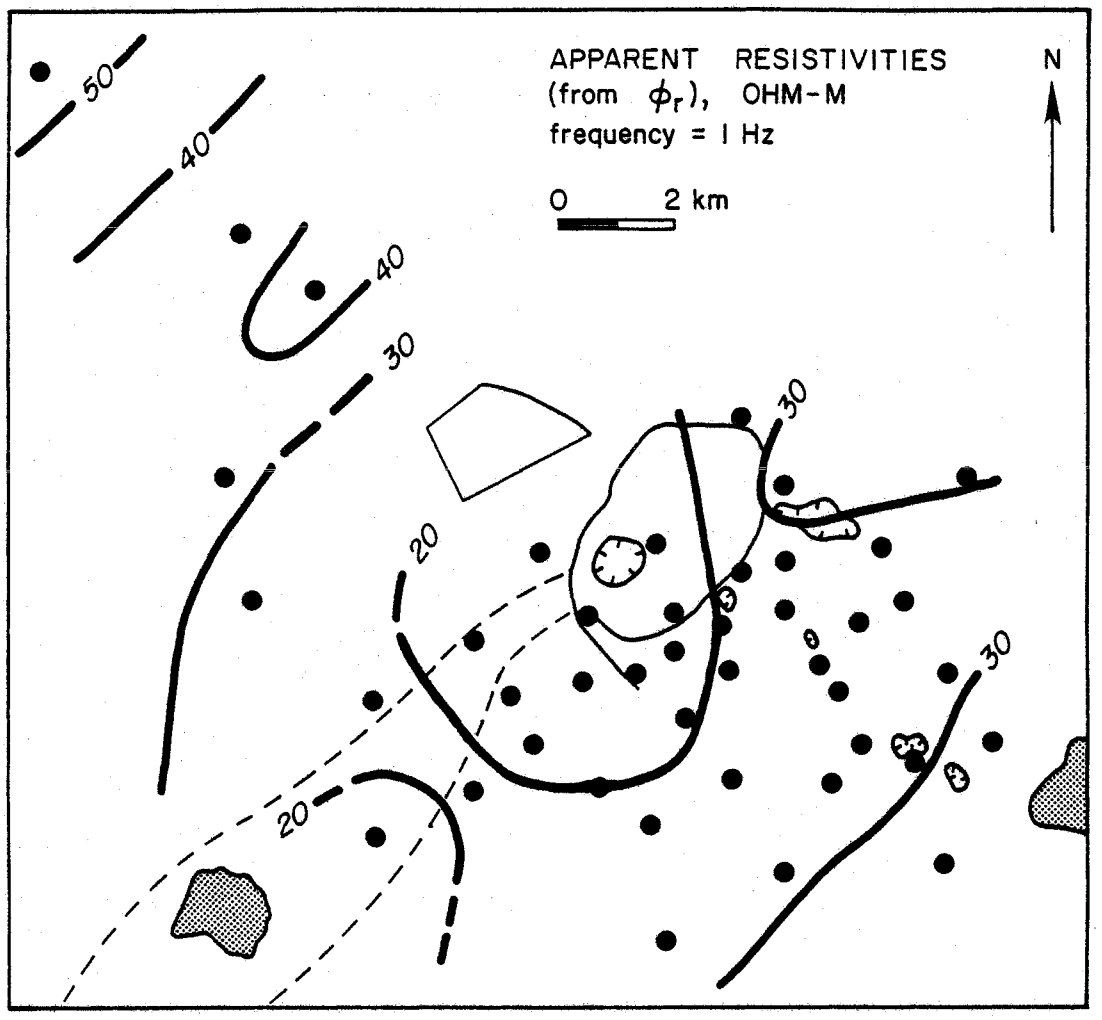

Figure 34. Map of apparent resistivities data for 1 Hz derived from radial field phase measurements, using the halfspace procedure.

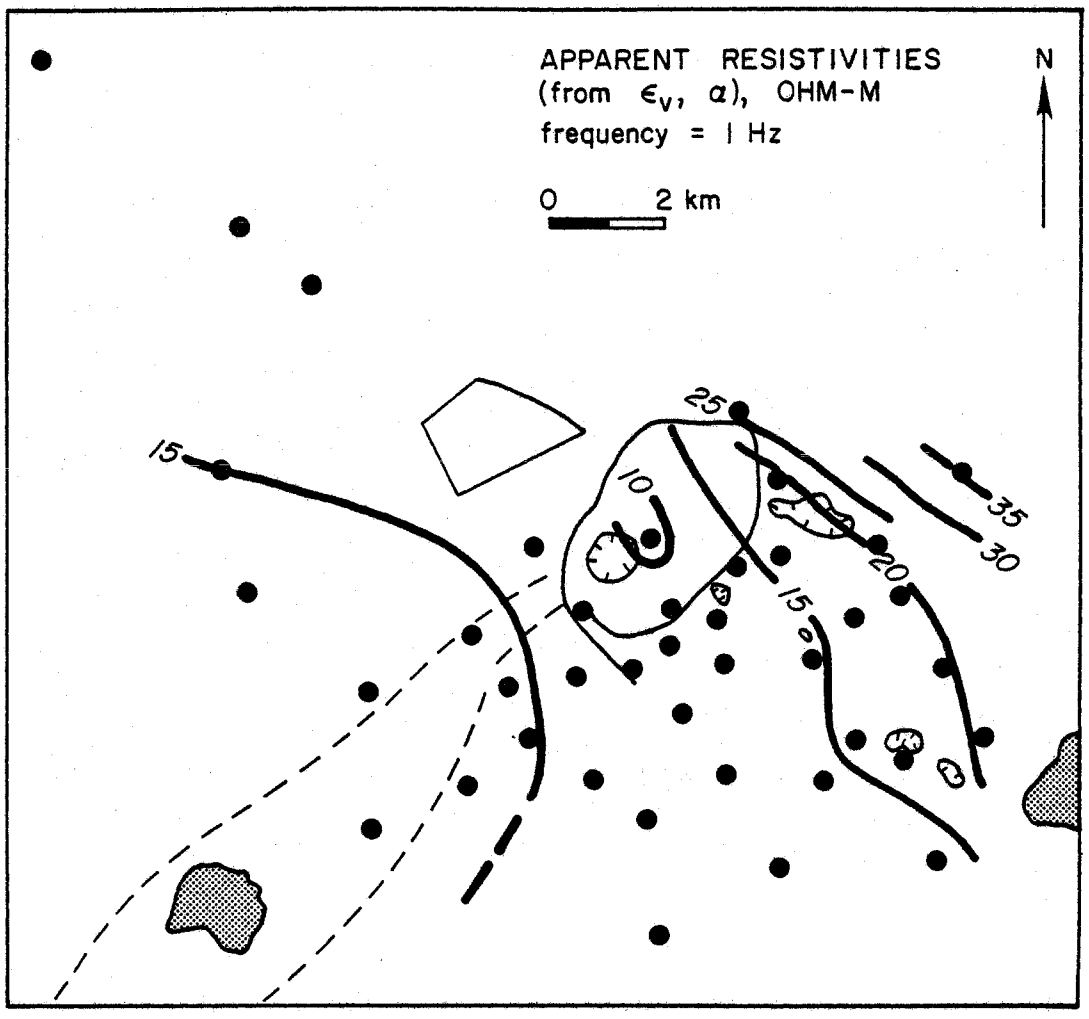

Figure 35. Map of apparent resistivity data for 1 Hz derived from tilt angle and vertical ellipticity data, using the two-layer procedure which removes the effect of the highly resistive overburden.

diminished by the fact that values are low over most of the study area.

The generally low values from polarization ellipse data are a consequence of the two-layer model used in apparent resistivity computation for those data types, and really should not be compared directly with apparent resistivities computed from phase data using the half-space model. Including the effects of a resistive overburden, where they had previously been removed, would tend to raise the apparent resistivity values.

Apparent resistivity data are easier to visualize when presented as frequency-distance plots. In such a plot, several locations are chosen along a line, and the apparent resistivities are plotted at a point determined by the location's position along the line (horizontal axis) and by the data's frequency (vertical axis is log frequency decreasing downward to imply increasing depth in accordance with the skin depth definition in Eq. 30). Once plotted, the values are contoured to provide a quick, two-dimensional view of the data. A three-dimensional view can be achieved by constructing several frequency-distance plots to cover the entire area of interest.

Most of the apparent resistivity values derived from vertical polarization ellipse, parameters were compiled into five frequency-distance plots, whose locations are shown in Figure 36; the plots are shown in Figures 37 to 40. Sections in which apparent resistivities are less than 15 ohm-m have been shaded for emphasis. Each of the five plots shows a low-resistivity area between 0.4 and 4 Hz beneath Kilauea volcano. The area does not extend beyond the east rift in the northeast direction, nor does it extend beyond the southwest rift in the

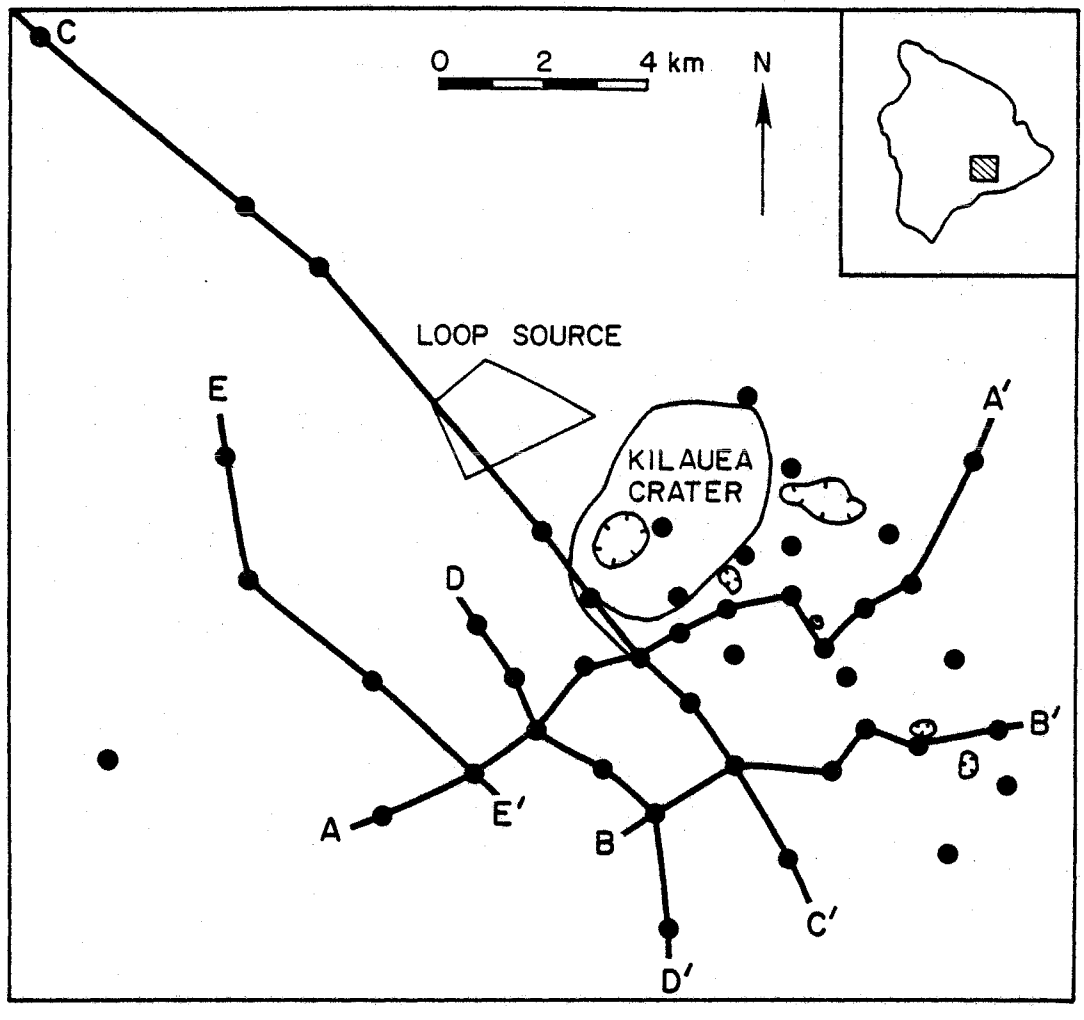

Figure 36. Map of the Kilauea summit area showing the locations of five profile lines, A-A' to E-E', along which data will be presented.

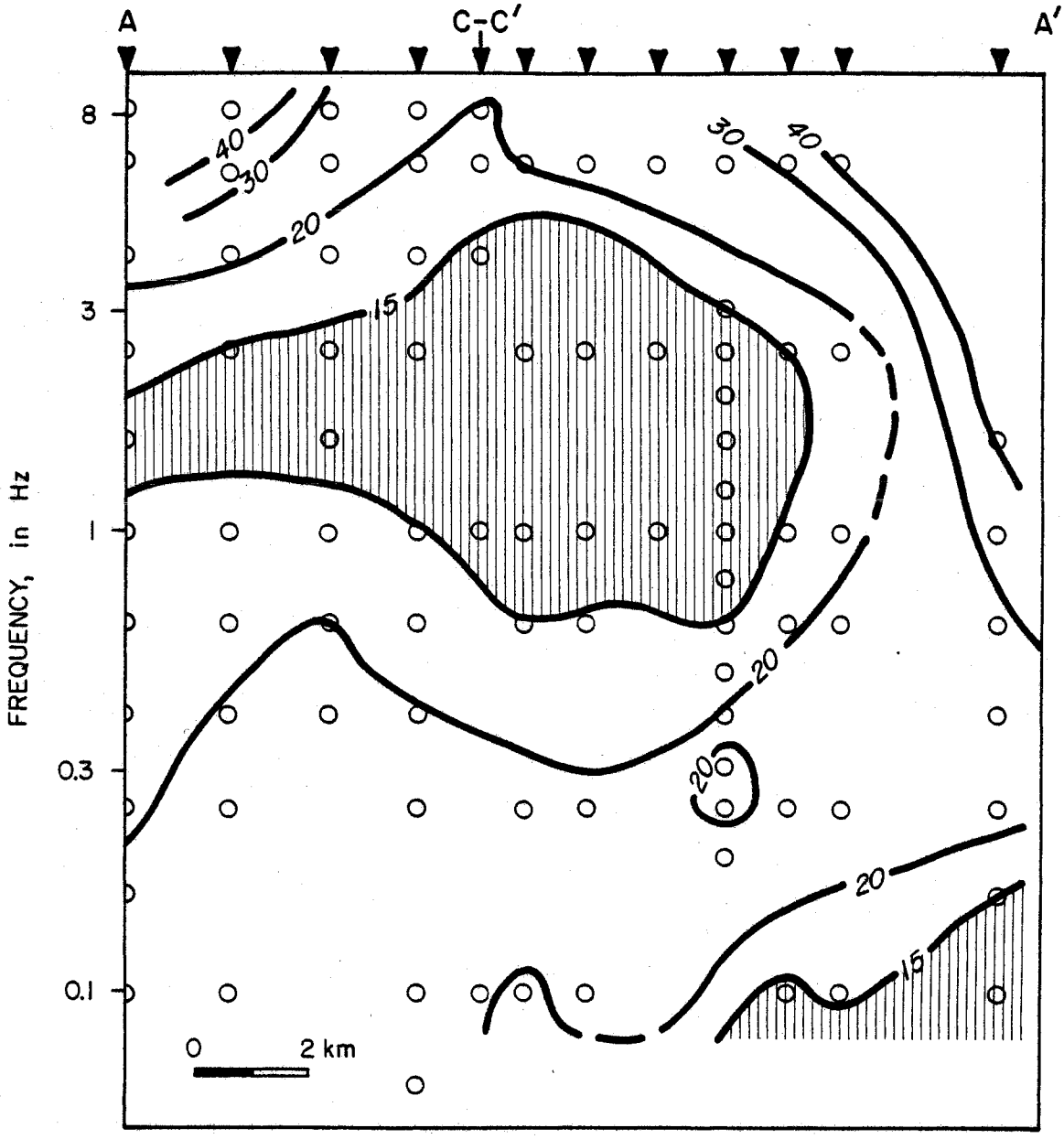

Figure 37. Plot of apparent resistivity data (from vertical polarization ellipse data) versus frequency along A-A' in Figure 36. Contour values are in ohm-m; values less than 15 ohm-m have been shaded for emphasis. Open circles represent data points and solid, inverted triangles represent sounding locations.

Figure 38. Plot of apparent resistivity data (from vertical polarization ellipse data) versus frequency along profiles B-B' and D-D' in Figure 36. Contour values are in ohm-m; values less than 15 ohm-m have been shaded for emphasis. Open circles represent data points and solid inverted triangles represent sounding locations.

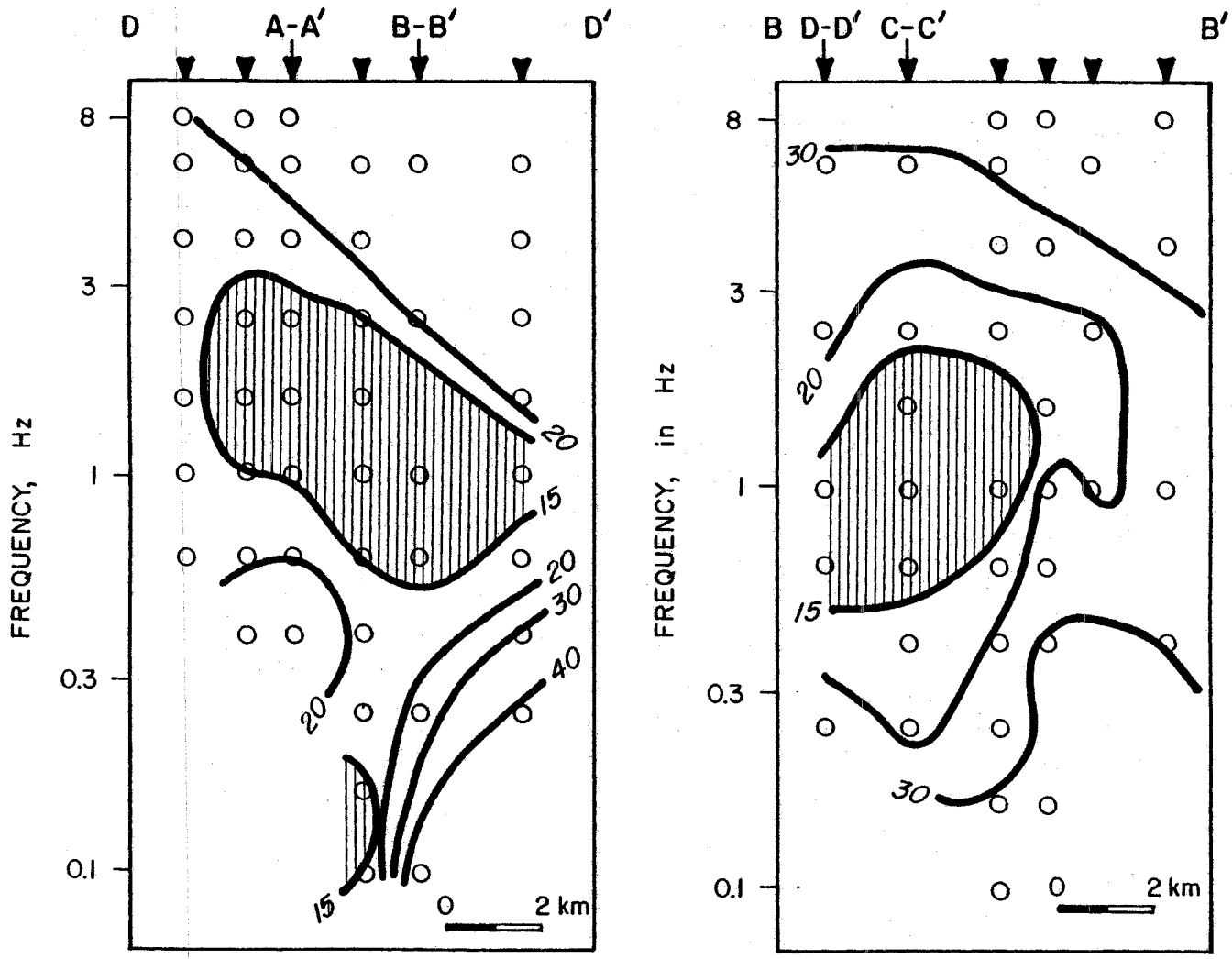
D
A-A′
B-B′
D′
B
D-D′
C-C′
B′
FREQUENCY, Hz
FREQUENCY, in Hz
8
3
1
0.3
0.1
15
20
30
40
0
2 km

Figure 39. Plot of apparent resistivity data (from vertical polarization ellipse data) versus frequency along profile C-C' in Figure 36. Contour values are in ohm-m; values less than 15 ohm-m have been shaded for emphasis. Open circles represent data points and solid, inverted triangles represent sounding locations.

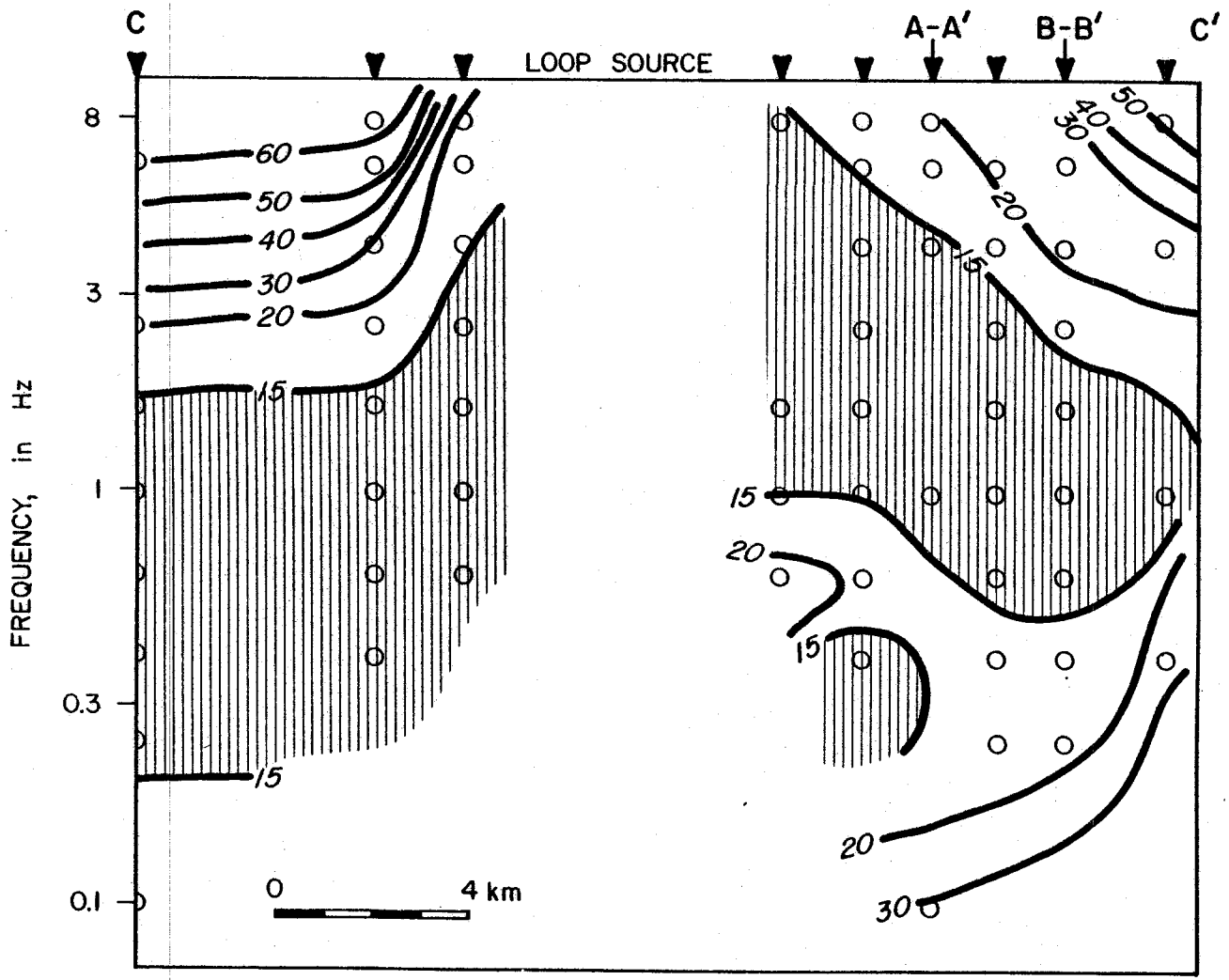
C
A-A′
B-B′
C′
LOOP SOURCE
FREQUENCY, in Hz
8
3
1
0.3
0.1
60
50
40
30
20
15
15
20
15
20
30
50
40
30
20
15
0
4 km

Figure 40. Plot of apparent resistivity data (from vertical polarization ellipse data) versus frequency along E-E' in Figure 36. Contour values are in ohm-m; values less than 15 ohm-m are shaded for emphasis. Open circles represent data points and solid, inverted triangles represent sounding locations.

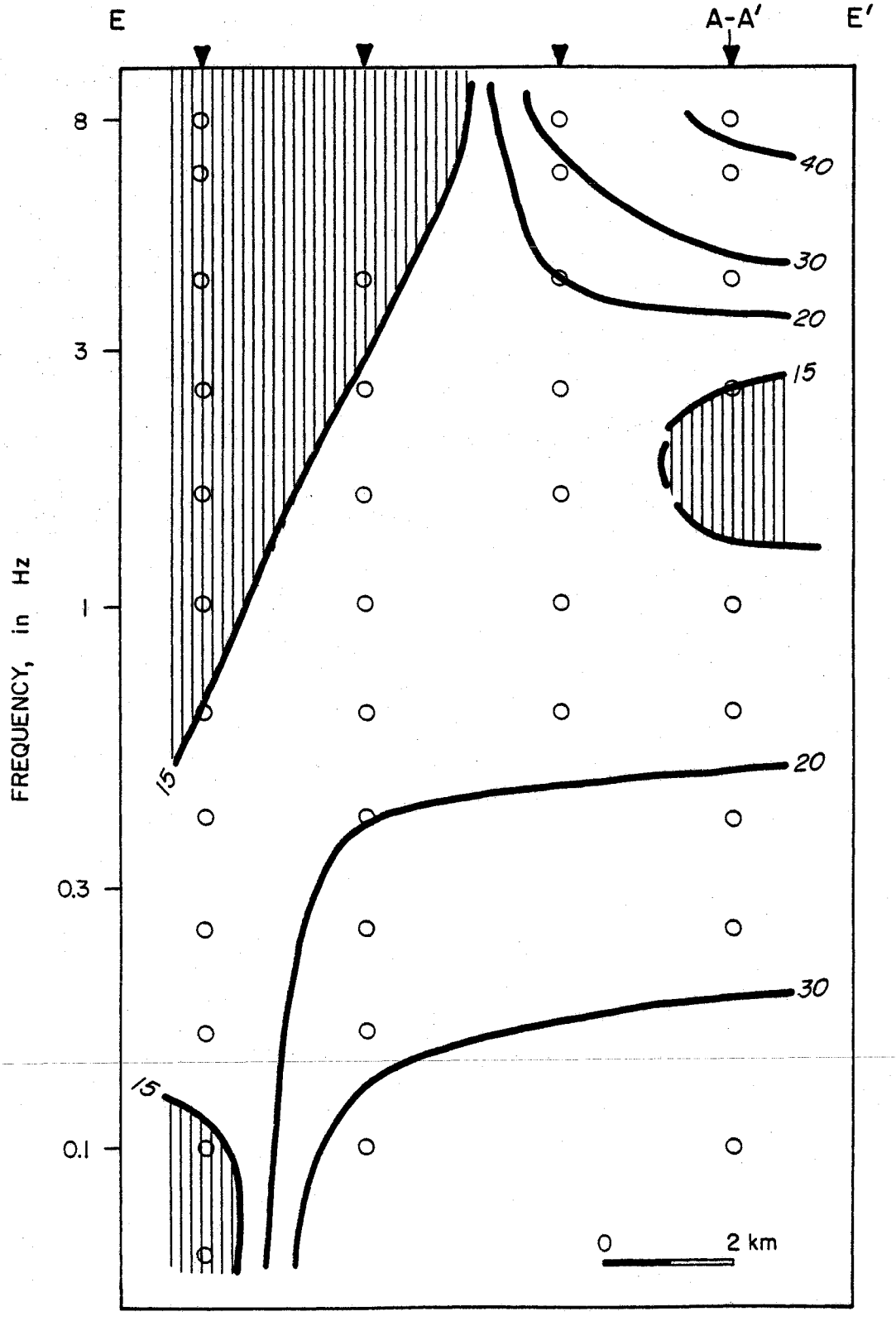
E
A-A'
E'
8
3
1
0.3
0.1
FREQUENCY, in Hz
40
30
20
15
15
20
30
15
0
2 km

northwest direction. From the results for line C-C', it is unclear what happens near Halema'uma'u and the source loop. Both lines C-C' and D-D' also suggest that the low resistivity area does not extend beyond the Koa'e fault system in the south (see Figs. 38 and 39). A similar area is mapped beneath the flank of Mauna Loa although at lower frequencies. Below 0.30 Hz, low apparent resistivites are also encountered as separate zones beneath Kilauea.

V. INTERPRETATION IN TERMS OF RESISTIVITY STRUCTURE

To determine the subsurface geologic structure, the CSEM data must first be analyzed to find the range of resistivity models which fit the data, and then the resistivity models can be translated into geologic structures. This is the inverse of the problem solved in Chapter II, the determination of the magnetic field induced by a horizontal loop source given a model geometry and resistivities. The inverse is to determine the earth resistivity structure given observations of the induced magnetic fields.

The relationship between the resistivity structure and the induced magnetic field is a non-linear one, as shown in Chapter II for models consisting of horizontal layers. Although general methods are available for determining the magnetic fields directly from the resistivity structure, no general methods are known for the inverse determination. At present, indirect, or trial and error, methods offer the only practical method for solving inverse problems of this sort. In fact, inverse problem solutions, or inversions, are really only practical for a few classes of structures. The most general of these classes is the one that was studied in Chapter II - horizontally layered halfspaces.

Because of these limitations, contemporary interpretations of CSEM data is based on compilations of several horizontally layered halfspace inversions[3]. The data set for one inversion consists of all data measured at several frequencies at one receiver location.

---

[3] for example, see Wilt and others (1980) and Kauahikaua (1981).

Each inversion is assumed to yield the average vertical resistivity sequence beneath a point somewhere between the source and receiver. The exact location of that point depends on the combination of source used and fields measured. For example, the inversion of vertical polarization ellipse data induced by a horizontal loop source would represent resistivities below the receiver location (see Appendix B).

After the vertical polarization ellipse data were inverted and compiled into a three-dimensional resistivity structure, the horizontal polarization ellipse data was qualitatively interpreted to see whether there is agreement in the two sets of data. This latter step relied heavily upon earlier theoretical modeling studies and the fields obtained by exciting a laboratory scale model of the structure with an appropriately scaled-down horizontal loop.

V.1 Interpretation of the Vertical Polarization Ellipse Data

V.1.1 Automatic Inversion of Sounding Data

The term "sounding" refers to the fact that we are interpreting data in terms of a horizontally layered halfspace model whose electrical resistivity varies only as a function of depth. Inversion of sounding data can be computerized as long as one has the three necessary ingredients: a routine which solves the forward problem for a layered halfspace, a meaningful criterion for testing the goodness-of-fit of the data to the forward problem solutions, and an efficient algorithm for modifying model parameter guesses so as to improve the fit as measured by the above criterion.

A computer program called MQLV_BIGLOOP (Kauahikaua, 1982a) was written for the interpretation of the Kilauea CSEM data. The equations for the one-dimensional forward solution were developed in Chapter II and both field components were found to require evaluation of a Hankel transform. Computation of the required equations was programmed using FORTRAN subroutine ZHANKS (Anderson, 1979a) for the Hankel transforms, and several auxiliary subprograms from Anderson (1979b). The final program differed from previous programs in that it allowed the use of either a VMD, horizontal circular loop, or horizontal polygonal loop source, and it produced output in the form of vertical and radial field components or polarization ellipse parameters.

The goodness-of-fit criterion and the guess-modification strategy were provided by subprogram ZXSSQ (IMSL, 1979) and the attendant interface routines published by Anderson (1979c). Goodness-of-fit is quantified as the sum of the squares of the residuals (difference between data and theoretical values) divided by the square of the data variance, and is known as the "weighted least-squares criterion"; a minimum of the criterion is sought for the best possible match. ZXSSQ seeks this minimum using the Levenburg-Marquardt method (Brown and Dennis, 1972). Aside from the data and various numerical parameters relevant only to subprogram ZXSSQ, the only input requirements were the starting model (in terms of layer conductivities and thicknesses), the lateral distance between source and receiver, and the difference in elevation between source and sounding location. An excellent discussion of the mathematics of inversion can be found in Inman (1975); a brief summary is included as Appendix C.

Besides the ability to computerize the process, automatic inversion offers another important advantage over manual interpretation methods. That advantage is the ability to obtain statistics on the inverse solution. Computations are available with which to determine how well the data are fit by the model response. This measure can be used to determine the minimum number of layers that the model must have in order to fit the data to within the accuracy of the original field measurements. More layers in the model will cause the inversion to fit the data too closely, thereby allowing the possibility of fitting data errors as well; too few layers in the model may result in the masking of important detail in the data. If the data cannot be fit closely enough by any number of layers, then the choice of a horizontally layered halfspace model is clearly not appropriate.

If the inverse solution has been found and the model appears appropriate, then estimates of the reliability of each of the parameters in that solution can also be calculated. The estimates are precise only for a linear problem, but because the CSEM problem is "quasi-linear" when the parameters are close to the solution (Glenn and Ward, 1976), the parameter estimates can be used qualitatively. In practice, the inversion statistics need to be interpreted just as if they were additional data. A brief summary of the statistical computations can also be found in Appendix C.

Interpretation of horizontal-loop CSEM sounding data by automatic inversion has been applied successfully in several studies since the initial test by Glenn and others (1973). Daniels and others (1976) interpreted a permafrost section on Alaska's north slope. Glenn and

Ward (1976) and Ward and others (1976) compared the resolution of several techniques, including CSEM with a VMD source, in a desert environment. The latter reference includes a good example of the interpretation of the inversion statistics along with the data. Smith and others (1977) interpreted EM soundings over Kilauea Iki lava lake in Hawai'i. Studies by Jain (1978) and Wilt and others (1980) apply CSEM sounding to Basin and Range structures. Wilt and others (1979) determined depths to potential geothermal targets at Mt. Hood, Oregon. Connerney and others (1980) interpreted deep crustal CSEM soundings in the eastern U.S.

Guides to inversion based on the results of these investigators can be summarized in four main points:

1. The polarization ellipse parameters offer slightly better resolution of layered earth parameters than the amplitudes or phases of the magnetic field components,
2. allowances should be made for data which do not asymptotically approach the estimated primary field values at low frequencies,
3. obtaining a geologically-reasonable inverse is aided considerably by having a good starting model, and
4. the best resolution is obtained by interpreting several nearby soundings together, so that the resulting models for neighboring locations are mutually consistent,

The first two points are mutually exclusive in that the polarization ellipse parameters do not require absolute amplitudes.

V.1.2 Application to the Kilauea CSEM Data

Thirty-five sets of sounding data were inverted using the computer program described previously. The ten data sets that were not inverted, were excluded either because they had too few data for a meaningful inversion (locations 47, 48, 49, 50), or because they were severely distorted at most frequencies (locations 1, 5, 31, 32, 36, 41). Following the recommendations in previous sections, the data were inverted in the form of polarization ellipse parameters.

The initial model parameters were chosen from the results of the earlier Kilauea surveys described in the Introduction. After a few successful runs, a standard initial model was adopted which seemed to be close enough to most inverse solutions so that no more than a few iterations were required for convergence. That model is listed in Table 1. Two resistivities, ρ_1 and ρ_4, were fixed because the inversion did not seem to be sensitive to these values and consistently made them so large that computer underflow or overflow errors halted the computer run. The insensitivity to the resistivity of resistive layers is characteristic of horizontal loop sounding (Frischknecht, 1967); however, the layer thickness can still be resolved, in most cases.

Most of the soundings were fit quite closely with a four-layer model similar to the one in Table 1. The actual values differed slightly at each location, but they all satisfied the inequality $\rho_1 > \rho_2 > \rho_3 < \rho_4$. Many of the inversion results also had similar parameter statistics.

Table 1

Standard Initial Model Parameters

Note: d is layer thickness

ρ_1 = 1000 ohm-m	d_1 = 500 m
ρ_2 = 30 ohm-m	d_2 = 1000 m
ρ_3 = 10 ohm-m	d_3 = 1500 m
ρ_4 = 1000 ohm-m	

For the locations south of Kilauea crater and as far east as the east rift trace, the third-layer resistivity was positively correlated with the third-layer thickness. The correlation coupled with large parameter error estimates for these two parameters, suggests that neither the resistivity nor the thickness can be uniquely resolved for layer three, but that only the ratio of thickness to resistivity (the layer conductance) can be resolved. Keller and Frischknecht (1966, p. 227) point out that the EM plane wave response to a conductive layer sandwiched between two more resistive layers is dependent only upon the intermediate layer's conductance. Because the z-dependence of the horizontal-loop CSEM forward problem is a solution to the same equation with the same boundary conditions as the EM plane wave problem (i.e., the diffusion equation), this behavior should be expected in CSEM sounding inversions as well. The high correlations and large parameter errors are a characteristic result of applying inversion to the estimation of two interdependent parameters.

A second, but less important, correlation occurs between the thickness of the first-layer (the resistive overburden) and the

resistivity of the second layer in the four-layer model. The large, negative correlation suggests that only the product of the two is being resolved; however, the parameter errors are generally very small (less than 10 percent of the parameter value) so that the interpreter may be confident in those parameters regardless of the correlation. An example of the inversion results for a sounding in this group is shown in Figure 41.

Some of the inversions, especially for the soundings immediately on the rift traces or on the flanks of Mauna Loa, obtained four-layer solutions with excessively large parameter errors and high parameter correlations. Another characteristic of these inversions was that the first-layer thickness in the solution was very small. The large errors and correlations suggest that the model has too many parameters; therefore, the logical alternative was to rerun the inversion with only three layers (removing the resistive overburden). This generally reduced the parameter errors and correlations while not significantly affecting the model fit. An example of the inversion results for a sounding in this group is shown in Figure 42.

Most of the soundings obtained off the edifice of Kilauea required even fewer parameters. In particular, soundings 23, 24, 41, and 45 required only two-layer models; that is, they did not require resistive basements. Including the fixed resistive basement in inversion characteristically resulted in an impossibly large depth to basement in the solution. The final inversion results for sounding 23 are shown in Figure 43.

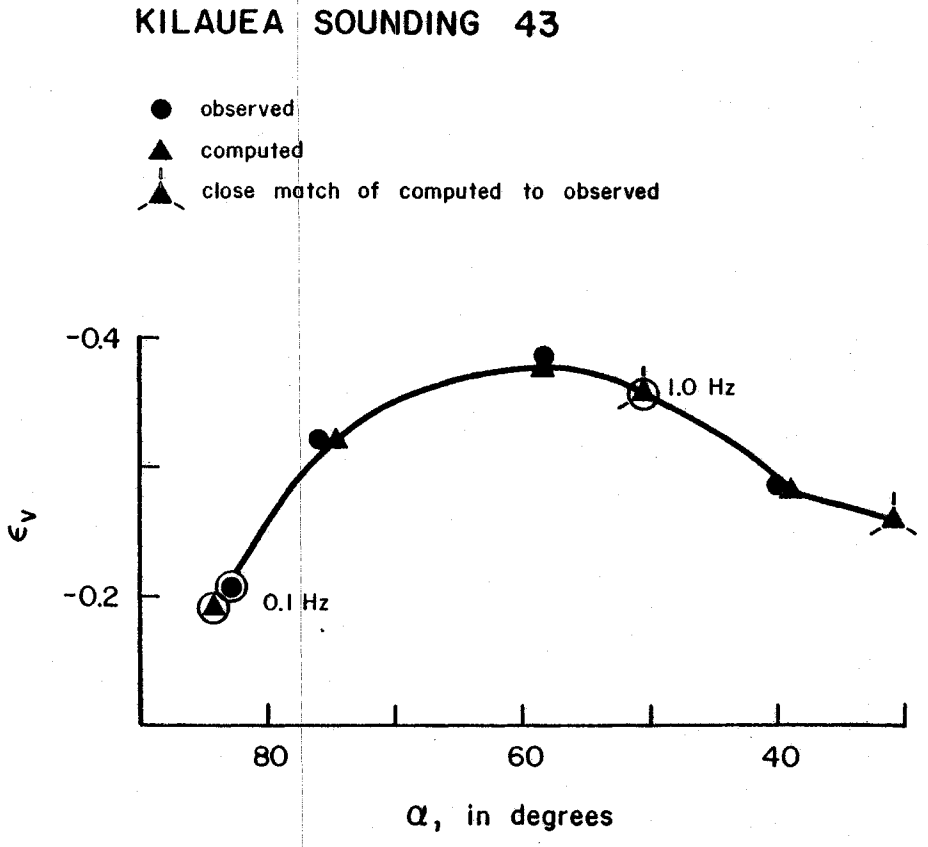

rms error = 1.1

$\rho_1 \equiv 1000\ \Omega m$

$\rho_2 = 24\ \Omega m \pm 31\%$

$\rho_3 = 3.8\ \Omega m \pm 218\%$

$\rho_4 \equiv 1000\ \Omega m$

$d_1 = 333\ m \pm 32\%$

$d_2 = 1136\ m \pm 36\%$

$d_3 = 466\ m \pm 255\%$

CORRELATION MATRIX

	ρ_2	ρ_3	d_1	d_2	d_3
ρ_2	1.0	0.77	-0.97	-0.80	0.78
ρ_3		1.0	-0.69	-0.99	1.0
d_1			1.0	0.71	-0.70
d_2				1.0	-0.99
d_3					1.0

Figure 41. Inversion results for sounding 43 showing the data and best-fit model in a pseudo-phasor plot and listing the parameter correlation matrix and the best-fit parameters and their errors. An equal sign with three bars signifies that the parameter has been fixed. Layer resistivities and thicknesses are represented by ρ and d, respectively.

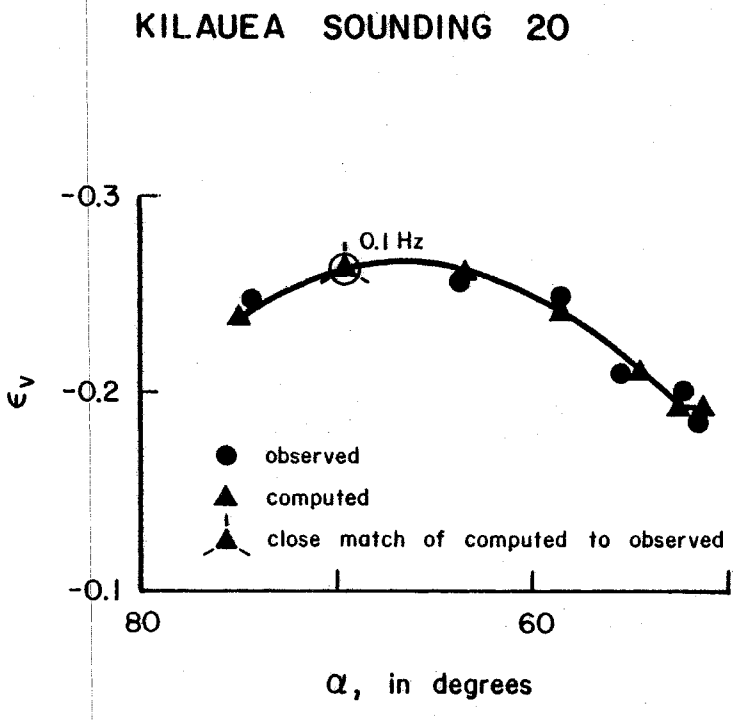

rms error = 0.62

ρ_1 = 230 Ωm ± 19%

ρ_2 = 8.5 Ωm ± 26%

ρ_3 ≡ 1000 Ωm ±

d_1 = 1160 m ± 8%

d_2 = 884 m ± 34%

CORRELATION MATRIX

	ρ_1	ρ_2	d_1	d_2
ρ_1	1.0	0.95	-0.96	0.93
ρ_2		1.0	-0.99	0.99
d_1			1.0	-0.98
d_2				1.0

Figure 42. Inversion results for sounding 20 showing the data and the best-fit model in a pseudo-phasor plot and listing the parameter correlation matrix and the best-fit parameters and their errors. An equal sign with three bars signifies that the parameter has been fixed. Layer resistivities and thicknesses are represented by ρ and d, respectively.

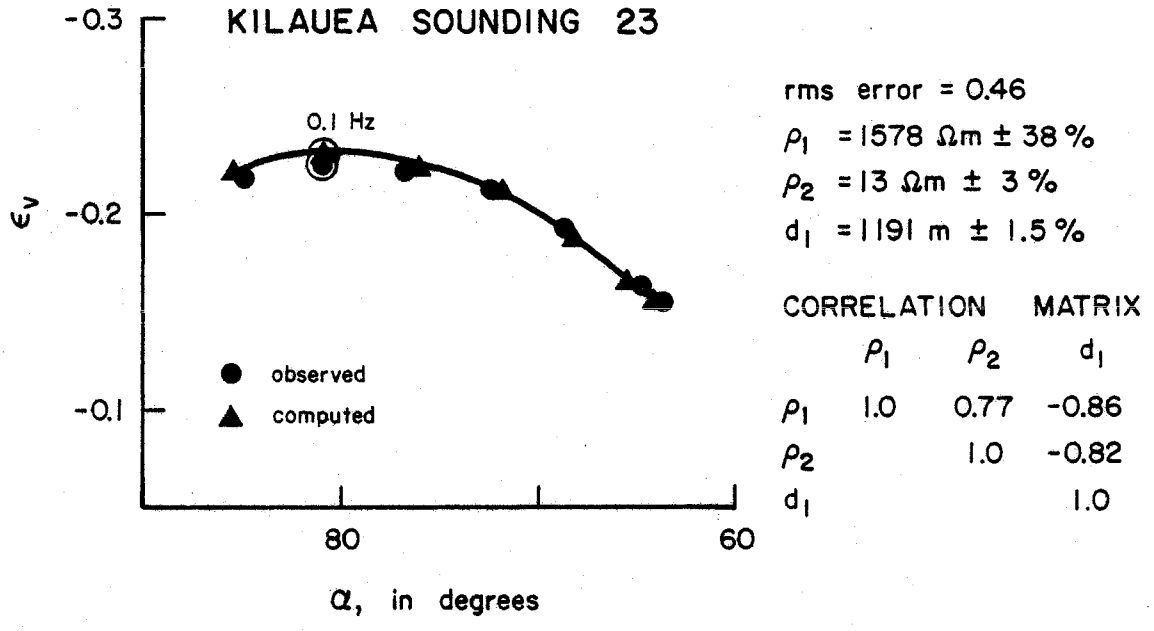

Figure 43. Inversion results for sounding 23 showing the data and the best-fit model in a pseudo-phasor plot and listing the parameter correlation matrix and the best-fit parameters and their errors. Layer resistivities and thicknesses are represented by ρ and d, respectively.

Of particular interest are the handful of sounding inversions which required a deep, conductive layer in the model in order to obtain an adequate fit to the data. The additional conductor is placed at a depth of greater than 4.5 km; its resistivity is generally not well resolved, except in sounding 46 where a value of 2 to 6 ohm-m was obtained. That the additional layer is required is clear from Figure 44 which shows the best-fitting four- and five-layer model responses compared to the data from sounding 44.

The various inversion results are compiled and plotted along four profile lines in Figures 45 through 48. Line locations are shown in Figure 36. Note that the cross sections derived from the inversion results are very similar to the corresponding pseudo cross sections of apparent resistivities shown previously in Figures 37 through 39.

V.1.3 Evaluation of the Kilauea Inversion Results

Judging by the rms errors associated with each of the sounding inversions, 1D models seem to be adequate descriptors of the data at most locations. The rms error relates the misfit between model response and data to the estimated data error and is defined as

$$\hat{\sigma} = \sqrt{\frac{\sum_{i=1}^{n} (r_i/s_i)^2}{n - k}}$$

where r_i = (data) - (model response) at the ith frequency,

s_i is the data error for the ith frequency,

n is the number of data values at that site, and

k is the number of model parameters. An rms error value near one

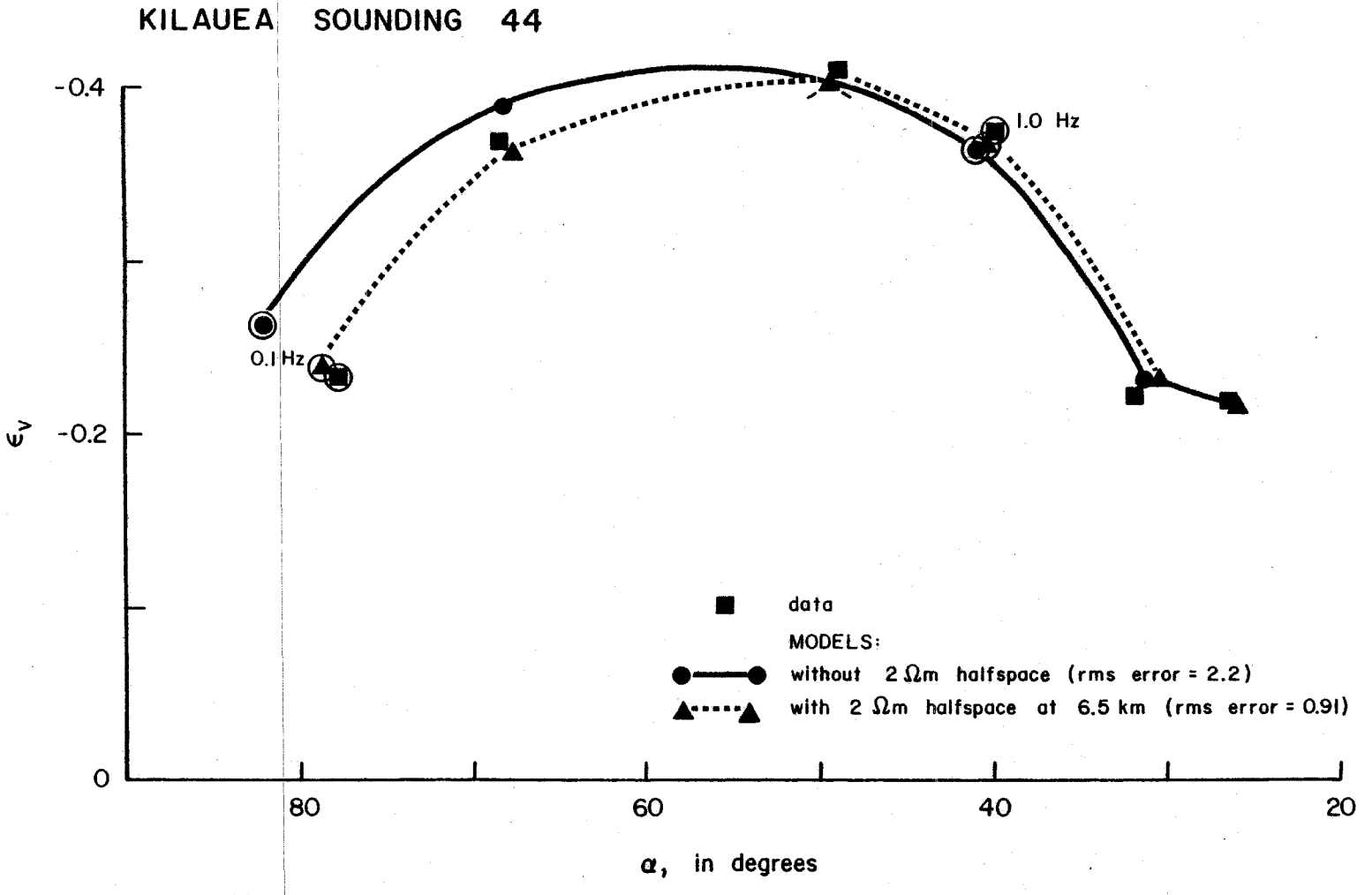

Figure 44. Pseudo-phasor plot of two models along with the data from sounding 44. The only significant difference between the two models is the presence of a 2 ohm-m halfspace at 6.5 km depth.

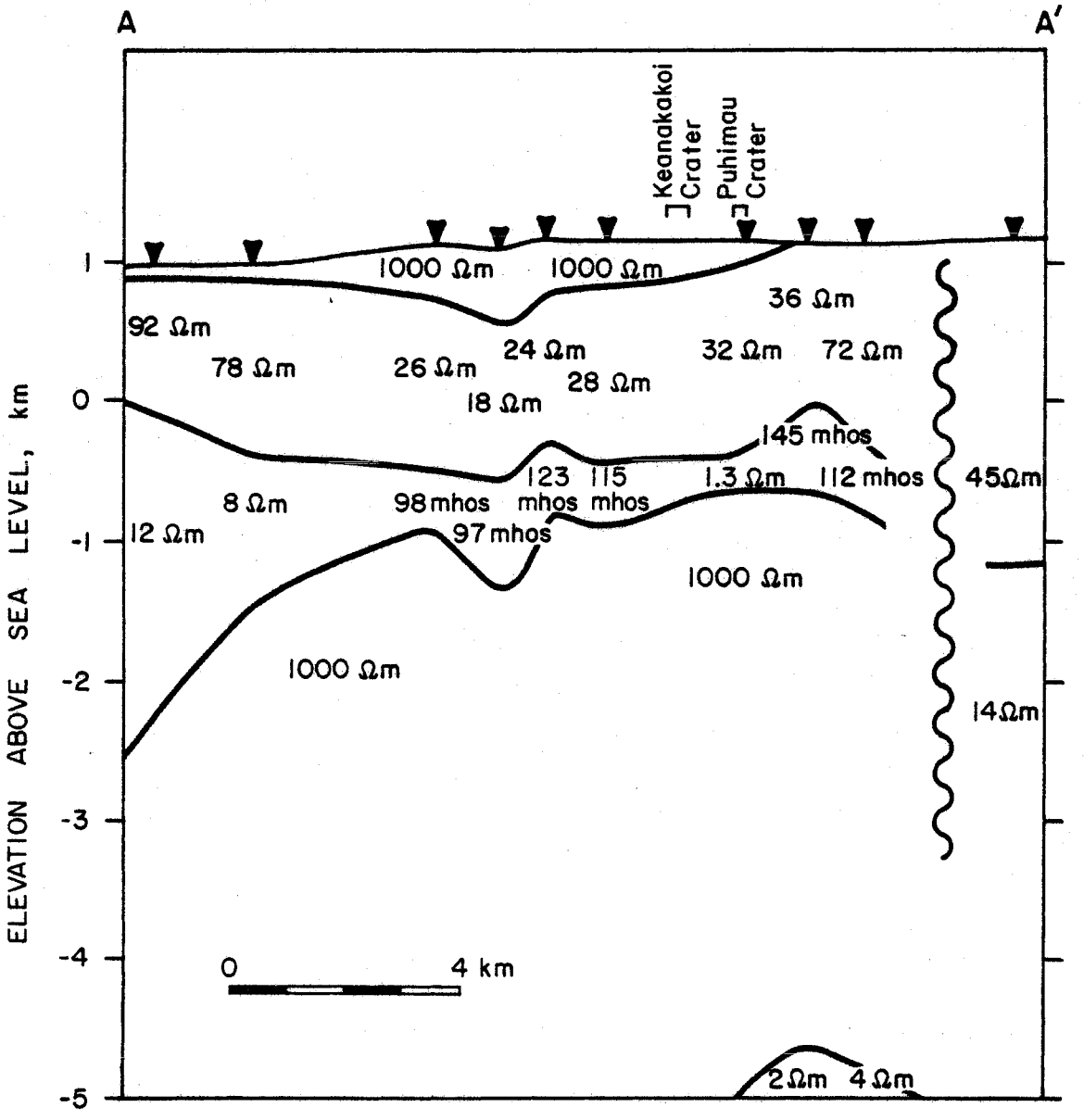

Figure 45. A compilation of inversion results along line A-A' in Figure 36. The vertical wavy line at right denotes an apparent lateral discontinuity.

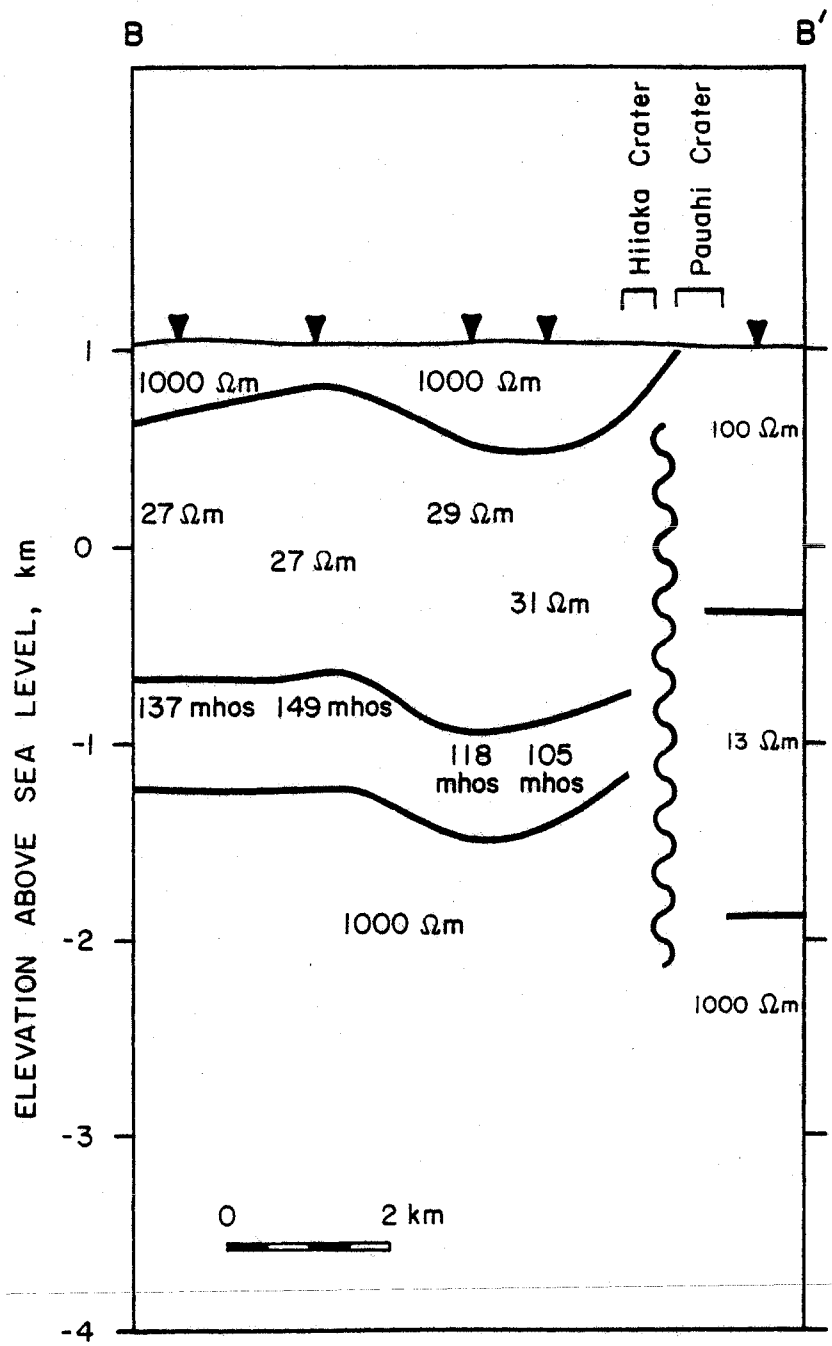

Figure 46. A compilation of inversion results along B-B' in Figure 36. The vertical, wavy line at right denotes an apparent lateral discontinuity.

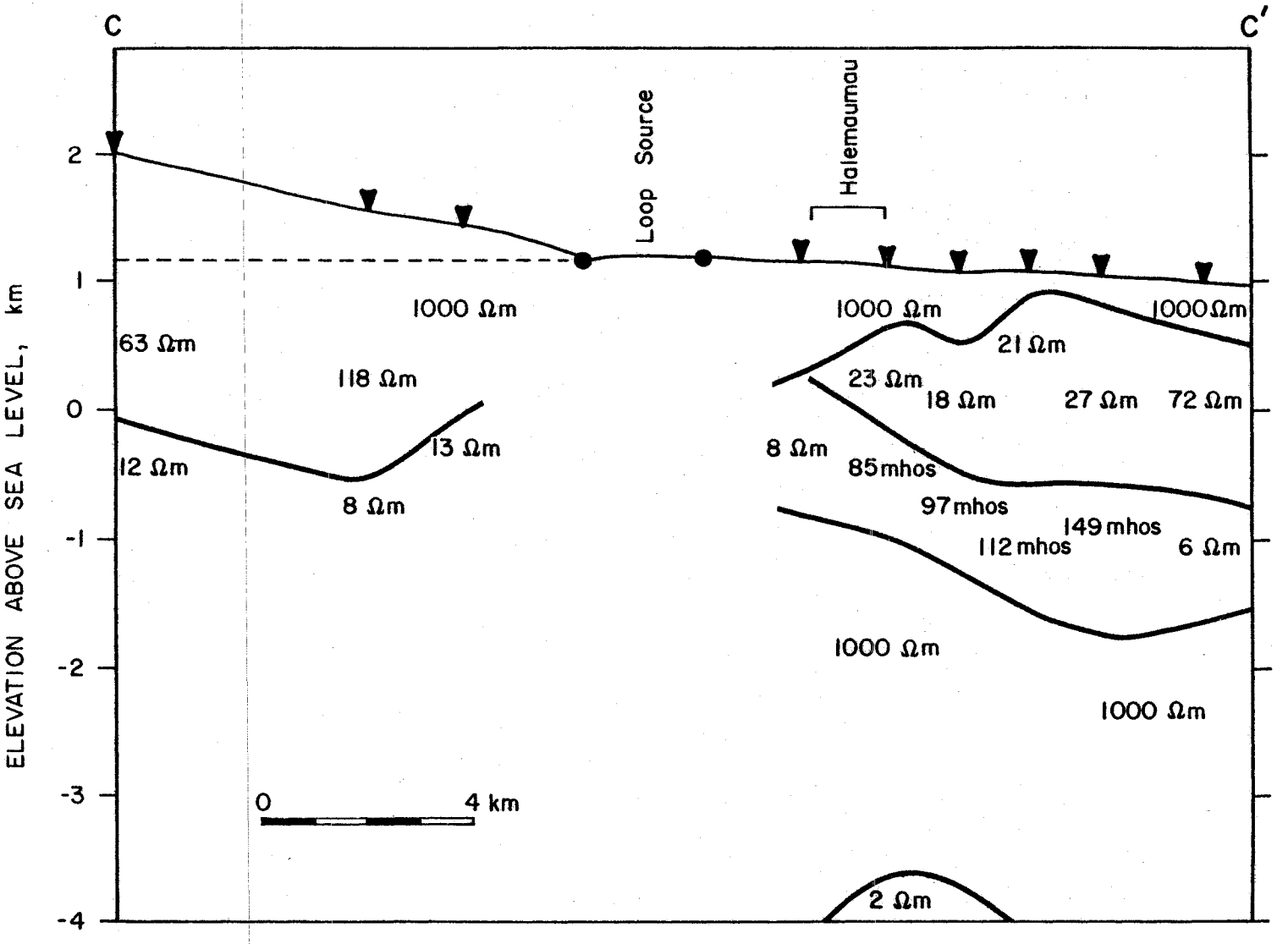

Figure 47. A compilation of inversion results along line C-C' in Figure 36.

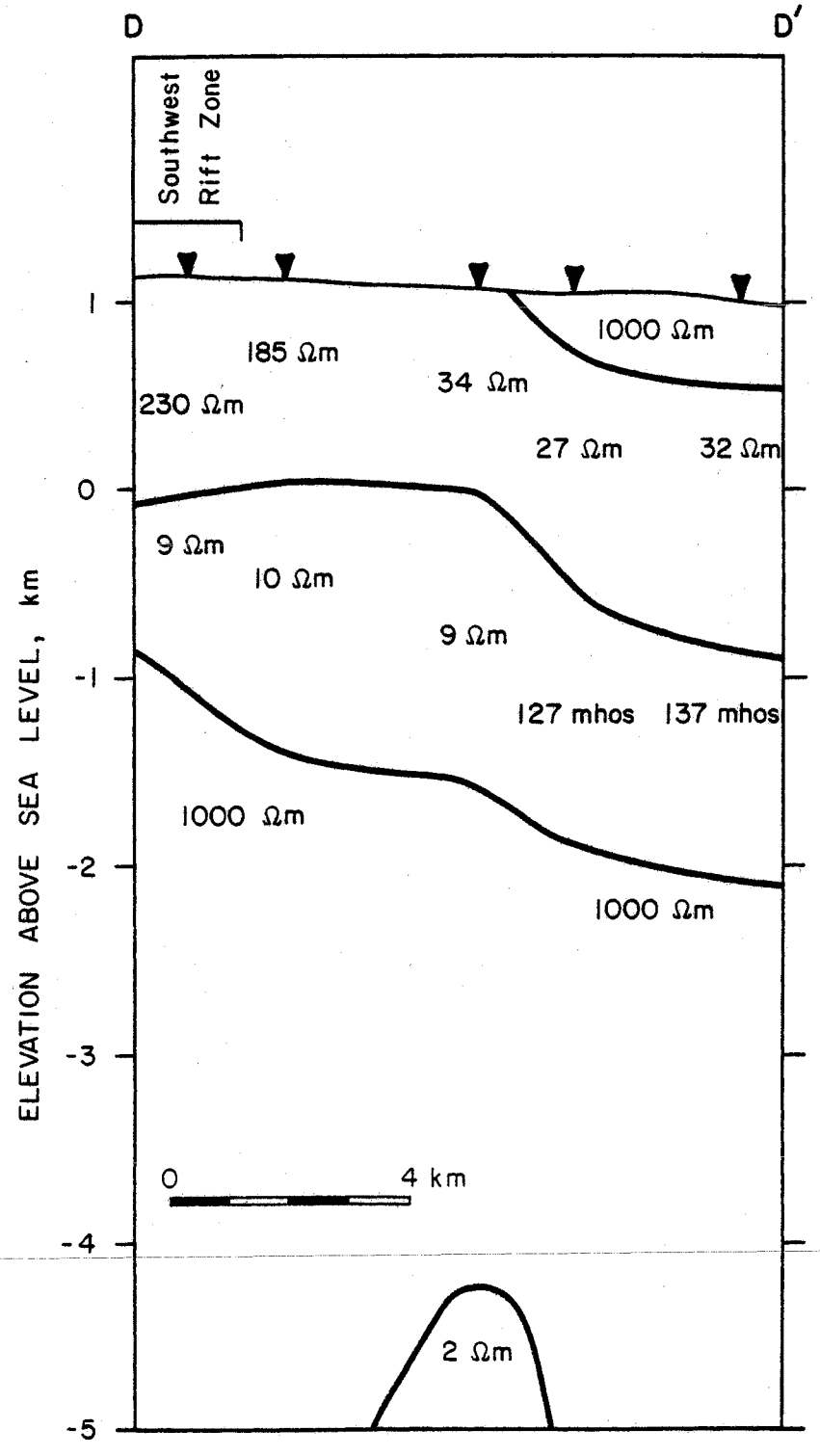

Figure 48. A compilation of inversion results along line D-D' in Figure 36.

signifies that the average misfit between model response and data is approximately equal to the average data error. Average errors for the Kilauea polarization ellipse parameter data were 1 percent in ellipticity and 1° in tilt angle based on observed errors of 2-3 percent in in-phase and out-of-phase measurements, and standard formulas for error propagation (Young, 1962). The distribution of rms errors for the Kilauea data is shown in histogram form in Figure 49. In general, the rms errors cluster between one-half and two. There are a few large values which come from soundings at the southern and western edge of the study area (locations 4, 30, 35, 37, 45). The disposition of each of the sounding data sets are summarized graphically in Figure 50.

The above analysis only shows that 1D models are adequate descriptors of the data within a triangular region bounded by the southwest rift zone, the east rift zone and the Koa'e fault zone. The east rift and, to a lesser extent, the southwest rift zone are also the locations of anomalous horizontal polarization ellipse parameters (see Figs. 27 to 32). From both lines of evidence, we may only conclude that the presented cross sections represent real structure within these boundaries. The 1D models outside this area are generally two-layer, resistor-over-conductor type models but they may be strongly influenced by the distant effect of induced currents with the summit block.

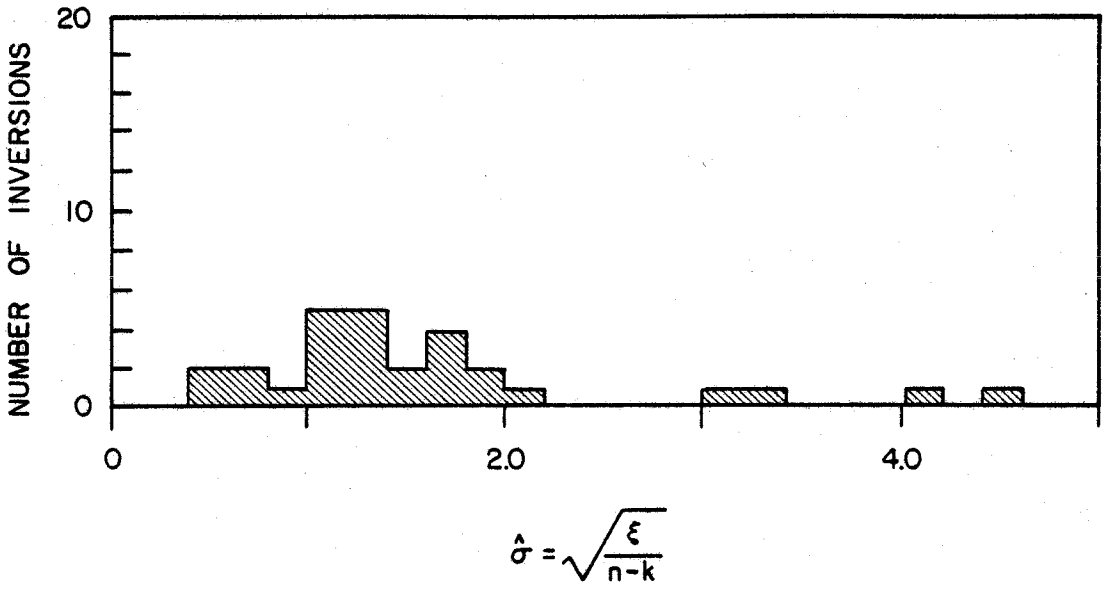

Figure 49. A histogram showing the distribution of rms errors obtained from the 35 sounding inversions. Most of the values are between 0.5 and 2.

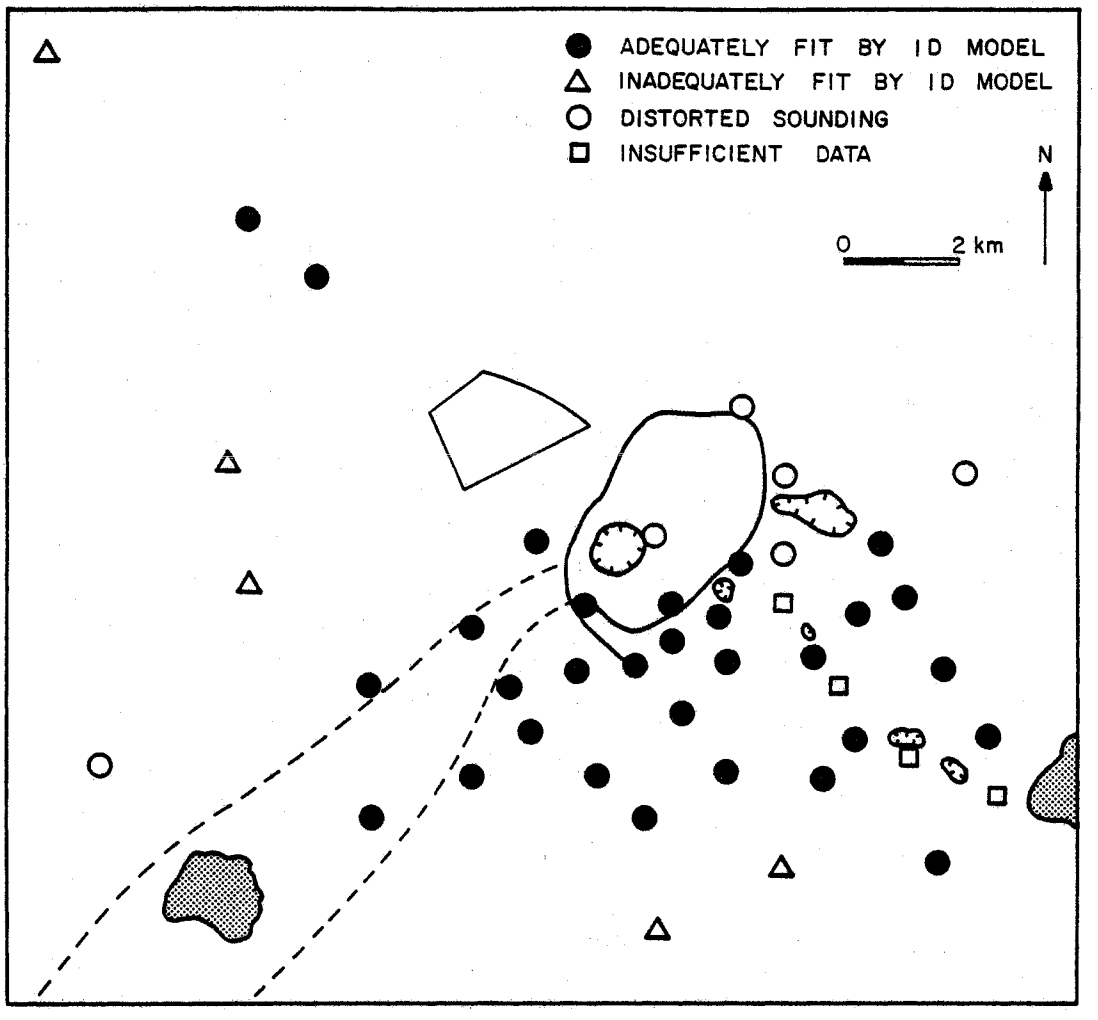

Figure 50. A map of the Kilauea summit area summarizing the disposition of the sounding inversions.

V.2 Interpretation of the Horizontal Polarization Ellipse Data

As stated previously, horizontal polarization ellipse parameters deviate from a strike angle of 90° and a horizontal ellipticity of zero only if the earth structure upon which the VMD source rests departs significantly from cylindrical symmetry. Any interpretation of this data would therefore require solutions to a more complex forward problem than does interpretation of vertical polarization ellipse data as soundings. To date, no universally applicable algorithms are available with which to solve two- and three-dimensional CSEM forward problems; therefore, automatic inversion computer programs cannot be written; however, interpretational guidelines may be compiled from a few recent studies of specialized modeling algorithms.

V.2.1 Guidelines from Numerical Modeling Studies

By approximating the EM equations as finite-difference equations, Stoyer (1976) and Stoyer and Wait (1976) computed the horizontal and vertical polarization ellipse parameters over a two-dimensional, conductive inhomogeneity for a buried VMD source. My examination of their model results suggests that the following generalizations can be made:

1. horizontal ellipticity peaks over a laterally-finite, conductive body,
2. for a laterally semi-infinite body, the horizontal ellipticity peak locations are variable depending on the source location and the location of the body edge, and

3. vertical ellipticity is anomalously low over shallow conductive bodies, but can be anomalously high over deep conductors.

Stoyer and Greenfield (1976) modeled only vertical polarization ellipse parameters along profiles over two-dimensional models (source-receiver distance fixed); anomalies over conductive inhomogeneities were characterized by a decrease in both tilt angle and vertical ellipticity. The peak anomaly was observed when the receiver passed over the inhomogeneity.

By using the finite-element method for solving the EM equations, Pridmore and others (1981) also computed vertical polarization ellipse parameters for a horizontal loop source near a conductive slab embedded in a less-conductive halfspace. This study differs from those by Stoyer in that the slab is three-dimensional and the source is fixed at the earth's surface. I summarize the characteristics of the finite-element models as follows:

1. along a line between source center and slab center, the anomaly peaks just beyond slab center from source,
2. anomaly characteristics are a decreased tilt angle and vertical ellipticity,
3. when the host resistivity is decreased, the vertical ellipticity anomaly due to the conductive slab is diminished, but the tilt angle anomaly is still significant.

These studies are far from complete in showing the relationships between polarization ellipse data and electrical resistivity structure

(different from a layered halfspace); however, they serve to affirm our expectations regarding data and isolated structural anomalies. First, anomalies generally peak near the center of the anomalous body, but can be offset slightly for the smaller bodies. Second, the sense of the anomaly (at least in the vertical polarization ellipse parameters) is in agreement with the contrast in resistivities of the anomalous body and its host, based on that parameter's behavior over layered-earth models. For example, a decreased tilt angle suggests a decreased resistivity over a 1D model and is also a characteristic of anomalies due to conductive bodies within a less-conductive host rock. Peaks in horizontal polarization ellipse parameters mark lateral changes in resistivity and may be used to locate either small anomalous bodies or the edges of very large ones.

Application of these generalizations to the Kilauea CSEM data proved to be surprisingly straightforward. Both horizontal ellipticity and strike angle showed a major anomaly over the east rift zone. The area north of the rift was characterized by anomalously high tilt angles and anomalously negative vertical ellipticities, both of which suggest more resistive rock in that area (see Figs. 21 through 26). This general structural discontinuity is certainly in accord with the one determined from a compilation of 1D models in Figure 50. The only discordant set of data is the vertical ellipticities at 0.25 Hz (Fig. 23) which show that ellipticities become more positive in the general area of the east rift. This trend may reflect the effects of the deep conductor detected in a few of the 1D inversions of data collected here, but over a broader area than originally suggested by

the inversion results. The reader may remember from Figure 44 that the effect of this deep conductor was more significant for vertical ellipticity than for the tilt angle data.

V.2.2 Results of a Scale Model Study

In order to confirm the correspondence between the observed polarization ellipse features and the above suggested model, CSEM measurements were made over a physical scale model designed for this study to be similar to the interpreted structure. Physically, the model consists of a horizontal slab of conductive graphite 2.5 cm thick, which is effectively infinite in lateral dimensions, and second graphite slab 1.25 cm thick which rests on top of the first and is shaped to represent the conductive region confined by two barriers at roughly right angles to one another. A horizontal loop source (radius = 1 cm) excites this model from a position 0.625 cm above and just off the upper slab (see Figure 63). The model results were not expected to match the data exactly, but rather to exhibit some of the same features. This would strengthen the above interpretation of the location and nature of lateral changes in resistivity structure beneath Kilauea. Further details of the scale model design and its results are discussed in Appendix D.

The scale model results (Figs. 64 to 87) do show strong anomalies in all polarization ellipse parameters over the east edge of the upper sheet, with markedly smaller anomalies over the western edge. A detailed summary of the scale model results follows:

1. strong anomaly over east edge of upper sheet, weaker anomaly over west edge; anomalies are of opposite sign,
2. magnitude of the anomalies increases with increasing frequency,
3. anomaly axis moves away from edge towards interior of upper sheet as frequency increases, and
4. at low frequencies, all parameters go asymptotically to the single slab model results (only the lower slab in the model).

Comparison of the model results and the Kilauea data show good agreement in the locations of the anomalies, but not in the signs of the anomalies. For example, the strike angle anomaly is positive over the east edge of the scale model and the east rift zone in the field data; however, the horizontal ellipticity anomaly is negative over the east edge of the scale model but it is positive over the east rift zone in the field data. The tilt angles are too high over the east rift zone of Kilauea and over the east edge of the model, but the vertical ellipticities are more negative in the data while more positive in the model at the same location, compared to the regional values.

The most probable reason for these discrepancies is that the ellipticities may be very sensitive to the actual resistivities in the structure. Ward and others (1974) show that the vertical ellipticity anomaly over a two-dimensional, conductive slab excited by an infinite line source can completely change sign simply by decreasing

the resistivity contrast between the slab and its host rock. In our case, since only the one scale model was run, the sensitivity of the anomalies to the model resistivities is not known. Therefore, the significance of the scale model results lies in the position of the produced anomalies and their agreement with the data anomaly positions. The discrepancy in the signs and magnitudes of the anomalies might have been reduced if the resistivity contrast in the scale model could have been adjusted more freely.

The scale model results do show that the addition of the second slab (atop the first) does not change the vertical polarization ellipse parameters observed west of the source over areas not covered by the second slab. Figures 88 to 92 compare the pseudo-phasor plots for the one- and two-slab models at several locations; the plots are nearly identical west of the source and off the second slab, but differ significantly elsewhere. The implication for the Kilauea data is that the simple layered structure interpreted for the flank areas is probably accurate.

V.3 Interpretation Summary

The three-dimensional structure derived from the previous compilation of 1D interpretations appears to be an accurate descriptor of the vertical and horizontal polarization ellipse data, with some reservations. The gross features of this structure are depicted in Figure 51. The most prominent aspect is the shaded region in which the resistivity structure is one of subhorizontal layers, with a resistive basement. This region is bounded on the east by the east

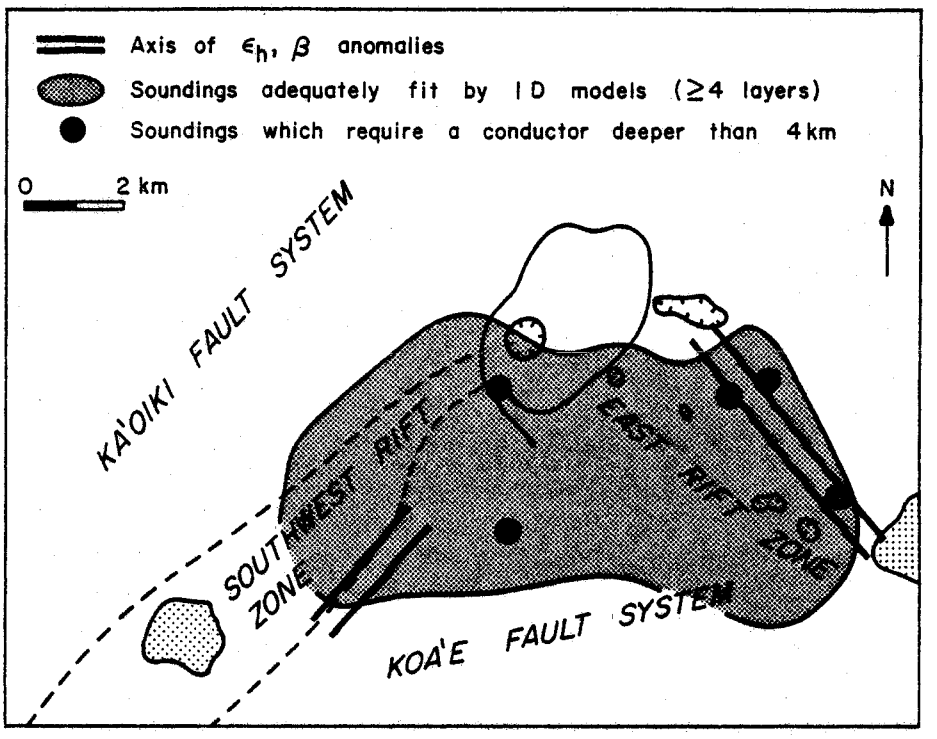

Figure 51. A map of the Kilauea summit area showing the region (shaded) in which the resistivity structure consists of at least four, subhorizontal layers. Superimposed on this shaded area are five soundings which detected a deep conductor in addition to these four layers. Soundings to the northwest show a much simpler, two-layer structure.

rift zone, on the west by the southwest rift zone, and possibly on the south by the Koa'e fault system. Superimposed on this region are the five locations where soundings require another conductor more than 4.5 km below the surface.

The resistivity structure outside this area appears to be much simpler. The data are adequately described by a two-layer model, the first layer resisitivity being greater than 40 ohm-m over an approximately 10 ohm-m basement. The interface between the two layers is below sea level, but at no otherwise consistent depth. The two types of models are summarized in Table 2.

Table 2

Summary of Resistivity Models from CSEM Sounding
(Depth ranges shown in Figs. 45-48)

	Kilauea Summit	Flanks
layer 1	>500 ohm-m	45-118 ohm-m
layer 2	18-230 ohm-m	8-14 ohm-m
layer 3	1-12 ohm-m	
layer 4	>100 ohm-m	
layer 5	2-4 ohm-m	

VI. KILAUEA'S VOLCANIC STRUCTURE

The final task is to translate the resistivity structure deduced in the previous sections into more meaningful geologic terms. To do this, we must first review the factors which are known to control the resistivity of earth materials, and then examine, in detail, how those factors affect material resistivities for the range of values expected beneath Kilauea and Mauna Loa. The values of these factors can then be interpreted from the resistivity information.

The most important factors controlling resistivity are rock type, degree of fluid saturation, porosity, temperature, and salinity of the saturating fluid. The predominant rock type in Kilauea is tholeiitic basalt occurring as thin, subhorizontal lava flows and is not expected to vary significantly over the entire study area. Both Kilauea and Mauna Loa consist of a great number of these flows laid one upon another from the seafloor to the present volcanic surface. The occasional layers of volcanic ash, cinder, or soil are insignificant in total volume relative to basalt and in terms of the rather large probing wavelengths used in this study. The factors that affect basalt resistivities are, to a good approximation, the only ones that affect Kilauea and Mauna Loa resistivities.

Degree of saturation can also be neglected once we recognize that, because of their relatively large permeabilities, basalts are either completely saturated with water (rocks below the water table) or they are only slightly wetted (rocks above the water table). The transition is abrupt and is marked by an abrupt decrease in resistivity.

Slightly saturated basalts can have resistivities in excess of 2000 ohm-m (Kauahikaua and Klein, 1977), whereas completely saturated basalts usually have resistivities less than a few hundred ohm-m. A 1260 m research drill hole located about 1 km southeast of Halema'uma'u (see Fig. 1) has shown that the water table is only 488 m deep beneath this area of the volcano (Zablocki and others, 1974); the interface is responsible for a drop in resistivity by a factor of almost 10 in the well logs, the resistivity decrease observed in the CSEM interpretations (layer 1 to layer 2), and in several VES soundings in the same area (D.B. Jackson, 1980, oral communication). Below this depth, the rocks are completely saturated. Porosity, temperature, and saturant salinity are considered in the next section.

VI.1 The Resistivity of Water-Saturated Basalts

The remaining three factors - porosity, temperature and fluid salinity, can vary considerably beneath Hawai'i volcanoes. Vesicular porosity values of 35 percent down to less than 1 percent have been reported for basalt flow samples. Expected temperatures range from ambient air temperature, 20°C, to above the melting temperature of basalt, 1100°C. Finally, salinity values reported from Hawai'i water wells range from less than 0.035 ppt (parts per thousand) to 35 ppt, the value for seawater.

The porosity-resistivity relationship commonly used in resistivity studies of porous rocks where fracture porosity is not dominant is an empirical formula known as Archie's law (Keller and Frischknecht, 1966),

$$\frac{\rho b}{\rho w} = a\,\Phi^{-m}$$

where ρb is the resistivity of the saturated basalt, ρw is the resistivity of the saturating fluid, Φ is the porosity fraction, and a and m are constants. Several sets of values for the constants have been determined for Hawaiian basalts and are summarized in Table 3. At first glance, the differences in the determined coefficients seems so large that it would render Archie's law unusable; however, with the exception of two sets of the constants, each version of Archie's law is no more than a factor of two different from any other version for porosities between 4 and 30 percent (see Fig. 52). Obviously, Archie's law can only be used as a guide for determining a range of possible values for the ratio ρb/ρw, known as the formation factor.

It is clear from Table 3 that there is another parameter involved in determining formation factor besides porosity; Rai and Manghnani (1981) show that it is salinity of the saturant fluid. They determined

Table 3

Archie's Law Constants for Hawaiian Basalts

a	m	Salinity of Saturant (ppt)	Reference
18.	1.05	15.	Keller, 1974
3.5	1.8	not reported	Keller and others, 1977
8.5	0.9	not reported	Keller and others, 1979
2.64	0.95	.071	Rai and Manghnani, 1981
7.13	1.44	8.9	
8.20	1.46	17.7	
5.28	1.65	34.8	

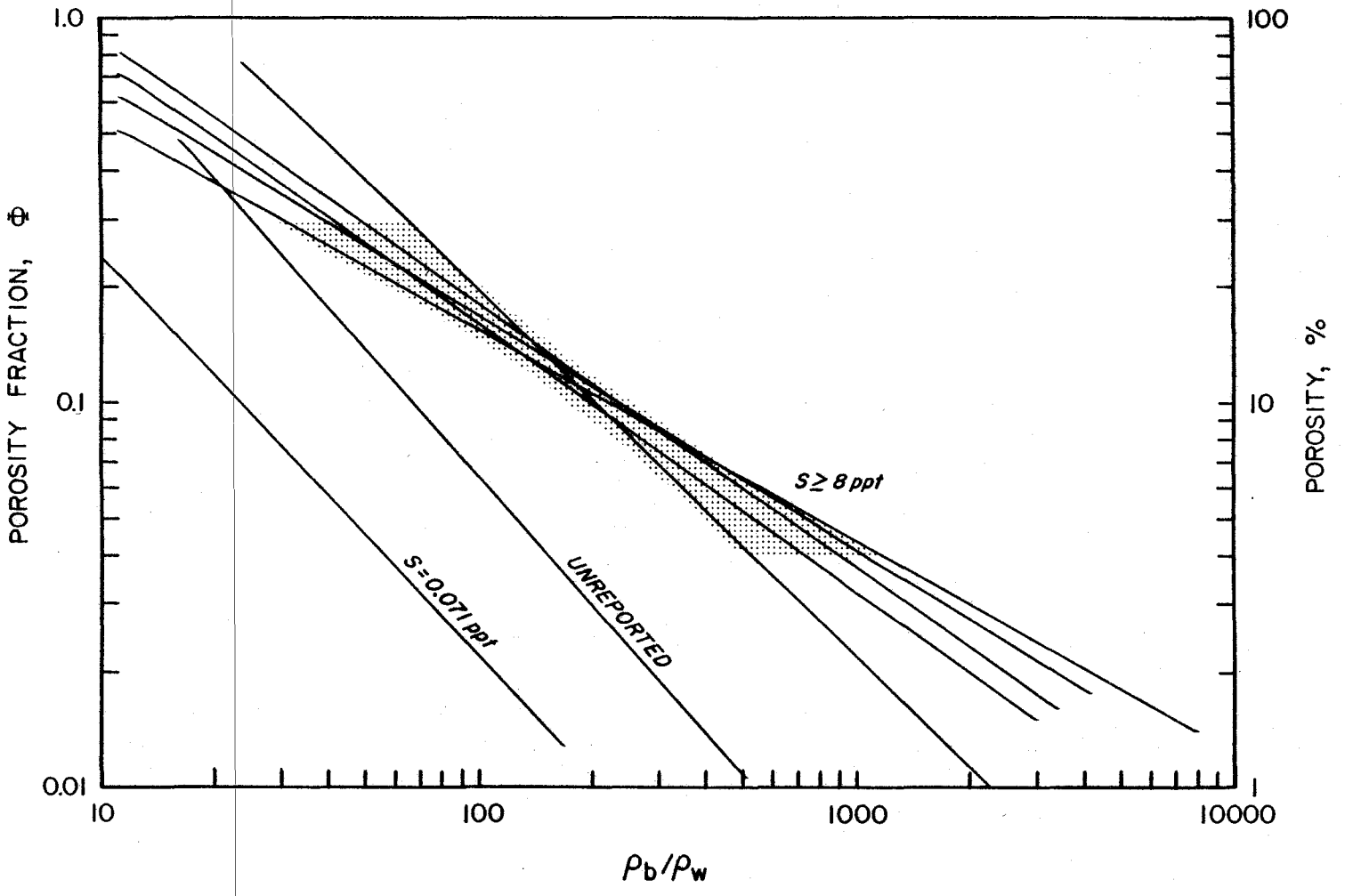

Figure 52. A log-log plot illustrating different versions of Archie's law corresponding to the constants listed in Table 3. The values listed alongside some of the lines are the salinity values of the saturants employed. The shading shows the area in which most of the sets of constants agree most closely.

constants separately for four different fluid salinities. The three sets for fluid salinities greater than 8 ppt were nearly equivalent, but the set for very low salinity fluids was radically different, yielding values of formation factor that were up to 10 times lower than with higher salinity fluids. This can be shown more clearly with a plot of formation factor divided by the value for seawater saturation versus salinity of saturant fluid. Figure 53 shows plots for samples with several different porosities. Note that the values depart from unity for salinities less than about 15 ppt and that the degree of departure is greater for the rock samples with smaller porosities.

To further complicate matters, recent studies by Olhoeft (1977) and Ucock and others (1980a) show that formation factor can also vary with temperature. The ratio is constant for temperatures below 80°C, but it can decrease by as much as 16 percent at higher temperatures. The ratio stabilizes again at temperatures above 175°C.

The reason for this complicated behavior is that rocks can conduct electric current along two different paths. The main path is electrolytic conduction through the pore fluid and is completely controlled by the resistivity of that fluid (Archie's law). The second path is conduction along the surface of the pores due to the "build-up of electrically-attracted ions at the solid-liquid interface" (Rai and Manghnani, 1981). Surface conduction is insignificant when the pore fluid has a very low resistivity (high salinity), but becomes increasingly more important as the fluid resistivity increases (salinity decreases). Similarly, surface condition becomes more important as temperatures are increased. Electrolytic conduction

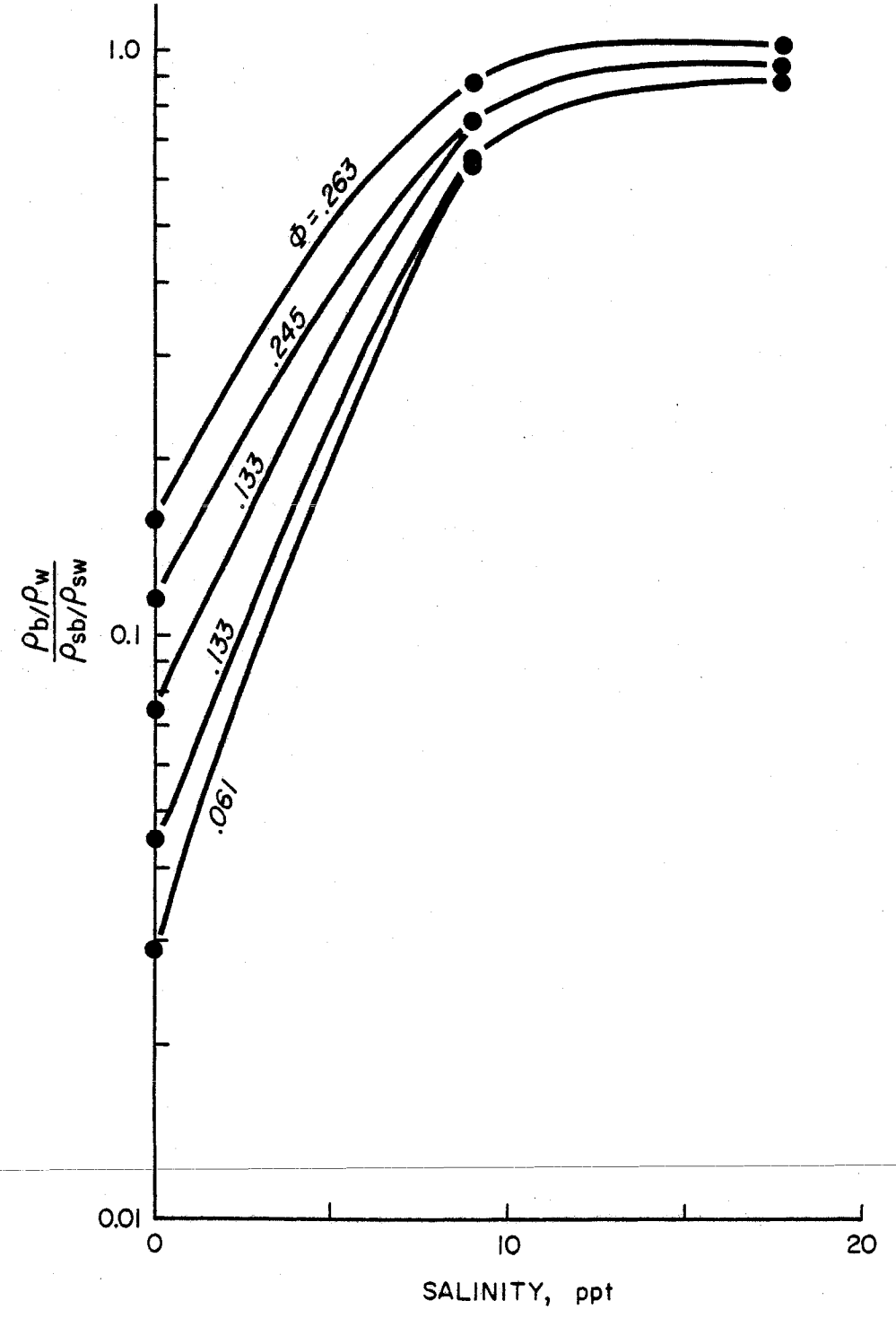

Figure 53. Corrections to the formation factor due to variations in saturant salinity are shown for several porosity fractions. These data are from Rai and Manghnani (1981) and they show the effect of pore-wall conduction at low salinities.

is dominant for temperatures less than 80°C and saturant salinities greater than 8 ppt; therefore, Archie's law can be used for determining the fluid resistivity if the saturated basalt resistivity is known, but it will require correction for the effects of surface conduction for temperatures or saturant salinities outside this range.

The remaining uncertainty is the manner in which salinity and temperature variations affect water resistivities. Using the values in Slichter and Telkes (1942) for water resistivities at 20°C and fitting them to a power-type equation, the relation between water resistivity and salinity is

$$\rho w = 5.532\ S^{-0.925}$$

where S is salinity in ppt. This formula may differ from those used by other authors, but it has proved sufficient for this study.

The water resistivity-temperature relationship is far more complicated. Quist and Marshall (1968) and Ucock and others (1980b) show that, as temperatures increase, a fluid resistivity will initially decrease, but will taper off and remain fairly constant between 175° and 325°C, the critical temperature of water. At higher temperatures where water has turned to vapor, resistivity increases dramatically (Quist and Marshall, 1968).

To the water resistivity-temperature relationship, the rock resistivity-temperature relationship must be appended. Rai and Manghnani (1977) demonstrate that Hawaiian basalts decrease in resistivity exponentially with increasing temperature. The resistivity they measured represents electronic conduction through the rock matrix

because all the samples were dried. Above temperatures of about 600°C, the basalt matrix conducts electric current better than does the pore "fluid", and the basalt resistivity again begins to decrease as temperature increases, reaching a value of about 2 ohm-m at melting temperature. The rather complicated resistivity variations of a basalt saturated with seawater and heated from 20° to 1400° are summarized in Figure 54.

The interdependence between the effects of porosity, temperature, and saturant salinity on rock resistivities makes it difficult to determine the value of each if only the rock resistivity is known; however, if one or two of them can be constrained by the results of other research, then the remaining factors may be more accurately deduced. The most direct source of information on the subsurface of Kilauea is the core and log studies from the 1260 m research drill hole southeast of Halema'uma'u. There is enough data on the 500 to 1260 m section of this hole to illustrate the relationships in this section by trying to reconstruct the resistivity log from the porosity and temperature logs and salinity measurements on the well waters. This exercise will then form a base for extrapolating these properties to greater depths knowing only the resistivity structure and a little about porosities at large depths from geological and geophysical studies.

The downhole fluids appear to be brackish. A salinity of about 3 ppt was measured by McMurtry and others (1977) from samples collected at the surface of the water table and 30 m below it. Keller (1974) reports that analyses of pore-waters extracted directly from the wall

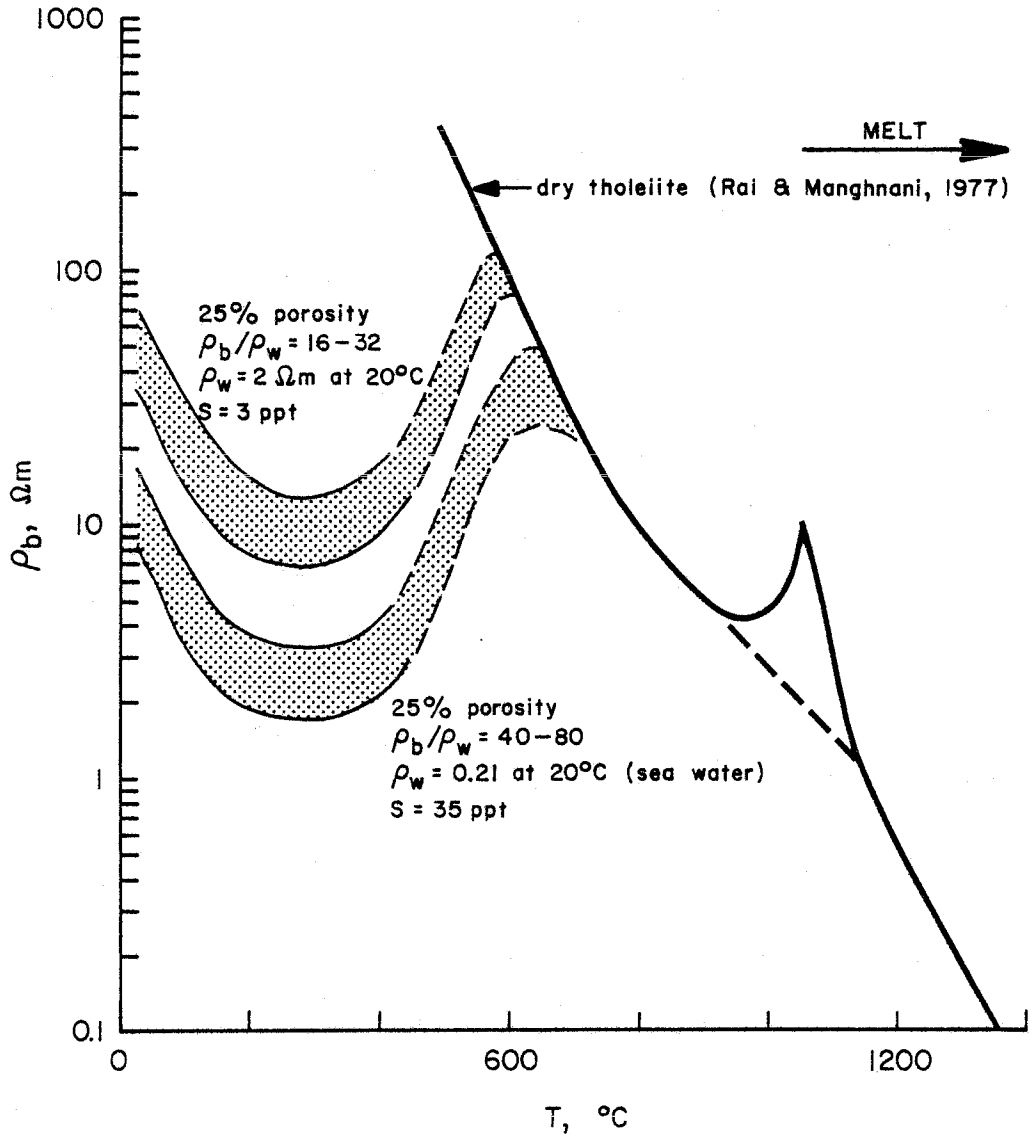

Figure 54. Expected variations in basalt resistivity are shown for temperatures from 20° to 1400°C. The solid line shows the resistivity expected for completely dry rock; the two shaded areas show ranges of resistivities for typical basalts saturated with two different salinity fluids. The cusp in the curve for dry tholeiite is probably an effect of the speed of experimental heating and cooling (Rai and Manghnani, 1977) and is not significant for field survey interpretation.

of the borehole were "deficient in chloride" with respect to seawater, but did not publish the analyses. Keller and others (1979) show, from analysis of the well logs, that the pore fluids are several times more resistive than seawater and are therefore brackish. The resistivities that they derive for the pore fluids are compatible with a saturant salinity of about 4.5 ppt.

Knowing the approximate fluid salinity, the expected basalt resistivities can be computed using the following steps.

1. determine the porosity from neutron porosity logs,
2. get range of formation factors for that porosity from Figure 52,
3. determine correction for salinity from Figure 53 and multiply by formation factor,
4. determine ρw for appropriate salinity and temperature and multiply by salinity-corrected formation factor.

The smoothed porosity and temperature logs in Keller (1974) were used with an assumed saturant salinity of 3 ppt; the expected basalt resistivities are compared to the smoothed resistivity log in Figure 55.

The two plots compare very well, although there is a tendency for the expected resistivities to be less than the logged resistivities between 500 and 730 m. The discrepancy may be due either to salinity variation in the well fluids or an improper salinity correction to the formation factor[4]. Nevertheless, the logged resistivities are described very well as a whole by resistivities derived from porosity,

[4] those used here are the values measured on a single set of samples by Rai and Manghnani (1981); I use them here only as guidelines in the absence of a more definitive study.

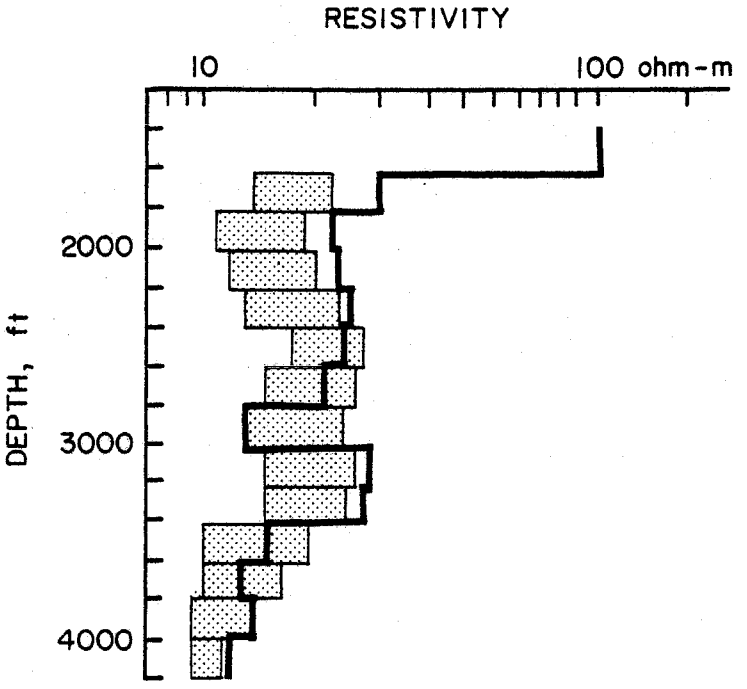

Figure 55. The solid line is the smoothed resistivity log from the summit research drill hole (see Fig, 1 for location). The shaded boxes are the range of resistivities predicted from the porosity and temperature logs assuming complete saturation with a fluid having a salinity of 3 ppt.

temperature, and saturant salinity measurements and the relationships discussed above.

VI.2 Porosity, Temperature, and Saturant Salinity Beneath Kilauea

The resistivities that are expected in CSEM interpretations may be different from those logged in a drill hole because the two types of measurements have different sampling volumes. Logging tools generally respond to the rocks within a meter or two of the tool. On the other hand, a CSEM sounding averages rock properties over distances of several hundred meters vertically and laterally because of the large probing wavelengths used.

The much larger sampling volume also means that the CSEM interpretations lack the detail available in logs. For example, CSEM interpretations are fairly insensitive to porosity variations because any significant small-scale variations are averaged out. Porosity values on this scale can better be obtained from gravity and P-wave seismic velocity investigations. Island-wide gravity variations suggest that the basalts above sea level have an average bulk porosity of 23 percent (Strange and others, 1965). Huber and Adams (1971) estimate a porosity of 27 percent from density logs in a well 32 km southwest of Kilauea's summit. Both density and P-wave velocity appear to increase with depths (Strange and others, 1965; Zucca and Hill, 1980) attaining values that are compatible with a bulk porosity of around 10 percent at the base of the volcanic pile[5]. The general decrease in porosity with depth is also observable in the vesicular porosities of core

[5] the relations in Manghnani and Woollard (1968) were used to estimate the deep porosity from density and P-wave velocity.

samples from a 2 km deep well on Kilauea (Johnson, 1980) and submarine dredge samples (Moore, 1965). The decrease is not uniform with depth, but appears to be complete about 2 km below sea level.

The decrease from a porosity of about 25 percent at the surface to 10 percent at a depth of 2 km or more might be expected to drastically change the expected resistivities; however, if the saturant salinities are low then the rock resistivities won't change significantly. The average formation factor at 25 percent is about 55, and at 10 percent it is 210. Assuming a saturant salinity of 3 ppt again, the corrected formation factor becomes 18 at 25 percent and 21 at 10 percent; the difference is insignificant. If the salinity at depth is greater than 10 ppt, the salinity correction becomes insignificant and the resulting formation factors can be considerably different for the two porosities.

A saturant salinity of 3 ppt has already been established for the 500 to 1260 m portion of the summit research hole. To test whether this might be a reasonable saturant salinity for the entire volcano, Figure 54 also shows the variations expected in a basalt resistivity for temperatures between 20° and 1400°C, assuming a constant saturant salinity of 3 ppt and a porosity of 25 percent (the decrease to 10 percent has already been shown to have virtually no effect for low saturant salinities). The values range from 30 to 70 ohm-m at 20°C to 7 to 13 ohm-m at about 300°C. Above 300°C, the resistivities increase to around 100 ohm-m at about 600°C. At this temperature, the saturated-rock curve meets the dry rock curve and resistivities again decrease with increasing temperature.

The range of resistivities provided by this constant salinity model, along with the resistivity sequence as temperature increases, closely parallels the resistivity models interpreted from the CSEM data (summarized in Table 2). Resistivities in the CSEM models decrease steadily in the first three layers, but increase in the fourth; the occasional fifth layer is due to another decrease in resistivity. A total temperature variation from 20° at the surface to 1100-1200°C within the fifth layer can account for the sequence of layers in that five-layer model.

These various factors are modeled in miniature in Kilauea Iki lava lake, a feature caused by the filling of an ancient pit crater with molten lava in 1959. Resistivity studies coupled with extensive drilling have recorded the progressive cooling of the magma lens within an already-chilled crust. The gross resistivity structure of the cooling "lake" has several features in common with the general Kilauea summit resistivity models; in Kilauea Iki, there are five layers which alternate between being very resistive and very conductive (Smith and others, 1977). These zones and their interpretations are summarized below:

1. relatively dry basalt - >500 ohm-m
2. basalt wetted with hot water - about 50 ohm-m
3. basalt with all water turned to resistive vapor - >500 ohm-m
4. basaltic melt - about 4 ohm-m
5. basalt with all water turned to resistive vapor - >500 ohm-m.

Coupled with the temperature logs in Zablocki and Tilling (1976) for nearby drill holes, the interface between layer 2 and layer 3

correlates with a temperature of about 600°C.

For Kilauea, a steady temperature increase from 20° to 1200°C (the first four zones in Kilauea Iki) can account for the sequences of resistivities, but constant salinity cannot completely account for the values of resistivities in layers two and three. Those in layer 2 are at or above the resistivity range in the constant 3 ppt salinity model, whereas those in layer 3 are at or below. The variations within layers are primarily lateral. The tendency appears to be that the shallower rocks in layer 2 are saturated with fluids having salinities of 3 ppt or lower, while the deeper fluids have salinities of 3 ppt or higher. The resistivities within each layer tend to be higher towards the edges of the triangular summit block, suggesting lower salinities there.

Layer 3 also has a tendency to dip away from Halema'uma'u in the cross sections. Coupled with the tendency for fluids to be more saline (less resistive) in the central summit region, these facts suggest an upwelling of heat and possibly saline fluids beneath Halema'uma'u. Keller and others (1979) model the temperature profile in the summit drillhole as due to a 700 m thick convective cell atop a 700 m thick conductive layer, all about 200 m laterally way from the highest heat flow area. The probable source of saline water is the sea and the source of fresh water is undoubtedly rainwater from the high recharge areas on the flanks of Mauna Loa to the north and west.

The resistivity structure deduced for the flanks is much simpler than that for the summit block (see Table 2). Because it is simpler,

there are more possible combinations of salinity and temperature which may fit the resistivities equally well. The range for layer 1, 45 to 118 ohm-m, must represent cold (20°C) fluids with a salinity of 1 ppt or less. The uncertainty comes in trying to determine the reason for the decreased resistivities in layer 2. A constant salinity model would require a temperature increase of 300°C to account for the drop. A constant temperature model would require a salinity increase to at least 35 ppt, the salinity of seawater.

Each of the possibilities is no less likely than the other considering that there are no other sources of deep information for the flanks. The absence of a resistive basement suggests that, in the constant salinity model, thermal gradients must taper off within layer 2. In any event, it also confirms that porosities are still significant at depth and that layer 4 beneath the summit model represents a thermal feature, not a structural one.

The CSEM data do not offer any direct evidence of the nature of the zones separating the triangular region from the flank areas outside. Instead, there is only indirect evidence of its properties, primarily based on our interpretations of the resistivity structure within each area. The barrier structure is not anomalously conductive, because the data only require a discontinuity in the otherwise horizontally-layered structures on either side. It must be relatively impermeable and thermally insulating because it appears to be a barrier between different hydrological units with different thermal characteristics. Finally, the barriers are roughly coincident in location with the southwest rift zone, the east rift zone, and the

Koa'e fault zone, respectively.

The structural interpretation for Kilauea summit and flank areas is summarized pictorially in Figure 56.

VI.3 Location of Magma

An integral part of the interpreted thermal structure beneath the summit block is the deep, conductive layer 5 which probably represents molten basalt, or magma. This layer is only recognized in a few soundings at a depth of 3.5 km below sea level just southeast of Halema'uma'u and 4.5 km below sea level further to the east and south. The soundings which resolved the conductor are located along linear concentrations of persistent earthquake activity also interpreted to outline magma conduits; however, the earthquakes occur at 2 to 5 km depth whereas the resistivity shows the top of the magma at a depth of 4.5 to 5.5 km. Magma depth interpreted from the CSEM data are also deeper than the storage areas deduced from deformation studies.

The agreement in lateral location between the deep, conductive zones and earthquake zones substantiates the conclusions that both are probably due to accumulations of magma; however, the discrepancy in depths is puzzling. Two possibilities suggest themselves. Both phenomena may be due to different aspects of magma. The low resistivities may represent the actual magma bodies while the earthquakes may represent expansion of water due to heat within pores and fractures above the magma. The other possibility is that the earthquakes do represent magma conduits, but that the CSEM soundings place the conductive magma too deep because of its limited lateral extent. That is, soundings portray more accurate depths to a body if that body is very

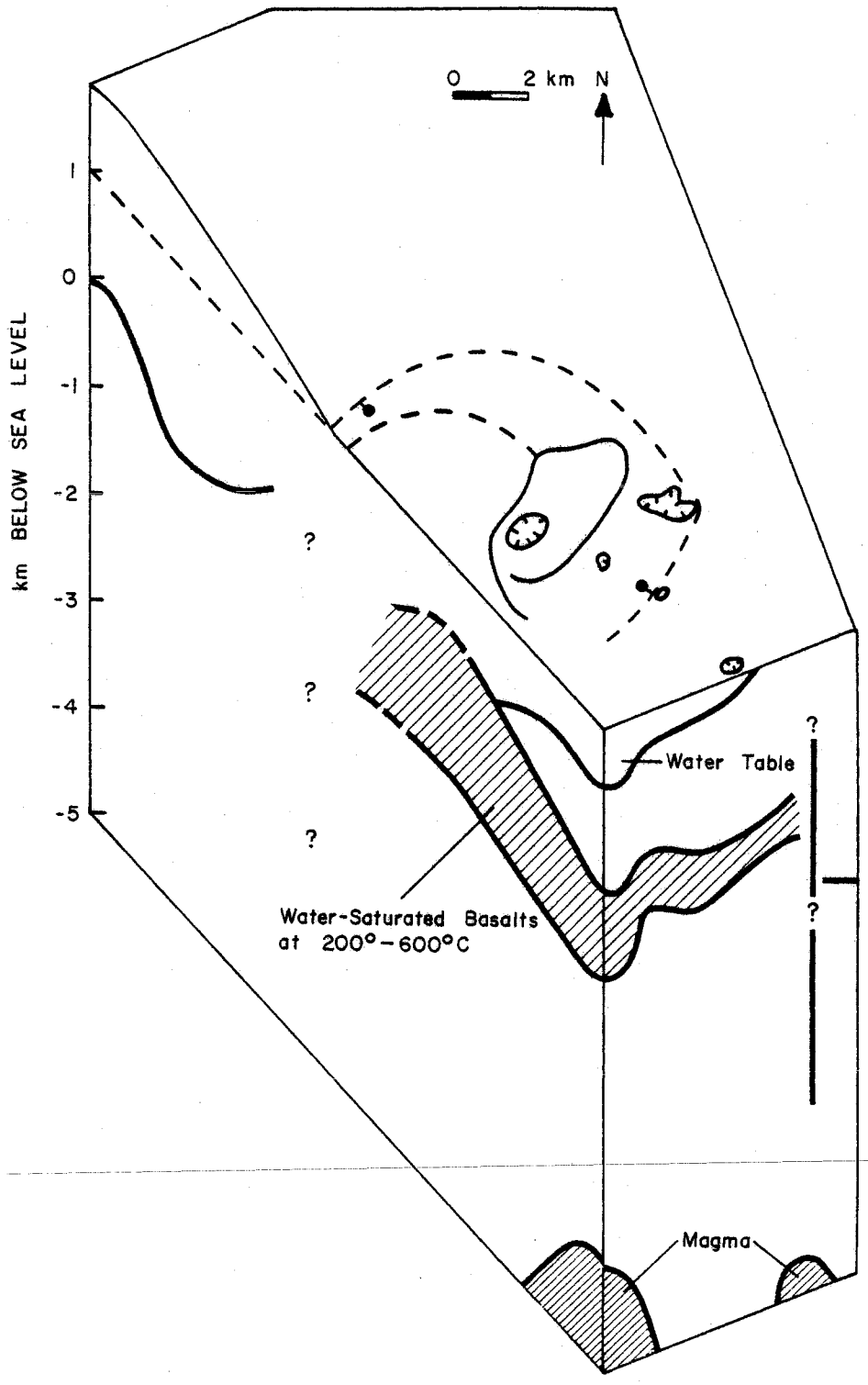

Figure 56. Schematic illustration of Kilauea's volcanic structure in three-dimensions.

wide. For narrower bodies, accuracy of the interpreted depths in the sounding are uncertain.

VI.4 Conclusions

In any event, magma appears to be detectable with low frequency CSEM measurements and has been sporadically mapped beneath Kilauea volcano. Although magma has been located, its depth is in some doubt due to possible complicating factors outlined above. The uncertainty is in a large part, due to the difficulties of penetrating the thick conductive zone of basalts saturated with hot water between the surface and the magma with the CSEM technique. More reliable magma mapping in basaltic volcanoes must minimize this penetration problem.

Appendix A

COMPUTATION OF THE HORIZONTAL AND VERTICAL POLARIZATION ELLIPSE PARAMETERS

The three orthogonal components of the magnetic field induced by a controlled source are generally not in phase and therefore any two will trace out an ellipse in time. Figure 5 shows such an ellipse in the vertical and horizontal planes. Each ellipse can be completely characterized by two parameters, an ellipticity which is the ratio of the minor axis to the major axis, and the angle between the major axis and one of the component directions. Both of these quantities are graphically defined in Figure 5. The two parameters for each ellipse can be computed from amplitude and phase measurements of two orthogonal components (Smith and Ward, 1974). For the vertical ellipse,

$$\alpha = 0.5 \tan^{-1} \left[\frac{2 H_z/H_r \cos(\phi_z - \phi_r)}{1-(H_z/H_r)^2} \right]$$

$$\epsilon_v = \frac{H_z H_r \sin(\phi_z - \phi_r)}{\left| H_z e^{i(\phi_z - \phi_r)} \sin\alpha + H_r \cos\alpha \right|^2}$$

For the horizontal ellipse,

$$\beta = 0.5 \tan^{-1} \left[\frac{2 H_r/H_\phi \cos(\phi_r - \phi_\phi)}{1-(H_r/H_\phi)^2} \right]$$

$$\epsilon_h = \frac{H_r H_z \sin(\phi_r - \phi_\phi)}{\left| H_r e^{i(\phi_r - \phi_\phi)} \sin\beta + H_\phi \cos\beta \right|^2}$$

where

H_r - amplitude of radial magnetic field

H_z - amplitude of vertical magnetic field

H_ϕ - amplitude of tangential magnetic field

ϕ_r - phase of radial field

ϕ_z - phase of vertical field

ϕ_ϕ - phase of tangential field.

Appendix B

JUSTIFICATION FOR THE USE OF 1D INTERPRETATIONS TO REPRESENT THE RESISTIVITY STRUCTURE LOCAL TO THE SOUNDING LOCATION

There is a conceptual difficulty in understanding what is meant when different one-dimensional models are required to describe multi-frequency data measured at different locations around the same source. The forward problem is solved assuming the same vertical resistivity structure everywhere horizontally. When data from two different receiver locations about the same source can be fit quite closely by two different, 1D models, is it necessarily inconsistent with the 1D model formulation which assumes lateral uniformity?

The answer is "no". The horizontal layering is assumed for mathematical reasons and is not a necessary condition for the existence of magnetic fields like those observed over a 1D model; that is to say, the interpretation of magnetic field data at one receiver location is non-unique. Each receiver location is particularly sensitive to the currents flowing nearest to it. If the observed data can be fit with a 1D model, then perhaps the model whould be viewed as a descriptor of the data that is representative of the structure nearest that location.

This region can be quantitatively defined using an idea presented by Sidorov and Gubatenko (1974) in a study on the lateral resolution of common EM prospecting equipment. They examined the relative contribution to the magnetic field made by currents induced in a thin, infinitely extensive, conducting sheet as a function of the current's position in the sheet. By noting where the largest contributions were

made for various configurations of source and receiver, they were able to determine which configurations were least affected by lateral variations in resistivity.

The same approach can define the regions which most affect the magnetic fields at a particular location. The region can be outlined in three-dimensions if the thin sheet is alternately placed at several different depths. Once this is done, the idea that 1D interpretations represent the vertical structure in that region can be tested with an example.

The magnetic field produced by a known distribution of electric currents can be computed using the Biot-Savart law (Lorrain and Corson, 1970).

$$\vec{B}(x,y,z) = \frac{\mu_0}{4\pi} \int \frac{\vec{J}(x',y',z) \times \hat{r}}{r^2} \, dV$$

where $r^2 = (x-x')^2 + (y-y')^2 + (z-z')^2$, $\hat{r} = \vec{r} \; / \; |r|$, and $\vec{J}$ is the known current density. A thin sheet has asymptotically high conductivity, σ, and small thickness, d (such that the product remains finite), requiring that the currents induced in the sheet be constant vertically within the sheet. This requirement reduced the Biot-Savart volume integral over the thin sheet to a surface integral,

$$\vec{B}(x,y,z) = \frac{\mu_0}{4\pi} \, s \int \frac{\vec{E}(x',y') \times \hat{r}}{r^2} \, dA$$

where $s = \sigma d$ is the conductance of the thin sheet (note $\vec{J} = \sigma \vec{E}$). For a VMD source, $\vec{E} = E\hat{\phi}$, as this is the only nonzero component of the electric field produced by such a source in a laterally homogeneous medium (see Chapter II).

The surface integral need not be evaluated, because the contributions that we are interested in are the vector components of the integrand, i.e.

$$\vec{B} = \iint \vec{b}(x',y')dx'dy'$$

The distribution of $\vec{b}(x',y')$ over the surface of the thin sheet is the contribution made to $\vec{B}$ per unit area by the currents at (x',y'). A combined map of these quantities is shown in Figure 57 for a thin sheet located 1 km below a source and receiver which are 10 km apart.

The major contributions lie along the line joining source and observation point. The quantity, b_z/B_z, is positive only within the circle where the source and receiver are on opposite ends of a diameter. The quantity, b_r/B_r, is positive everywhere on the same side of the source as the receiver. Both quantities are identically zero directly below the source because no currents are induced there. The quantity b_z/B_z again goes to zero beneath the observation point while b_r/B_r is a maximum there. Each also has a small positive maximum near the source.

As an aside, the relative magnitude of the maximum near the source changes with frequency relative to the maximum near the observation point. Figure 58 is a plot of b_z/B_z and b_r/B_r along the line joining source and observation point for two different frequencies of excitation. The two frequencies are indicated by two values for the combined parameter, frequency times conductance. As noted by Sidorov and Gubatenko (1974), the maximum near the source diminishes with respect to the maximum near the observation point as

Figure 57. A composite map showing the contribution of the currents induced in a thin sheet to the magnetic field at the observation point. The contributions vary according to location and are denoted by a lower case b while the total magnetic field is a capital B. Definition of variables: r is distance between source and observation point, h is depth of sheet below source plane, f is frequency, and σ and d are conductivity and thickness, of the thin sheet, respectively.

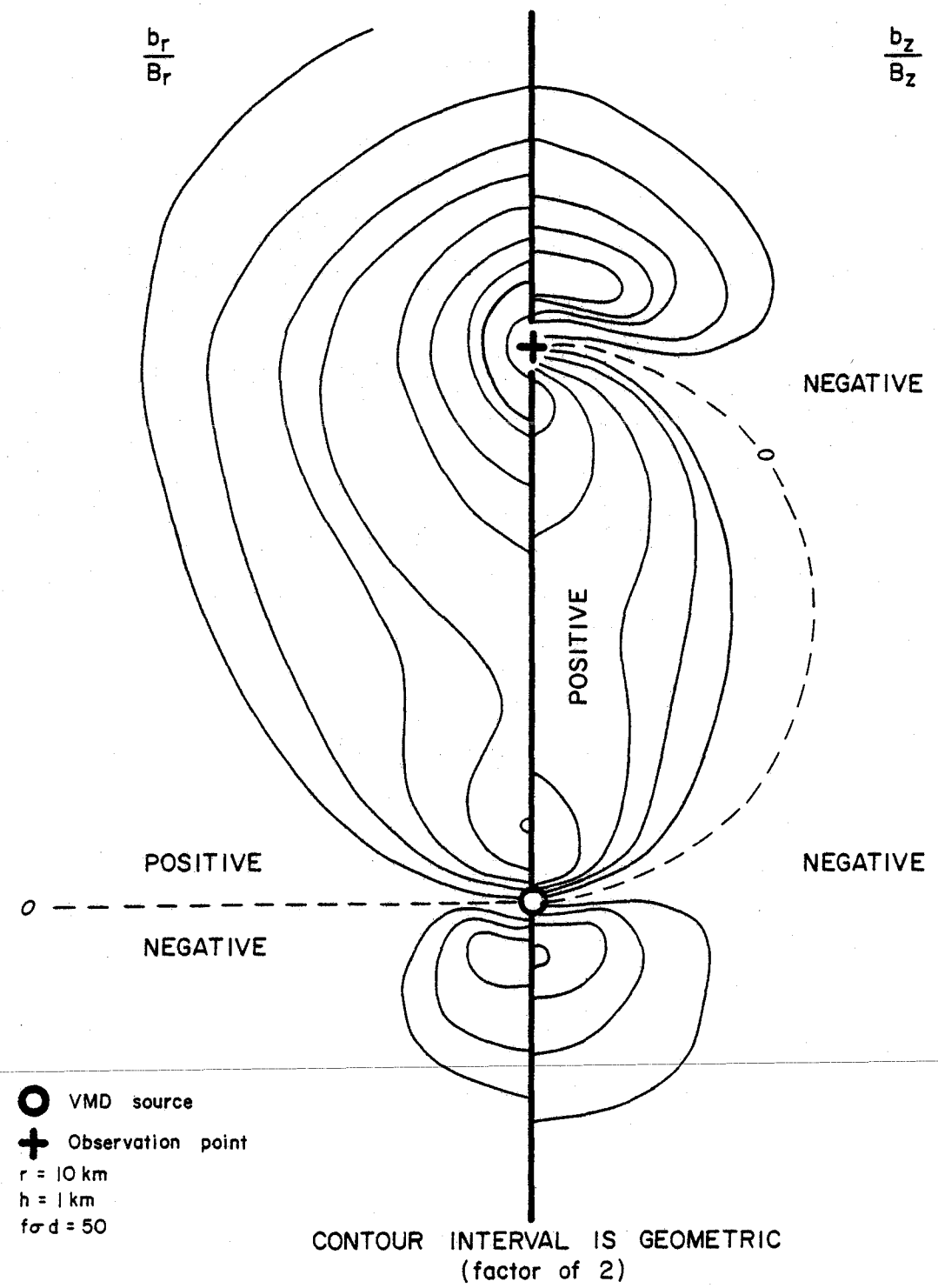
$\frac{b_r}{B_r}$
$\frac{b_z}{B_z}$
NEGATIVE
0
POSITIVE
POSITIVE
NEGATIVE
0
NEGATIVE
VMD source
Observation point
r = 10 km
h = 1 km
fσd = 50
CONTOUR INTERVAL IS GEOMETRIC
(factor of 2)

Figure 58. Contribution of the currents induced in a thin sheet to the magnetic field at the observation point (RX) along the line through the source (TX) and receiver (RX) are plotted for two different combinations of frequency and sheet conductance. Same variable definition as in Figure 57.

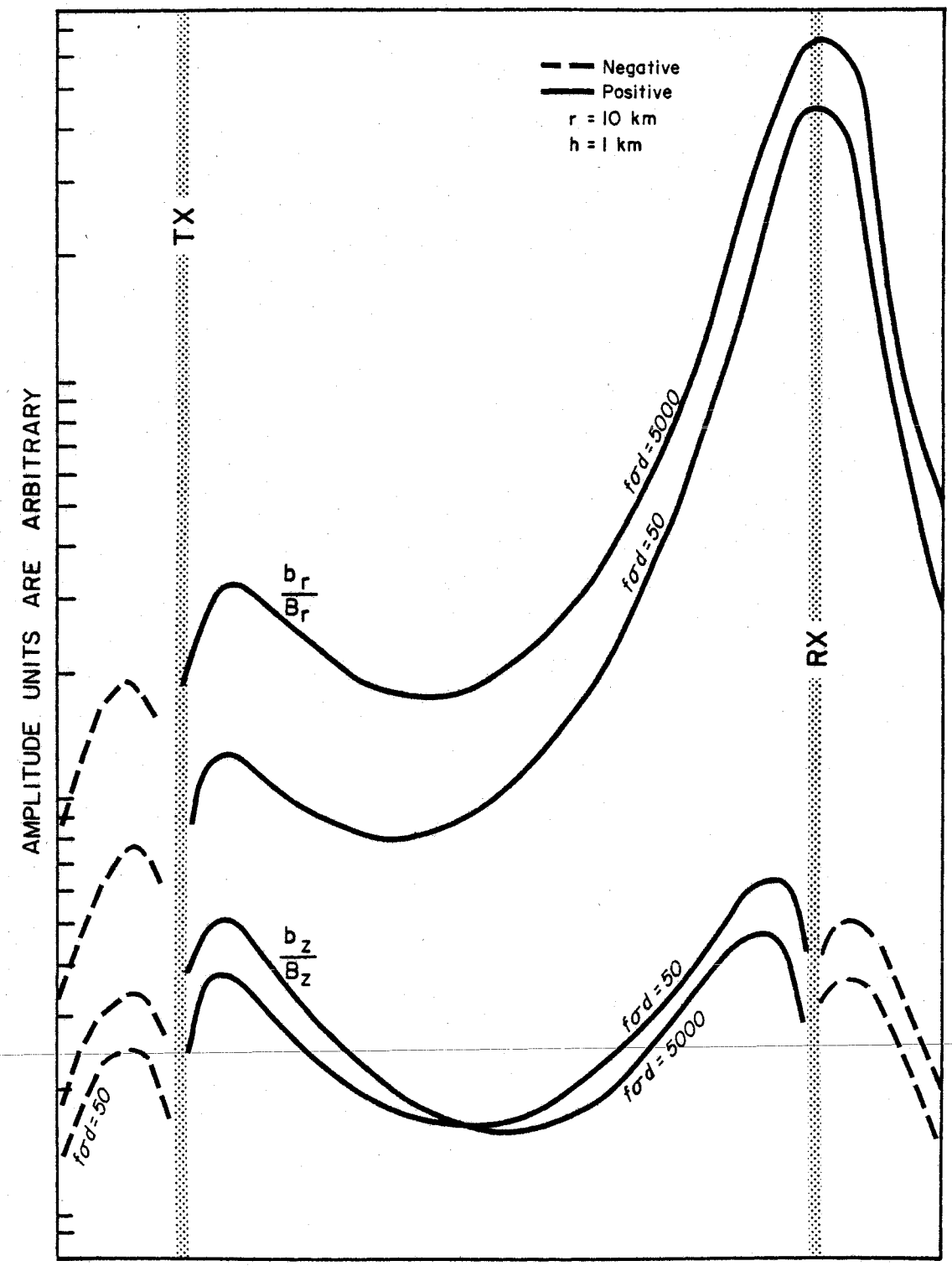
Negative
Positive
r = 10 km
h = 1 km
TX
RX
AMPLITUDE UNITS ARE ARBITRARY
$\frac{b_r}{B_r}$
$\frac{b_z}{B_z}$
fσd = 5000
fσd = 50
fσd = 50
fσd = 5000
fσd = 50

the frequency decreases.

The distributions of the two quantities also change as the vertical distance to the sheet is varied. To show this change in two dimensions, the areas with the largest values of b_z/B_z and b_r/B_r for thin sheets at several depths are combined in Figure 59. At each level, the areas in which the magnitudes of the contributions are greater than half the value of the maximum contribution at that level have been indicated by a solid, horizontal line (dashed if negative). For this figure, only relative contributions at each level are considered; absolute contributions decrease with depth, but the relative values are most descriptive if we are trying to answer questions about lateral variations in sensitivity.

The two components behave very differently in Figure 59. Major contributions to the vertical field come from two areas at shallow depths, one near the source and the other near the receiver. Below 0.2 times the source-receiver distance, the areas of major contribution for that level become one broad area centered midway between source and receiver. Major contributions to the radial field come from an area roughly centered beneath the receiver location. The width of this area becomes broader at greater depths.

Another point of interest is that the magnitude of b_r/B_r is always much greater than b_z/B_z. The difference in magnitudes is due primarily to the fact that the radial field is all secondary field (it would disappear if the thin sheet were removed) whereas the vertical field is a sum of primary and secondary. The magnitude of b_r/B_r also decreases much more slowly as the depth to the sheet is

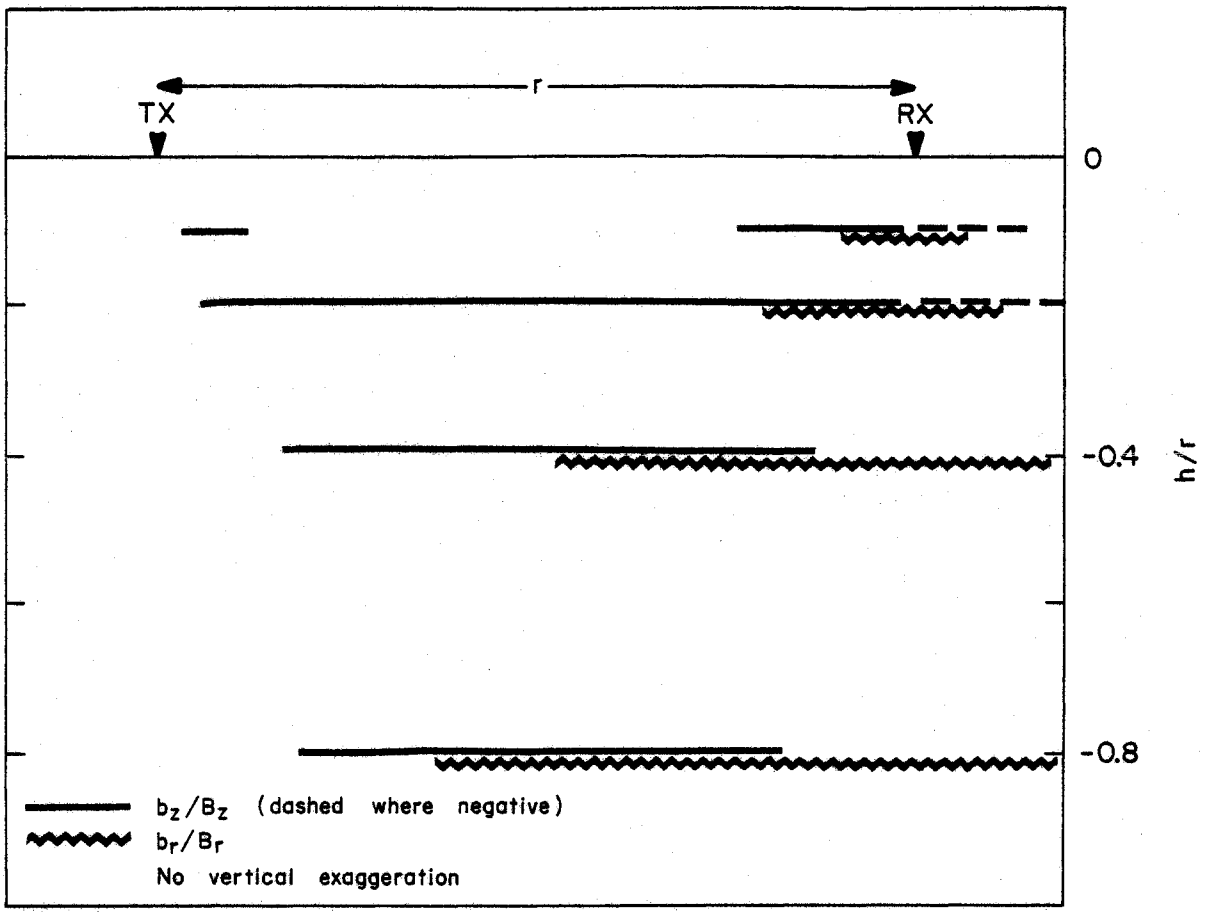

Figure 59. A diagram showing the zones of contributions greater than half the maximum contribution for discrete depths in a vertical plane including source (TX) and receiver (RX).

increased, confirming Ryu and others (1970) contention that radial magnetic field data offer superior resolution of deep structures when compared with vertical field data.

On the basis of this thin sheet study, the following conclusions can be drawn regarding a CSEM sounding survey with a VMD source:

1. vertical magnetic field data are most representative of the shallow regions just below the source and receiver location; deeper than 0.2 times the source-receiver distance, these data are most representative of a region centered on the midpoint between the source and receiver,
2. radial magnetic field data are most representative of the region directly below the receiver,
3. vertical ellipticity and tilt angle data, which combine both radial and vertical field data, are most representative of the region beneath the receiver.

A sufficient condition for the validity of these conclusions is that the electric currents be induced in the broad region beneath both source and receiver. This condition is really meant to exclude cases where currents are induced in small concentrations and are not reasonably dispersed in space. Horizontality of the induced currents is not required despite the use of horizontal thin sheets in the study, as will be demonstrated in the following example.

To test these conclusions, the theoretical magnetic fields were computed over a dipping thin sheet, illustrated in Figure 60. The

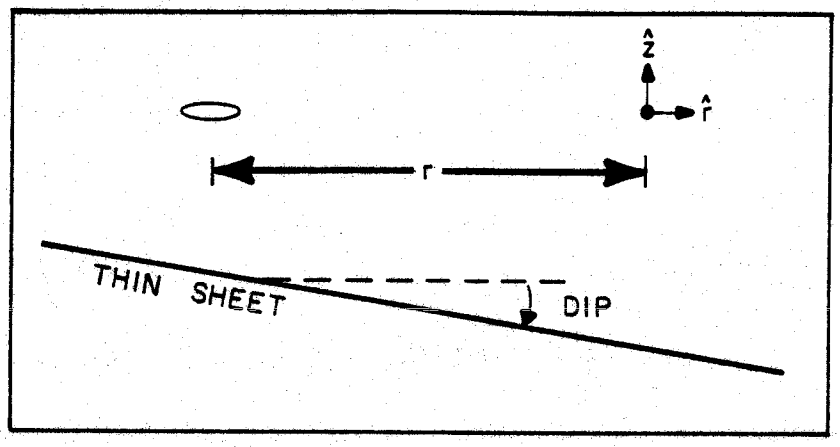

Figure 60. Geometry of the dipping thin sheet model showing the loop source and the observation point.

desired fields are actually a combination of the magnetic fields of a VMD and a HMD (horizontal magnetic dipole) source over a horizontal thin sheet. The HMD fields were derived by Dey and Ward (1970). For the model in Figure 60, the fields are

$$H_z = H_1 \cos(DIP) - H_2 \sin(DIP)$$

$$H_r = H_1 \sin(DIP) + H_2 \cos(DIP)$$

where

$$H_1 = H_z^{VMD}(r',z') \cos(DIP) - H_z^{HMD}(r',z') \sin(DIP)$$

$$H_2 = H_r^{VMD}(r',z') \cos(DIP) - H_r^{HMD}(r',z') \sin(DIP)$$

$r' = r \times \cos(DIP)$

$z' = r \times \sin(DIP)$

r is source-receiver distance

DIP is the angle that the sheet dips below horizontal

(note horizontal is defined as the plane containing source and receiver).

Five examples of vertical ellipticity and tilt angle over dipping thin sheets are plotted in pseudo-phasor form in Figure 61 along with the responses over horizontal thin sheets at various depths (solid lines). A table in one corner of the figure gives the dip angle and the depths to the thin sheet vertically below both the source and receiver. As can be seen in the figure, comparison between the dipping and horizontal sheet data show that the polarization parameters respond to the dipping sheet approximately as if it were

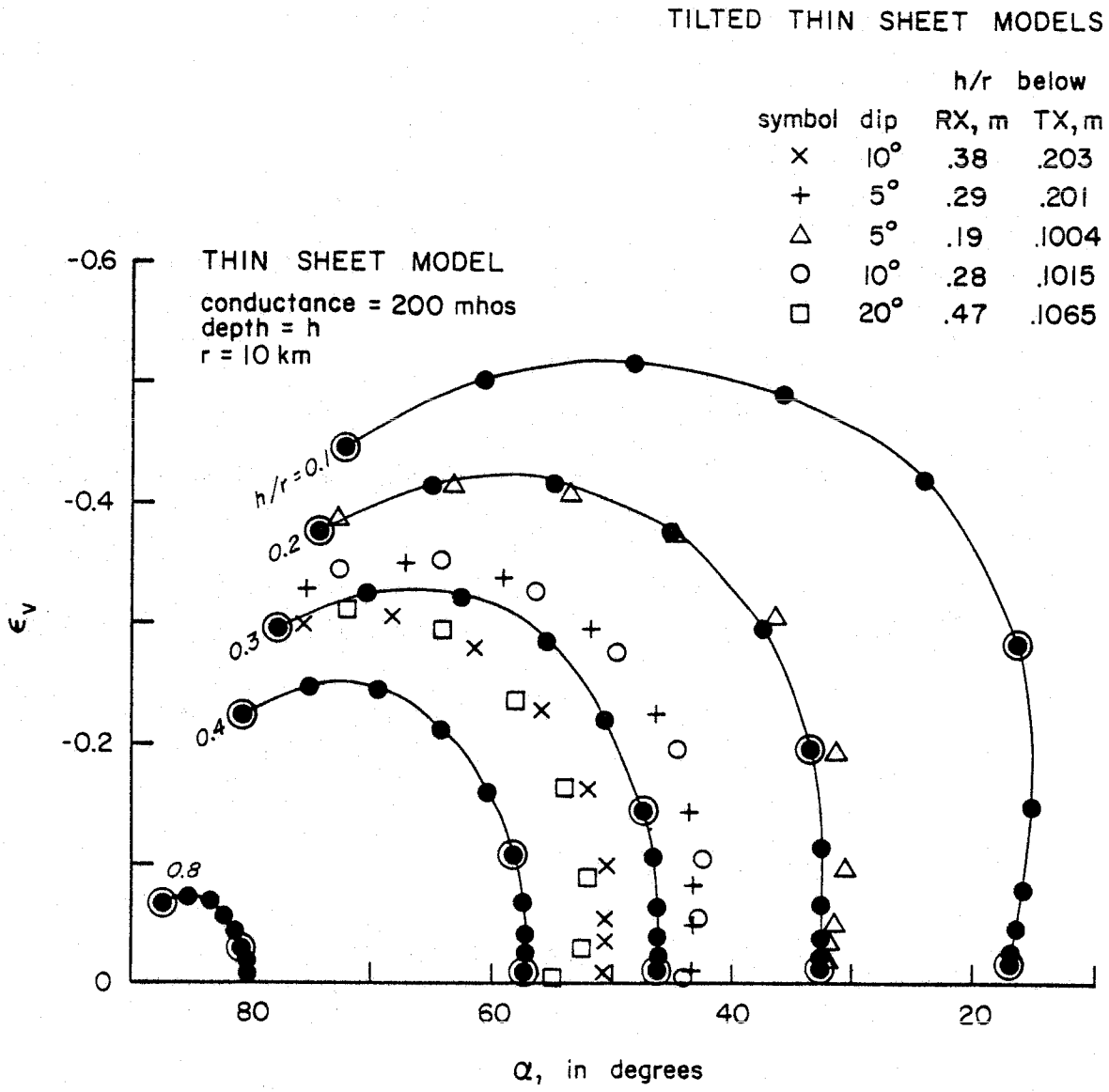

Figure 61. Pseudo-phasor plots of horizontal thin sheet models (solid lines) and dipping thin sheet models (individual symbols).

horizontal. The depth that would be interpreted from the dipping sheet data is very close to its actual depth below the receiver, at least for dip angles of up to 10°. The interpreted depths underestimate the depth below the receiver for deeper sheets, but the agreement is good enough to support the above contentions. The interpreted conductance of the dipping sheet is also slightly underestimated (the data points are shifted clockwise along the pseudo-phasor curve compared with the horizontal sheet plots).

How meaningful are interpretations based on compilations of one-dimensional models when the actual structure is three-dimensional? Although by no means comprehensive, the arguments in this section show that such interpretation can be meaningful if the 1D models are thought of as representing a particular region relative to the source and receiver location. That region can be different depending on the type of data measured. For polarization parameter data, that region appears to be centered below the receiver location; however, it should be noted that depths may be underestimated for steeply dipping layers.

Appendix C

MATHEMATICS OF INVERSION

C.1 Goodness-of-Fit Criterion

The goodness-of-fit criterion is defined for each data set (i.e., sounding) as

$$\xi = \sum_{i-1}^{n} \{y_i - f_i(x_{ij} p_1, p_2, p_3, \ldots p_k)\}^2 \frac{1}{s_i^2} \tag{C.1}$$

where y_i is the observed value at x_i (i.e., tilt angles and ellipticities),

x_i is the ith independent variable (i.e., frequency),

f_i is the predicted value (i.e., predicted tilt angle and ellipticities) at x_i,

$p_j (j=1,k)$ are the k parameters of the model (i.e., layer resistivities and thicknesses) used to compute f_i, and s_i is the standard error of y_i.

C.2 Linearization of the Problem

First, the function $f_i(p)$ is expanded as a Taylor series about $\vec{p}_o$ keeping only linear terms,

$$f_i(\vec{p}) = f_i(\vec{p}_o + \overrightarrow{\Delta p}) \cong f_i(\vec{p}_o) + \sum_{j=1}^{k} \left(\frac{\partial f_i}{\partial p_j}\right) \Delta p_j \tag{C.2}$$

where $\Delta p_j = p_j - p_{oj}$.

If $\vec{p}$ represents the correct set of parameters and $\vec{p}_o$ represents the guessed set, then

$$y_i = f_i(\vec{p}) = f_i(\vec{p}_o) + \sum_{j=i}^{k} \left(\frac{f_i}{p_j}\right) \Delta p_j \tag{C.3}$$

So

$$\vec{y} - f(\vec{p}_o) = \underset{\sim}{B}\,\overrightarrow{\Delta p} \qquad \text{where } B_{ij} = \frac{\partial f_i}{\partial p_j} \tag{C.4}$$

If the problem was really linear (i.e., eq. C.2 was exact),

$$\overrightarrow{\Delta p} = \underset{\sim}{A}\,[\vec{y} - \vec{f}(\vec{p}_o)] \tag{C.5}$$

and $\underset{\sim}{A} = \underset{\sim}{B}^{-1}$.

Once equation (C.5) is solved for $\overrightarrow{\Delta p}$, then we may compute p from the set of initial guesses, $\vec{p}_o$, $\vec{p} = \vec{p}_o + \overrightarrow{\Delta p}$.

Since the problem is nonlinear, equation C.5 must be used iteratively to arrive at consecutively better guesses of $\vec{p}$.

C.3 Computation of the Matrix A

Most of the differences between the various iterative methods in use today are in the computation of $\underset{\sim}{A}$. For the usual case where the number of observations, n, exceeds the number of model parameters to be estimated, k, the matrix $\underset{\sim}{B}$ is rectangular, and its inverse, $\underset{\sim}{A}$, can be computed by

$$\underset{\sim}{A} = (\underset{\sim}{B}^T\,\underset{\sim}{B})^{-1}\,\underset{\sim}{B}^T \tag{C.6}$$

known as the least squares inversion. Use of the above formula is nonconvergent for many nonlinear problems, so alternate methods of computing $\underset{\sim}{A}$ have been devised.

In generalized linear inversion theory, $\underset{\sim}{B}$ is decomposed into eigenvectors and eigenvalues and the inverse matrix A is formed from these components, after those eigenvectors with very small associated

eigenvalues have been eliminated. Use of only the largest eigenvectors in forming the inverse makes the inverse more stable than when all the eigenvectors are used. With Marquardt inversion, or ridge regression, $\underset{\sim}{A}$ is computed with the formula,

$$\underset{\sim}{A} = (\underset{\sim}{B}^T \underset{\sim}{B} + \lambda \underset{\sim}{I})^{-1} \underset{\sim}{B}^T \tag{C.7}$$

where $\underset{\sim}{I}$ is the identify matrix. Addition of the constant λ along the diagonal has the effect of minimizing the small eigenvectors of $\underset{\sim}{B}$ also. Other methods are discussed in Twomey (1977).

C.4 Statistics of Inversion (following Inman, 1975)

When the set of parameters p has been found which satisfactorily minimizes ξ (eq. C.1), the residual variance is

$$\hat{\sigma}^2 = \frac{(\vec{\Delta g})^T (\vec{\Delta g})}{n-k} \quad \text{where } \vec{\Delta g} = [\vec{y} - \vec{f}(\vec{p}_o)] \frac{1}{\vec{s}} \tag{C.8}$$

and is already compared with the variance of observed values because $\vec{\Delta g}$ is the residuals weighted by the data errors $\vec{s}$. If $\hat{\sigma}$ is much greater than unity, then the data have not been fully explained by the model. If $\hat{\sigma}$ is much less than unity, then $\vec{s}$ is overestimated or the model is fitting noise along with the data. "The residual variance is independent of the linearity or nonlinearity of the problem with respect to the model parameters" (Inman, 1975, p. 803).

The covariance of the parameters, $\vec{p}$, is calculated from the covariance of the change in parameters,

$$\text{cov}(\vec{\Delta p}) = \hat{\sigma}^2 (\underset{\sim}{A}^T \underset{\sim}{A})^{-1} \tag{C.9}$$

Since $\overrightarrow{\Delta p} = \vec{p} - \vec{p}_o$ and $\vec{p}_o$ is known so $\text{cov}(\vec{p}_o) = 0$,

$$\text{cov}(\overrightarrow{\Delta p}) = \text{cov}(\vec{p}) \ .$$

Appendix D

ELECTROMAGNETIC SCALE MODELING

The scaling from the field parameters to the model parameters can be accomplished by preserving the dimensionless ratio of length to electromagnetic skin depth (the induction number, B, in eq. 30; Frischknecht, 1971). This reinforces the importance previously placed on B and makes the transformation between field and model parameters a simple matter of holding B constant, or

$$B = \underset{\text{MODEL}}{[r'(\frac{\mu'\sigma'\omega'}{2})^{\frac{1}{2}}]} = \underset{\text{FIELD}}{[r(\frac{\mu\sigma\omega}{2})^{\frac{1}{2}}]} \qquad (D.1)$$

or, since μ, the magnetic susceptibility, does not vary between field and model materials,

$$r'^2\sigma'f' = r^2\sigma f \qquad (D.2)$$

If B is the same for the field and model measurements, then the phasor plots, especially those for tilt angle and vertical ellipticity, will be identical for the same value of B. In the model, then, for a particular scaled down distance, r', the model values of σ' can be held constant and various field combinations of σf can be modeled by a change in model frequency only.

The choice of scale factors must take into account constraints on available modeling materials and equipment. Because the ratio of r/r' will probably be between 1,000 and 100,000, the model conductivity-frequency product must be 10^8 to 10^{10} times larger than the field conductivity-frequency product. A convenient choice for

model materials is graphite sheets which come in various thicknesses and have a conductivity of about 10^5 mho/m (Frischknecht, 1971). Sheets 1.25 cm and 2.5 cm thick were available for this study. Therefore, an obvious choice for the ratio r/r' is 1 km/1.25 cm = 80,000 because of the need to model 1 and 2 km thick, conductive layers. The values for the field σf product have been shown to range from about 0.001 (σ=0.01 mho/m and f=0.1 Hz) to 0.8 (σ=0.1 mho/m and f=8 Hz) so we seek model $\sigma' f'$ products between 6.4×10^6 and 5.2×10^9. The model σ' has already been chosen to be that of graphite (10^5 mho/m), so the needed frequency range is 64 Hz to 51.2 kHz. The lowest available model frequency was 320 Hz which still allows most of the range of field parameters to be represented.

The choice of $\sigma'=10^5$ mho/m, r/r'=80,000, and $320<f'<32{,}000$ means that these scale model results represent field σf products between 0.005 to 0.5. Details of the modeling at the U.S. Geological Survey scale-modeling facility will be discussed in the next section.

D.1 Scale-Modeling Procedures

The equipment consisted of a horizontal coil of 1 cm radius as the source and another multiturn coil alternately placed in the three orthogonal orientations as the receiver. The signals were run through a synchronous detector system to obtain complex field strengths. The source was stationary while the receiver unit was run along profile lines. Source location and profile lines are shown in Figure 62. Prior to each profile run, the receiver circuitry was first adjusted for maximum vertical field at the closest point to the source along

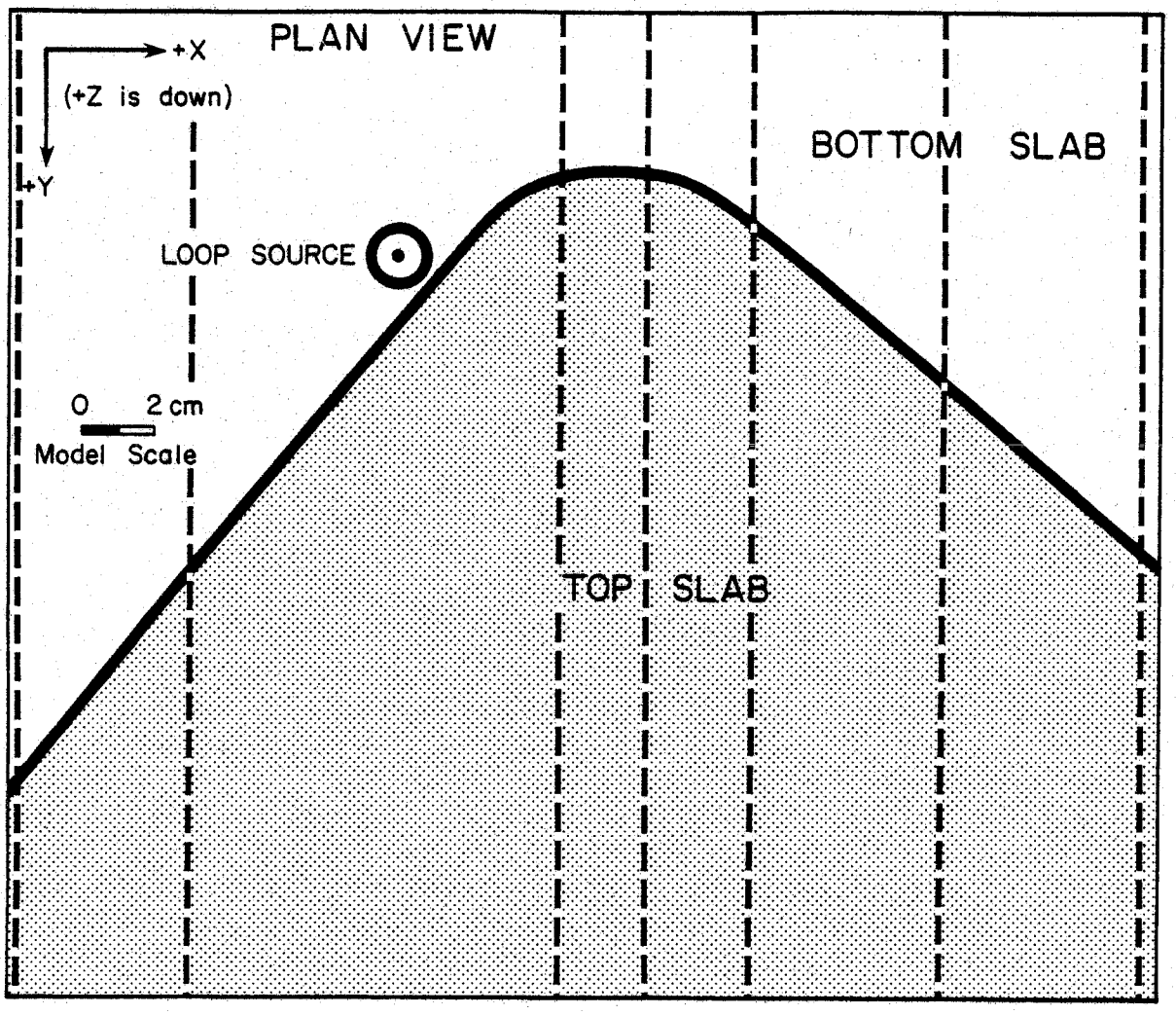

Figure 62. Plan view of the scale model showing the outline of the upper slab and the location of the loop source. The dashed lines are the measurement profile tracks.

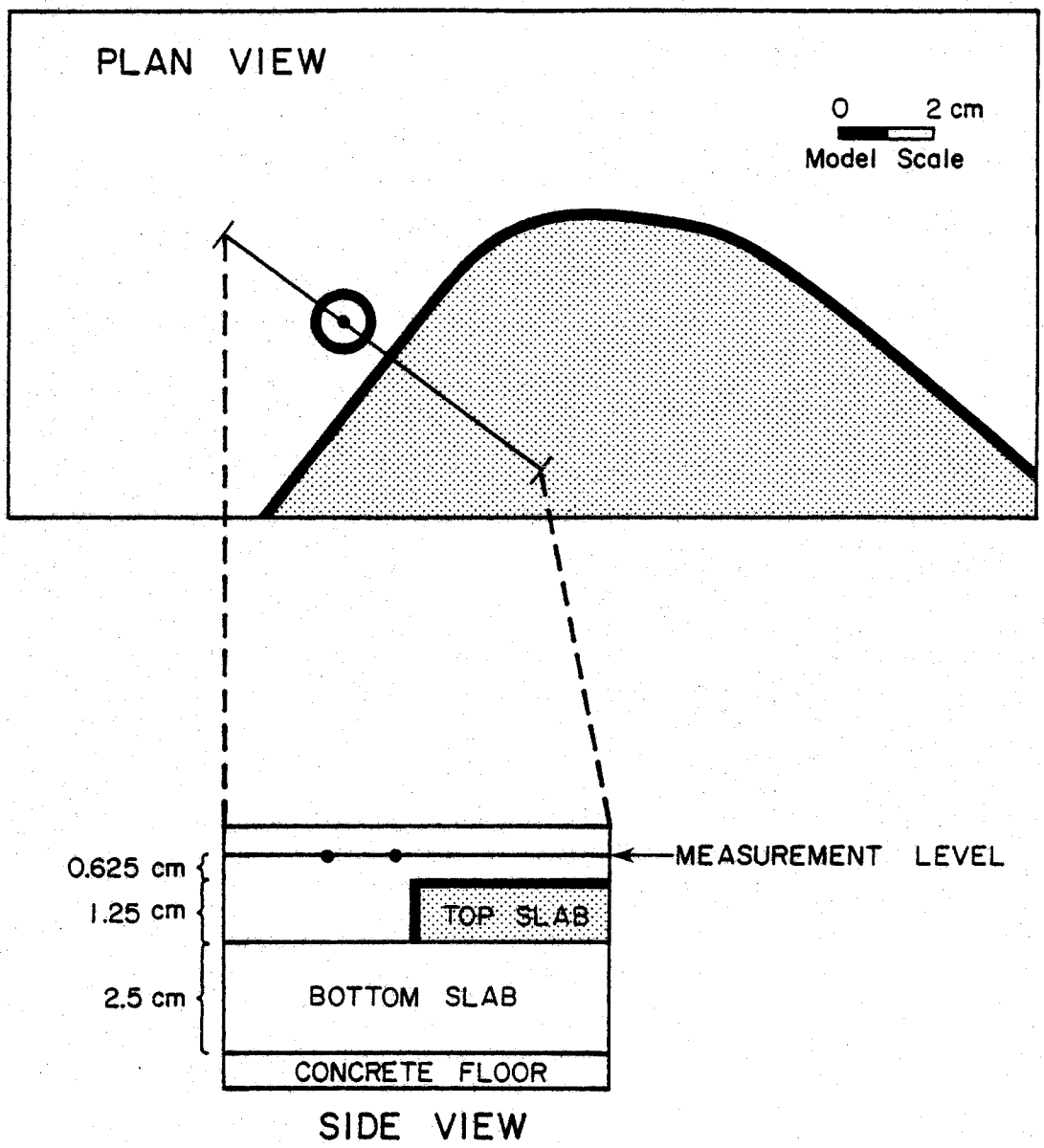

Figure 63. Plan view and side view of the scale model showing the model dimensions. Transformation from model to field lengths is 1.25 cm to 1 km.

the profile in the absence of any conductors. This assures that the signal will not go off scale. All seven profiles were run nine times each - once for each frequency (320, 3200, and 32,000 Hz) and once for each receiver coil orientation. Three profiles were also run at two additional frequencies - 1000 and 10,000 Hz.

Two separate models were run. The first, called the one-slab model in the following plots, consisted of a single, large sheet of graphite. The second, called the two-slab model, had an additional graphite sheet that had been cut into a particular shape on top of the one-slab model (see Fig. 63). After all runs were completed, the model data were appropriately compiled and reduced and the vertical and horizontal polarization ellipse parameters were computed as a function of position on the model. Maps at three frequencies for the four polarization ellipse quantities for both models are presented in Figures 64 to 87. Sets of pseudo-phasor plots are also presented along three profiles, shown in Figures 88 to 92.

The abundance of modeling results allowed two checks on the model setup. First, the horizontal polarization ellipse parameters (strike angle and horizontal ellipticity) for the one-slab models should be constant over the entire model. Departures from the expected strike angle of 90° or horizontal ellipticity of zero do occur in the scale model results and seem to be the worst at the low frequency (320 Hz). They are most likely the result of inhomogeneities in the graphite and should be mentally subtracted from the two-slab model results. By far, most of the one-slab model results are those expected for a thin, uniform sheet and generally confirm the validity of this

approach. For the second test, several of the one-slab pseudo-phasor results were reduced to apparent resistivities along the lines already described in the data reduction section. The derived value of 7.58×10^4 mho/m compares quite well to the assumed value of 10^5 mho/m for the graphite sheets.

Figures 64 to 87. The following 24 figures present the scale model results as maps (same scale as Fig. 62) for four polarization ellipse parameters at three frequencies over two different models (4×3×2=24). The values of each of these three types of variables are listed at the top of each map. The four polarization parameters are vertical ellipticity, tilt angle, horizontal ellipticity, and strike angle (see Fig. 5). The frequencies are 320, 3200, and 32000 Hz. The two models are the one-slab (consisting of the bottom graphite slab in Fig. 63 only) and the two-slab model (consisting of both graphite slabs in Fig. 63).

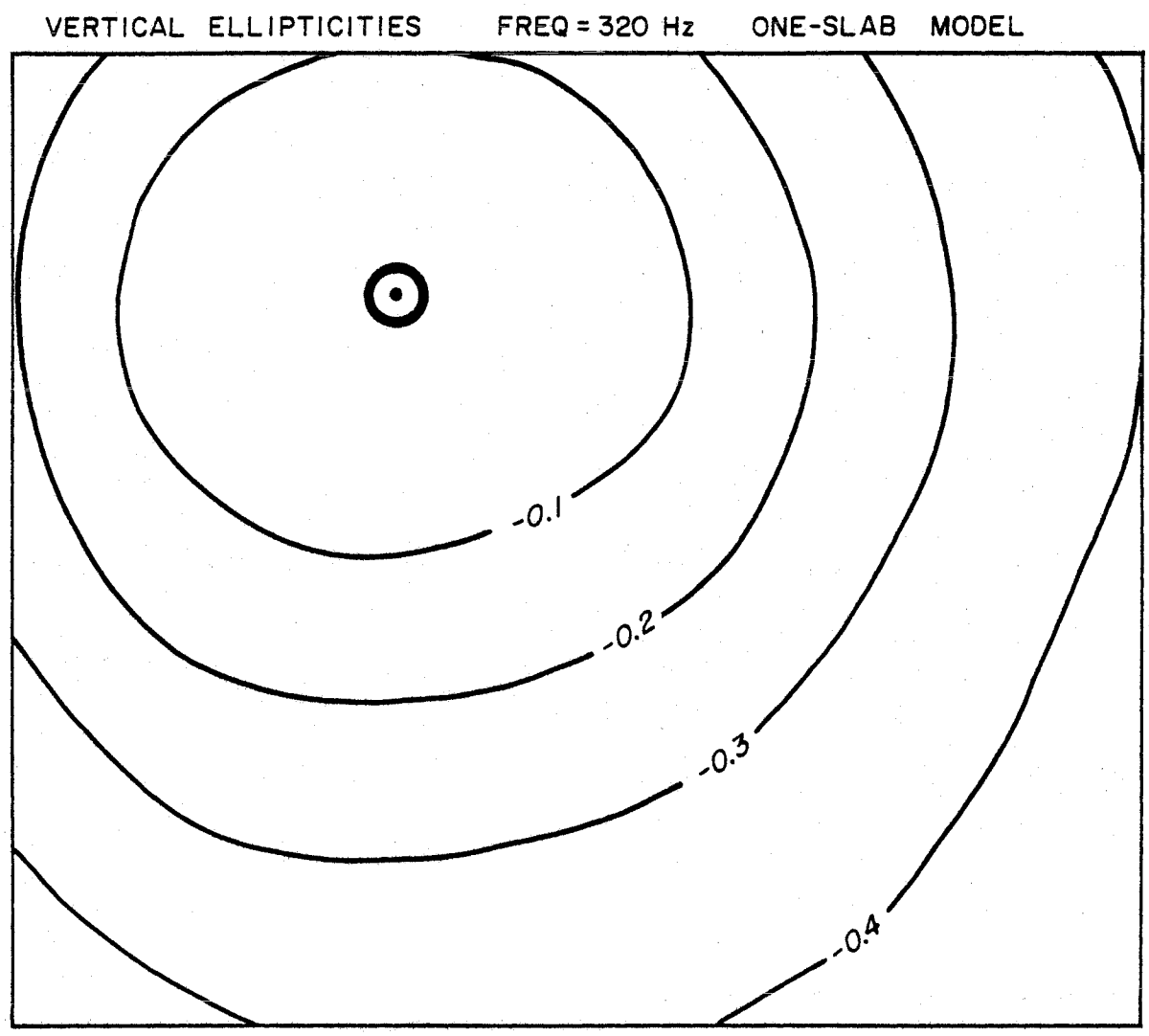
VERTICAL ELLIPTICITIES
FREQ = 320 Hz
ONE-SLAB MODEL
-0.1
-0.2
-0.3
-0.4

Figure 64.

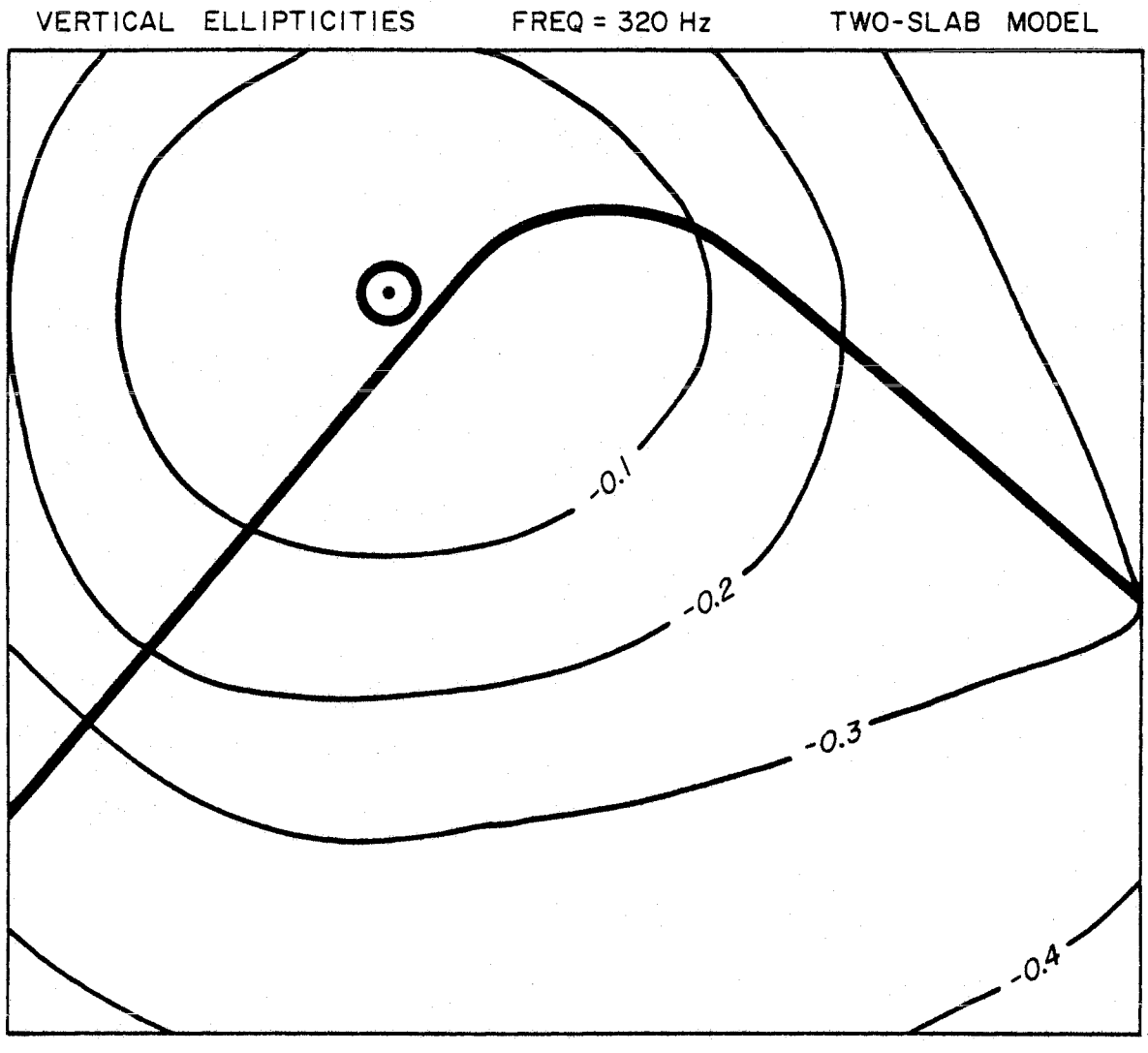
VERTICAL ELLIPTICITIES
FREQ = 320 Hz
TWO-SLAB MODEL
-0.1
-0.2
-0.3
-0.4

Figure 65.

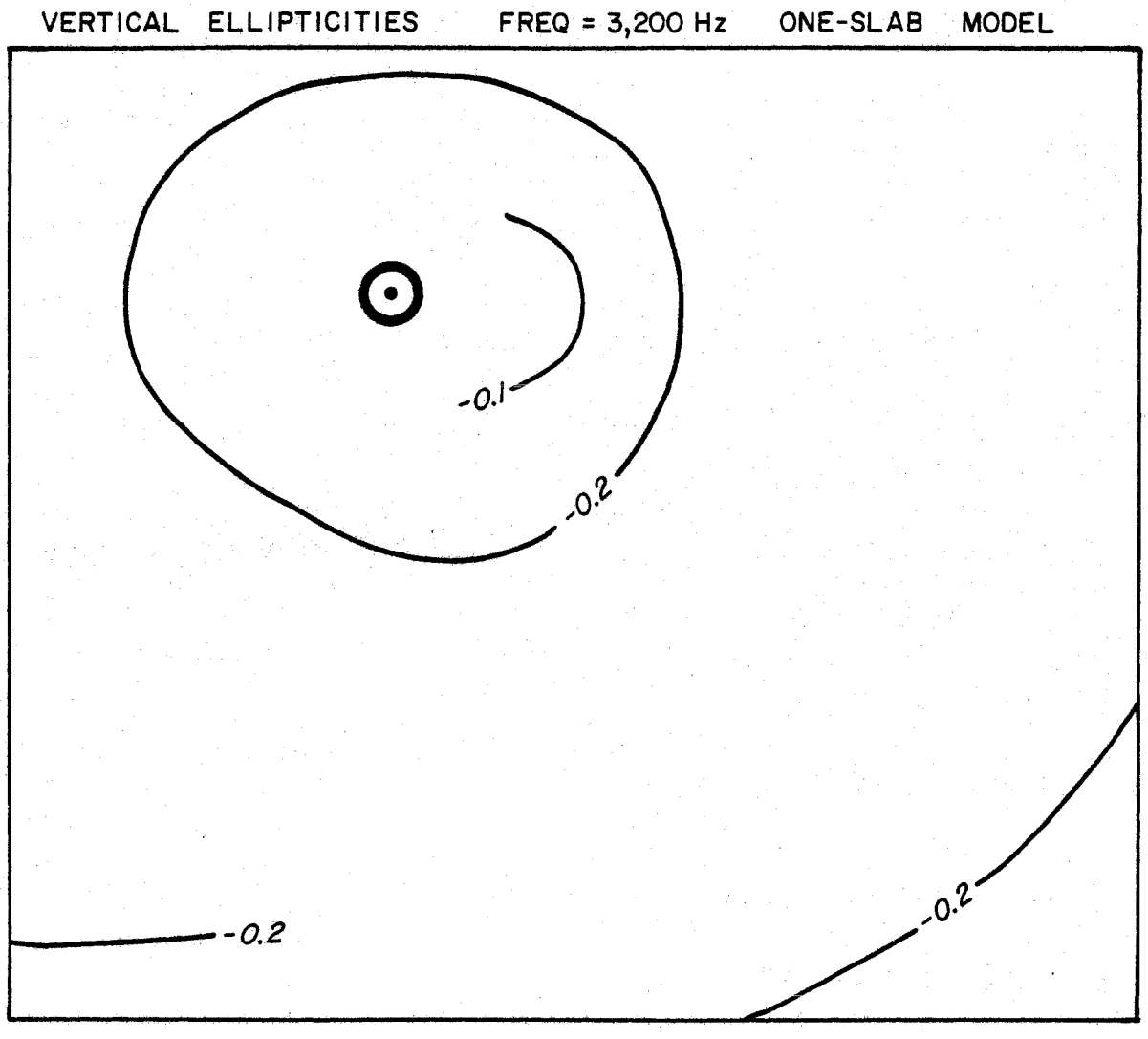
VERTICAL ELLIPTICITIES
FREQ = 3,200 Hz
ONE-SLAB MODEL
-0.1
-0.2
-0.2
-0.2

Figure 66.

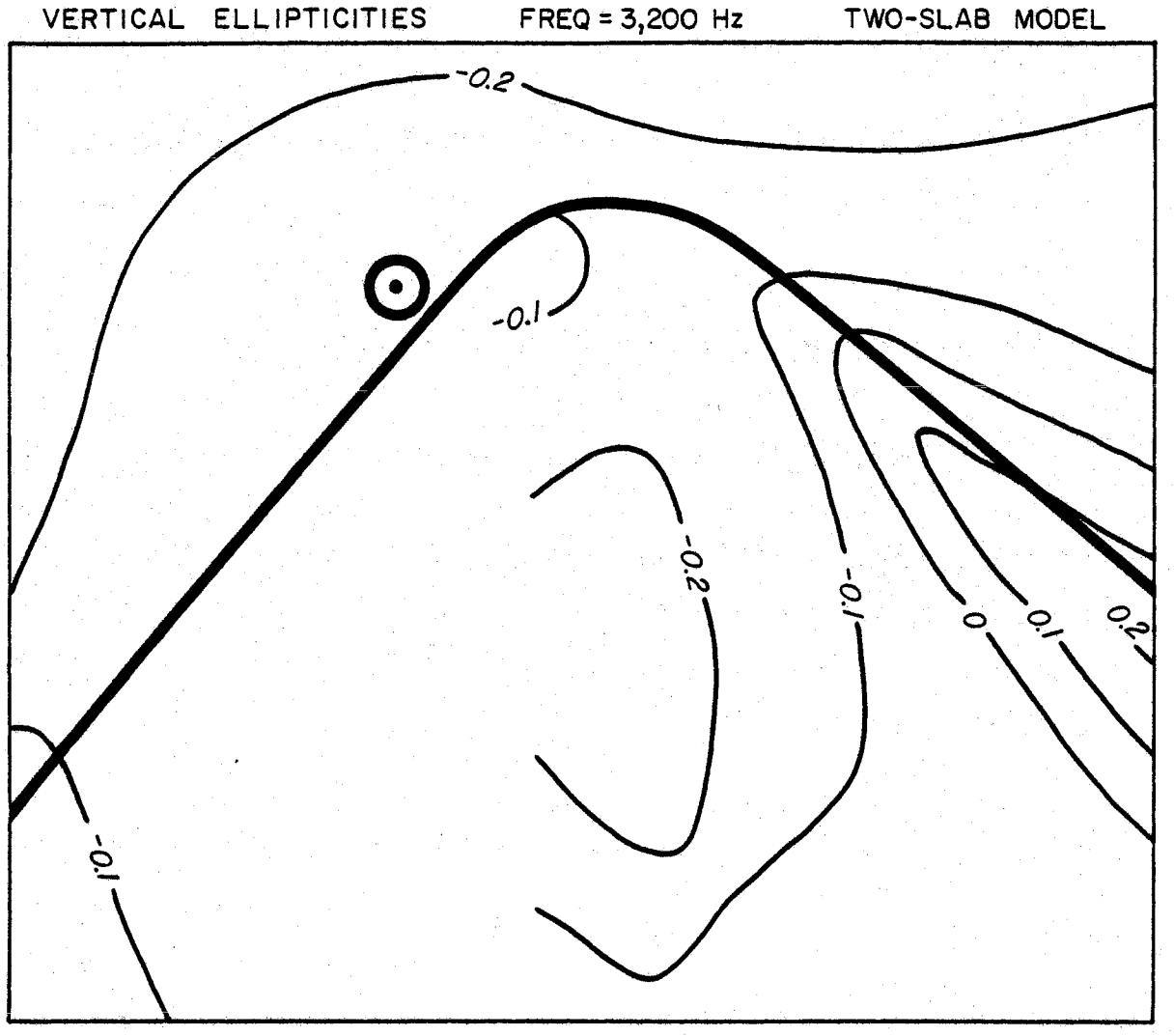
VERTICAL ELLIPTICITIES
FREQ = 3,200 Hz
TWO-SLAB MODEL
-0.2
-0.1
-0.2
-0.1
0
0.1
0.2
-0.1

Figure 67.

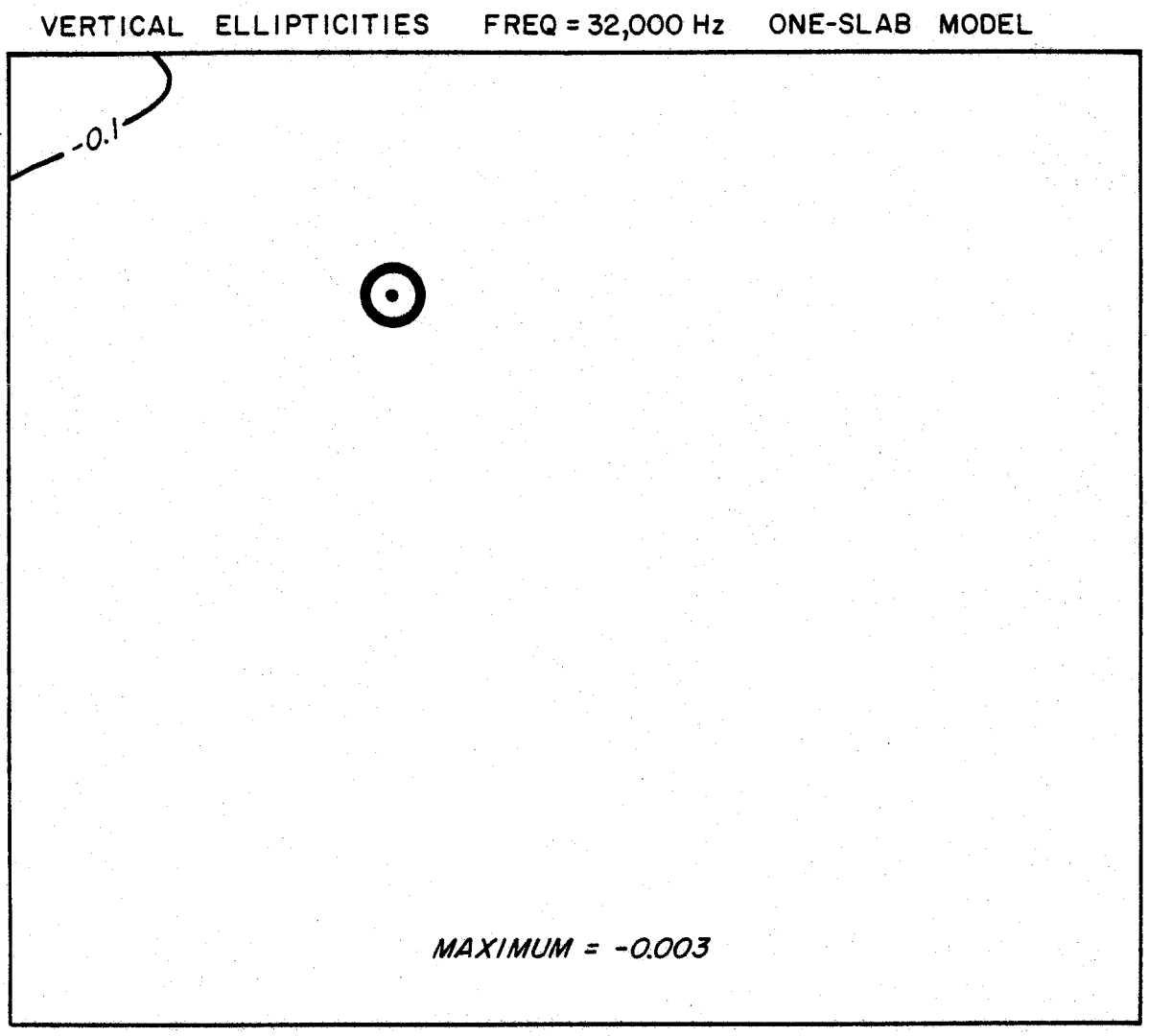
VERTICAL ELLIPTICITIES FREQ = 32,000 Hz ONE-SLAB MODEL
-0.1
MAXIMUM = -0.003

Figure 68.

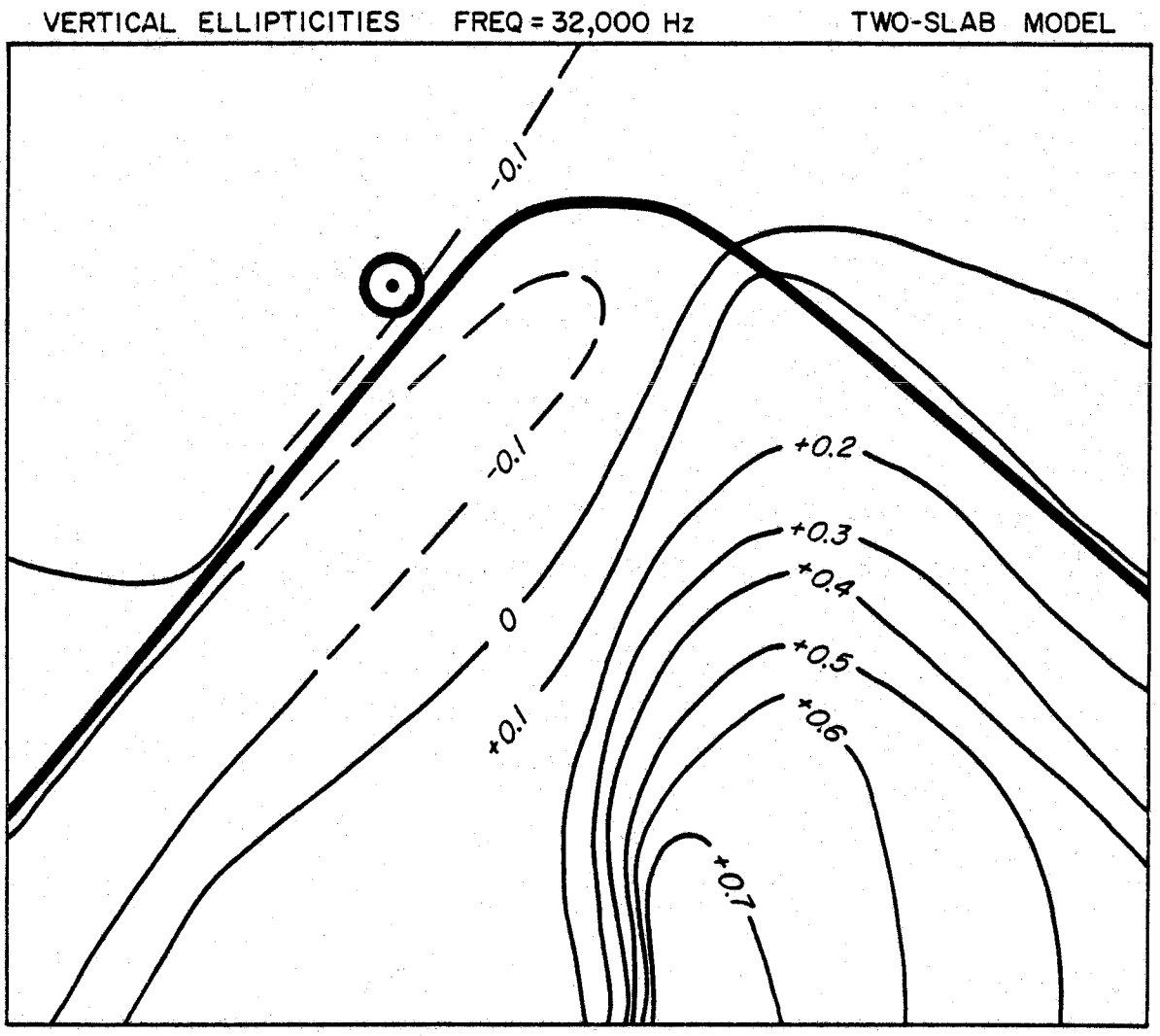
VERTICAL ELLIPTICITIES
FREQ = 32,000 Hz
TWO-SLAB MODEL
-0.1
-0.1
0
+0.1
+0.2
+0.3
+0.4
+0.5
+0.6
+0.7

Figure 69.

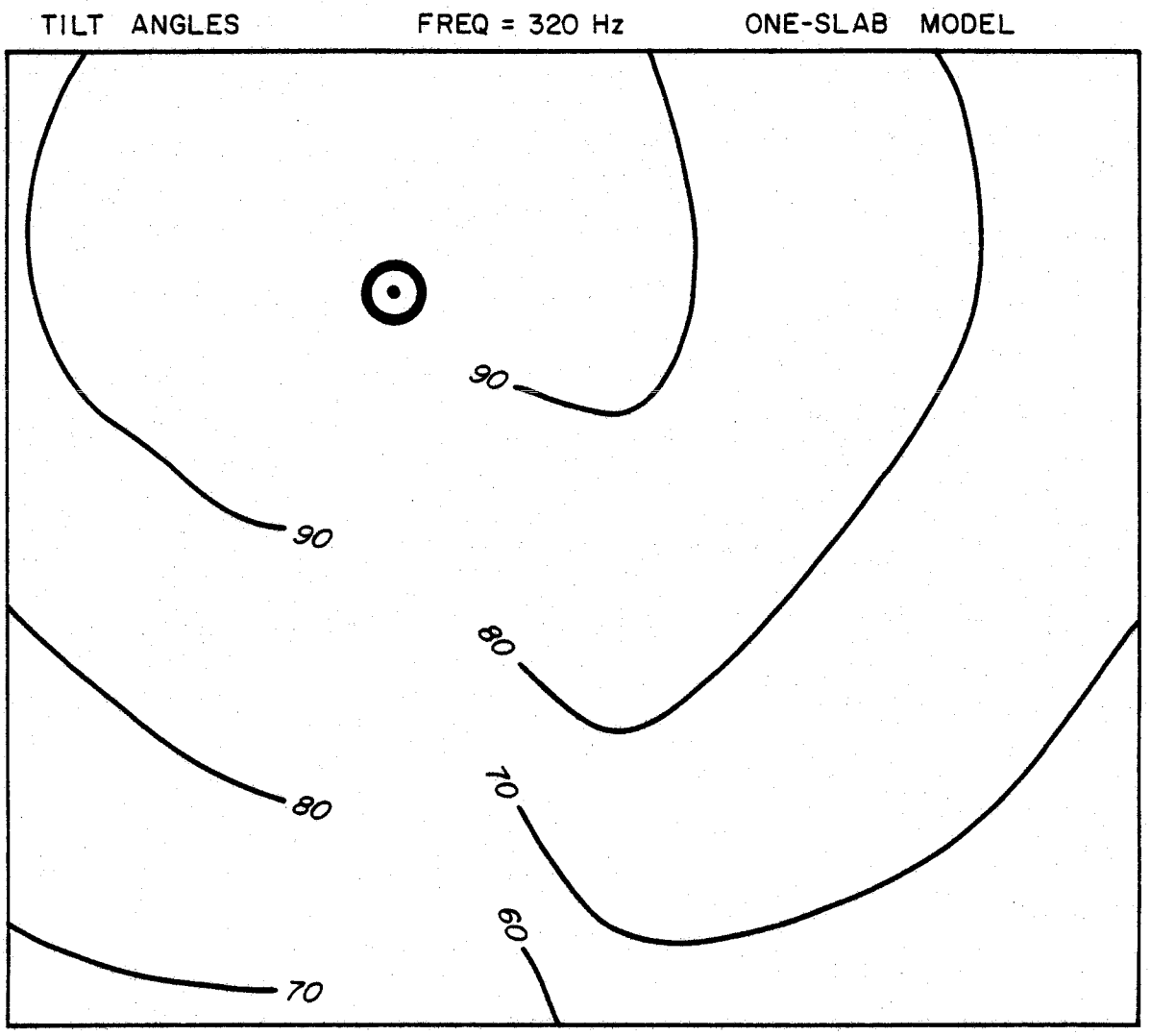

Figure 70.

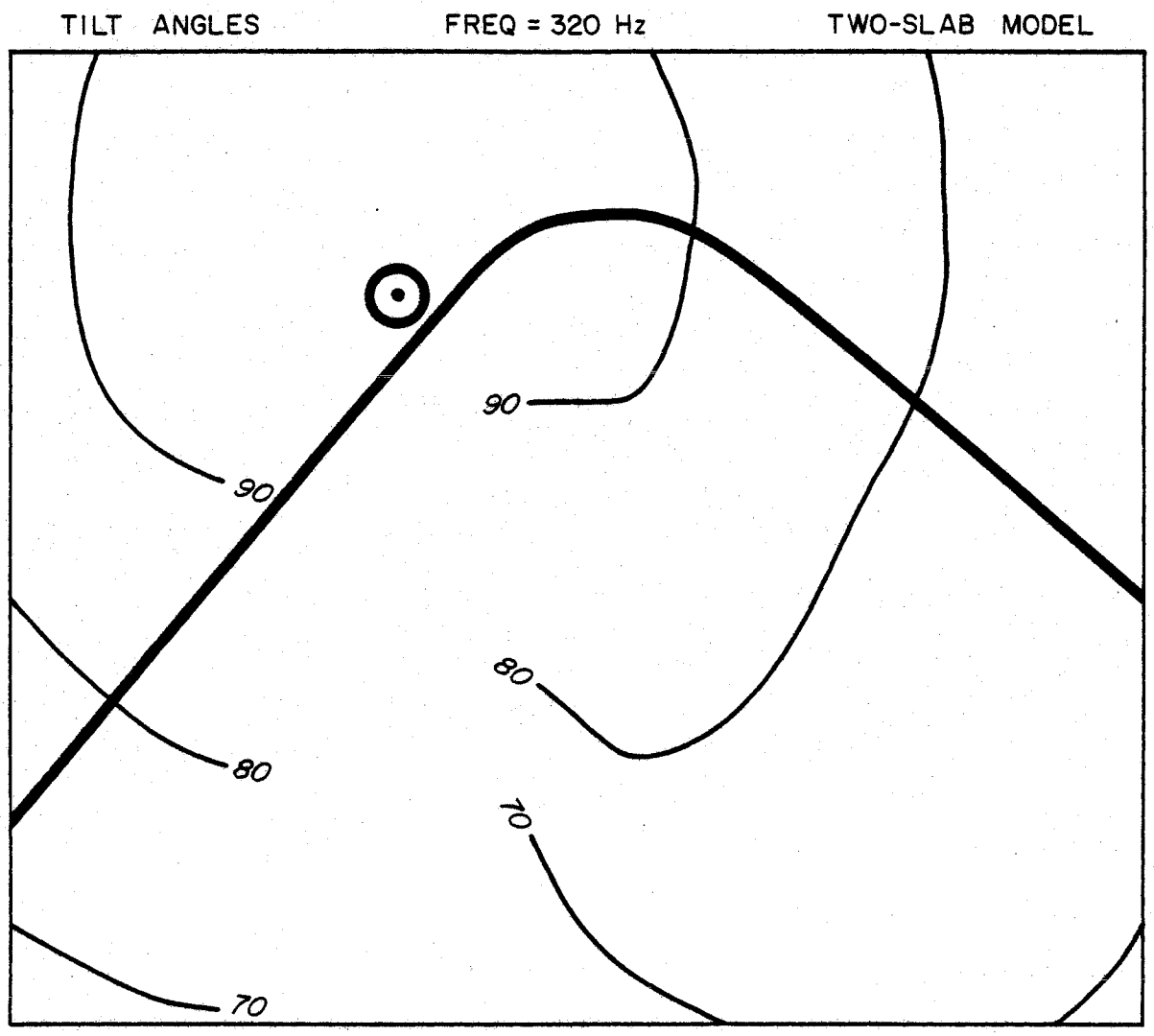

Figure 71.

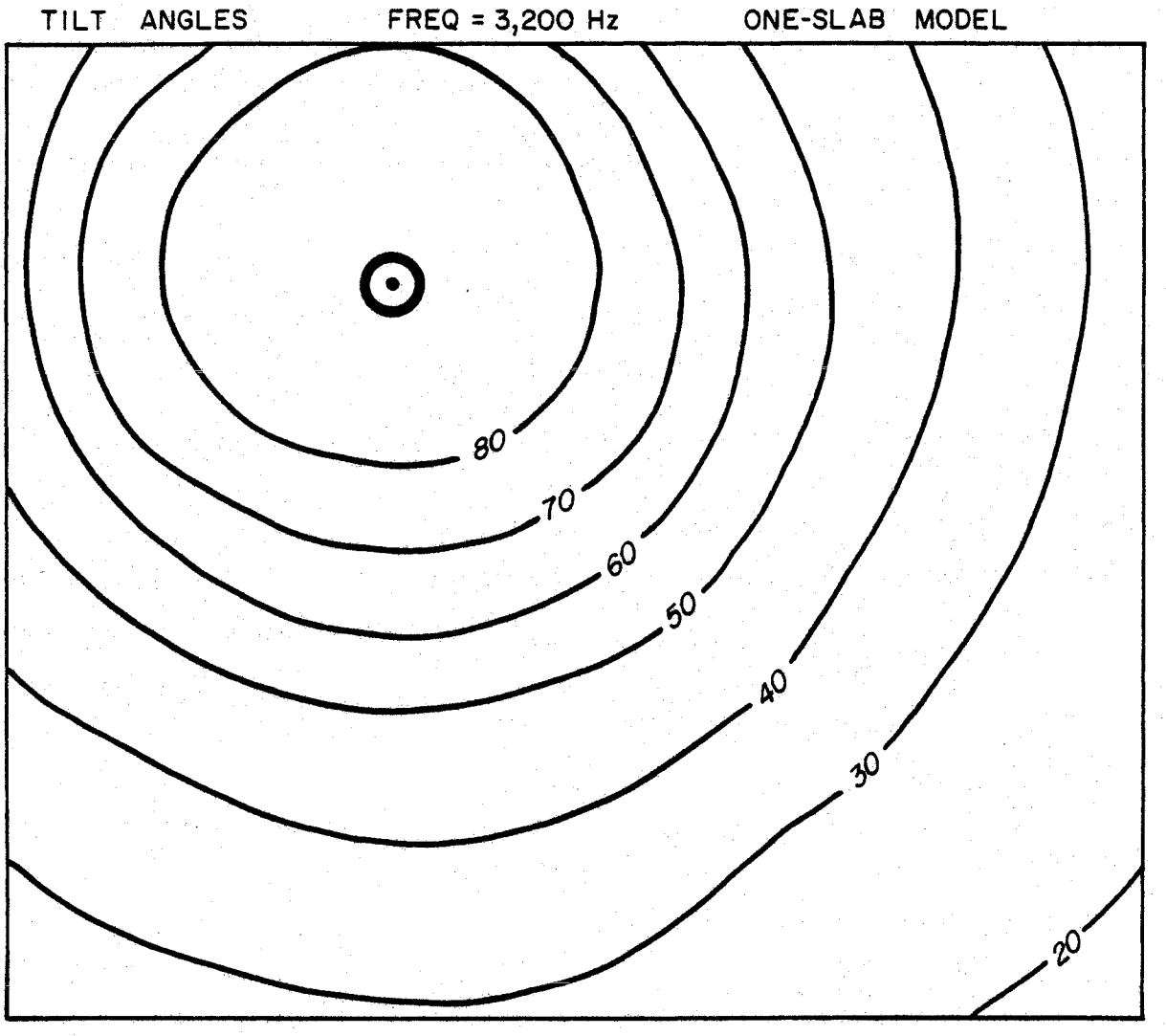

Figure 72.

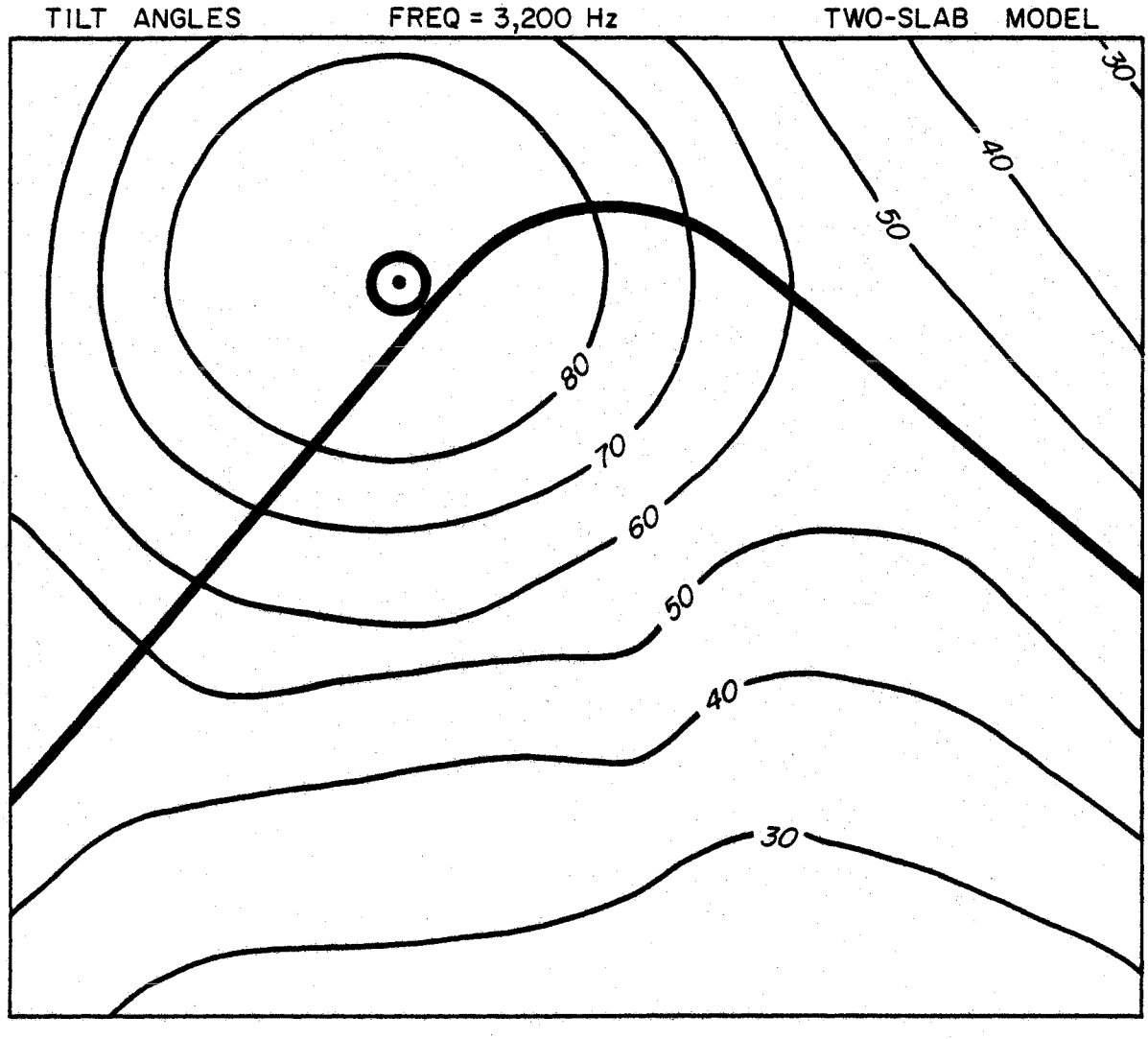
TILT ANGLES
FREQ = 3,200 Hz
TWO-SLAB MODEL
30
40
50
80
70
60
50
40
30

Figure 73.

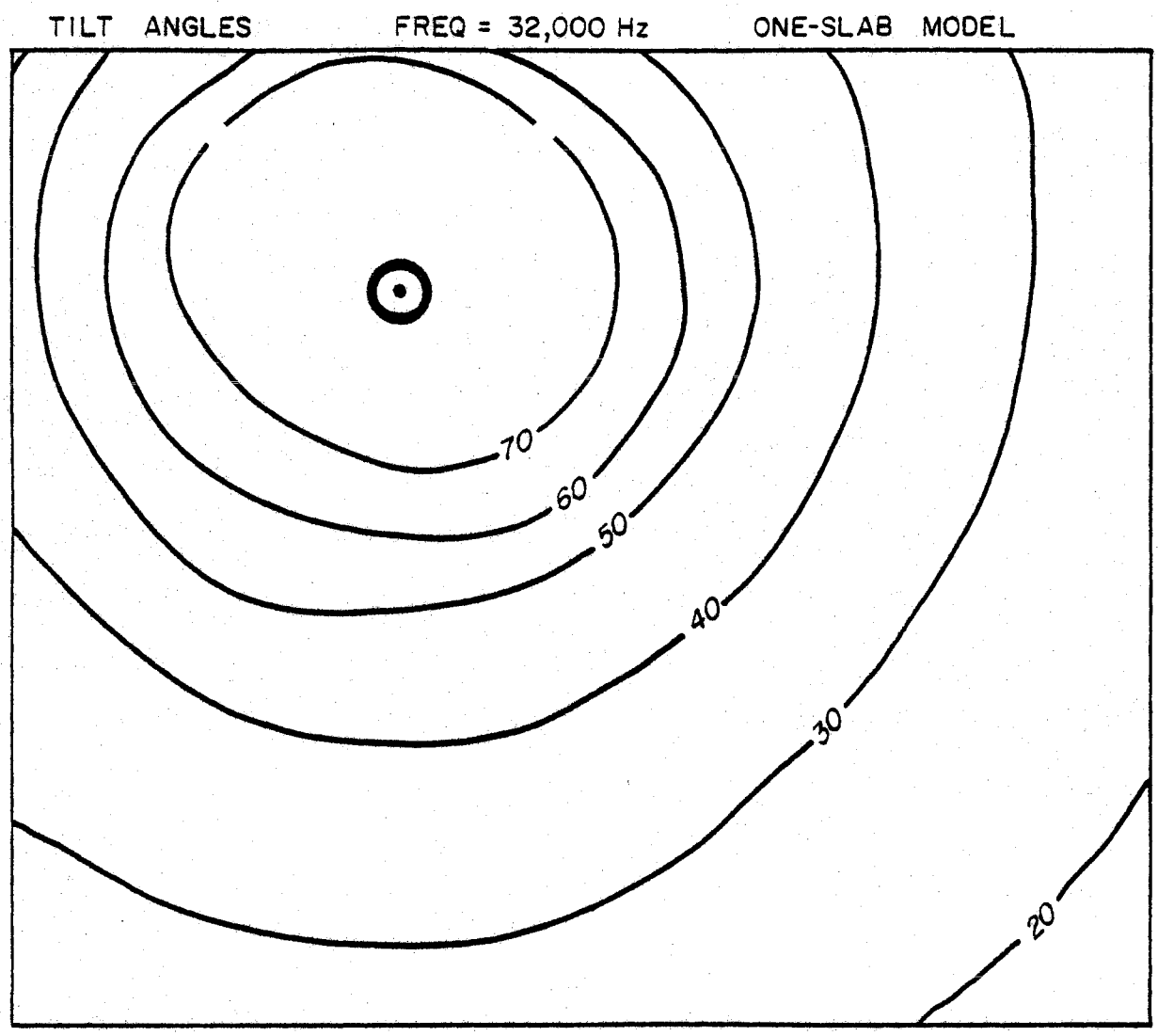

Figure 74.

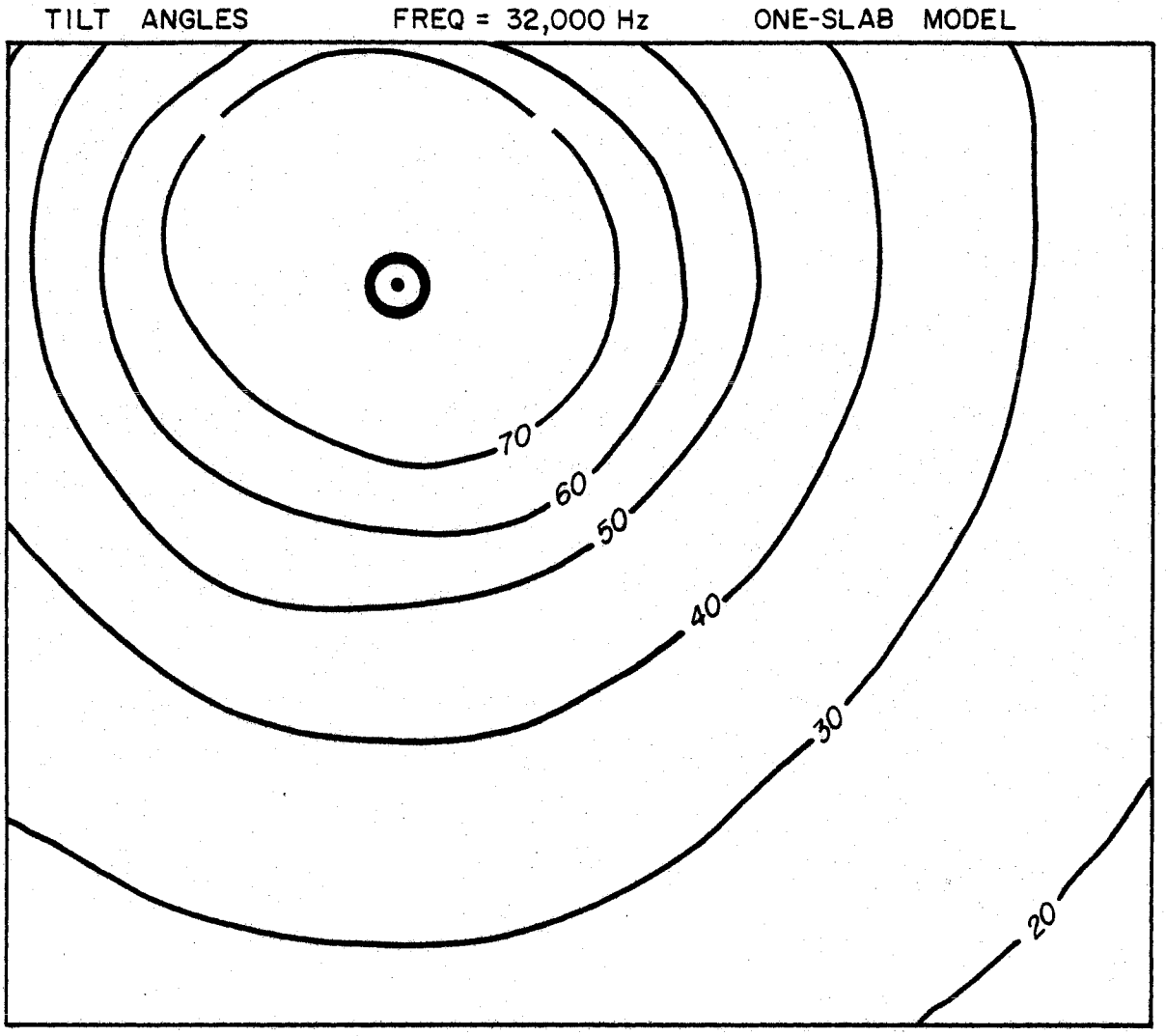

Figure 74.

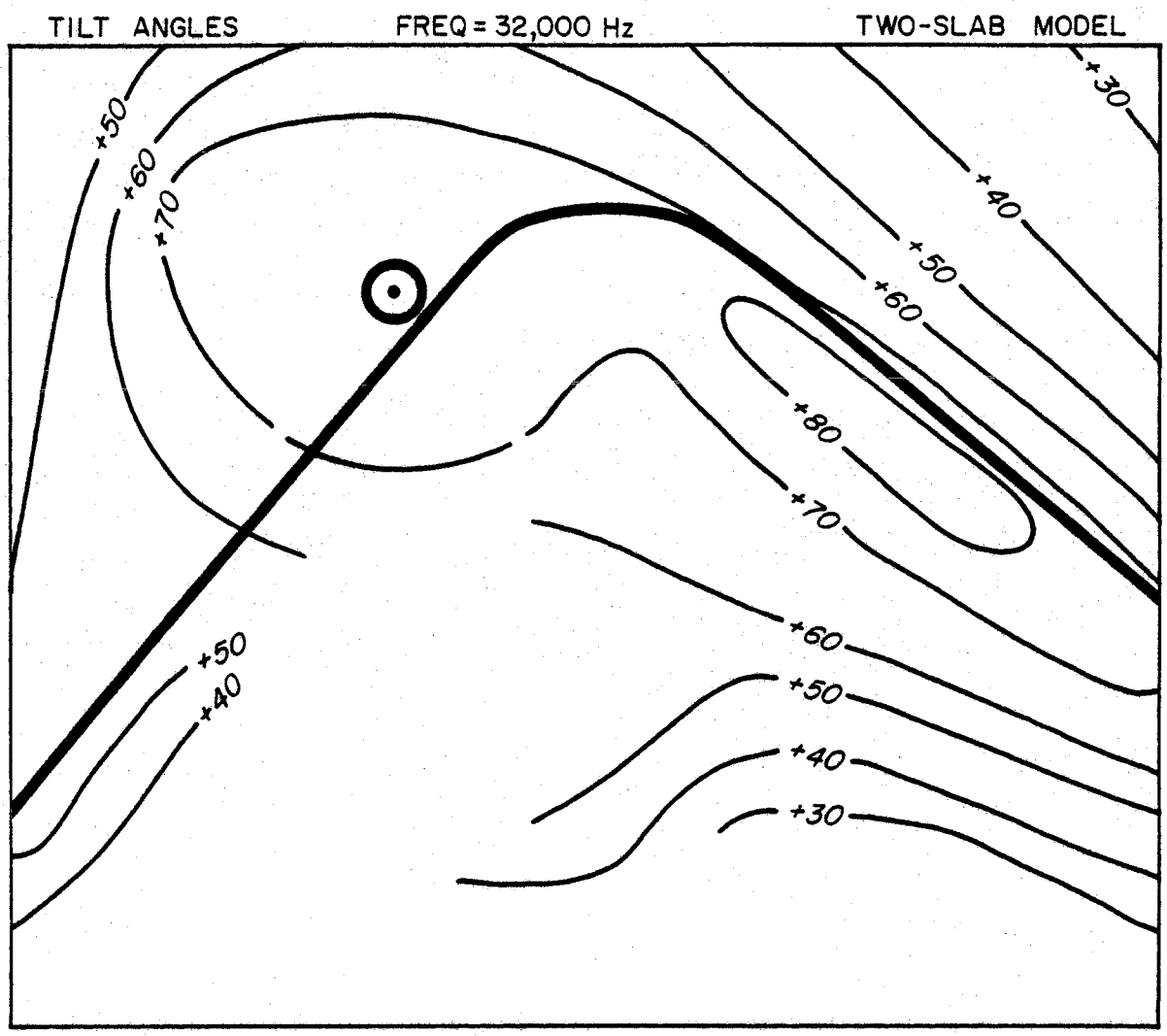
TILT ANGLES
FREQ = 32,000 Hz
TWO-SLAB MODEL
+50
+60
+70
+30
+40
+50
+60
+80
+70
+60
+50
+40
+30
+50
+40

Figure 75.

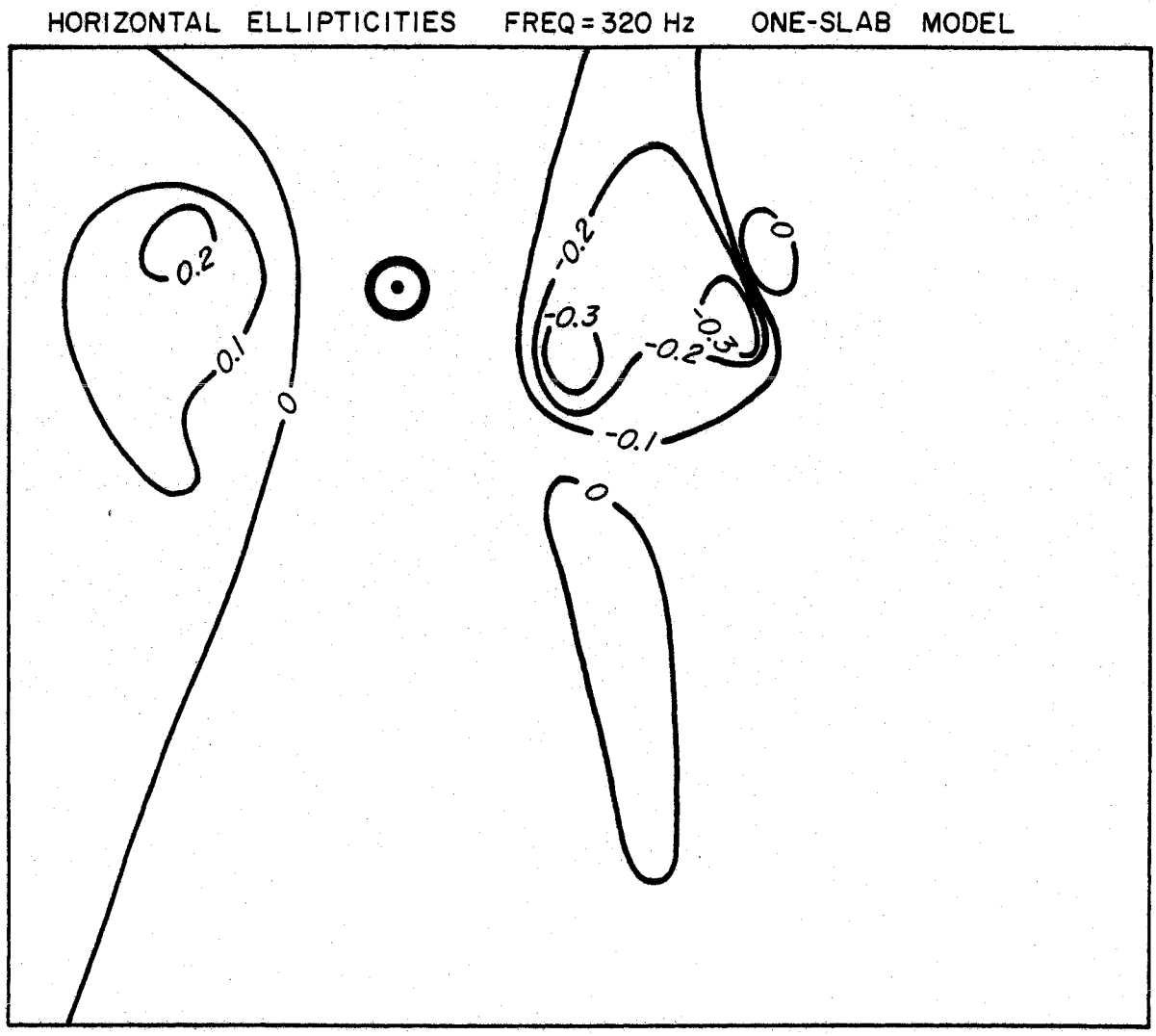
HORIZONTAL ELLIPTICITIES FREQ = 320 Hz ONE-SLAB MODEL
0.2
0.1
0
-0.2
-0.3
-0.2
-0.3
-0.1
0
0

Figure 76.

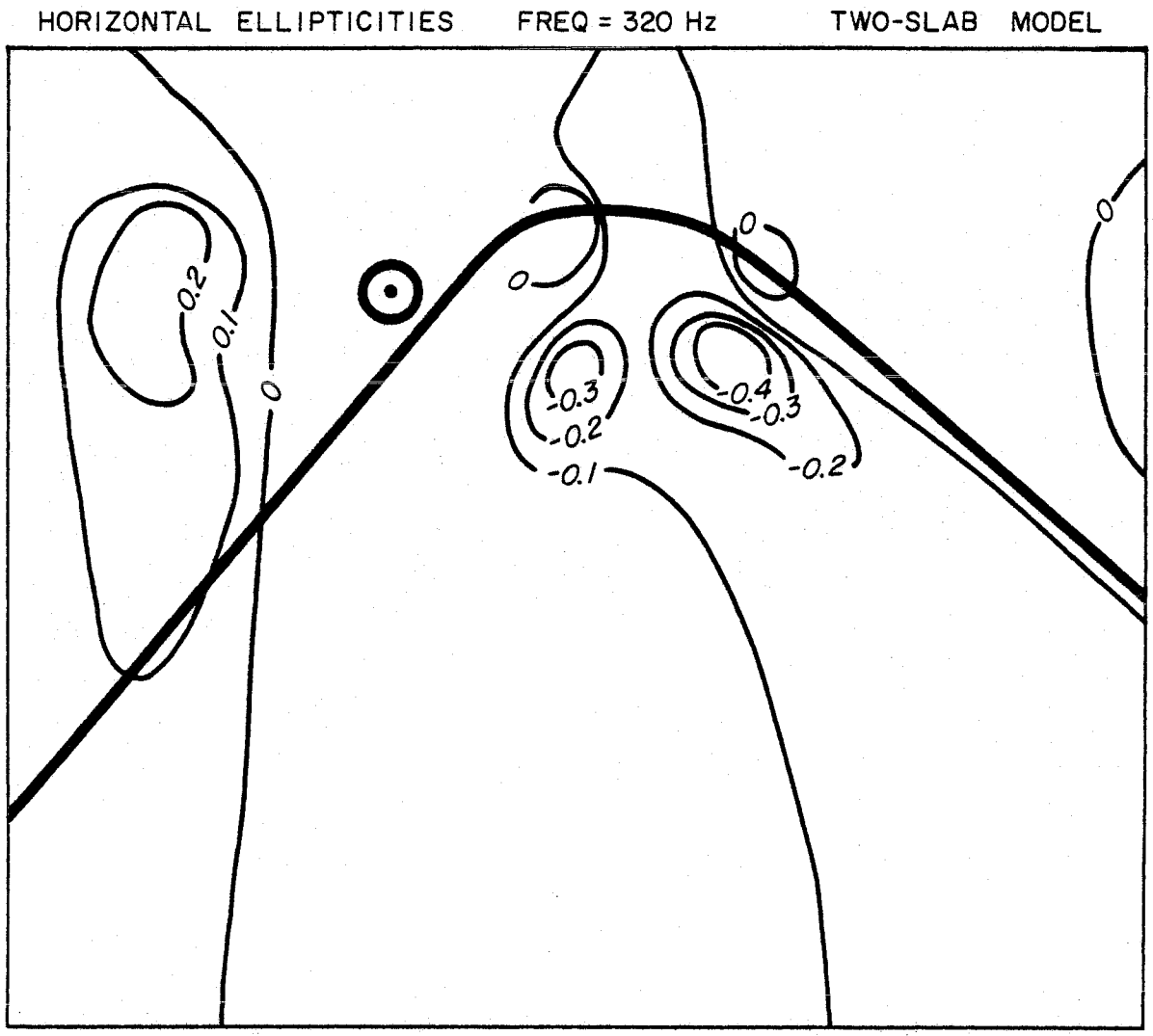
HORIZONTAL ELLIPTICITIES
FREQ = 320 Hz
TWO-SLAB MODEL
0.2
0.1
0
0
0
0
-0.3
-0.2
-0.1
-0.4
-0.3
-0.2

Figure 77.

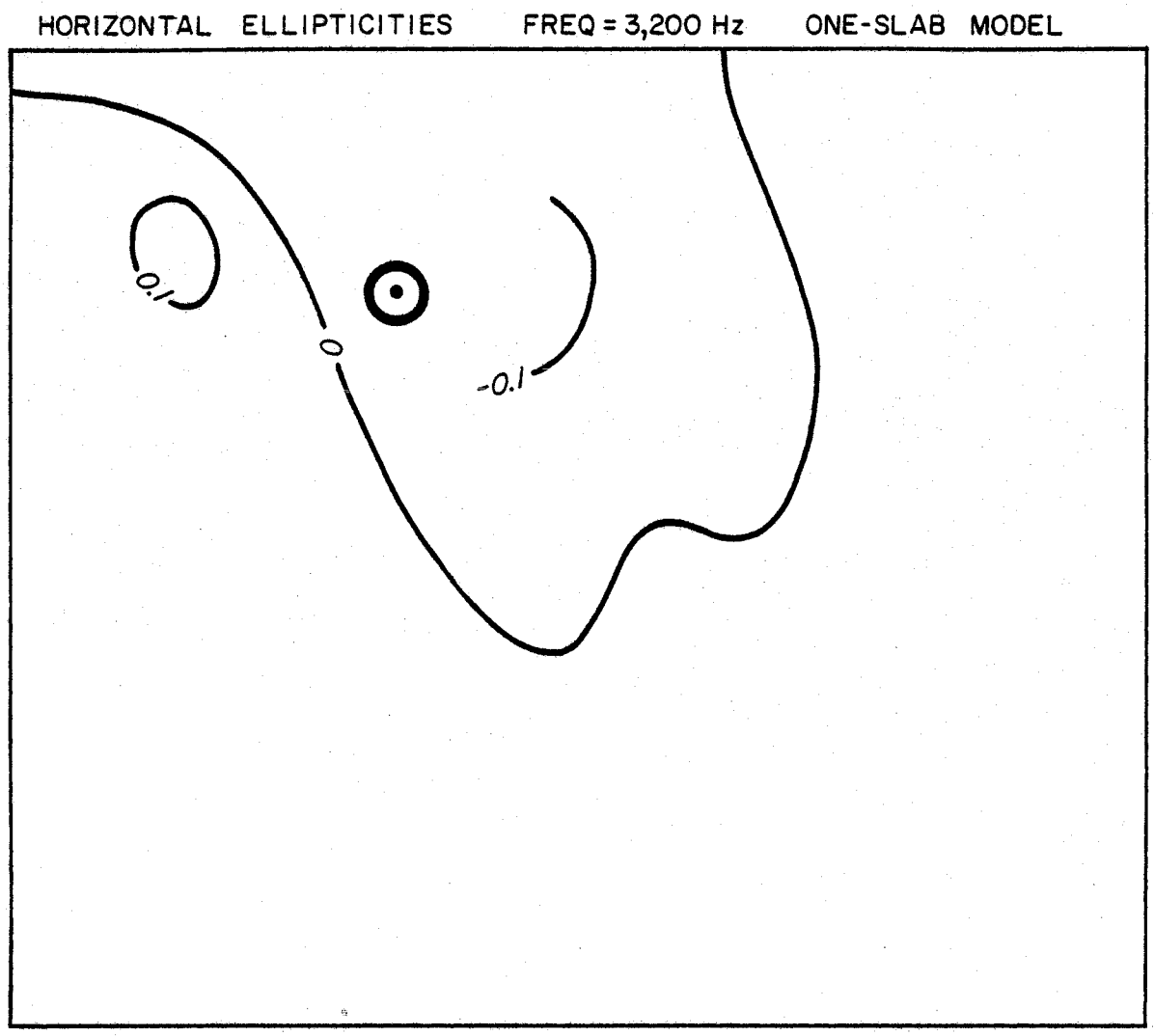
HORIZONTAL ELLIPTICITIES
FREQ = 3,200 Hz
ONE-SLAB MODEL
0.1
0
-0.1

Figure 78.

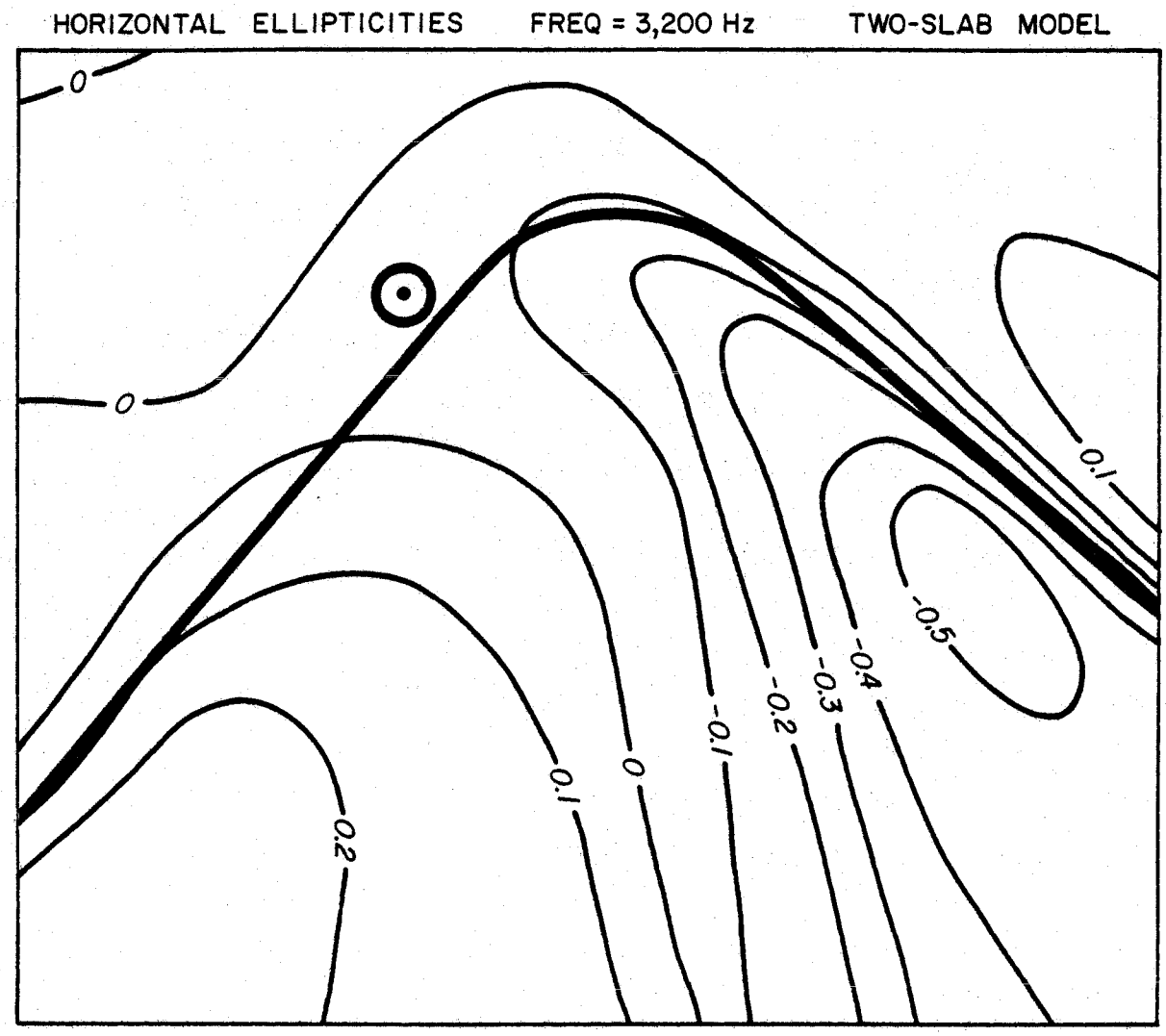
HORIZONTAL ELLIPTICITIES
FREQ = 3,200 Hz
TWO-SLAB MODEL
0
0
0.1
-0.5
-0.4
-0.3
-0.2
-0.1
0
0.1
0.2

Figure 79.

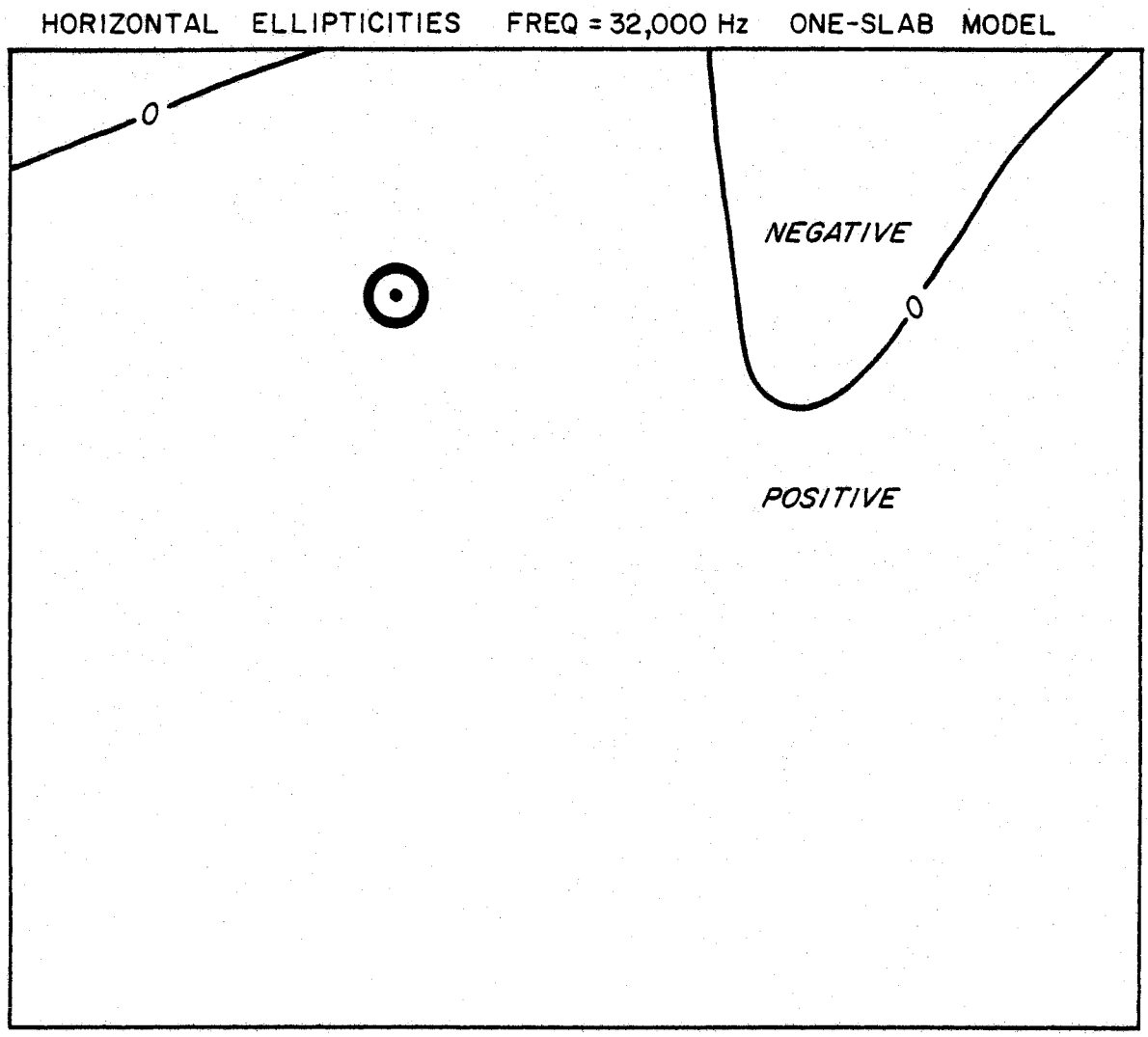
HORIZONTAL ELLIPTICITIES FREQ = 32,000 Hz ONE-SLAB MODEL
0
NEGATIVE
0
POSITIVE

Figure 80.

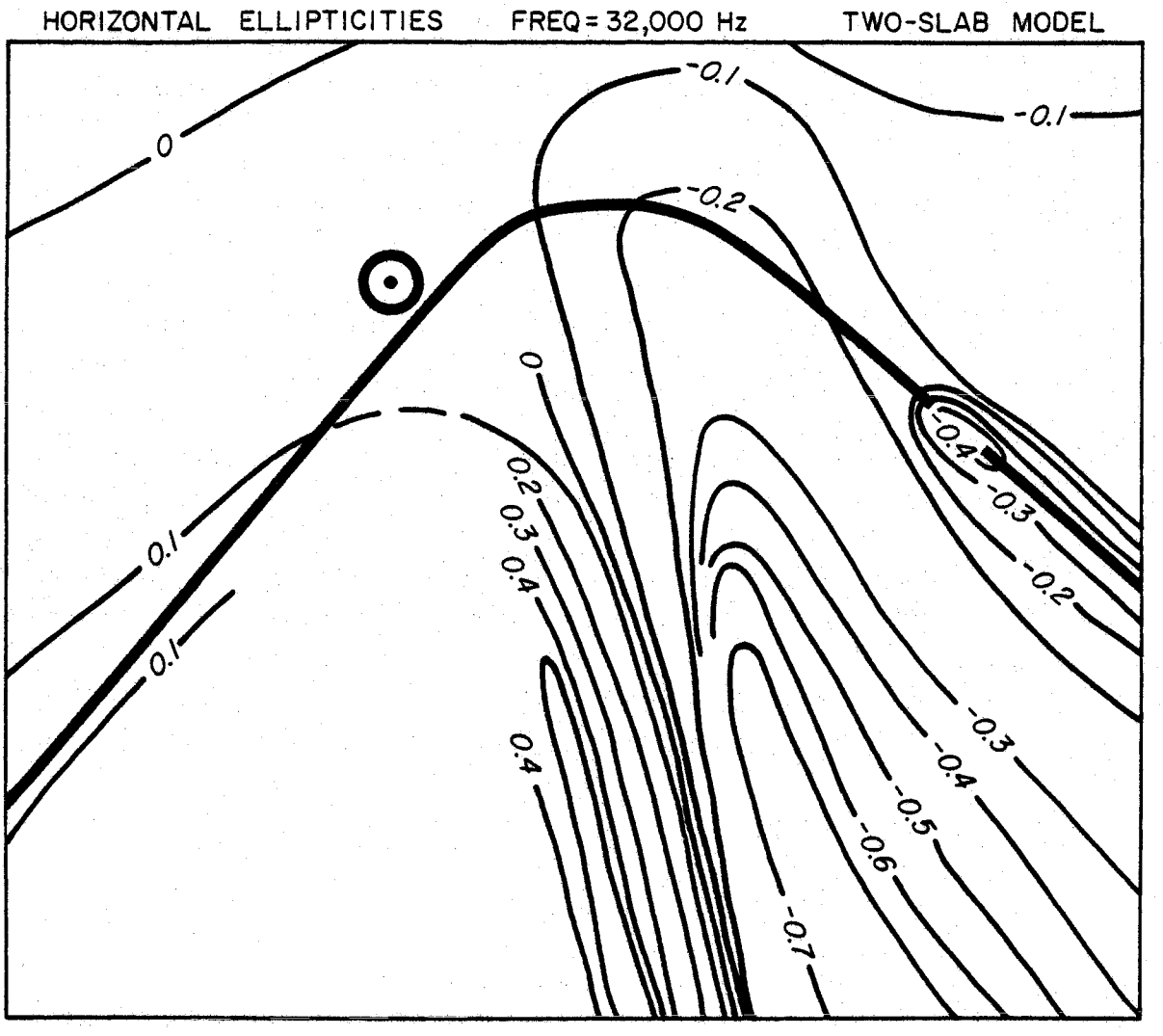
HORIZONTAL ELLIPTICITIES
FREQ = 32,000 Hz
TWO-SLAB MODEL
0
-0.1
-0.1
-0.2
0
0.2
0.3
0.4
-0.4
-0.3
-0.2
0.1
0.1
0.4
-0.3
-0.4
-0.5
-0.6
-0.7

Figure 81.

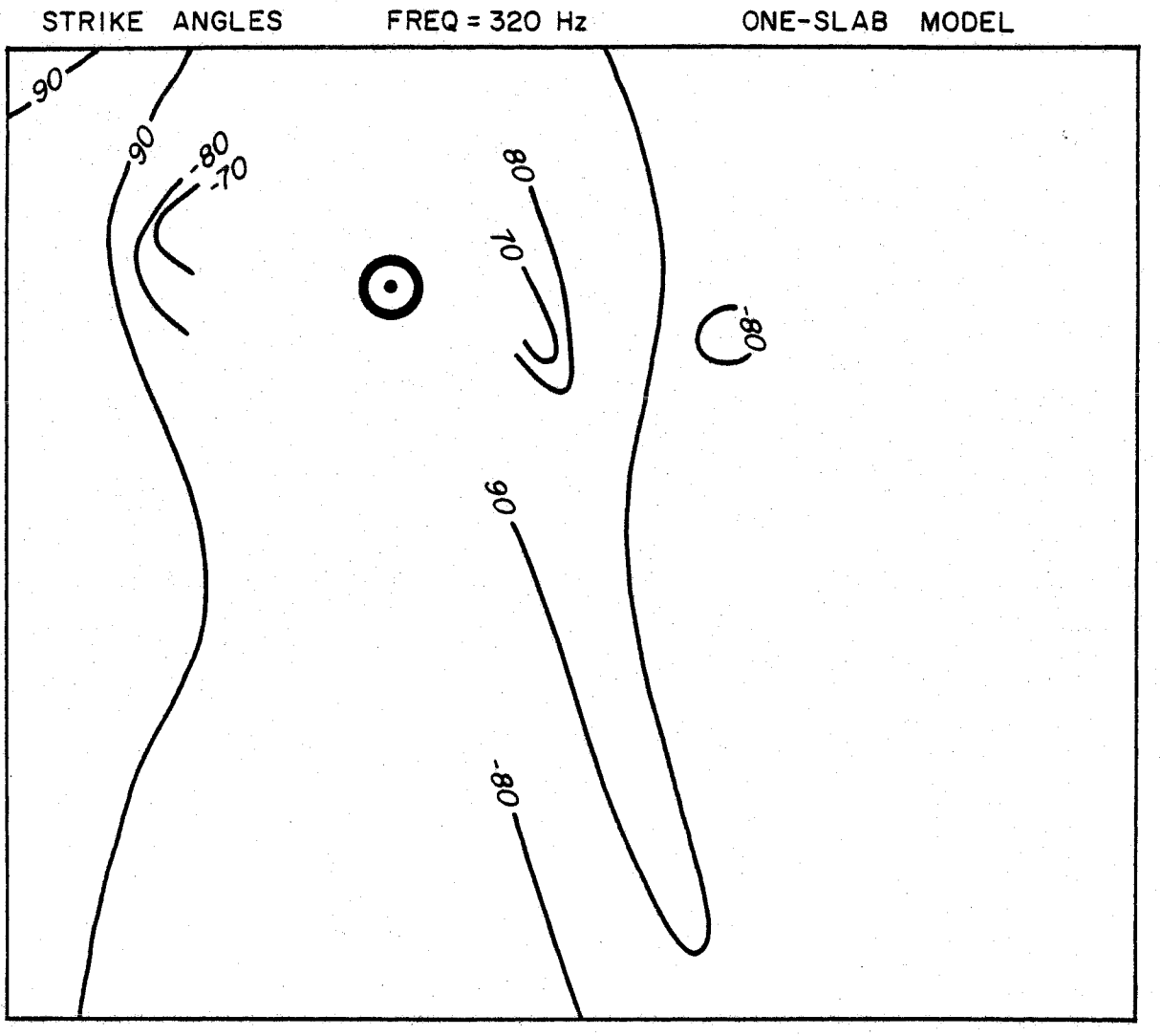
STRIKE ANGLES
FREQ = 320 Hz
ONE-SLAB MODEL
-90
-90
-80
-70
80
70
-80
90
-80

Figure 82.

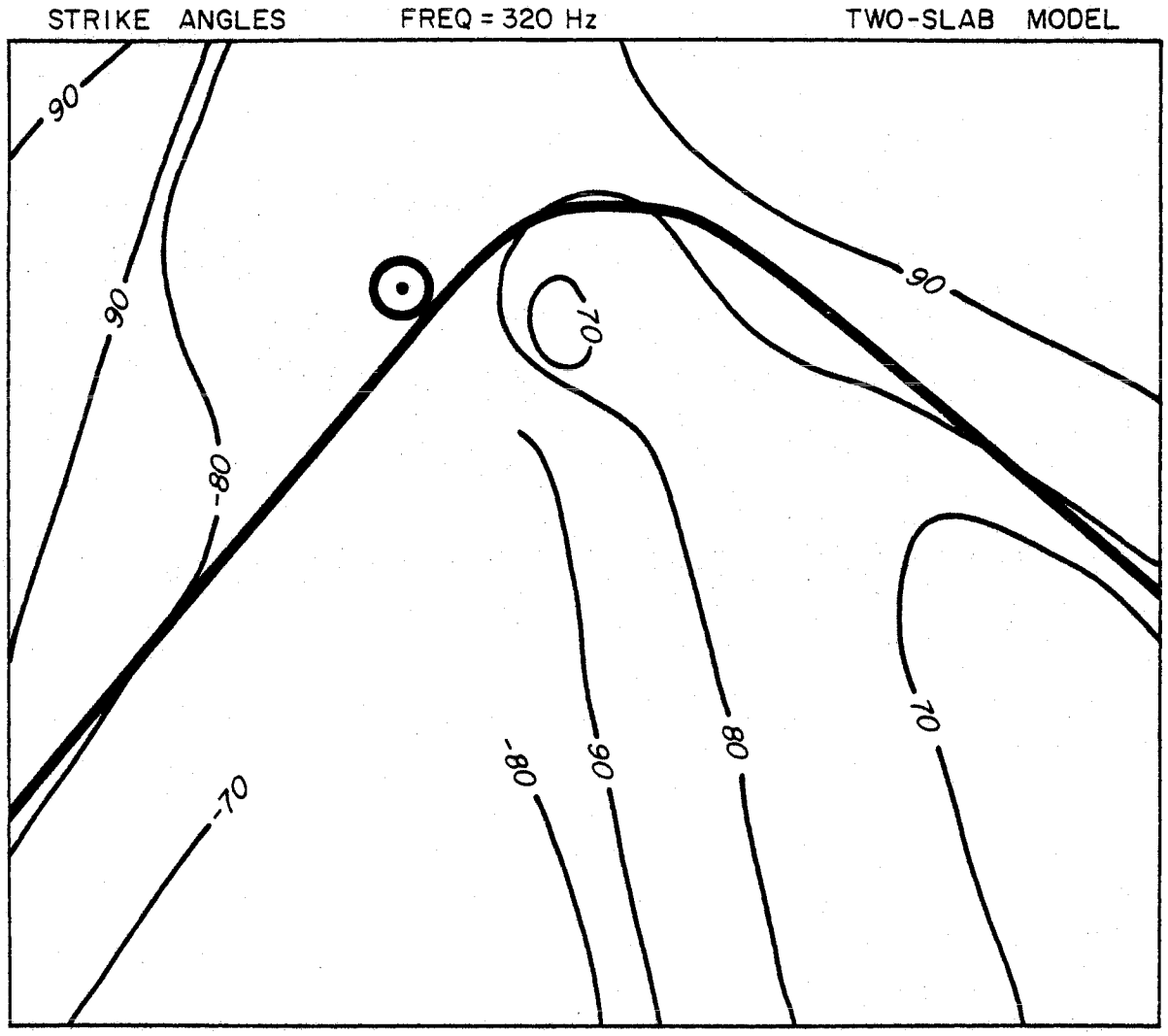
STRIKE ANGLES
FREQ = 320 Hz
TWO-SLAB MODEL
90
90
90
80
70
80
90
80
70
70

Figure 83.

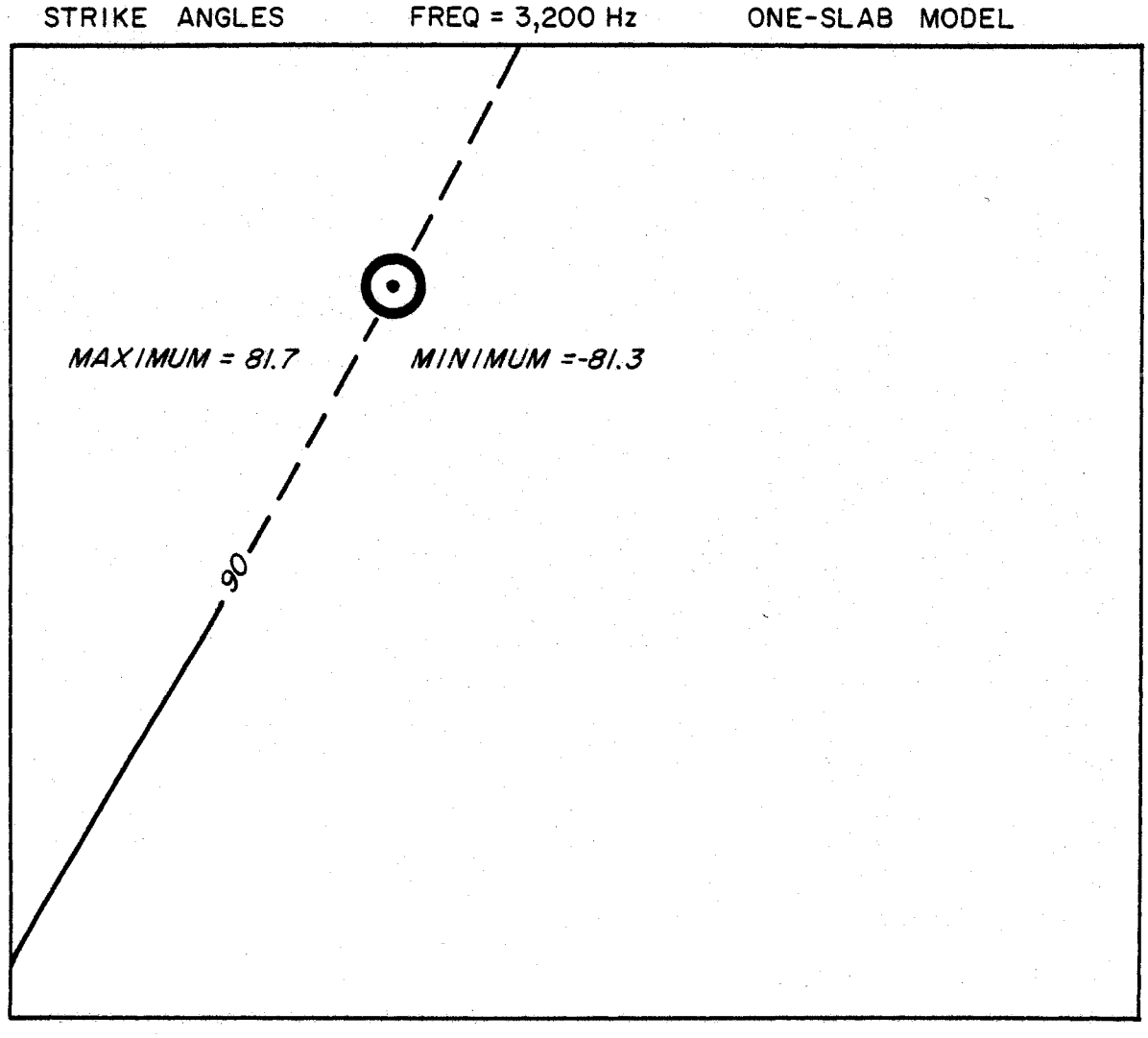
STRIKE ANGLES
FREQ = 3,200 Hz
ONE-SLAB MODEL
MAXIMUM = 81.7
MINIMUM =-81.3
90

Figure 84.

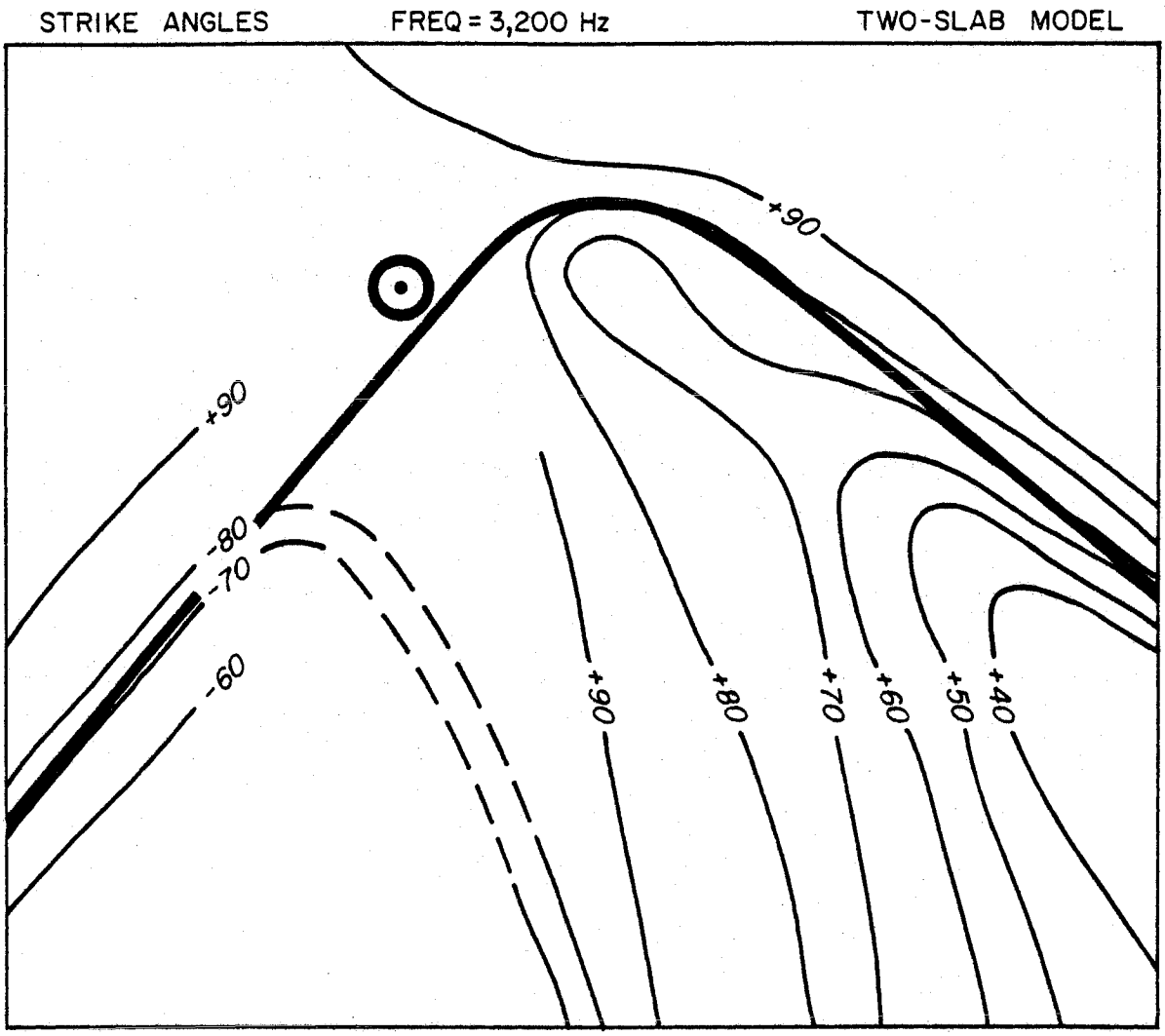
STRIKE ANGLES
FREQ = 3,200 Hz
TWO-SLAB MODEL
+90
+90
-80
-70
-60
+90
+80
+70
+60
+50
+40

Figure 85.

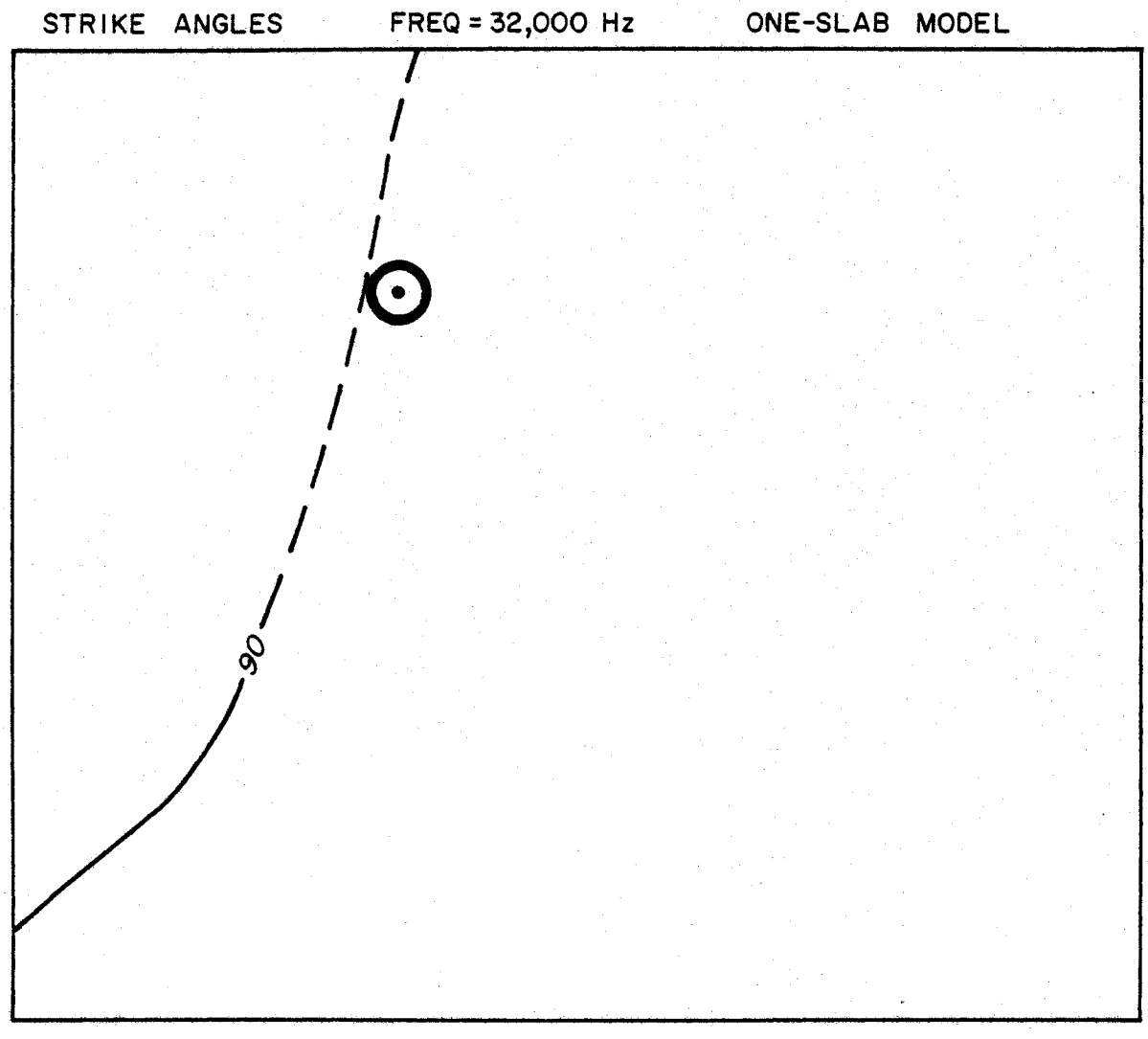

Figure 86.

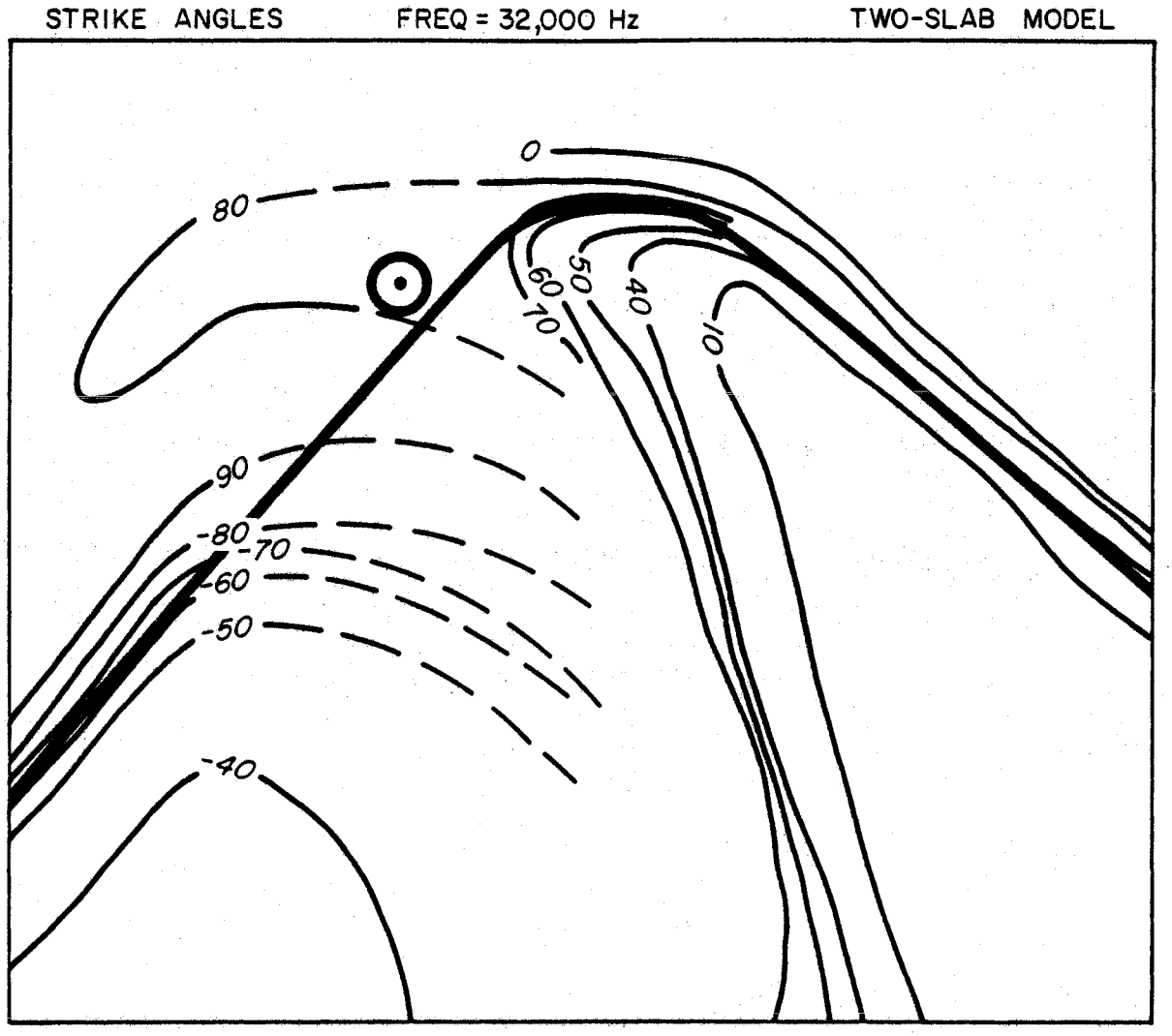
STRIKE ANGLES
FREQ = 32,000 Hz
TWO-SLAB MODEL
0
80
60
50
40
10
10
90
-80
-70
-60
-50
-40

Figure 87.

Figures 88 to 92. The following five figures present the scale model results as pseudo-phasor plots at fifteen different locations (three per figure). Each plot has two lines for the two models - one-slab (without top slab) and two-slab (with top slab). Each line has five symbols representing five different frequencies - 320, 1000, 3200, 10000, and 32000 Hz (clockwise). The map in the upper left corner of each figure shows the locations of the pseudo-phasor plots relative to the model.

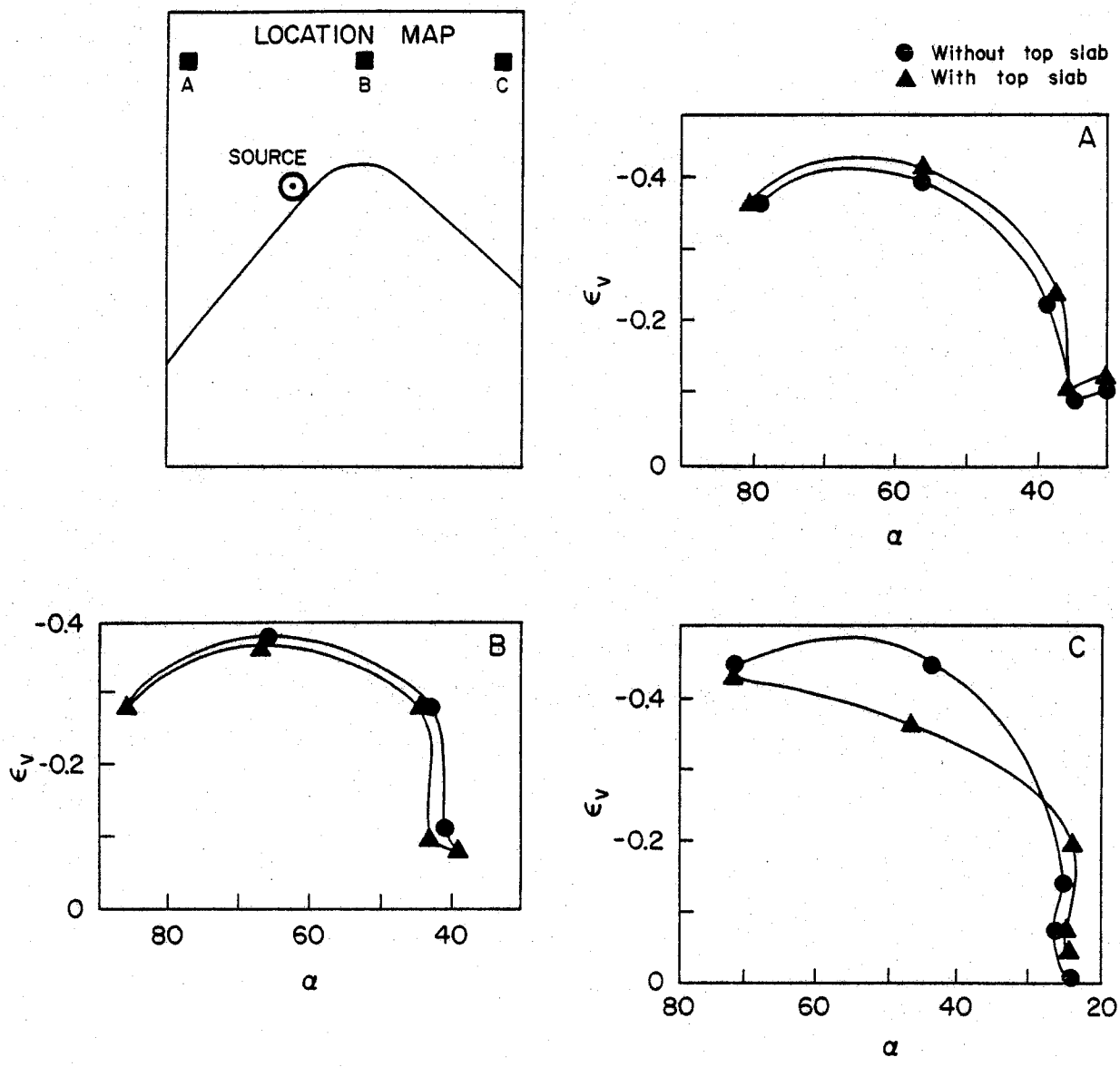
LOCATION MAP
A
B
C
SOURCE
Without top slab
With top slab
A
B
C
-0.4
-0.2
0
80
60
40
20
α
ϵ_v

Figure 88.

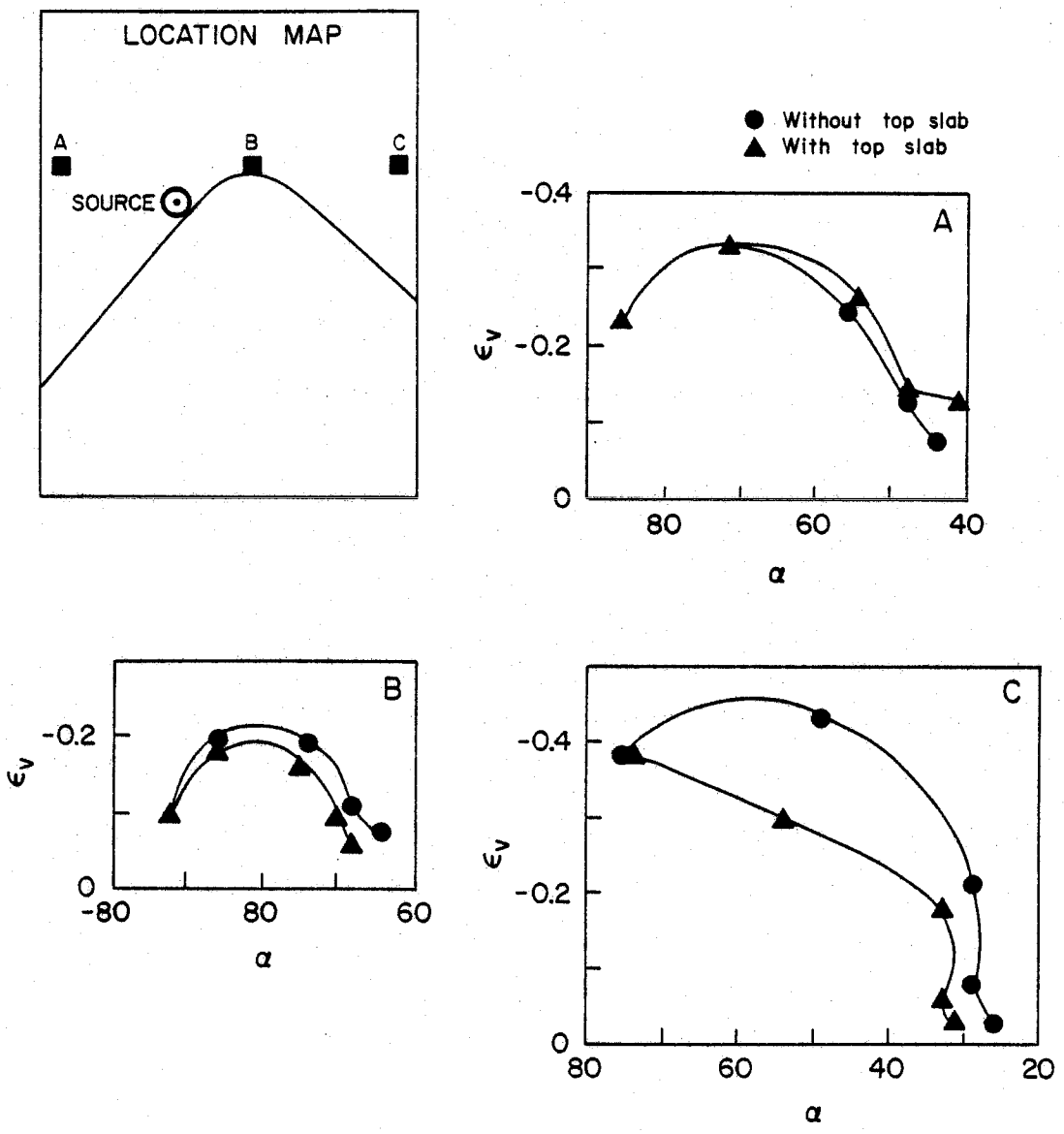
LOCATION MAP
A
B
C
SOURCE
Without top slab
With top slab
A
B
C
ϵ_v
α
-0.4
-0.2
0
80
60
40
-80
20

Figure 89.

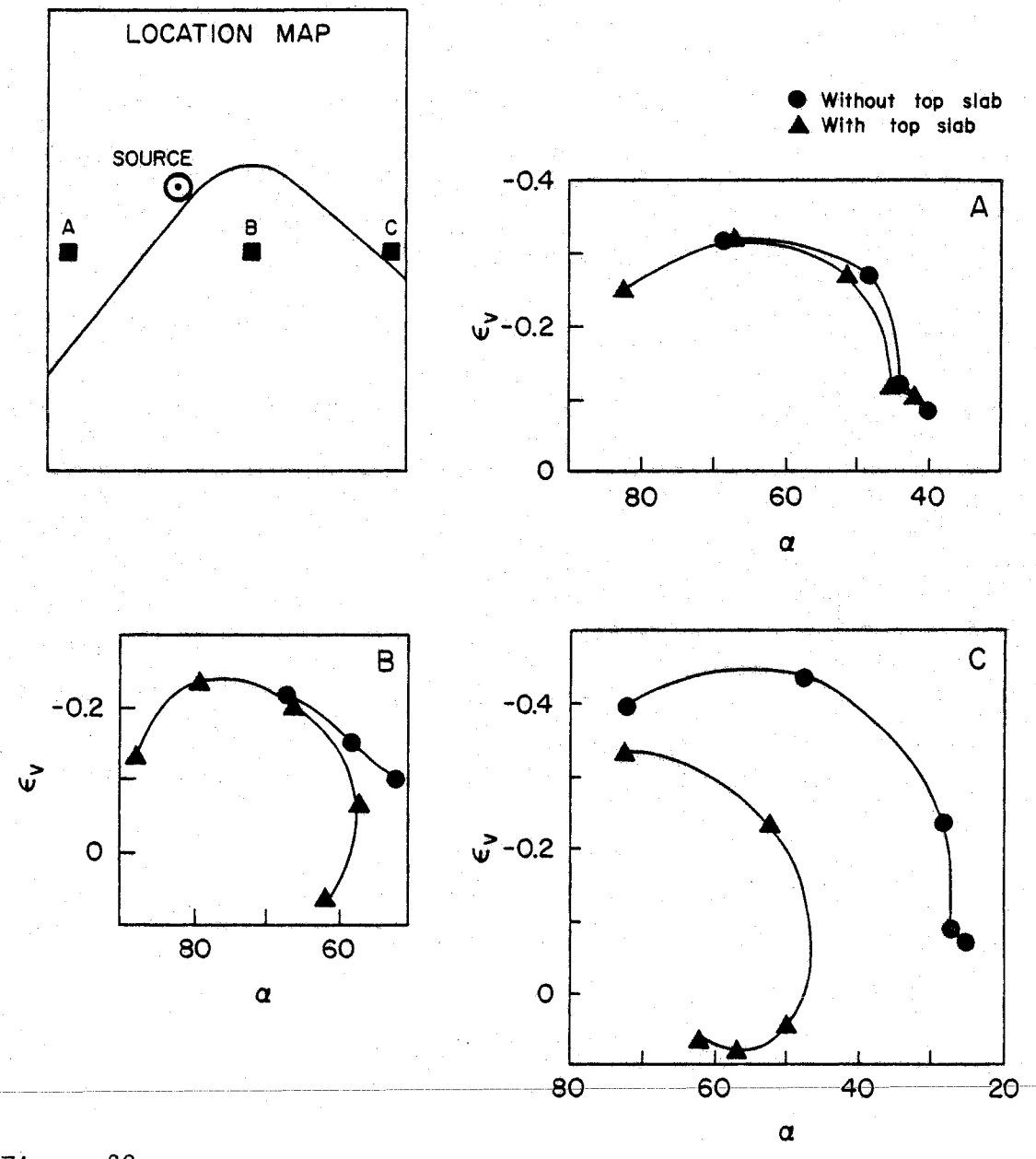
LOCATION MAP
SOURCE
A
B
C
Without top slab
With top slab
A
B
C
ϵ_v
-0.4
-0.2
0
80
60
40
20
α

Figure 90.

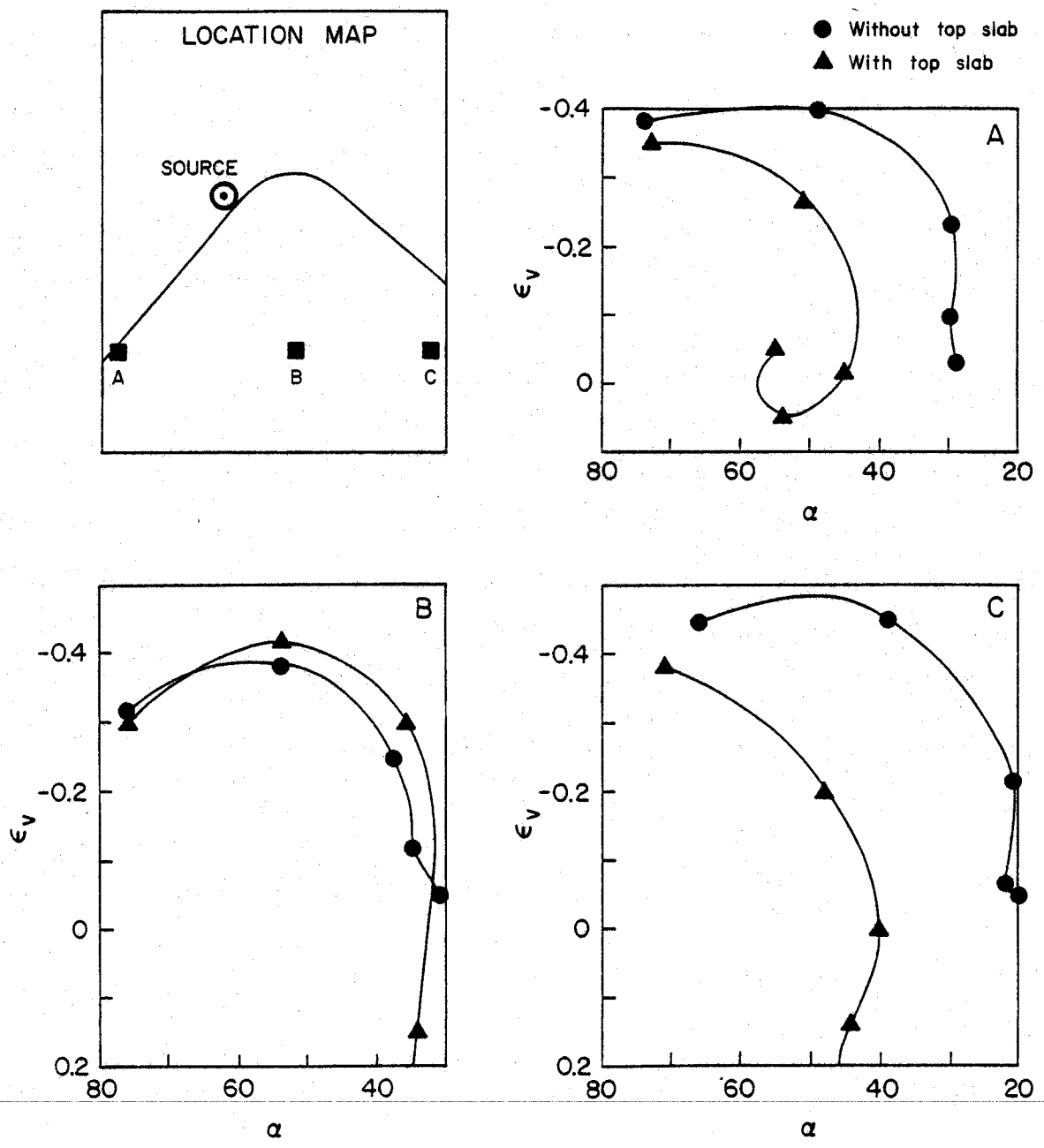
LOCATION MAP
SOURCE
A
B
C
Without top slab
With top slab
A
B
C
-0.4
-0.2
0
0.2
80
60
40
20
α
ϵ_v

Figure 91.

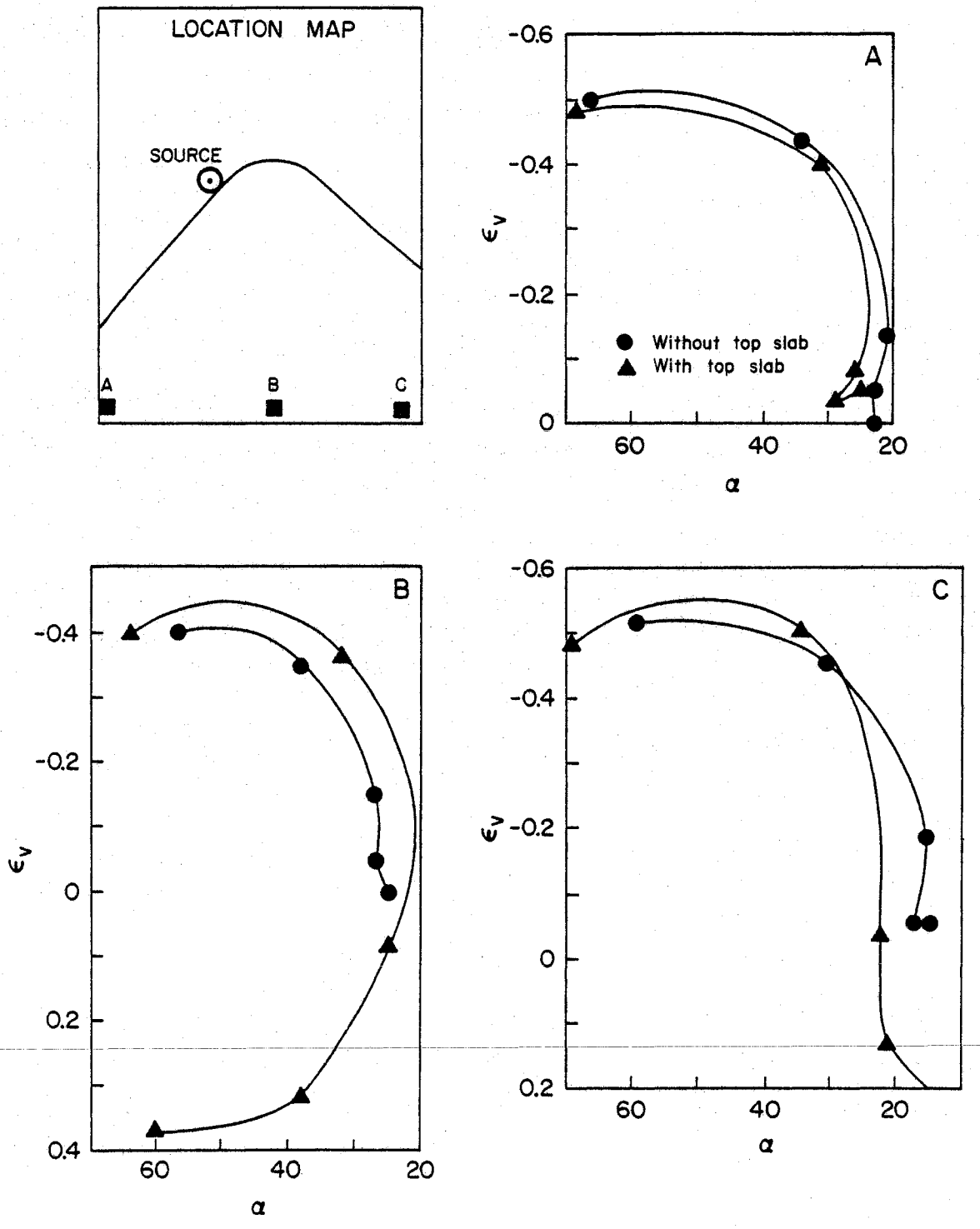
LOCATION MAP
SOURCE
A
B
C
-0.6
-0.4
-0.2
0
ϵ_v
Without top slab
With top slab
60
40
20
α
0.2
0.4

Figure 92.

REFERENCES

Abramowitz, M. and Stegun, I.A. (ed.), 1970, Handbook of Mathematical Functions: Dover Publications, Inc., New York, 1046 p.

Anderson, W.L., 1977, Interpretation of electromagnetic soundings in the Raft River geothermal area, Idaho: U.S. Geological Survey Open-File Report 77-557, 21 p.

----------, 1978, Interpretation of electromagnetic extra-low-frequency soundings in the Randsburg, California, known geothermal resource area: U.S. Geological Survey Open-File Report 78-562, 22 p.

----------, 1979a, Numerical integration of related Hankel transforms of orders 0 and 1 by adaptive digital filtering: Geophysics, v. 44, p. 1287-1305.

----------, 1979b, Program MARQLOOPS: Marquardt inversion of loop-loop frequency soundings: U.S. Geological Survey Open-File Report 79-240, 75 p.

----------, 1979c, Program IMSLPQ: Marquardt inversion of plane-wave frequency soundings: U.S. Geological Survey Open-File Report 79-586, 37 p.

Brown, K.M. and Dennis, J.E., 1972, Derivative-free analogues of the Levenburg-Marquardt and Gauss algorithms for nonlinear least squares approximations: Numerische Mathematik, v. 18, p. 289-297.

Connerney, J.E.P., Nekut, T. and Kuckes, A.F., 1980, Deep crustal electrical conductivity in the Adirondacks: J. Geophys. Res., v. 85, p. 2603-2614.

Cooke, J., Bradley, J., Mitchell, C. and Lescelius, R., 1981, A description of an extremely low-frequency loop-loop geophysical system: U.S. Geological Survey Open-File Report 81-1130, 64 p.

Crosson, R.S. and Koyanagi, R.Y., 1979, Seismic velocity structure below the island of Hawaii from local earthquake data: J. Geophys. Res., v. 84, p. 2331-2342.

Daniels, J.J., Keller, G.V. and Jacobson, J.J., 1976, Computer-assisted interpretation of electromagnetic soundings over a permafrost section: Geophysics, v. 41, p. 752-765.

Dey, A. and Ward, S.H., 1970, Inductive sounding of a layered earth with a horizontal magnetic dipole: Geophysics, v. 35, p. 660-703.

Ellsworth, W.L. and Koyanagi, R.Y., 1977, Three-dimensional crust and mantle structure of Kilauea volcano, Hawaii: J. Geophys. Res., v. 82, p. 5379-5394.

Fiske, R.S. and Kinoshita, W.T., 1969, Inflation of Kilauea volcano prior to its 1967-1968 eruption: Science, v, 165, p. 341-349.

Frischknecht, F.C., 1967, Fields about an oscillating magnetic dipole over a two-layer earth and application to ground and airborne electromagnetic surveys: Q. Colo. Schl. of Mines, v. 72, no. 1, 81 p.

----------, 1971, Electromagnetic scale modeling: in Electromagnetic Probing in Geophysics, Wait, J.R. (ed.), The Golem Press, Boulder, Colo., p. 265-320.

Glenn, W.E. and Ward, S.H., 1976, Statistical evaluation of electrical sounding methods, Part I -- experiment design: Geophysics, v. 41, p. 1207-1221.

Glenn, W.E., Ryu, J., Ward, S.H., Peeples, W.J. and Phillips, R.J., 1973, The inversion of vertical magnetic dipole sounding data: Geophysics, v. 38, p. 1109-1129.

Huber, R.D. and Adams, W.M., 1971, Density logs from underground gravity surveys in Hawaii: Water Resources Research Center (Univ. of Hawaii) Technical Report No. 45, 39 p.

IMSL (International Mathematical and Statistical Libraries), 1979, IMSL Library Reference Manual: available from IMSL, 7500 Bellaire Blvd., 6th Flr., GNB Bldg., Houston, TX 77036, 3 vol.

Inman, J.R., 1975, Resistivity inversion with ridge regression: Geophysics, v. 40, p. 798-817.

Jackson, D.B. and Keller, G.V., 1972, An electromagnetic sounding survey of the summit of Kilauea volcano, Hawaii: J. Geophys. Res., v. 77, p. 4957-4965.

Jain, B.K., 1978, A low frequency electromagnetic prospecting system: Lawrence Berkeley Labs Technical Report LBL-7042, 128 p.

Johnson, G.R., 1980, Porosity and density of Kilauea volcano basalts: U.S. Geological Survey Prof. Paper 1123B, 6 p.

Kauahikaua, J., 1978, Electromagnetic fields about a horizontal electric wire source of arbitrary length: Geophysics, v. 43, p. 1019-1022.

Kauahikaua, J., 1981, Interpretation of time-domain electromagnetic soundings in the Calico Hills area, Nevada test site, Nye County, Nevada: U.S. Geological Survey Open-File Report 81-988, 30 p.

----------, 1982a, Program MQLV_BIGLOOP: automatic inversion of horizontal loop controlled-source electromagnetic sounding data: U.S. Geological Survey Open-File Report (in preparation).

----------, 1982b, Complete data listings for CSEM soundings on Kilauea volcano, Hawaii: U.S. Geological Survey Open-File Report (in preparation).

Kauahikaua, J. and Klein, D.P., 1977, Electromagnetic induction sounding measurements in the Puna district, Hawaii: in Geoelectric Studies on the East Rift, Kilauea Volcano, Hawaii Island: Hawaii Institute of Geophysics Technical Report HIG-77-15, p. 91-120.

Keller, G.V., 1974, Drilling at the summit of Kilauea volcano: report prepared for the National Science Foundation, 45 p.

Keller, G.V. and Frischknecht, F.C., 1966, Electrical Methods in Geophysical Prospecting: Pergamon Press, Oxford, 517 p.

Keller, G.V., Furgeson, R., Lee, C.Y., Harthill, N. and Jacobson, J.J., 1975, The dipole mapping method: Geophysics, v. 40, p. 451-472.

Keller, G.V. and Rapolla, A., 1976, A comparison of two electrical probing techniques: IEEE Trans. on Geoscience Electronics, v. GE-14, p. 250-256.

Keller, G.V., Skokan, C.K., Skokan, J.J. and Daniels, J., 1977, Electrical resistivity and time-domain electromagnetic surveys of the Puna and Ka'u districts, Hawaii County, Hawaii: Geoelectric Studies on the East Rift, Kilauea Volcano, Hawaii Island: Hawaii Institute of Geophysics Technical Report HIG-77-15, p. 1-90.

Keller, G.V., Grose, L.T., Murray, J.C. and Skokan, C.K., 1979, Results of an experimental drill hole at the summit of Kilauea volcano, Hawaii: J. Volc. Geoth. Res., v. 5, p. 345-385.

Kinoshita, W.T., Krivoy, H.L., Mabey, D.R. and Macdonald, R.R., 1963, Gravity survey of the island of Hawaii: U.S. Geological Survey Prof. Paper 475 C, p. C114-C116.

Koyanagi, R.Y., Unger, J.D., Endo, E.T. and Okamura, A.T., 1976, Shallow earthquakes associated with inflation episodes at the summit of Kilauea volcano, Hawaii: in Proc. of Symp. on Andean and Antarctic Volcanology Problems, Ferran, O.G. (ed.), IAVCEI Spec. Series, p. 621-631.

Lorrain, P. and Corson, D.R., 1970, Electromagnetic Fields and Waves: W.H. Freeman & Co., San Francisco, 706 p.

Manghnani, M.H. and Woollard, G.P., 1968, Elastic wave velocities in Hawaiian rocks at pressures to ten kilobars: in The Crust and Upper Mantle of the Pacific Area, AGU Monograph No. 12, p. 501-516.

McMurtry, G.M., Pan, P.-F. and Coplen, T.B., 1977, Chemical and isotopic investigations of groundwater in potential geothermal areas in Hawaii: Am. J. Sci., v. 277, p. 438-458.

Moore, J.G., 1965, Petrology of deep-sea basalt near Hawaii: Am. J. Sci., v. 263, p. 40-52.

Morrison, H.F., Goldstein, N.E., Hoverstein, M., Oppliger, G. and Riveros, C., 1978, Description, field test and data analysis of a controlled-source EM system (EM-60): Lawrence Berkeley Labs Technical Report LBL-7088, 150 p.

Morrison, F., Phillips, R.J. and O'Brien, D.P., 1969, Quantitative interpretation of transient electromagnetic fields over a layered halfspace: Geophysical Prospecting, v. 17, p. 82-101.

Olhoeft, G.R., 1977, Electrical properties of water-saturated basalt -- Preliminary results to 506K (233°C): U.S. Geological Survey Open-File Report 77-785, 6 p.

Pridmore, D.F., Hohmann, G.W., Ward, S.H. and Sill, W.R., 1981, An investigation of finite-element modeling for electrical and electromagnetic data in three dimensions: Geophysics, v. 46, p. 1009-1024.

Quist, A.S. and Marshall, W.L., 1968, Electrical conductances of aqueous sodium chloride solutions from 0 to 800°C and pressures to 400 bars: J. Phys. Chem., v. 72, p. 684-703.

Rai, C.S. and Manghnani, M.H., 1977, Electrical conductivity of basalts to 1550°C: Proc. Chapman Conf. on Partial Melting in the Earth's Upper Mantle, Dick, H.J.B. (ed.), Oregon Dept. Geol. Miner. Ind. Bull., 96, p. 219-232.

----------, 1981, The effects of saturant salinity and pressure on the electrical resistivity of Hawaiian basalts: Geophys. J. R. astr. Soc., v. 65, p. 395-405.

Ryan, M.P., Koyanagi, R.Y. and Fiske, R.S., 1981, Modeling the three-dimensional structure of macroscopic magma transport systems -- application to Kilauea volcano, Hawaii: J. Geophys. Res., v. 86, p. 7111-7129.

Ryu, J., Morrison, F. and Ward, S.H., 1970, Electromagnetic fields about a loop source of current: Geophysics, v. 35, p. 862-896.

Sidorov, V.A. and Gubatenko, V.P., 1974, On the resolution of electromagnetic prospecting by the build-up method: Physics of the Solid Earth (Engl. ed.), No. 3, p. 173-176.

Slichter, L.B. and Telkes, M., 1942, Electrical properties of rocks and minerals: in Handbook of Physical Constants, Birch, F. (ed.), Geol. Soc. Am. Sp. Paper 36, p. 299-319.

Smith, B.D. and Ward, S.H., 1974, On the computation of polarization ellipse parameters: Geophysics, v. 39, p. 867-869.

Smith, B.D., Zablocki, C.J., Frischknecht, F. and Flanigan, V.J., 1977, Summary of results from electromagnetic and galvanic soundings of Kilauea Iki lava lake, Hawaii: U.S. Geological Survey Open-File Report 77-94, 27 p.

Stoyer, C.H., 1976, Numerical study of the effect of two-dimensional conductors on the surface fields of a buried vertical magnetic dipole: Radio Science, v. 11, p. 343-349.

Stoyer, C.H. and Greenfield, R.J., 1976, Numerical solutions of the response of a two-dimensional earth to an oscillating magnetic dipole source: Geophysics, v. 41, p. 519-530.

Stoyer, C.H. and Wait, J.R., 1976, Analysis of source location errors for a magnetic dipole buried in a laterally inhomogeneous conducting earth: Pure & Applied Geophys., v. 114, p. 39-51.

Strange, W.E., Woollard, G.P. and Rose, J.C., 1965, An analysis of the gravity field over the Hawaiian Islands in terms of crustal structure: Pacific Science, v, 19, p. 381-389.

Twomey, S., 1977, Introduction to the Mathematics of Inversion in Remote Sensing and Indirect Measurements: Elsevier Sci. Pub. Co., Amsterdam, 243 p.

Ucock, H., Ershagi, I., Olhoeft, G.R. and Handy, L.L., 1980a, Resistivity of brine saturated rock samples at elevated temperatures: paper presented at 1980 Stanford Geothermal Workshop.

----------, 1980b, Electrical resistivity of geothermal brines: J. Petrol. Tech., April, p. 717-727.

Wait, J.R., 1962, Electromagnetic Waves in Stratified Media: Pergamon Press, Oxford.

Ward, S.H., Ryu, J., Glenn, W.E., Hohmann, G.W., Dey, A. and Smith, B.D., 1974, Electromagnetic methods in conductive terranes: Geoexploration, v. 12, p. 121-183.

Ward, S.H., Smith, B.D., Glenn, W.E., Riji, L. and Inman, J.R. Jr., 1976, Statistical evaluation of electrical sounding methods. Part II--applied electromagnetic depth sounding: Geophysics, v. 41, p. 1222-1235.

Wilt, M., Goldstein, N.E., Hoverstein, M. and Morrison, H.F., 1979, Controlled-source EM experiment at Mt. Hood, Oregon: Geothermal Resources Council Transactions, v. 3, p. 789-792.

Wilt, M., Goldstein, N., Stark, M. and Haught, R., 1980, An electromagnetic (EM-60) survey in the Panther Canyon area, Grass Valley, Nevada: Lawrence Berkeley Labs Technical Report LBL-10993, 97 p.

Young, H.D., 1962, Statistical Treatment of Experimental Data: McGraw-Hill Publishing Co., New York, 172 p.

Zablocki, C.J., Tilling, R.I., Peterson, D.W., Keller, G.V. and Murray, J.C., 1974, A deep research drill hole at the summit of an active volcano, Kilauea, Hawaii: GRL, v. 1, p. 323-326.

Zablocki, C.J. and Tilling, R.I., 1976, Field measurements of apparent Curie temperatures in a cooling basaltic lava lake, Kilauea Iki, Hawaii: GRL, v. 3, p. 487-490.

Zucca, J.P. and Hill, D.P., 1980, Crustal structure of the southeast flank of Kilauea volcano, Hawaii, from seismic refraction measurements: Bull. Seis. Soc. Am., v. 70, p. 1149-1159.